The analysis of UWB Radar System for Microwave Imaging Application

A thesis submitted to the University of London in partial fulfilment
of the requirements for the Degree of Doctor of Philosophy

By

Lei Li

Supervisors: Prof. X. Chen and Prof. C. G. Parini

School of Electronic Engineering and Computer Science

Queen Mary, University of London

May 2015

Statement of originality

I, Lei Li, confirm that the research included within this thesis is my own work or that where it has been carried out in collaboration with, or supported by others, that this is duly acknowledged below and my contribution indicated.

I attest that I have exercised reasonable care to ensure that the work is original, and does not to the best of my knowledge break any UK law, infringe any third party's copyright or other Intellectual Property Right, or contain any confidential material.

I accept that the College has the right to use plagiarism detection software to check the electronic version of the thesis.

I confirm that this thesis has not been previously submitted for the award of a degree by this or any other university.

To My Family

ACKNOWLEDGEMENTS

I would like to thank my supervisors, Professor Xiaodong Chen and Prof Clive for their guidance over the years.

I would like to thank all my colleagues in the antenna group, particularly Ms Yu Ping and Dr Min Zhou, Dr Su Hansheng, Dr Liu Xiaoming and Imran Shoaib, who gave me such a great enlightenment in my work.

My thanks also go to Dr Massimo Candotti, Mr Tony Stone, who devoted their time in helping me out in experiments.

Last but not least, a sincere thanks to my family. Their support was my ultimate motivation and I really appreciate their unconditional love and care for me.

ABSTRACT

Many research groups have conducted the investigation into UWB imaging radar system for various applications over the last decade. Due to the demanding security requirements, it is desirable to devise a convenient and reliable imaging system for concealed weapon detection. Therefore, this thesis presents my research into a low cost and compact UWB imaging radar system for security purpose.

This research consists of two major parts: building the UWB imaging system and testing the imaging algorithms. Firstly, the time-domain UWB imaging radar system is developed based on a modulating scheme, achieving a receiver sensitivity of -78dBm and a receiver dynamic range of 69dB. A rotary UWB antenna linear array, comprising one central transmitting antenna and four side-by-side receiving antennas, is adopted to form 2D array in order to achieve a better cross-range resolution of the target. In operation, the rotation of the antenna array is automatically controlled through the computerised modules in LabVIEW.

Two imaging algorithms have been extensively tested in the developed UWB radar system for a number of scenarios. In simulation, the "Delay and Sum (DAS)" method has been shown to be effective at mapping out the metallic targets in free space, but prone to errors in more complicated environments. However, the "Time Reversal (TR)" method can produce better images in more complex scenarios, where traditionally unfavorable multi-path interference becomes a valuable asset. These observations were verified in experiment in different testing environments, such as penetration through wooden boards, clutters and a stuffed sport bag. The detectable size of a single target is $8\times8\times1$ cm^3 with 30cm distance in a stuffed bag, while DAS can achieve the estimation of 7cm cross-range resolution and 15cm down-range resolution for two targets with sizes of $8\times8\times1$ cm^3 and $10\times10\times1$ cm^3, which fits within the theoretical prediction. In contrast, TR can distinguish them with a superior 4cm cross range resolution.

Contents

Vector wave equation in TR analysis

The specifications of some components used in the developed UWB imaging radar system

List of Figures

List of Tables

Abbreviations and Glossary

A/D   Analogue/Digital

BW   Band Width

BAVA   Balanced Antipodal Vivaldi Antenna

CW   Continuous-Wave

DAS   Delay and Sum

DAQ   Data Acquisition

DORT   Decomposition of Time Reversal Operator

EC   European Commission

EM   Electromagnetic

EVD   Eigen-Value Decomposition

FCC   Federal Communications Commission

FDTD   Finite Difference Time Domain

FFT   Fast Fourier Transform

FM   Frequency Modulation

GPR   Ground Penetrating Radar

HPBW   Half Power Beam Width

IFFT   Inversed Fast Fourier Transform

LNA   Low Noise Amplifier

LPF   Low Pass Filter

LOS   Line of Sight

MDM   Multi-static Data Matrix

MUSIC   Multiple Signal Classification

NI   National Instrument

PA   Power Amplifier

PSD   Power Spectral Density

RCS   Radar Cross Section

RF   Radio Frequency

RX   Receiving Antenna

SAR   Synthetic Aperture Radar

SNR   Signal-to-Noise Ratio

SVD   Singular Value Decomposition

TR   Time Reversal

TRM   Time Reversal Mirror

TRO   Time Reversal Operator

TX   Transmitting Antenna

TWI   Through-Wall Imaging

UWB   Ultra Wideband

VCO   Voltage Controlled Oscillator

VNA   Vector Network Analyser

Chapter 1 Introduction

1.1 Background

There are an abundance of radio signals propagating in the world, which simultaneously share the same medium. These signals are differentiated by various frequency bands. Each and every specific radio signal occupies a unique location in the radio spectrum. An Ultra-Wide Band (UWB) signal covers a relatively wider spectrum. Technically, UWB refers to signals or systems that either have a large absolute bandwidth (no less than 500MHz) or a large relative bandwidth (larger than 20% of the used Centre frequency).

UWB technology has been ever-developing over a century. In 1893, Heinrich Hertz used a spark discharge to produce electromagnetic waves, which naturally gave impulse signals with a very wide bandwidth. In 1894, Marconi Gugliemo used this large signal bandwidth to transmit and receive the first electromagnetic signals. However, nobody could effectively exploit the advantages of a large signal bandwidth at that time [1-3]. After more than half a century of slow progress, the UWB in military application was investigated in the 1960s. The development of the sampling oscilloscope by Tektronix and Hewlett Packard in the early 1960s and the corresponding techniques such as avalanche transistors and tunnel diodes in early 1970s for generating sub-nanosecond baseband pulses sped up the development of UWB radio [4]. Gradually, the success of UWB in the military field soon attracted attention and the focus of UWB technology has moved onto the domain of communications, detection, localisation and imaging.

The popularity of UWB technology, especially in radar systems, is well understood. Its ultra-short pulses can deliver more target information than the conventional long-pulse ones. In 1974, the first UWB radar system for penetrating the ground became commercially successful at Geophysical Survey Systems Inc. In 1989, the term UWB was introduced by the Department of Defense in USA. Since then the wide global attention has driven UWB technology from the military domain to the commercial one. Many commercial applications started to use UWB signals in such a way that free spectral bands became scarce and their allocation became difficult. The need to protect the existing UWB systems became crucial. In 1998, the FCC

started a commission on UWB system regulation for license-free power density levels. In March 2002, a final spectral-mask was introduced by the FCC for different application scenarios. Figure 1.1 illustrates the evolution of UWB technology. The major events that led to the evolution of UWB are highlighted in Table 1.1
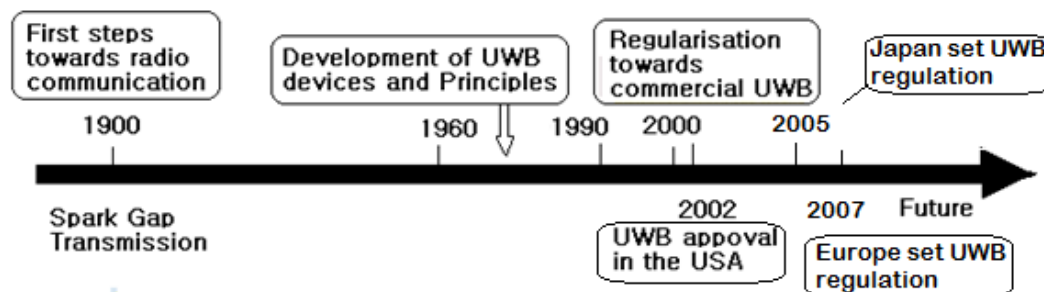
Figure 1-1 Evolution of UWB technology

According to the First Report and Order defined by FCC, the UWB system is very strictly regulated. The operating frequency band ranges from 3.1GHz to 10.6GHz at a limited transmitting power of -41.3dBm/MHz in the United States [5]. In Europe, the European Community has chosen a spectrum narrower than its American counterpart, including two separate bands: 3.1-4.8GHz and 6.0-8.5GHz [6].

The short pulse duration of the UWB signal makes it a perfect candidate in radar detection and imaging applications. More information on the targets can be obtained due to the broader bandwidth. For instance, a typical UWB pulse lasts for less than 1ns, which equals to less than 30cm of wavelength in free space, thus a down range resolution of 15cm. In contrast, a traditional narrow band radar system with pulse duration of 1 μs, which is equal to 300 m of wavelength in free space, can only provide a down-range resolution of 150m. This wavelength can be significantly larger than the size of the target of interest, making it almost impossible to achieve detection purpose. Therefore, the reduction of pulse duration can improve the down-range resolution and acquire more information about the nature of the target. [7-9]. Meanwhile, lower power output and pulsed data processes in UWB technology can also be instrumental in the design of UWB systems. They can improve the speed of data transmission, lower the probability of interception, reduce the multipath effect and offer more precise ranging and localisation. In general, UWB technology has been regarded as one of the most promising wireless technologies in the industry.

Table 1.1 Major events in the evolutions of UWB technology in history

Year/Period	Events
1893	Electromagnetic Waves Experiment
1950s	Phased array radar
1960s	Advanced development in time-domain electromagnetics
1970s	Avalanche transistor and tunnel diode detector
1972	Short range radar sensor
Late 1970s	Narrow baseband pulse fixture
1980s-1990s	Advances in radar technology
Late 1990s	Commercial UWB devices and systems
2000s	IEEE standard on UWB

The applications of UWB can be generally categorised by three purposes: medical testing, industrial detection and civil engineering. A few examples can include: wireless network communications, remote sensing and tracking, ground penetrating radar, "see-through" wall systems, diagnostic medical imaging and breast cancer detection. Although some of the applications are not yet mature, two of them have drawn more attention than others. These are short distance communication systems and radar imaging systems. This thesis is mainly focusing on the latter. Table 1-2 presents some major applications of UWB technology [10].

Table 1.2 Current main applications of UWB [10]

Wireless Communications Systems	High speed local and personal area networks (WLAN/WPAN); Short range radios; Military communications; Indoor broadband cellular phones
Radar / Imaging and Sensing	High-resolution radar systems; Vehicular & collision avoidance radars; Ground penetrating radar (GPR); Through wall imaging (Police, Fire, Rescue) and motion sensing; Underground imaging; Medical imaging (Breast cancer imaging and Diagnosis; Surveillance; Robotic sensors
Location Detection	Precision location; Identifying individuals; Asset tracking
Intelligent Transportation Systems	Driving and parking aids, electronic signs

1.2 Challenges and motivations

Microwave imaging radar systems should be able to provide effective capabilities for reconstructing and remapping obscured objects of interest. Most of the applications developed so far mainly aim at addressing detection issues in real-life scenarios. For instance, the need to "see-through" the ground brought about the development of "Ground-Probing Radar". Buried objects, including deserted landmines, archaeological remnants and underground natural resources, now have a high likelihood of being positively detectable. Another application of interest arises from "See-Through-Wall (STW)" Imaging. Obscured vehicles and personnel can no longer be kept invisible or undetectable within or behind extremely complex environments, such as woods, bricks, concrete, bushes and even forests. STW Imaging is invaluable for many organisations including the military, law enforcement and rescue/search agencies. Due to the expansion of globalisation, security check-ups nowadays also require more than just one module to assure public safety. Microwave imaging systems are expected to detect drugs, contraband, explosives and even ceramic and metallic weapons. The prospect of reliable detection is necessary in the design of these imaging platforms.

There are many different technologies used for See-Through purposes, including: Ultrasound imaging, Thermal (IR) imaging, Magnetic detection, X-ray imaging, Millimeter wave and

UWB Radar. Each of them has its own strength. For example, Ultrasound is able to see through metal sheets; Magnetic detection can detect submarines and minerals due to their disturbance of normal earth field; Optical and infrared-based systems are able to see through darkness with high imaging resolution; Radar can provide good resolution relative to other approaches. However, most techniques have their own weaknesses as well. For instance, millimeter wave and IR have limited penetration capabilities in certain media such as airy smoke; Traditional narrow band radar suffers from multipath issues; Ultrasound detection relies too much on line-of-sight propagation and its penetrating range is only a few inches; an X-ray system is often expensive, bulky, non-portable and exhibits health-risky ionising effects for people. By comparison, UWB radar stands out for its inherent fine resolution, good penetration into many common materials and all-weather operational capability.

However, challenges still exist for the full exploitation of UWB radar imaging systems and these can be summarised below:

1) **Vulnerability to certain obstructions with severe signal attenuation in high loss materials.**

   UWB pulse radars operating at higher UWB band work well for line-of-sight or "see-through" low-loss materials detection, such as wood and glass, but suffer from the high attenuation when seeing through high-loss materials, such as wet soil, human tissue, and other high water-content materials. When UWB signals propagate into opaque material, they suffer reflections and absorption.

2) **The need for a robust radar system with adequate dynamic range to differentiate useful signals from irrelevant ones and noise.**

   Signals from targets can be very weak and unavoidably distorted by clutter and unwanted multipath signals. This makes it difficult to extract relevant information, leading to detection confusion, erratic tracking and drawing erroneous conclusions. Multipath components can also cause inter-symbol interferences, resulting in errors while making decisions as to whether a signal is wanted or not. A robust dynamic range can offer the capability of capturing small scattered signals from the target notwithstanding other undesired and irrelevant wave propagations.

3) **Traditional imaging reconstruction techniques find difficulty in coping with some complicated testing scenarios.**

The down range and cross range resolutions of a UWB imaging system can be greatly influenced by adopted image reconstruction algorithms. Appropriate beam-forming methods are vital to achieving higher quality imaging. When a severe multipath effect exists, a traditional imaging method finds it difficult to differentiate multiple targets..

4) **Development of a cost-effective and portable UWB radar system with an unconventional antenna structure to acquire more data.**

A portable system is more desirable because of various practical operational scenarios, such as installation behind walls, mounting on the top of cars, carrying in suitcases and even being used as handheld devices. Furthermore, as the only part which cannot be integrated into the system, antenna design and arrangement needs proper consideration. The number of antennas needs to be controlled to balance the cross range resolution and system portability. Most receiving antennas nowadays are synthetic arrays, so the more antennas that are used, the more complicated the switches are and the more likely that noise and structural complexity would be brought to the system itself.

Above all, what is required is a cost-effective and portable UWB See-through radar system aided with various imaging methods. The crucial active and passive components in radar systems, such as oscillators, mixers, filters, and amplifiers, can be off-the-shelf products from various suppliers; while the UWB signal generator and acquisition system need customised designs. A cost-effective UWB imaging system should provide experimental verification and evaluation of any see-through imaging applications. The primary goal of this research is to develop a cost-effective and portable real-time UWB image system.

1.3 Objectives and contributions

The project aims to develop a compact, cost-effective and stand-alone UWB imaging system for detecting and imaging metallic targets in various environments with the aid of two different imaging methods. The complementary effect of each method can help the radar imaging system to cope with difficult propagation media and achieve satisfactory resolutions. The objectives of the project are as follows:

1) To develop a UWB radar system for imaging purpose. However, the usable frequency band is limited by the UWB Pulse generator and VCO and covers from 4GHz to 5GHz with a centre frequency of 4.5GHz.

2) In order to ensure the compactness of the system, the bulky motor and its driving box needs to be replaced by smaller one with the LabVIEW controlling module. The heavy power supplies need to be replaced by smarter power adapters. All the wires need to be arranged in a concise and convenient way.

3) Two image reconstruction methods are discussed and achieved. Multipath effect is the main issue of discussion. The "Delay-and-Sum (DAS)" method can produce confusing imaging results in a very complicated medium. However, this complexity can be converted to a performance-boosting element in another imaging technique called the "Time-Reversal (TR)" method. The comparison of these two methods will be made and analysed.

The main contributions of the thesis are presented below in detail:

1) **Measures taken to simplify the UWB radar imaging system**

   The adoption of the step motor, its driver and the LabVIEW module has simplified the design of the rotating antenna array. The use of a DAQ device from the National Instrument Company to control the switch electronically and the introduction of power adapters to simplify the powering system, make the most congested part of the system into a 50 x 50 cm^2 wooden box. This has avoided the original sprawling cables and greatly enhanced the reliability of the system.

2) **Assessing the time-reversal method in the UWB imaging system**

   A standard TR technique has been applied to UWB image reconstruction. A comparison between "Delay and Sum (DAS)" and Standard "Time Reversal (TR)" has been made to assess the strength and weakness of these two imaging methods.

3) **A study of UWB imaging results sensitivity**

The sensitivity of the UWB imaging system has been studied, through varying the array aperture, range distance and size of a single target.

4) **Experimental analysis of down-range and cross-range resolutions of the UWB imaging system**

The UWB imaging system is tested in four different scenarios, i.e. free space, multipath space, "see-through" a wooden board and "see-through" a packed sports bag. The down-range and cross-range resolutions have been analysed by employing DAS and TR imaging methods.

1.4 Organisation of the thesis

The rest of the dissertation is organised as follows:

Chapter 2 gives a detailed system analysis of UWB radar for imaging purposes. It first presents the basic UWB radar technology in frequency domain and time domain. Then the latest developments of UWB imaging systems are reviewed. Imaging facilities for medical purposes, ground-probing investigations, security detection and industrial services are summarised in different universities, commercial companies and national departments.

Chapter 3 mainly focuses on the two beam-forming methods used in the thesis. First, the history of various beam-forming methods for imaging reconstruction is reviewed. The Delay and Sum imaging algorithm is discussed first and then the Time Reversal method follows. Simulation in CST Microwave Studio is used to demonstrate the effectiveness of both methods in the different environments. The spatial and temporal focusing ability of TR and its super-resolution feature are highlighted. The advantages and disadvantages of each method are presented.

Chapter 4 describes the implemented UWB imaging system. The system architecture is introduced first, including its transmitting-end and receiving-end. The link budget is discussed to demonstrate its dynamic range for detection purposes. The rotating antenna array is used to collect the received signals and some steps have been taken to simplify the whole system for the purpose of portability.

Chapter 5 presents detailed measurements using the developed UWB imaging system in four different scenarios, i.e. free space, multipath space with highly-reflective rods, through a wooden board and in a packed sport bag. The detecting range and cross range estimations of a single target are researched first, then the down-range and cross-range resolutions of the UWB imaging system are investigated. Full analyses have been adopted to explain the limitations and strengths of each image reconstruction method.

Chapter 6 concludes the research work covered in this project. The contributions are highlighted and future work to improve the UWB imaging system is also proposed.

Reference

[1] "Ultra-Wide Band: a Disruptive RF Technology?" September 10, 2002, Intel Research &Development, Intel Corporation 2002

[2] T. W. Barrett, "History of ultra wideband (UWB) radar & communications: Pioneers and innovators" in Proc. Progress in Electromagnetics Symposium, Cambridge, MA 2000

[3] B. Mihai, "Ultra Wide Band Technologies", Research Seminar on Telecommunications Software, Autumn 2002, Available on: www.tml.hut.fi/Studies/T-110.557

[4] K. K. Siwiak, "A Gentle Introduction to Ultra-wide Band (UWB) radio Technology", Available on: www.SunCam.com

[5] Federal Communications Commission, First Report and Order 02-48, February 14, 2002

[6] Draft amended CEPT ECC Decision ECC/DEC/(06)12: "ECC Decision of [1 December 2006] on complementary regulatory provisions for devices using Ultra-Wideband (UWB) technology", June 2008

[7] James D. Taylor, Introduction to Ultra-Wideband Radar Systems, 1994

[8] E. Perl, "Review of Airport Surface Movement Radar Technology", Aerospace and Electronic Systems Magazine, IEEE, Vol: 21, Issue: 10, Page (s): 24-27, 2006

[9] B. Allen, M. Dohler, E.E. Okon, W.Q. Malik, A.K. Brown, D.J. Edwards, Ultra-wideband Antennas and Propagation for Communications, Radar and Imaging, John Wiley & Sons, Ltd. 2007

[10] V. Lakkundi, ―Ultra Wideband Communications: History, Evolution and Emergence‖, Acta Polytechnica Vol. 46 No. 4, 2006

Chapter 2 Review of the UWB Technology

The UWB radar system generates and transmits a very short pulse (normally the duration of a nanosecond) through the transmitting antenna. The signal travels in free-space at the speed of light. When it meets a target, some of the signal is reflected from the object and returns to the receiving antenna. The time delay between the transmitted and received signal represents the distance between antennas and the target. Based on the travelling distance, UWB radar can be categorised into two types: short range radar and long range radar. The latter is mostly used for surveillance purposes, such as over-the-horizon radar and remote sensing radar. In contrast, short range radar has more commercial and industrial applications. Due to the attractions offered by short range radar systems of a detecting range in centimeters or meters, and at relatively high resolutions, as well as affordable testing and assembly cost, more and more institutions and companies are working on such systems. A lot of effort has been made to design UWB radar systems to cater for as many scenarios as possible, but the integration of sub-systems is technically challenging and time-consuming. The classification of UWB radar systems is given in the Figure 2.1.
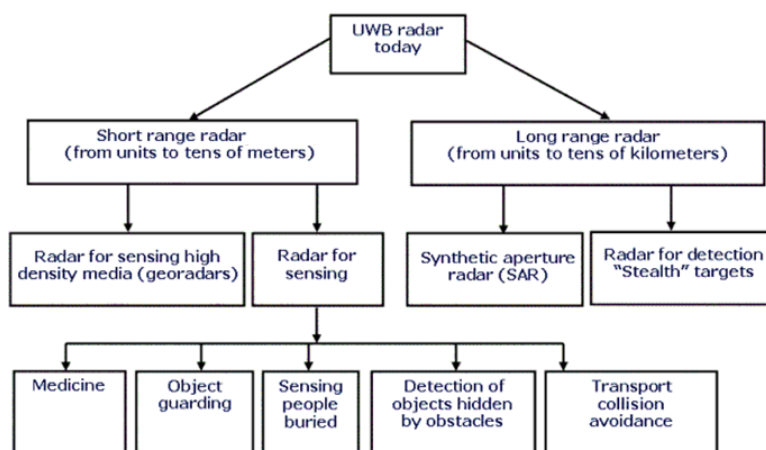
Figure 2-1 Classification of UWB radar system [1]

2.1 The Radar equation in "see-through" scenarios

The Radar equation indicates a useful mathematical relationship for many key factors in radar systems, such as radar system parameters, target parameters and background effects such as clutter and noise etc. So, when developing an effective system, the basic radar equation should be followed.

Assuming the maximum detection range for a radar system is R, the value is defined by the radar equation [2], as expressed below:

$$R^4 = \frac{P_A G_t G_r \sigma \lambda^2}{(4\pi)^3 kTBN_f L(SNR)} \qquad (2-1)$$

Where

P_A: Transmitted average power;

G_t: Transmitting antenna gain;

G_r: Receiving antenna gain;

L: System loss;

KT: Noise power density;

N_f: Noise figure;

SNR: the minimum detectable Signal to Noise ratio;

σ: Radar cross section (RCS).

B: Effective noise bandwidth of the radar

For "see-through" scenarios, the loss induced by the obstructions needs to be considered in the calculation. Thus, the Equation (2-1) is re-written as:

$$R^4 = \frac{P_A G_t G_r \sigma \lambda^2}{(4\pi)^3 kTBN_f LW(SNR)} \qquad (2-2)$$

Here, W is added as the obstacle loss in dB.

For different obstructions in the "see-through" application, the loss depends on both dielectric properties of the media and the operating frequency range. M. Farwell's team have done some experiments and obtained the signal attenuation of five different obstructions within a rather broad frequency band from 0.5 to 6GHz, as shown in Figure 2.2 [3].
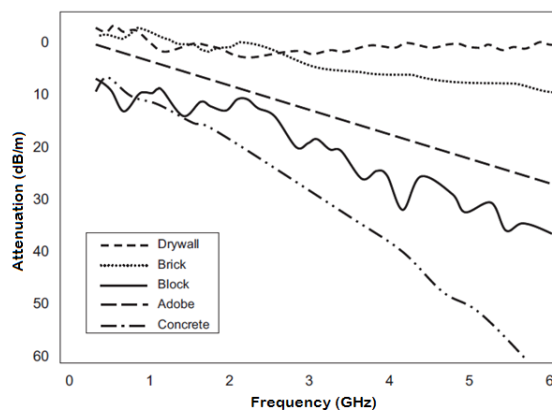
Figure 2-2 Wall attenuation vs. frequency (500 MHz to 6 GHz) [3]

The study shown in Figure 2.2 focused on the penetration of wall materials, and thus was an example for a "see-through the wall" scenario. Another use of the Radar equation is that it can estimate the dynamic range of Radar systems. Considering different targets, which may present varied "Radar Cross Section (RCS)" characteristics, dynamic and SNR can be estimated. For example, in the scenario of detection of a human being with a 1 m^2 RCS, if both the transmitting and receiving antenna gain are 10dB, the SNR would be estimated as 14dB for a reliable detection. Another example would be the wall penetrating scenario. If a concrete wall causes 30dB loss in operating frequency at 10GHz and the other parameters stay the same, the dynamic range for the system could be approximately evaluated to be 54dB.

For the proposed system in the thesis, the link budget and dynamic range study is presented in detail in Chapter 4.

2.2 Range accuracy, range resolution and cross range resolution

For a UWB radar system, range accuracy, range resolution and cross range resolutions are very important parameters to identify.

Range-accuracy represents the uncertainty in a measurement of the absolute distance from radar to an object; while range resolution means the minimum separable space between two targets in order to distinguish one from the other. In UWB radar imaging systems, these two factors play important roles in system design.

Range resolution reflects radar's ability to resolve multiple targets correctly, illustrated in Figure 2.3. Ideally, two echoes mean two targets. When the time delay between the echoes is greater than the pulse duration τ , they are separable as shown in Figure 2.3(a). When the targets are getting closer, to a degree that the time delay is shorter than the pulse duration, the echoes will merge which means the two targets are not distinguishable, as shown in Figure 2.3(b). The time limit of resolvability of two targets is the time delay similar to the pulse duration, as shown in Figure 2.3(c). The range resolution ΔR is expressed as $\Delta R = c\tau/2$, where c is the speed of light.
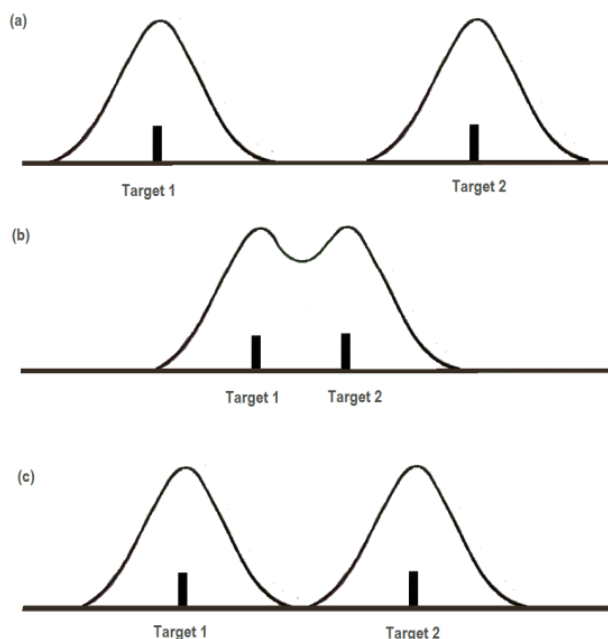
Figure 2-3 Range resolution expressed in two propagating echoes [2]

In conclusion, if the objects to be detected are small (small RCS), then the radar system needs shorter pulse duration to distinguish multiple objects. The UWB radar system has broader bandwidth, shorter pulse duration and higher range resolution than conventional narrowband

radar. The proposed UWB radar system in the thesis makes use of picosecond to nanosecond pulse duration, meaning that the range resolution can reach as small as 15cm.

Cross-range resolution is one parameter in distinguishing multiple targets placed horizontally along the same line parallel to the direction of the array. Its calculation is based on the beam width of the antenna array, as shown in Figure 2-4. Assuming the range from the antenna to the target is at the distance of R, the antenna's beam width is θ, the cross-range resolution δ is defined as $\delta = 2R\tan\frac{\theta}{2}$.
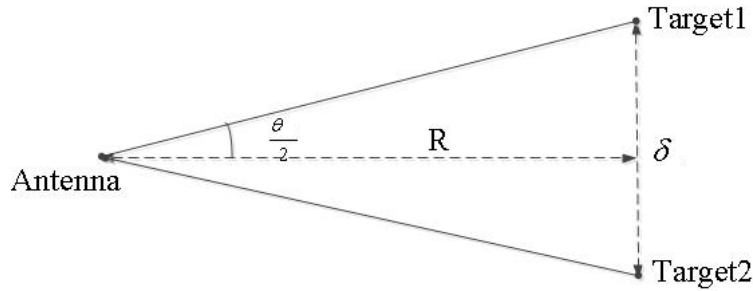
Figure 2-4 Cross-range resolution

In contrast, range accuracy relates to the bandwidth occupied by the radar system as shown in Figure 2.5. In Figure 2.5(a), the radar emits a continuous wave and measures the phase of the echo to find all the possible positions of the target. The result is ambiguous and non-determinate. A second signal with a different frequency is added to the transmission. This results in another set of ambiguous positions of the target. By combining two results, ambiguity can be reduced, shown in Figure 2.5(b). This process can repeat and a third signal with another frequency is added to the same scenario as shown in Figure 2.5(c). By overlapping all three results, the true position of the target can be sharpened and the target is estimated precisely. So as more frequencies are added, the ambiguity can be eliminated more effectively and the range measurement can achieve greater accuracy.

The other factor determining the accuracy of the range measurement is SNR. In general, any measurement made with a basic resolution of L has an error of $\delta L = \frac{L}{\sqrt{2SNR}}$. For UWB radar system, the error can be expresses as $\delta R = \frac{c}{2BW\sqrt{2SNR}}$.
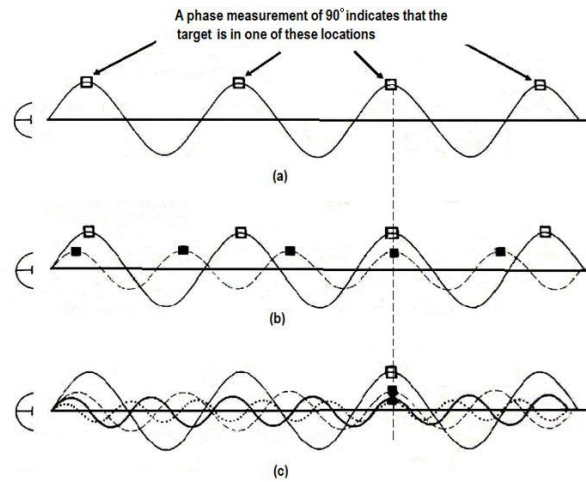
Figure 2-5 Radar range accuracy dependent on bandwidth [2]

2.3 Measurements based on frequency and time domain

2.3.1 The Frequency-domain measurement system

The basic architecture of a measurement system in frequency domain is shown in Figure 2-6.
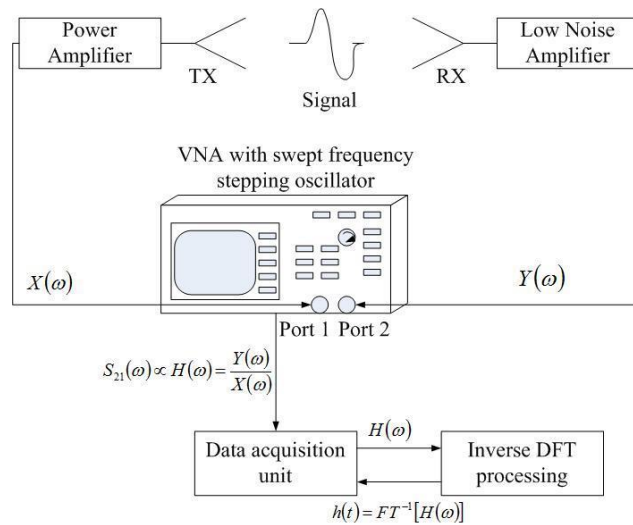
Figure 2-6 UWB imaging system based on frequency domain measurement [4]

It consists of a VNA withswept frequency oscillator and mainly measures the transfer function of the signals in terms of magnitude and phase. VNA plays the essential part in the measurement. One port acts as the signal source to activate a transmitting antenna and the other

port can effectively retrieve received signals via a receiving antenna. In order to reduce the system loss, RF cables of high quality are required for connections.

The frequency domain measurement method has its own advantages. It may provide a larger dynamic range. Its structure is relatively simpler and quicker to assemble compared with the time domain system. Because the frequency domain measurement is carried out at a single frequency point over the entire frequency range, it translates to a high frequency resolution and a probable high cross-range resolution in imaging.

The disadvantage of the frequency domain measurement method is also straightforward in its own nature. The frequency domain testing system needs to sweep all the segmented frequencies to complete the whole measurement. UWB system measurement would inevitably be time-consuming. A possible way of reducing the time would be to adopt stepping mode rather than sweeping mode in VNA. Besides, the down-range resolution is proportional to the time duration. It would be necessary to increase the bandwidth, but the number of measured points will increase correspondingly to maintain accuracy, which will lead to a longer testing time. So there is always a compromise between good frequency resolution, the required number of measurements and the whole operating time, making it impossible to achieve fast imaging in real time with high resolutions.

Another complexity lies in the data processing. FD measurement results can only be analysed through "Inverse Fast Fourier Transform (IFFT)" in time domain. This will increase computational difficulty and may result in longer calculation time.

2.3.2 The time-domain measurement system

Generally, there are two types of UWB see-through systems based on the time-domain technique: the carrier-free system and the modulating system. For the former, as shown in Figure 2.7, there are transmitting antennas, receiving antennas, a pulse generator, a digital sampling oscilloscope and a triggering signal generator [5]. In contrast, there are more components in a modulating system, as shown in Figure 2.8. They are: a function generator, mixers, splitter and hybrid circuit, low noise amplifier (LNA) and power amplifier (PA) [6].
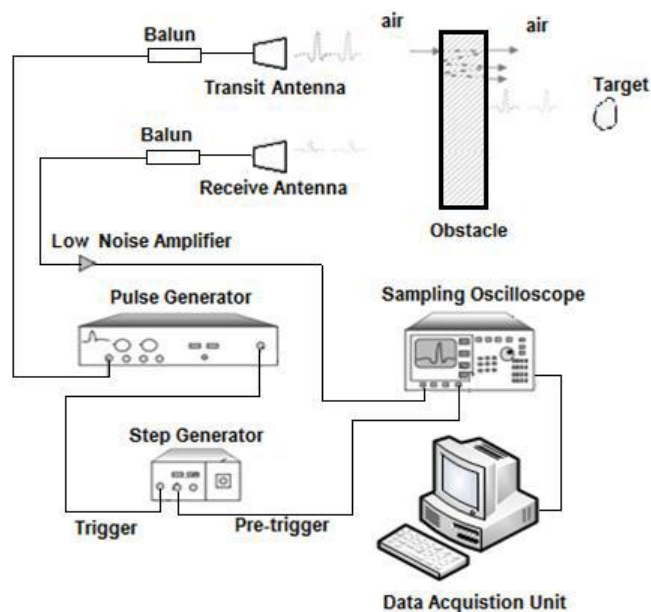
Figure 2-7 Schematic set-up of a carrier-free system for time-domain measurement [5]
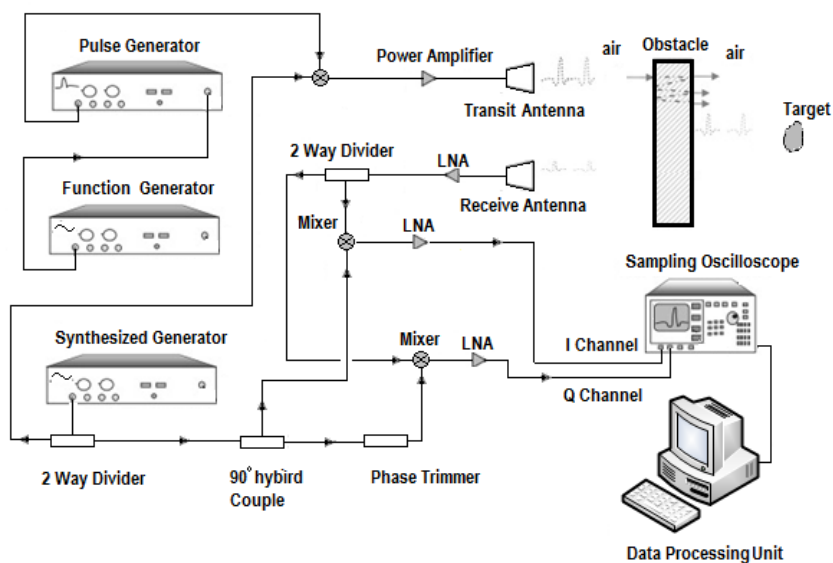
Figure 2-8 Schematic set-up of a modulating system for time-domain measurement [6]

Another difference in the time domain measurement system is the structure of the transmitting and receiving ends. For a carrier-free system, the impulse signals are fed to the transmitting antenna via a Balun which converts the unbalanced coaxial cable terminals to balanced antenna feed terminals, while a digital sampling oscilloscope is used to acquire the signals from the receiving antenna. In a modulating system, the impulse signal needs to be "up-converted" to a higher frequency range by mixing with a local oscillator signal and the received modulated

signals should be "down-converted" to base frequencies and separated into two channels (I and Q) for further processing. No matter which testing method is considered, all the components should have the required UWB frequency band and have linear phase characteristics. Any mismatch will induce errors in the test.

One important issue in UWB time domain measurement is the synchronisation of transmitting and receiving signals. In theory, the time delay introduced by the propagation path can be calculated and compensated by adjusting the time delay between the pre-trigger signal and the delayed trigger signal. In practice, this part can be pre-tested and excluded in the first round of signal processing. Another issue is the calibration, which must eliminate the effects of non-ideal characteristics of measuring instruments from the measured data before each experiment is carried out. Proper calibration can remove any possible interference and guarantee the consistency of all the measurement.

The choice of either frequency domain or time domain measurement largely depends on the purpose of radar construction. Currently, due to its great potential, the time domain system is prevalent in system designing and construction. It can be cost effective, made for portable application and offers direct testing results. So the imaging radar system in this thesis is based on time domain. In order to demonstrate the complexity of equivalent frequency domain measurement, a comparative analysis is carried out below.

For a time window size T and number of sampling points N, the sample spacing is $\tau = {}^{T}/_{N}$ and the sample points $t_k = k\tau$, for k = 0, 1, ..., (N-1), then define a discrete time domain signal as $f_k = f(t_k)$. The frequency sampling points $\omega_n = {}^{2\pi n}/_{T}$.

For example, assuming a time domain pulse signal with a period of 50ns, this can be translated to 7.5m detection range.

$$D = \frac{50ns * c}{2} = 7.5m \qquad (2-3)$$

Assuming the pulse signal is sampled at 100ps/sample (which is 10Gs/s) interval for a desired range resolution 0.15m, the system bandwidth is:

$$BW = \frac{0.15m}{100ps/sample} = 1.5GHz \qquad (2-4)$$

To replicate the same system in the frequency domain with the same system bandwidth, assuming the sweeping step of 5MHz, the total number of frequency points is 1.5GHz/5MHz.

So, 300 frequency points are needed to match the equivalent time-domain operation. It is impractical to design such a frequency domain system to meet this requirement.

2.4 Data acquisition methods

There are three basic data acquisition methods in radar systems. The mono-static system is the simplest one, as shown in Figure 2.9.
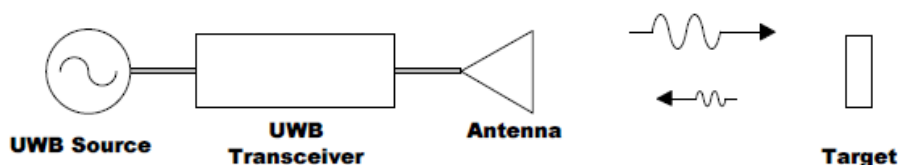
Figure 2-9 The mono-static system set-up

A single antenna acts as a transceiver. A duplexer is needed to separate transmitted and received signals. In order to increase the cross range estimation in imaging application, the antenna needs to move around to various locations to collect relevant information of the target. It is a simple set-up in which the size of the imaging system is extremely limited.

The bi-static radar system refers to two separate antennas, one acting as a transmitter and the other as receiver, as shown in Figure 2.10. The antennas are placed sufficiently far apart to ensure that the angles and range information of the target are well discriminated. The range distance estimation is based on the time delay in the propagation.
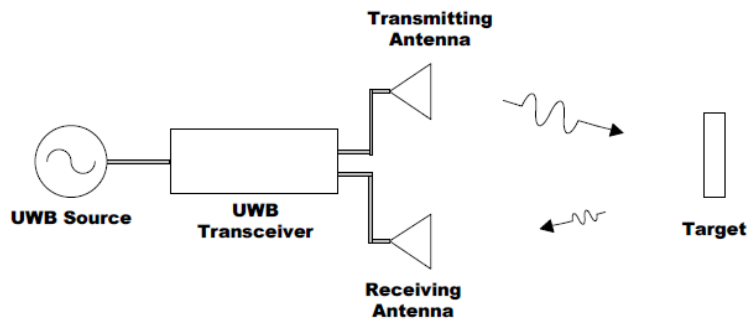
Figure 2-10 The bi-static system set-up

A multi-static radar system includes a multiple spatially diverse mono-static set-up, shown in Figure 2.11(a) and a multiple bi-static set-up, as shown in Figure 2.11(b). It has broader coverage, attains a higher SNR and would be much less vulnerable to interference. The RCS analysis can be made because of the different perspectives of the target observation. The spatial diversity offered by the distributed receiving elements allows for an increase in effective receiving antenna aperture, in favor of better cross-range resolution.
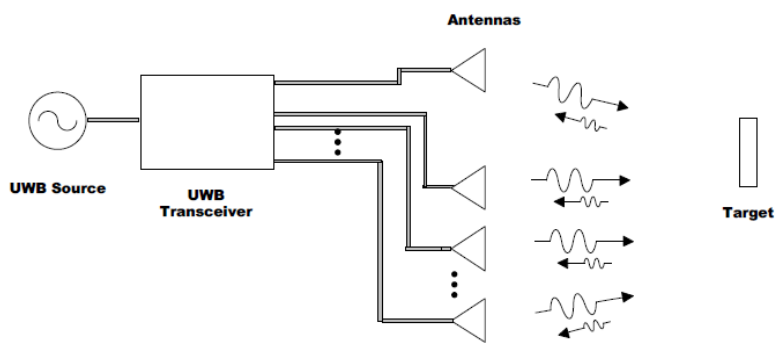
(a) Multiple Mono-static set-up
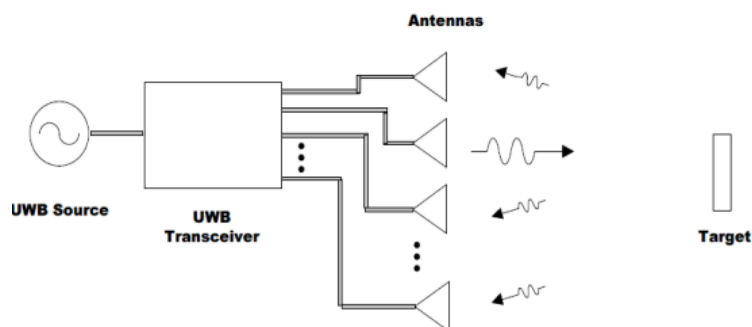
(b) Multiple Bi-static set-up

Figure 2-11 The multi-static radar system

It is worth mentioning that different choices of multi-static set-ups may cause differences in signal processing in a later stage. The proposed UWB radar imaging system is a rotary multiple Bi-static set-up, with only one antenna acting as transmitter and the rest as receivers. So the collected data can be viewed as a 1D matrix. However, if all the antennas in the system can be used as transceivers, it means the testing results can form into a 2D matrix. A linear algebra manipulation can be applied to a 2D matrix, also dubbed as Multi-static Data Matrix (MDM). This is also called inter-element impulse responses. When the measurement is conducted in time domain, assuming the time is discretised into multiple moments, this 2D MDM will become a 3D matrix. Further matrix manipulation can help with the imaging process, such as Single Value Decomposition (SVD) and Eigenvalue Decomposition (ED).

2.5 Review of the current UWB radar imaging systems

2.5.1 Research work in Universities

Research into UWB radar systems has been extensive in the academic world. Academic interest mainly focuses on radar system stereotype construction and its possible transition to industrial products. Practical and beneficial applications are the motivation for invention and innovation. Among these applications, breast tumour detection and imaging have attracted huge attention due to the medical benefits. Compared to other internal organs like the brain or heart, the breast is regarded as an easier model to investigate. The key detection and imaging method depends on a considerable dielectric difference between tumourous and healthy tissue [8].

Ground Penetrating Radar (GPR) is another useful application. GPR can equip researchers with the penetration capability of up to a few hundred meters in various geological terraces. The work can include a wide range of inspection tasks, such as the detection of buried pipes underground and embedded layers under roads, the mapping of steel structures concealed in concrete structures and examining and surveying the subsurface of the Moon and Mars [2]. The major challenge for GPR is that the electrical properties of the ground can directly interfere with the target signature [9]. So a customised algorithm is needed to remove the strong reflection and distortion from the ground.

Wall Penetrating Radar is another hot topic. Instead of penetrating vertically down the ground, detection through walls, or other similar obstructions, enables many useful applications, such as urban warfare, counterterrorism and disaster rescue. By replacing the wall with bags or luggage, another useful application arises in civil security inspection, showing potential advantages over X-ray radiation testing devices. Detecting metallic targets in a bag is one of the experimental subjects in Chapter 5.

A review of the latest academic advances is presented below:

Prof Paul Meaney's team in Dartmouth Engineering School, USA

Prof Paul Meaney's team carried out the first clinical trial actively to probe the breast with an antenna array working from 300MHz to 1GHz. The antenna array was immersed in 0.9% saline surrounding the pendant breast during the test. The system transmitted the signal from one antenna at a time and sequentially measured the received signals at each of the opposite antennas. The received signals were down-converted with a reference signal to produce a low-frequency response sampled by an analog/digital (A/D) board. The signal information of amplitudes and phases were extracted by a software-based lock-in amplifier technique [10-12]. In 2013, the research outcome from this group demonstrated that Magnetic Resonance (MR) and Microwave Tomography (MT) can be complementary and synergistic to each other. The integration challenges have been overcome in combining MT with MR to produce a new co-registered, multi-modality breast imaging platform, named as "magnetic resonance microwave tomography" shown in Figure 2.12.

(a)   (b)   (c)
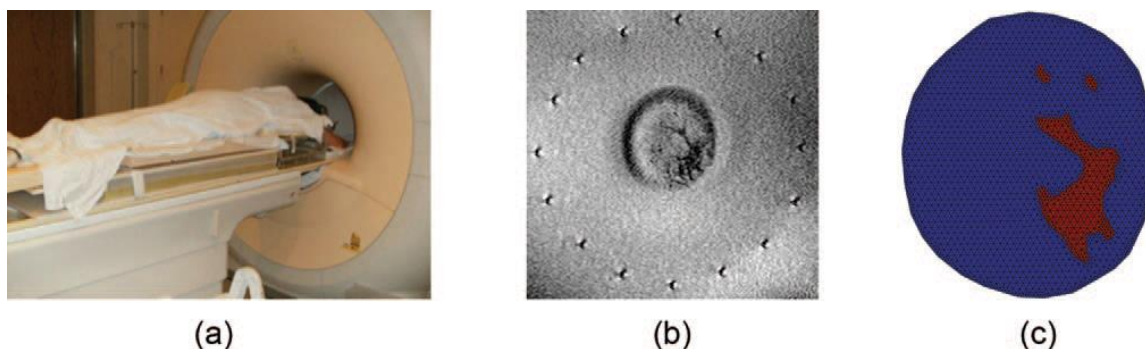
Figure 2-12 (a) Photograph of a subject ready to undergo a MRMT breast exam;
(b) Anatomically coronal T_1-weighted MR of the subject's left breast in the plane corresponding to the center of the active section of the MT antenna array;
(c) Segmented soft prior mesh derived from the MR image in (b) [13]

The algorithm used was a Gauss-Newton iterative solver with multiple optimisations to reduce the computation time of 3D image reconstruction. The promising results showed a MR SNR exceeding 40dB, and an MT SNR of 20dB, which are sufficient for image reconstruction. The errors between the recovered dielectric properties and actual ones can approach 5%. [13]

Prof Susan Hagness's team in University of Wisconsin, USA

As early as 2004, Prof. Susan Hagness presented a mono-static UWB radar system. This UWB system synthesised an antenna array by scanning the single horn antenna to each array position around the phantom breast, sequentially transmitting a swept-frequency signal and receiving the backscatter. This UWB radar imaging system with the frequency band of 1-11 GHz used the confocal algorithm based on FDTD method to detect and image a possible breast tumour, shown in Figure 2-13 (a), (b) and (c) [14-18].

(a) (b) (c)
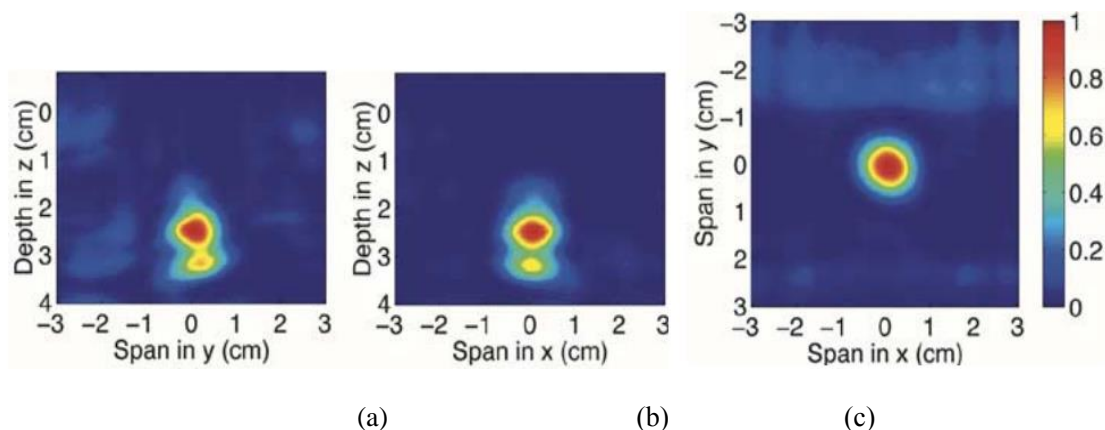
Figure 2-13 FDTD imaging results of a 4-mm-diameter synthetic tumor located at a depth of 2 cm below the skin surface. (a) Imaging in y-o-z plane; (b) Imaging in x-o-z plane; (c) Imaging in x-o-y plane [17]

Afterwards, the main research focus switched to the development of bio-compatible contrast agents that enhance the performance of diagnostic and therapeutic microwaves and the development of microwave thermal therapies. In 2014, a focal beam-forming enhanced formulation of the distorted "Born Iterative Method" (DBIM) for microwave breast imaging has been proposed. This incorporation has the potential to mitigate the effect of noise on the image reconstruction and creates reconstructions of higher fidelity with respect to the exact dielectric profiles of the phantoms than the non-focal schemes in low SNR scenarios. [19]

Prof Elise Fear's team in University of Calgary, Canada

Prof. Elise Fear's team has developed a mono-static "Tissue Sensing Adaptive Radar" (TSAR) over the frequency range of 50MHz to15GHz, as shown in Figure 2-14. A single sensor attached to an arm scanned a breast and reflections were recorded at a set of pre-set locations. The algorithm operated as follows: first, the skin's significant reflection due to its electrical properties was removed; then, the reflections were focused to form an image by time-shifting and summing the signals at a given focal point; lastly, a 3D image was created by scanning the focal point through the whole region of interest [20-22]. One of the phantom testing results is given in Figure 2-15 [23].

Figure 2-14 TSAR prototype system [23]
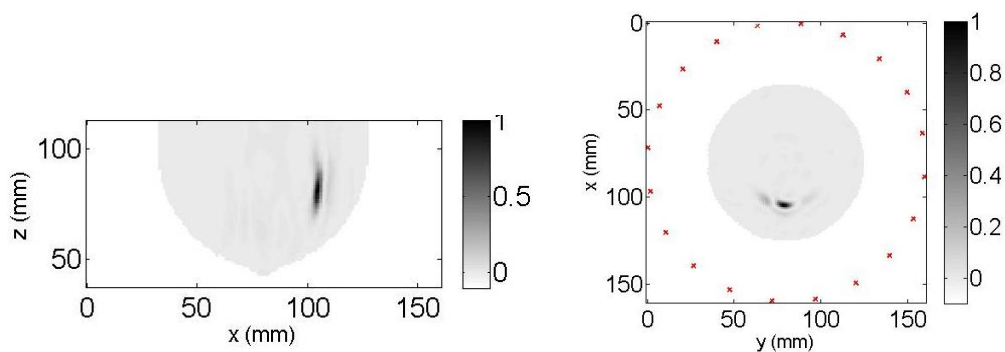
Figure 2-15 TSAR images of the phantom demonstrating the ability to detect and localise the inclusion [23]

Prof Ian Craddock's team at University of Bristol, UK

Prof. Ian Craddock's team has developed the world's first radar breast imaging system, named as "Multi-static Array processing for Radio-wave Image Acquisition" (MARIA). The system makes use of a multi-static structure, shown in Figure 2-16(a). Reportedly, MARIA has been undergoing extensive clinical testing at North Bristol NHS Trust and has experimentally demonstrated the ability to detect tumours as small as 4 to 6mm across, shown in Figure 2-

16(b). However, due to the inhomogeneity of breast tissue and individual body type difference among patients, it is a challenge to maintain a high detection rate. According to the large-scale clinical trial carried out at Frenchay Hospital in Bristol in 2008-2009, only 25% of around 200 patients were found to have malignant tumours with MARIA [24-30].

(a) (b)
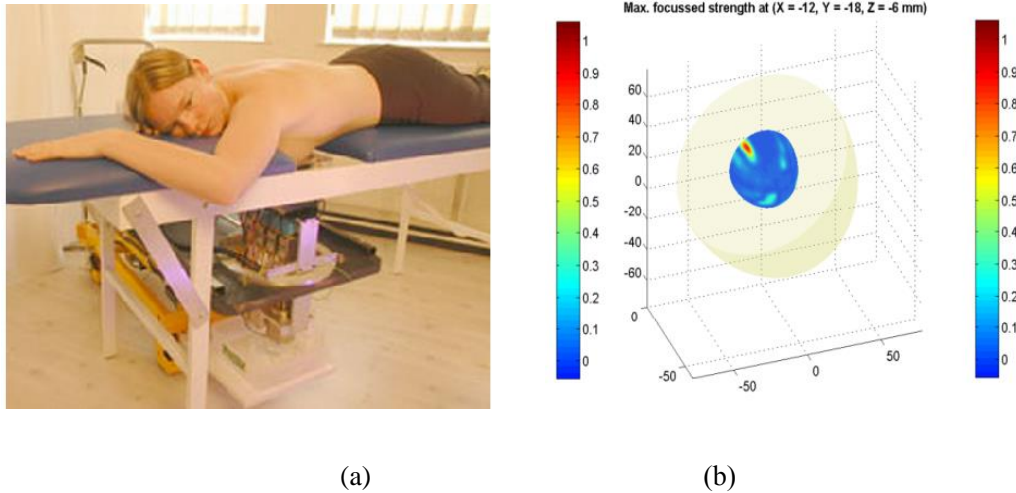
Figure 2-16 (a) MARIA system in patient care; (b) 3D detection of a tumor located at (x=-12mm, y=-18mm z=-6mm) [30]

Prof Alexander Yarovoy' team at Delft University of Technology, Netherlands

A multi-channel UWB radar sensor with digital footprint forming was developed in this team for landmine detection research in 2006 [31]. The mini-array GPR operated from 170MHz to 3.1GHz. In 2012, a 3-D near-field imaging algorithm was presented to re-create the image of a revolver gun placed at 0.5m, shown in Figure 2-17. The imaging system used wideband MIMO imaging array topology and the image reconstruction procedure was performed in frequency domain. The algorithm was able to completely compensate the curvature of the wave front in the near-field through a specifically defined interpolation process and could provide extremely high computational efficiency [32].

(a)   (b)
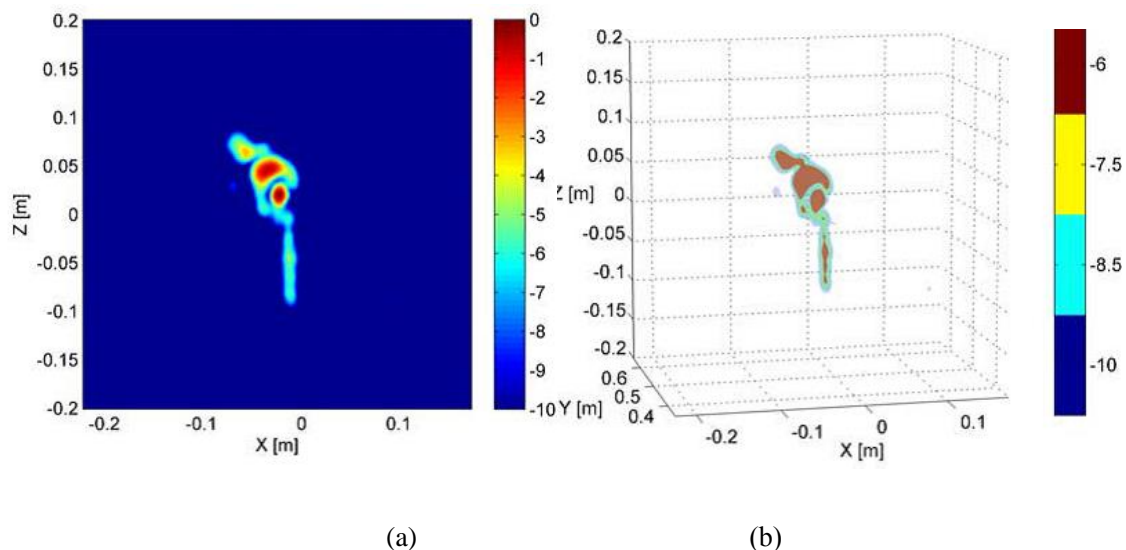
Figure 2-17 (a) The front view of image by the proposed MIMO-RMA; (b) Three-dimensional image by the proposed MIMO-RMA [31]

Prof Aly Fathy's team at the University of Tennessee, USA

This group has been developing UWB impulse Synthetic Aperture Radar (SAR) for real-time human imaging behind a wall, and indoor positioning based on time-domain techniques, for many years. Two frequency bands were adopted in their system: 1.5-4.5GHz and 8-10GHz, which were interchangeable by tuning into different carrier signals. The imaging result obtained of a seated man is shown in Figure 2.18. In 2012, two major breakthroughs were made by the group. The first was the successful design of a compact integrated sampling module, integrated with an equivalent time sampling method, which enabled a maximal 100GS/s sample rate [33-35]. The other was to achieve real-time 3D millimetre accuracy in a UWB positioning system for use in multipath indoor environments. The experimental results proved that a stand-alone integrated tag utilising a high phase noise voltage controlled oscillator can be tracked within 6.53 mm of 3D real-time root mean square error [36].

<table>
<tr><td>(a)</td><td>(b)</td></tr>
</table>
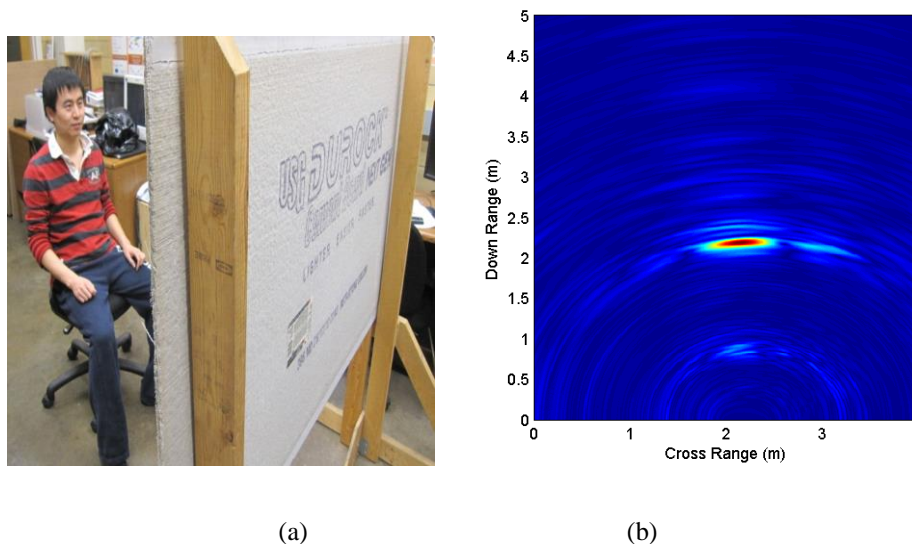
Figure 2-18 (a) Image of a seated man behind the wall; (b) Detection of the target in (a) [35]

Research teams in DEMR, LEAT and ESYCOM, France

In this joint research group, Time Reversal processing, combined with a multi-static-multi-view UWB radar system for Through-The-Wall detection of human targets, was investigated. As shown in Figure 2-19, an array of antennas was placed against the wall with absorbing materials attached behind. In the probed domain, two cylindrical metal objects were placed inside a room. A moving man was arranged to move in the room at four different locations. The resultant images are shown in Figure 2.20. Experimental data from realistic "see-through" the wall scenarios were collected to form the multi-static data matrix. "Singular Value Decomposition (SVD)" calculation of the matrix was used to build an efficient detection method. "Decomposition of Time Reversal Operator (DORT)" and "Multiple Signal Classification (MUSIC)" methods were developed in the group to enable quicker identification of the number of the targets and sharper differentiation of poorly-resolved scatters [37-39].

<table>
<tr><td>(a)</td><td>(b)</td><td>(c)</td></tr>
</table>
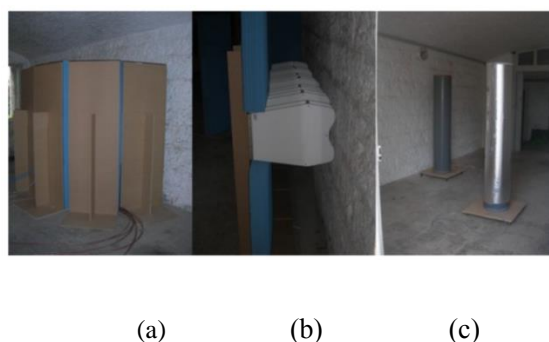
Figure 2-19 (a) Absorbing materials; (b) antenna array against the wall; (c) canonic targets [37]

-57-
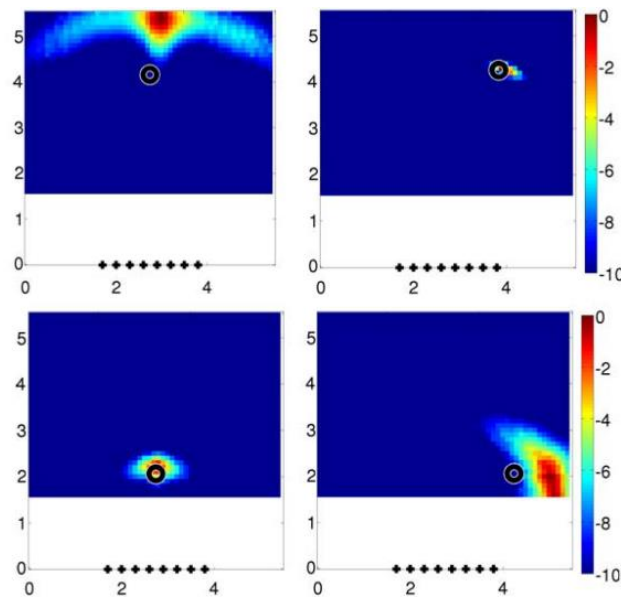
Figure 2-20 Detection of a human target in a room at four different locations [37]

2.5.2 Current commercial products in industry

UWB 3D Imager, Roke Manor Research Limited, Chemring Technology, UK

The demonstrator UWB 3D Imager consists of four transceiver units, configured for operation as two independent bi-static radars. One is configured for operation at co-polar vertical polarisation and the other at horizontal polarisation. The UWB RF switching controller software is programmed to transmit and receive signals through 25 elements. The two imaging algorithms include a 3D frequency-domain matched filtering method and 2D range-domain matched filtering method, repeatedly used for a number of positions. The latter was selected to cope with applications, particularly when needed for significantly faster detection with no significant reduction in image quality. Medical imaging of tumour and baggage/people scanning scenarios were both considered and illustrated in Figure 2.21(a) and (b) [40-41].

(a)   (b)
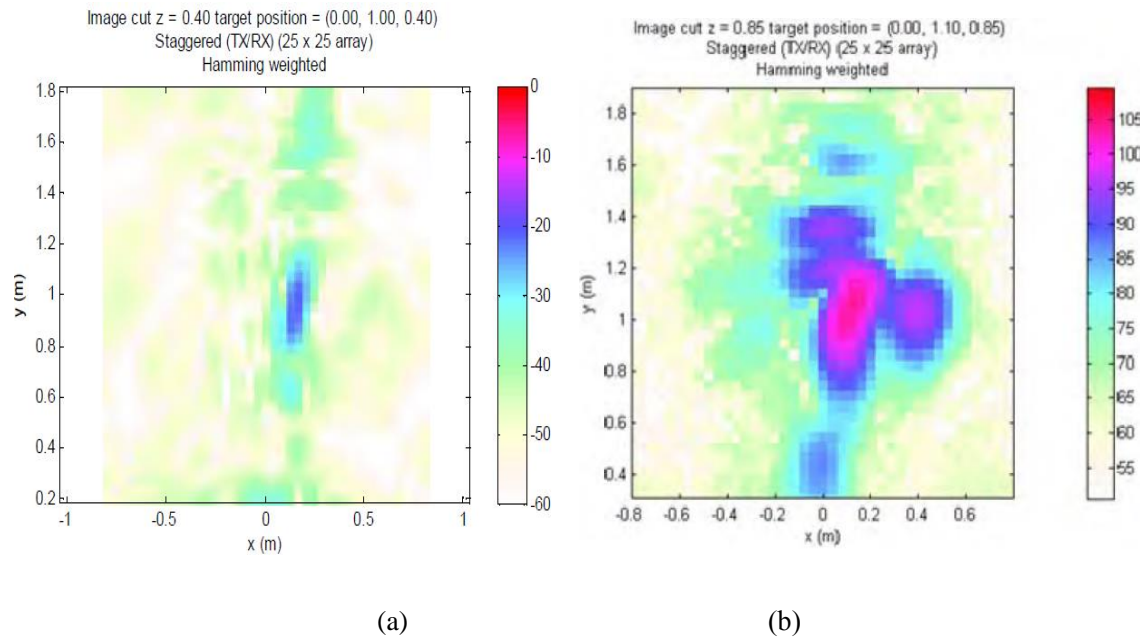
Figure 2-21 (a) Scaled target representing 1cm tumour 10cm inside body; (b) Imaging of a subject wearing rucksack containing a simulated nail bomb [40]

PulsON® 410 (P410) UWB Radar sensors, Time Domain, Alabama, USA

The product PulsON® 410 (P410) UWB module from Time Domain Company is a small, low cost, low power OEM device operating at a centre frequency of 4.3GHz with 1.4GHz of RF bandwidth. The P410 produces radar scanning data for proper filtering and detection strategies to target specific applications. Two embedded software modules in the system allow for mono-static operation, bi-static and multi-static operations. P410 communicates with a host (PC/microprocessor) over a USB or Serial interface using a standard Application Programming Interface (API). Both the software modules include graphical user interfaces (GUIs) to drive the API. These GUIs allow access to all of the API commands, configure the radar parameters, and capture/store/display radar scanning. As illustrated in Figure 2.22, the essence of P410 design is mainly integrated onto a single circuit board. Two ports are left for the connection of antennas. Typical Applications of P410 RCM include: Peer-to-peer ranging with moderate-rate wireless communications; GPS augmentation for multipath resistance; Robotics navigation and tracking, precision formation; Autonomous vehicle convoys; Distributed sensor automatic survey and dynamic mapping with fused data communications; Wireless channel impulse response (CIR) measurements; Wireless noise-like / covert data communications. [41]
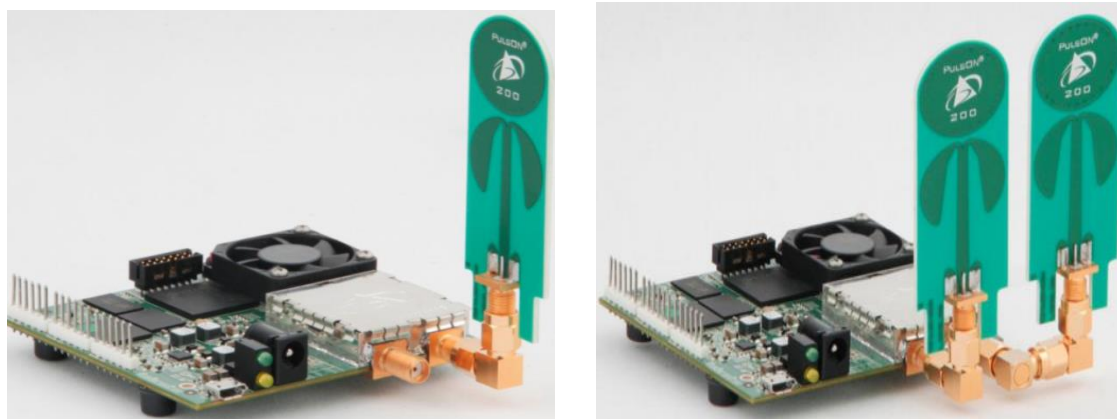
(a)   (b)

Figure 2-22 (a) P410 mono-static set-up with Broadspec antenna; (b)P410 bi-static set-up with a pair of Broadspec antennas [41]

Prism200 wall penetration radar, Cambridge Consultant, UK and USA

Prism 200 is a radar device, operating in a range of 1.6-2.2GHz and with a maximum detectable range of 20m, as shown in Figure 2.23. It is designed for extremely dangerous and life-threatening scenarios. The unit needs to be attached onto the wall directly and is able to analyse radar signals and instantly filter out objects that are not moving behind an obstruction. It implies great potential for the detection of abductees in urban environments without wasting valuable time during data translation. Transmitting power is 10dBm/MHz average and is adequate to see through brick, timber, cinder block, concrete block, reinforced concrete and other materials [42]. Its dimensions are 305 x 450 x 210 mm^3 and weight is 5.7kg, compact enough for military missions.

(a)   (b)

Figure 2-23 (a) Prism 200 frontal image; (b) Prism 200 in military use [42]

Xaver ™ wall penetration imaging radars, Camero-tech, Israel

In the current market, Camero-tech is the only company which can offer a serial Xaver product with consistently cutting-edge specifications. Xaver family products show an advanced UWB pulsed radar sensor technology. Its mathematical algorithms can cope with cluttered environments, producing highly reliable object imaging and range distance detection. The gradually reduced weight and ultra-portability make it a perfect candidate for military use [43]. The Xaver product family is summarised in Table 2.1.

Table 2.1 Xaver wall penetration imaging radars products [42]

	Xaver™ 800	Xaver™ 400	Xaver™ 100
Penetrable wall	Cement, plaster, brick, concrete, reinforced concrete, adobe, stucco, drywall	Cement, plaster, brick, concrete, reinforced concrete, adobe, stucco, drywall	Cement, plaster, brick, concrete, reinforced concrete, adobe, stucco, drywall
Detection range	4m/8m/20m	4m/8m/20m	4m/8m/20m
Field of view	80 degree in Azimuth and Elevation	120 degree in Azimuth and Elevation	120 degree in Azimuth and Elevation
Display modes	3D View, 2D plain view, 1.5D	3D View, 2D plain view, 1.5D	3D View, 2D plain view, 1.5D
Frequency range	3GHz-10GHz	3GHz-10GHz	3GHz-10GHz
Resolutions	Range: better than 3cm; Cross range: 30cm	Range: better than 5cm; Cross range: 50cm	Unknown

2.6 Summary

This chapter investigates the fundamentals and requirements necessary for UWB imaging radar systems, and a literature review of the latest developments across academia and industry. The radar equation and its variation are used to analyse the signal penetration of some materials. The definitions of range accuracy, range resolution and cross range resolution are then introduced, which form the foundation of the resolutions study for the proposed UWB imaging system in Chapter 4. Next, the differences between the time-domain and frequency-domain UWB radar systems are presented, thus indicating the advantages of the time-domain based UWB radar system in terms of overall cost saving, computation complexity and time for measurements. Three different data collection schemes are introduced and the adopted method is to use a multiple Bi-static set-up to suit the intended purpose, which is explained in detail in Chapter 4. The last section illustrates the review of the contributions made by various universities and companies. The applications of the UWB imaging systems designed to date vary from breast tissue imaging, metallic weapon imaging and detection to "seeing-through-wall". Different applications have their own requirements for the operational frequency band and system construction. Known imaging recovery methods are also explained in each group's research work.

Reference

[1] "Application UWB", Available on www.uwbgroup.ru/eng/uwb/applic.html

[2] Kingsley, S. Quegan, "Understanding Radar Systems", McGraw-Hill, 1992

[3] M. Farwell, J. Ross, R. Luttrell, D. Cohen, W. Chin and T. Dogaru, "Sense through the wall system development and design considerations", Journal of the Franklin Institute, Vol. 345, Issue 6, September 2008, Pages 570-591\

[4] M. Bury, Y. Yashchyshyn, J. Modelski, "Frequency domain measurements for an UWB imaging system", 17th International Conference on Microwaves, Radar and Wireless Communicatiions,2008. MIKON 2008, Page(s): 1-4, 2008.

[5] A. Muqaibel, A. Safaai-Jazi "Characterization of wall dispersive and attenuative effects on UWB radar signals", Journal of the Franklin Institute, Vol 345, Issue 6, pp.640-658, September 2008

[6] Y. Yang, C. Zhang, and A. E. Fathy, "Development and implementation of ultra-wideband see-through-wall imaging system based on sampling oscilloscope", IEEE Antennas and Wireless Propag. Lett., Vol.7, pp.465-468, 2008

[7] Ali Muqaibel, Ahmad Safaai-Jazi, "Characterization of wall dispersive and attenuation effects on UWB radar signals," Journal of the Franklin Institute Advances in Indoor Radar Imaging, Volume 345, Issue 6, September 2008, pp. 640–658.

[8] E.J. Bond, X. Li, S.C. Hagness, B.D. van Veen, "Microwave imaging via space-time beamforming for early detection of breast cancer", IEEE Trans Antennas and Propagation, Vol. 51, No. 8, Page(s): 1690-1705, 2003.

[9] M. Soliman, Z. Wu, "Desgin, Simulation and Implementation of UWB Antenna Array and It's Application in GPR System", The Second European Conference on Antennas and Propagation, 2007. EuCAP 2007, Page(s): 1-5, 2007.

[10] P.M. Meaney, M.W. Fanning, Dun Li, Steven P. Poplack, K.D. Paulsen, "A clinical prototype for active microwave imaging of the breast", IEEE Transactions on Microwave Theory and Techniques, Vol: 48, Issue: 11, Part: 1, Page(s): 1841-1853, 2000.

[11] P.M. Meaney, K.D. Paulse, M.W. Fanning, Steven P. Poplack, Tor D. Tosteson, Dun Li, Navin K.V. Yagnamurthy, "Microwave Breast Imaging with a Non-Contacting, Monopole Antenna Array", 30th European Microwave Conference, Page(s): 1-4, 2000.

[12] D. Li, P.M. Meaney, T. Raynolds, S.A. Pendergrass, M.W. Fanning, K.D. Paulsen, "Parallel-detection microwave spectroscopy system for breast imaging", Review of Scientific Instruments, Vol: 75, Issue:7, Page(s): 2305-2313, 2004.

[13] Paul M. Meaney, Amir H. Golnabi, Neil R. Epstein, Shireen D. Geimer, Margaret W. Fanning, John B. Weaver, and Keith D. Paulsen,"Integration of microwave tomography with magnetic resonance for improved breast imaging", Med. Phys. 40 (10), October 2013.

[14] X. Li, S.C. Hagness, "A confocal microwave imaging algorithm for breast cancer detection", IEEE Microwave Wireless Comp. Lett., Vol. 11, Page(s): 130-132, Mar. 2001.

[15] E.C. Fear, X. Li, S.C. Hagness, M. Stuchly, "Confocal microwave imaging for breast cancer detection: Localization of tumors in three dimensions", IEEE Trans. Biomed. Eng., Vol, 49, Page(s): 812-822, Aug. 2002.

[16] X. Li, E.J. Bond, SC.C. Hagness, B.D. Van Vee, D. van der Weide, "Three-dimensional microwave imaging via space-time beamforming for breast cancer detection", IEEE AP-S Int, Symp. And USNC/URSI Radio Science Meeting, San Antonio, TX, June 2002.

[17] X. Li, S.K. Davis, S.C. Hagness, D.W. Van Der Weide, B.D. Van Veen, "Mircrowave imaging via space-time beamforming: experimental investigation of tumor detection in multilayer breast phantoms", IEEE Transactions onMicrowave Theory and Tchniques, Vol: 52, Issue: 8, Part: 2, Page(s): 1856-1865, 2004.

[18] X. Li, E. J. Bond, B. D. Van Veen, S. C. Hagness, "An overview of ultra-wideband microwave imaging via space-time beamforming for early-stage breast-cancer detection", IEEE Antennas and Propagating Magazine, vol. 47, no. 1, pp(s): 19-34, 2005.

[19] Matthew J. Burfeindt, Member, IEEE, Jacob D. Shea, Member, IEEE, Barry D. Van Veen, Fellow, IEEE, and Susan C. Hagness, Fellow, IEEE, "Beamforming-Enhanced Inverse Scattering for Microwave Breast Imaging", IEEE Transactions on Antennas and Propagation, vol. 62, No. 10, Oct 2014

[20] T.C. Williams, J. Bourqui, T.R. Cameron, M. Okoniewski, E.C. Fear, "Laser Surface Estimation for Microwave Breast Imaging Systems", IEEE Transactions on Biomedical Engineering, Vol. 58, Issue. 5, Page(s): 1193-1199, 2011.

[21] B. Maklad et al., "Neghborhood-based algorithm to facilitate the reduction of skin reflections in radar-based microwave imaging", PIERB, Vol: 39, Page(s): 115-139, 2012.

[22] E.C. Fear, J. Bourqui, C. Curtis, D. Mew, B. Docktor, C. Romano, "Microwave Breast Imaging With a Monostatic Radar-Based System: A Study of Application to Patients", IEEE Transactions on Microwave Theory and Techniques, Vol. 61, No. 5, Page(s): 2119-2128, May 2013.

[23] http://www.ucalgary.ca/fear/research/tsar

[24] B. Cheeseman, Y. Huang, "Limited Multi-Static Calibration Technique without a Phantom for the Detection of Breast Cancer", 3rd European Radar Conference, EuRAD 2006, Page(s): 225-228, 2006.

[25] B. Cheeseman, Y. Huang, "Comparison of Shape Imaging between Pulse Integration, Correlation and Adaptive Filter". The Second European Conference on Antennas and Propagation, EuCAP 2007, Page(s): 1-6, 2007.

[26] Y. Chen, P. Kosmas, "Detection and Localization of Tissue Malignancy Using Contrast-Enhanced Microwave Imaging: Exploring Information Theoretic Criteria", IEEE Transactions on Biomedical Engineering, Vol. 59, No. 3, Page(s): 766—76, Mar. 2012.

[27] Y. Chen, P. Kosmas, "Microwave Breast Tumor Detection and Size Estimation Using Contrast-Agent-Loaded Magnetotactic Bacteria", 35th Annual International Conference of the IEEE Engineering in Medicine and Biology Society (EMBS), Page(s): 5481-5484, 2013.

[28] I.J. Craddock, M. Klemm, J. Leendertz, A.W. Preece, R. Benjamim, "An Improved Hemispherical Antenna Array Design for Breast Imaging", The second European Conference on Antennas and Propagation, 2007, EuCAP 2007, Page(s): 1-5, 2007.

[29] D. Gibbins, M. Klemm, I.J. Craddock, J.A. Leendertz, A. Preece, R. Benjamim, "A comparison of a wide-slot and a stacked patch antenna for the purpose of breast cancer detection", IEEE Transactions on Antennas and Propagation, Vol: 58, Issue: 3, Page(s): 665-674, 2010.

[30] T. Henriksson, M. Klemm, D. Gibbins, J. Leenderts, T. Horseman, A.W. Preece, R. Benjamin, I.J. Craddock, "Clinical trials of a multistatic UWB radar for breast imaging", Antennas and Propagation Conference (LAPC), 2011 Loughborough, Page(s):1-4, 2011.

[31] A. Yarovoy, P. Aubry, P. Lys, L. Ligthart, "UWB Array-Based Radar for Landmine Detection", 3rd European Radar Conference, 2006. EuRAD 2006, Page(s): 186-189, 2006.

[32] Xiaodong Zhuge and Alexander G. Yarovoy, "Three-Dimensional Near-Field MIMO Array Imaging Using Range Migration Techniques",IEEE TRANSACTIONS ON IMAGE PROCESSING, VOL. 21, NO. 6, JUNE 2012

[33] Y. Yang, A.E. Fathy, "Development and Implementation of a Real-Time See-Through-Wall Radar System Based on FPGA", IEEE Transactions on Geoscience and Remote Sensing, Vol: 47, Issue: 5, Page(s): 1270-1280, 2009.

[34] Y. Wang, A.E. Fathy, "Three-dimensional through wall imaging using an UWB SAR", 2010 IEEE Antennas and Propagation Society International Symposium (APSURSI), Page(s): 1-4, Jul. 2010.

[35] Y. Wang, A.E. Fathy, "Advanced System Level Simulation Platform for Three-Dimensional UWB Through-Wall Imaging SAR Using Time-Domain Approach", IEEE Transactions on Geoscience and Remote Sensing, Vol: 50, No: 5, Page(s): 1986-2000, May 2012.

[36] Michael J. Kuhn, Mohamed R. Mahfouz1, Nathan Rowe, Essam Elkhouly, Jonathan Turnmire, Aly E. Fathy, "Ultra Wideband 3-D Tracking of Multiple Tags for Indoor Positioning in Medical Applications Requiring Millimeter Accuracy", IEEE Topical Conference on Biomedical Wireless Technologies, Networks, and Sensing Systems (BioWireleSS), Page(s): 57 - 60, Jan 2012

[37] R. Dubroca, N. Fortino, J-Y. Dauvignac, L. Bellomo, S. Pioch, M. Saillard, Thomas Lepetit, J. de Rosny, C. Prada, P.Millot, N.Maaref, B.Boudamouz "Time reversal-based processing for human targets detection in realistic through-the-wall scenarios", Proceedings of the 8th European Radar Conference,2011.

[38] Nadia Maaref, Patrick Millot, "Array-based UWB FMCW Through-The-Wall Radar", Antennas and Propagation Society International Symposium (APSURSI), 2012 IEEE

[39] B. Boudamouz, P. Millot, C. Pichot, "Through The Wall Radar Imaging with MIMO beamforming processing", Microwaves, Radar and Remote Sensing Symposium, August 25 – 27, 2011, Kiev, Ukraine.

[40] http://www.roke.co.uk/sensing/radar.html

[41] http://www.timedomain.com/datasheets/320-0289E%20P410%20Data%20Sheet.pdf

[42] http://www.cambridgeconsultants.com/prism-200

[43] http://www.camero-tech.com/products.php

[44] A. Kuthi, M. Behrend, T. Vernier,M. Gundersen, "Bipolar Nanosecond Pulse Generation using Transmission Lines for cell electro-manipulation," 26th International Power Modulator Symposium, May 23, 2004.

[45] "Design and Analysis of UWB Down-Conversion Mixer with Linearization Techniques", D.SELVATHI,M.POWN, and S.MANJULA Department of ECE Mepco Schlenk Engineering College Sivakasi, Tamilnadu INDIA, WSEAS TRANSACTIONS on CIRCUITS and SYSTEMS, Volume 13, 2014.

Chapter 3 Microwave Beam-forming

Methods for Imaging

In radar systems, the beam-forming theory is generally based on the relative distance and movement between antennas and targets. The basic beam-forming method shares some similarities with the Synthetic Aperture Radar (SAR) method. In SAR imaging systems, the radar aperture is materialised by regarding each and every transceiver as one element in the antenna array [1]. The signal processing is based on the magnitude and phase information of the received signals over a series of pulses from the elements of the synthetic aperture. The target signal information of the time of the responses would be saved at every position and the process would include data weighting, shifting and summing up to achieve the final focus on targets at a time.

This chapter starts with a literature review of microwave beam-forming methods. The basic theories of the "Delay and Sum (DAS)" method and the "Time-Reversal (TR)" method are introduced and briefly discussed. The development of each method shows the different ways of recovering images. Next, the examination of DAS beam-forming is expanded in great detail, including its mathematical description, with the simulation for detection of one and two metallic targets in free space, behind a board and inside a box. The simulation of the DAS method reveals that target detection in free space is the optimal environment and too many multipath signals would compromise the images. The simulation work has shown that TR can re-focus an active Gaussian pulse in a multipath environment. Finally, images of one and two targets are recovered by TR in comparison with DAS. It is also shown in simulation that the rotating superposition can recreate images of the targets.

3.1 Review of beam-forming methods

Beam-forming methods are mainly based on processing of signals reflected from targets in order to construct their images. Some frequency domain based algorithms are often used for

SAR radars, such as the "Polar Format Algorithm (PFA)" [2], "Range Migration Algorithm (RMA)" [3] and "Chirp Scaling Algorithm (CSA)" [4]. PFA comes from optical signal processing. It is based on the polar nature of the backscattered data in frequency domain. It works in the far-field condition and requires an interpolation prior to the Fourier transformation, but only partially compensates the range curvature. RMA originates from seismic engineering and geophysics. It works with motion compensation to a line, requires a 1-D interpolation (known as Stolt interpolation [5]) and compensates the curvature of the wave-front. CSA does not require any interpolation [6]. It works with motion compensation to a line and corrects approximately the range curvature. It is widely used to process 2-D space airborne SAR data.

There are also some popular time domain based methods. Trilateration method is the most straightforward uncorrelated localisation method. It can help to position one target effectively. However, due to its poor practicality in a multi-target scenario, other correlated methods are more popular, such as "Back Projection Algorithm (BPA)" [7]. BPA is a point-by-point reconstruction method and does not neglect range curvature and range's high order terms. It is often used in bi-static SAR set-ups with wide-bandwidth continuous-wave illuminating sources and can offer reconstructed images with rather high resolutions.

The "Delay-and-Sum (DAS)" algorithm, with many possible refinements, has proved to be quite successful in [8-9]. This relies on the propagation difference in multiple receivers based on their different positions. The spatial and temporal differences would make the localisation of a single target in free space possible. The limitations of DAS occur when more complicated scenarios are considered. When the propagation environment becomes too complicated, it requires the dielectric permittivity distribution of the medium to sustain good imaging results. Multipath effect either caused by inter-reactions among targets or among targets and their surroundings has an adverse effect on DAS. While most methods are determined to reduce multipath effect, there is one method which, counter-intuitively, tries to make use of it, called "Time Reversal (TR)" method. TR is a clever concept to transform the inter-relationship existent within the multipath environment to an almost impossible advantage in imaging recreation. It helps to avoid imaging confusions and enhance resolutions.

TR originally came from Fink's successful low frequency acoustic waves and ultrasound "Time-Reversal" experiments in the early 1990s [10]. The concept of TR cavity and "TR Mirrors (TRM)" was developed and several devices were built to illustrate the feasibility of

TR [11-13]. More physical TR experiments have been conducted by using acoustics [14-18] and ultrasonic waves [19-24]. Underlying principles of TR have been investigated through theoretical analysis [25-28] and numerical simulations [29-33]. After a short period, the applicability quickly found its way in Radio Frequency electromagnetic waves. Fink's group also performed a TR focusing experiment using the EM waves where they demonstrated that a 1 MHz wide band pulse can be focused in a cavity environment [34-35]. Although there is a fundamental and inherent difference between acoustic waves and EM waves in nature, the basic principle of the TR method did not change. It has been found that in the frequency domain, TR corresponds to signal phase conjugation. This finding has inspired some applications in optics [36]. However, phase conjugation in frequency domain only applies to mono-chromatic waves, whereas time reversal in time domain can be applied to UWB pulse signals.

The TR method has had many applications in various fields. In medicine, it was used for the destruction of kidney stones [37-38], focusing RF energy in hyperthermia [39] and microwave breast cancer detection [40]. For the latter, TR was able to focus energy on the scattered malignant tissues. Various target detection and interference cancelation algorithms based on TR have been demonstrated in experiments [41-45]. TR has also found its application in the non-destructive detection of defects in materials and structures in industry [46-48]. In geo-physics and geo-science, TR has been employed to locate objects buried under the ground [49-50]. Sonar and acoustic communications have been carried out under water [51-52]. Furthermore, imaging using a synthetic TR method became possible [53-55]. TR focusing in a forest environment is numerically shown in [56]. In [57], TR synthetic aperture radar imaging was developed and applied in an environment filled with trees. Telecommunications and wireless communications applications include the development of TR based spatial-temporal matched filters to reduce channel dispersion and inter-symbol interference, thereby increasing the capacity of the channel [58-63]. A practical implementation of time-reversal of broadband microwave signals was demonstrated in [64]. Most of the imaging applications need analysis of the "TR Operator (TRO)", because Eigen space analysis of the TRO can provide crucial information about the target in many scattering scenarios under investigation. TRO for electromagnetic waves in homogeneous medium was analysed in [65].

For the detection of multiple targets, more advanced TR methods have been developed [66-68]. Decomposition of the TRO (French acronym: DORT "Decomposition de l'Operateur de

Retournement Temporel") can selectively focus on the multiple targets [69-73]. DORT method has been used for sensing buried objects [74]. Additionally, the Time Reversal Multiple Signal Classification (TR-MUSIC) method was investigated in [75-78], utilising TRO to obtain TR-based imaging for poorly-resolved multiple targets in a complex domain.

3.2 Delay and Sum beam-former

3.2.1 DAS deduction

The fundamentals of DAS method can be illustrated as follows: the transmitting wave impinges on an array of elements at a certain incidence angle; each element records a wave-field with a different time delay due to different wave propagation paths, the time-delayed recordings are weighted with various time parameters to interfere with each other constructively and sum up a beam-focused signal.
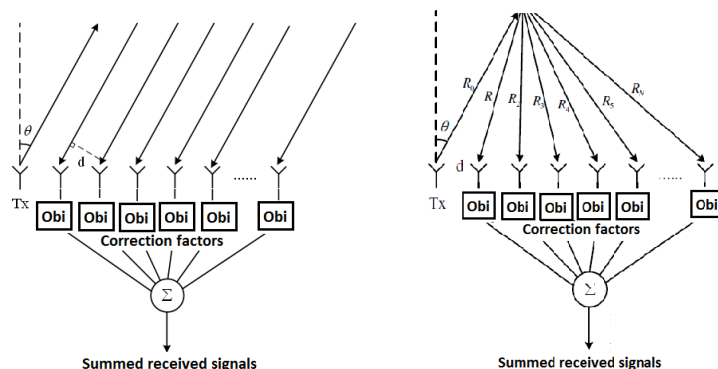
(a) Signal summation in the far field;   (b) Signal summation in the near field

Figure 3-1 Simplified synthetic beam-forming in the far/near field

There are two types of computation methods, relating to different detecting ranges. When the target is placed in a far field, wave propagation means that the reflected signal waves from the target can be seen as plane waves. This assumption can help to simplify the calculation. As illustrated in Figure 3.1 (a), all the incoming signals reach the antennas at the same time with an incidence angle of θ. Correction factors are added for signal adjustment.

I/Q channels in the imaging system can produce two components of the received signal: the in-phase component "$S_{in\text{-}phase}(n)$" and the quadrature component "$S_{quadrature}(n)$". So the complex

received signal from the i_{th} antenna is "$S_i(n)= S_{\text{in-phase};i}(n)+ S_{\text{quadrature};i}(n)$". "n" means the antenna number, relating to a certain range of a pixel cell of the probed area. In sum, the intensity of a specific picture pixel can be written as:

$$P_i(n) = \sum_{n=1}^{N} Ob_i S_i(n) e^{j\psi_i} \qquad (3-1)$$

In Equation 3-1, "N" means the total number of receiving antennas. "Ob_i" is the correction factor, compensating for the signal attenuation, loss and time-delay, and is assumed to be the same value for all the propagating channels on the grounds that wave propagations are regarded as plane waves in the far field. "$e^{j\psi_i}$" is the phase factor and "ψ_i" can be written as:

$$\psi_i = \pm(n-1)*d*sin\theta \qquad (3-2)$$

Summation of all the beams in the direction of "θ" means a maximum peak value in the imaging process.

However, when the target is placed in the near field as illustrated in Figure 3.1 (b), the deduction above becomes invalid because the receiving signals can no longer be seen as plane waves. The difference in propagation distances cannot be overlooked and each channel has its own contribution in the signal summation. The correction factor "Ob_i" is not a constant value and is related to the permittivity of the domain, wave incidence angles and refraction angles during the propagation. The phase factor also needs change and is related to the propagation lengths and incidence angles. All the tests in simulation and experiment are based on far field calculation.

The proposed UWB imaging system uses four corrugated BAVA antennas to scan the target. The distance is varied from 10cm to the furthest 50cm. To illustrate the DAS algorithm, simulation work has been done in CST MWS and the received signals are shown in Figure 3.2. There are three receivers and each one picks up a different signal colored in green, blue and red.
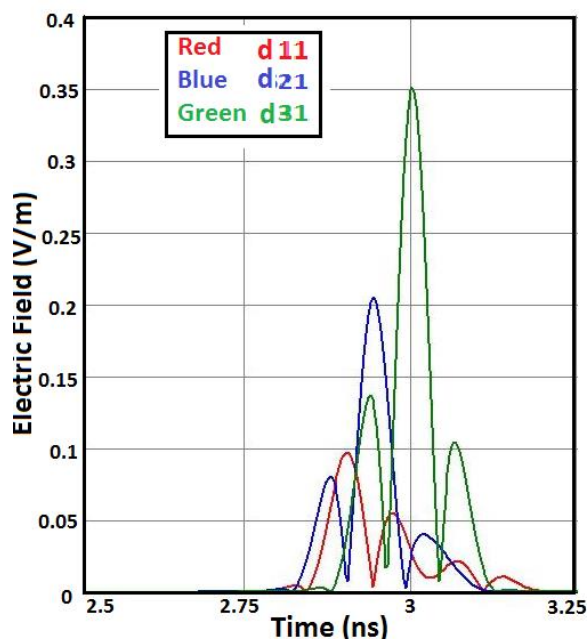
Figure 3-2 Three received signals as "d11", "d21" and "d31"

DAS algorithm can be carried out in the following steps:

1. The "d21" curve is used first. This curve covers a period of time, which contains hundreds of time moments with each indicating one possible detecting position in the probed domain. This can be explained in Equation 3.3. "c" indicates the known distance between the transmitting antenna and receiving one. "a" means one detecting range value, which relates to one particular time moment of the "d21" curve. The determination of one value "a" and a fixed value "c" can decide one elliptic circle. Only a half circle in the positive side is chosen due to forward radiation pattern. All the positions, situated on the half of the elliptic circle, are covered at this stage, indicated as "P" shown in Figure 3-3. All the "a" values within the "d21" curve need to be calculated in the same way so the step is repeated to form a cluster of ellipses or an elliptic band. When the brightness of this cluster of ellipses is graded in terms of signal intensity, the brightest ellipse indicates the possible target position. However, more information from other receivers is needed to determine the true target location.

$$r = \frac{a^2 - c^2}{a - c \cdot \cos(\theta)} \qquad\qquad (3-3)$$
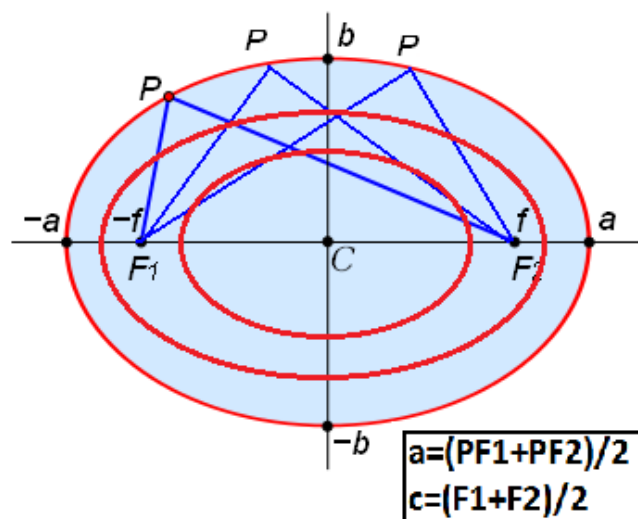
Figure 3-3 Ellipses/elliptic band based on the "d21"

2. Repeat step one with the "d31" curve. There are two changes in the calculation. First, In Equation 3-4, "c_1" equals to "c+d". "d" is the extra distance due to the introduction of the second receiver. Both values are pre-determined. The second change is "a_1". The value of "a_1" is different from the "a" at any chosen time moment because no two received signals would ever be the same. This means another cluster of ellipses or elliptic band can be drawn.

$$r = \frac{a_1^2 - c_1^2}{a_1 - c_1 \cdot \cos(\theta)} \qquad (3-4)$$

3. By overlapping these two ellipse clusters, two bright spots appear at the intersection, as shown in Figure 3.4. One bright spot has a larger intersection area than the other one, indicating the true location of the target. It is worth mentioning that this procedure can repeat itself until all the receiving signal data are used. By increasing the number of receivers, the superposition effect will make the prediction of the target location more accurate.
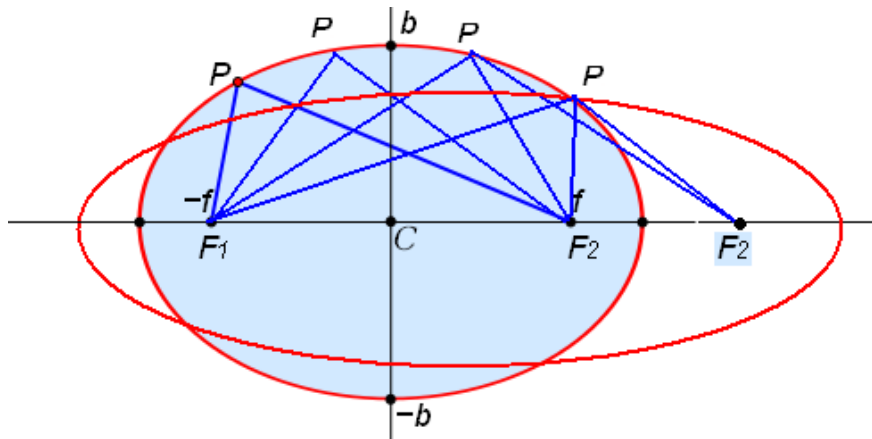
Figure 3-4 Intersection of two ellipses based on "d21" and "d31"

4. The angle "θ" and range "r" in the polar coordinate system are needed to ascertain each and every focal point in the probed area. These two parameters are determined by the ellipse parameters. Cosine Theorem is used for calculation and the final expression can be written in Equations 3-5 and 3-6 as below:

$$r = \frac{\frac{a^2}{c} - \frac{a_1^2}{c} + c_1 - c}{\frac{a}{c} - \frac{a_1}{c_1}} \qquad (3-5)$$

$$\cos(\theta) = \frac{a_1(a^2 - c^2) - a(a_1^2 - c_1^2)}{c_1(a^2 - c^2) - c(a_1^2 - c_1^2)} \qquad (3-6)$$

3.2.2 DAS beam-forming in free space

The impact of the receiving array aperture on images is investigated in this section. In simulation, one antenna is used as the transmitter and the number of receiving antennas is increased from two to five. The square metallic target with the size of 10 x 10 cm^2 is placed 40cm away from the array. The transmitting signal is one square wave with a width of 1ns and the radiant domain is presumed to be free space.

First, four scenarios of the receiving array are investigated in the generation of four images respectively, as shown in Figure 3.5. In Figure 3.5(a), there are two ellipses overlapping and one brightest hot spot, indicating the location of the target. In Figure 3.5(b), there are three ellipses which further focus on the target position. In Figure 3.5(c) and (d), more ellipses are added and the brightest focus is strengthened.

(a) Image with two receiving antennas;   (b) Image with three receiving antennas

(c) Image with four receiving antennas;   (d) Image with five receiving antennas
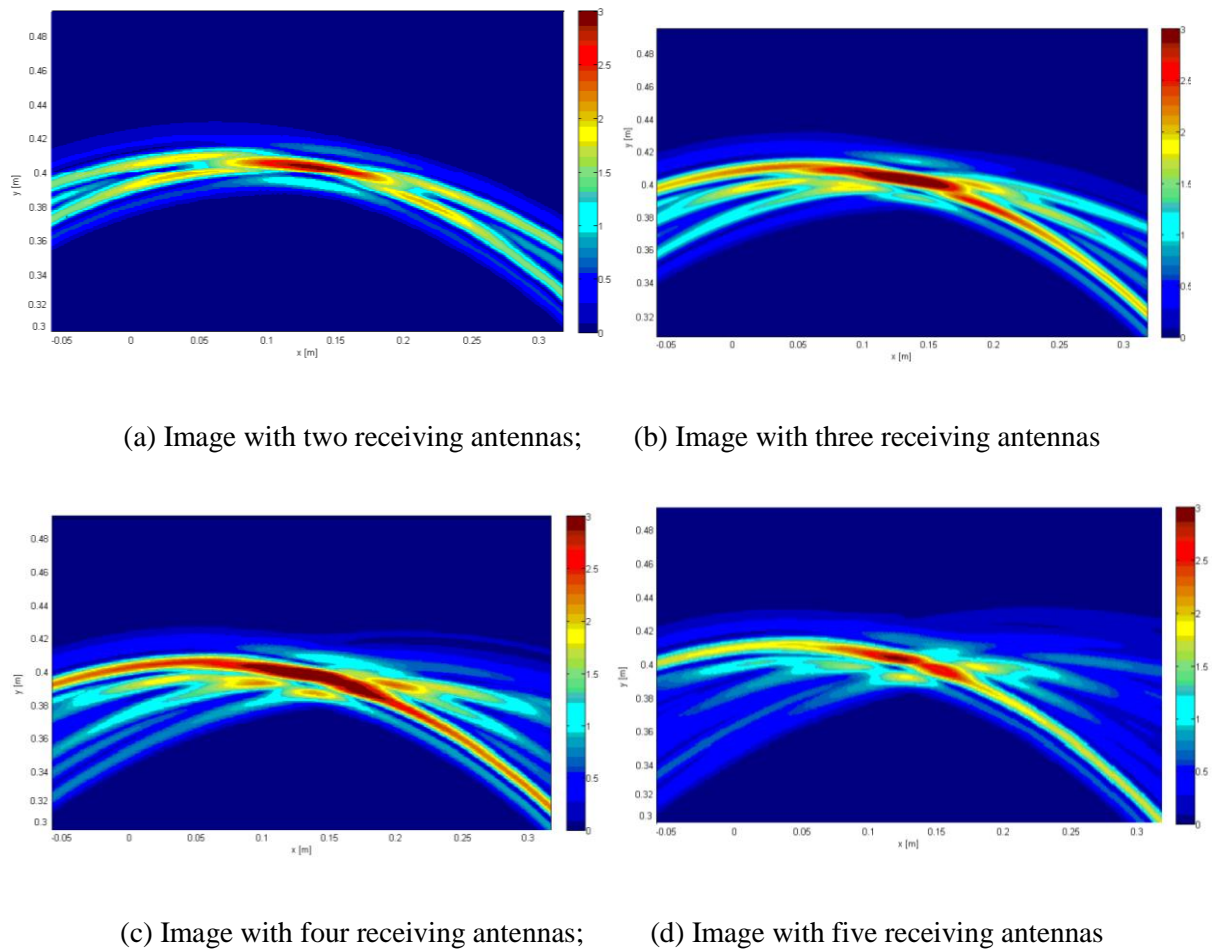
Figure 3-5 Original images of one metal target with an increasing number of receiving antennas by DAS

As demonstrated in Figure 3.5, the DAS imaging method can effectively focus on the position of the target. After the energy normalisation, the target images can be redrawn in Figure 3.6, in which only the top 20% of the energy is kept. The locations of the one transmitting antenna and five receiving antennas are indicated beneath the horizontal axis.
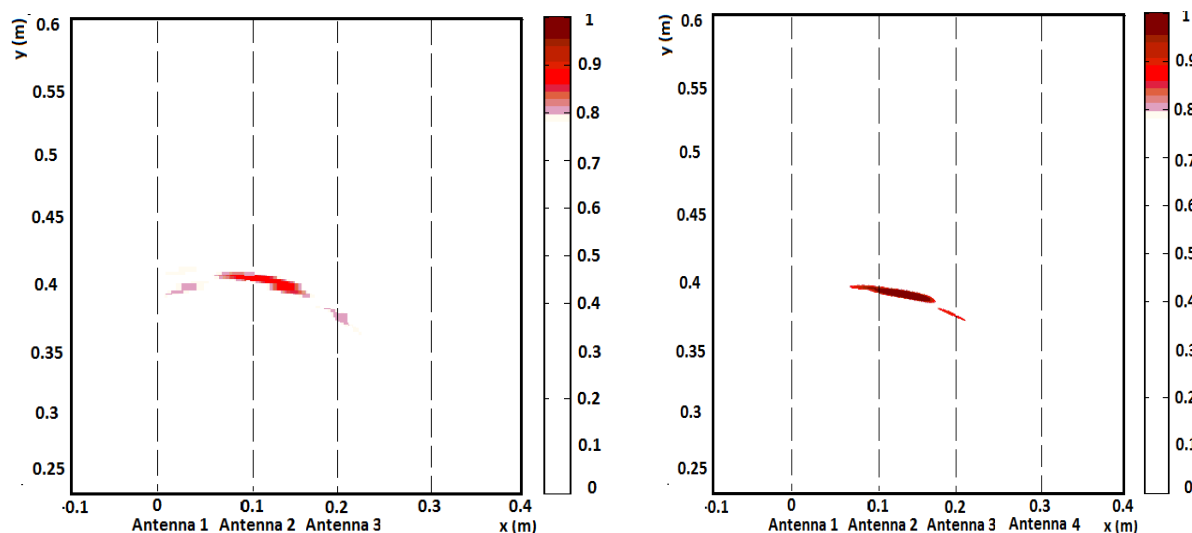
(a) Processed image with two receiving antennas;   (b) Processed image with three receiving antennas
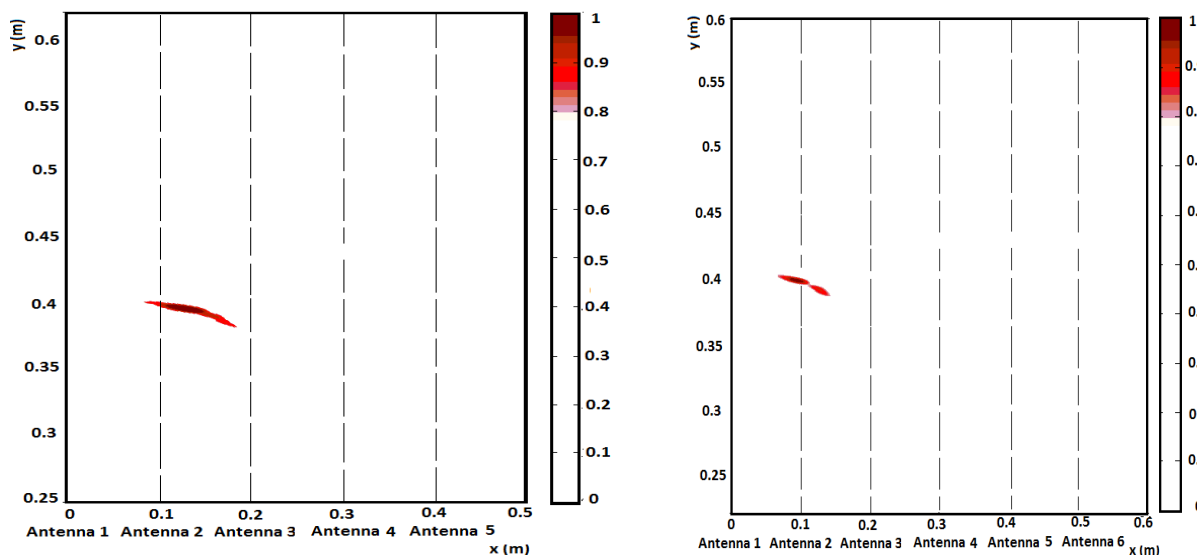
(c) Processed image with four receiving antennas;   (d) Processed image with five receiving antennas

Figure 3-6 Processed images of a single metal target with an increasing number of receiving antennas

The range and cross range estimations are summarized in Table 3-1 to show the impact of the increasing receiving elements. The error rate of range and cross range estimations compared to the true value is calculated based on Equation 3-7. In order to estimate and analyse the error rate, the change rate of error rates is given in Equation 3-8:

$$error\ rate = \frac{|Estimated\ distance - Real\ distance|}{Real\ distance} * \% \qquad (3-7)$$

$$changing\ rate = \frac{Estimated\ distance\ (n+1) - Estimated\ distance\ (n)}{Estimated\ distance\ (n+1)} * \% \qquad (3-8)$$

Table 3.1 Error rates of range and cross range estimations

Receiving antennas number	Range (Reference: 40cm)			Cross Range (Reference:10cm)		
	Estimated Range (cm)	Error rate (%)	Changing rate (%)	Estimated Cross Range (cm)	Error rate (%)	Changing rate (%)
2	40.2	0.5	-	20.0	100	-
3	39.9	0.25	-0.7	12.0	20	-40
4	40.0	0	+0.25	9.8	2	-18.3
5	40.2	0.5	+0.5	9.5	5	-3.1

In Table 3-1, it is shown that the DAS imaging reconstruction method can produce promising results in locating and imaging a single metal target in free space. The range estimation is particularly good and consistent. The estimated values are very close to the real one and the error rate is well below 0.5%. In terms of cross range estimation, when the number of receiving antennas is increasing from 2 to 5, the estimated values get more precise and the error rate decreases. This is because when more receiving antennas are introduced, the effective array aperture is widened, which can induce a better focusing of the cross range estimation of the target. The changing rate continuously drops and the error rate of estimation of cross range is slightly up when the receiving number is enlarged from 4 to 5. This means that when more receiving antennas are added, the effect of achieving a better cross range estimation starts to lessen. This observation can help to determine the number of antennas needed in a system.

Secondly, the different sizes of the target are tested in DAS imaging. Four receiving antennas and one transmitting antenna are used to detect and image one metal target fixed 40cm away from the array. The target is in the size of 10 x 10 cm^2, 8 x 8 cm^2, 5 x 5 cm^2 and 3 x 3 cm^2. The simulation has generated four received signals, as illustrated in Figure 3.7 and four images, as shown in Figure 3.8.
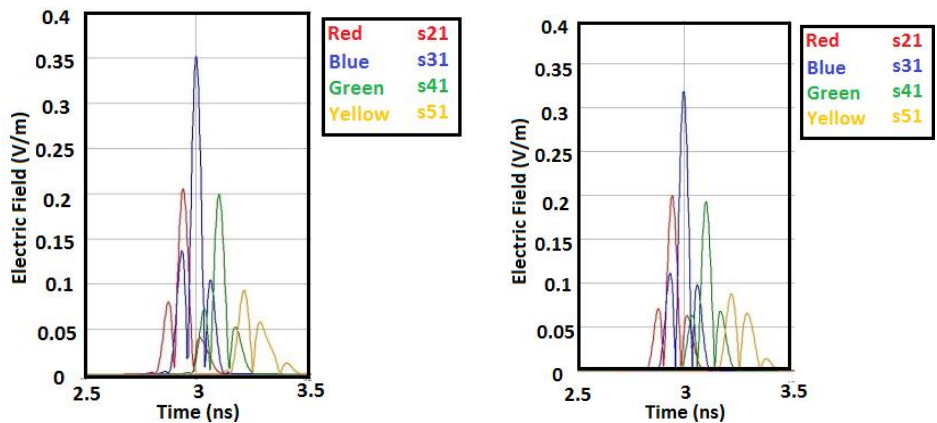
(a) Received signals from a target of 10 x10 cm^2 (b) Received signals from a target of 8 x 8 cm^2
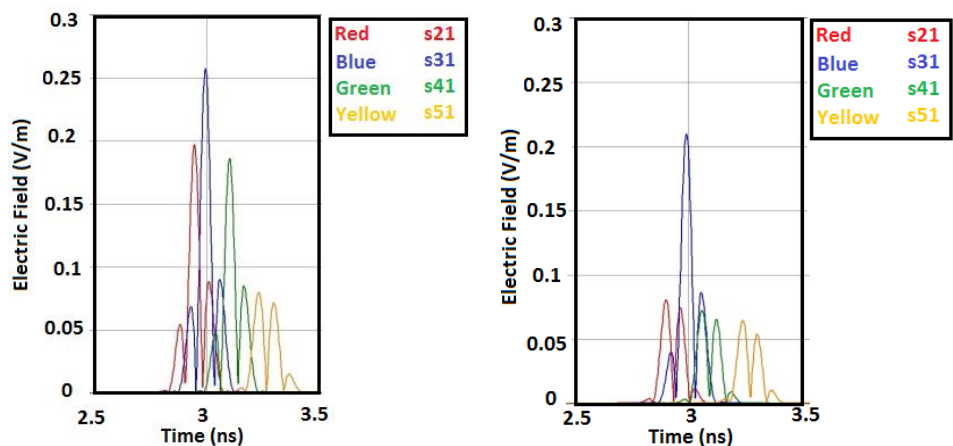
(c) Received signals from a target of 5 x 5 cm^2 (d) Received signals from a target of 3 x 3 cm^2

Figure 3-7 Received signals from a target of four different sizes

(a) Imaging of a target of 10 x 10 cm^2 (b) Imaging of a target of 8 x 8 cm^2

(c) Imaging of a target of 5 x 5 cm^2 (d) Imaging of a target of 3 x 3 cm^2
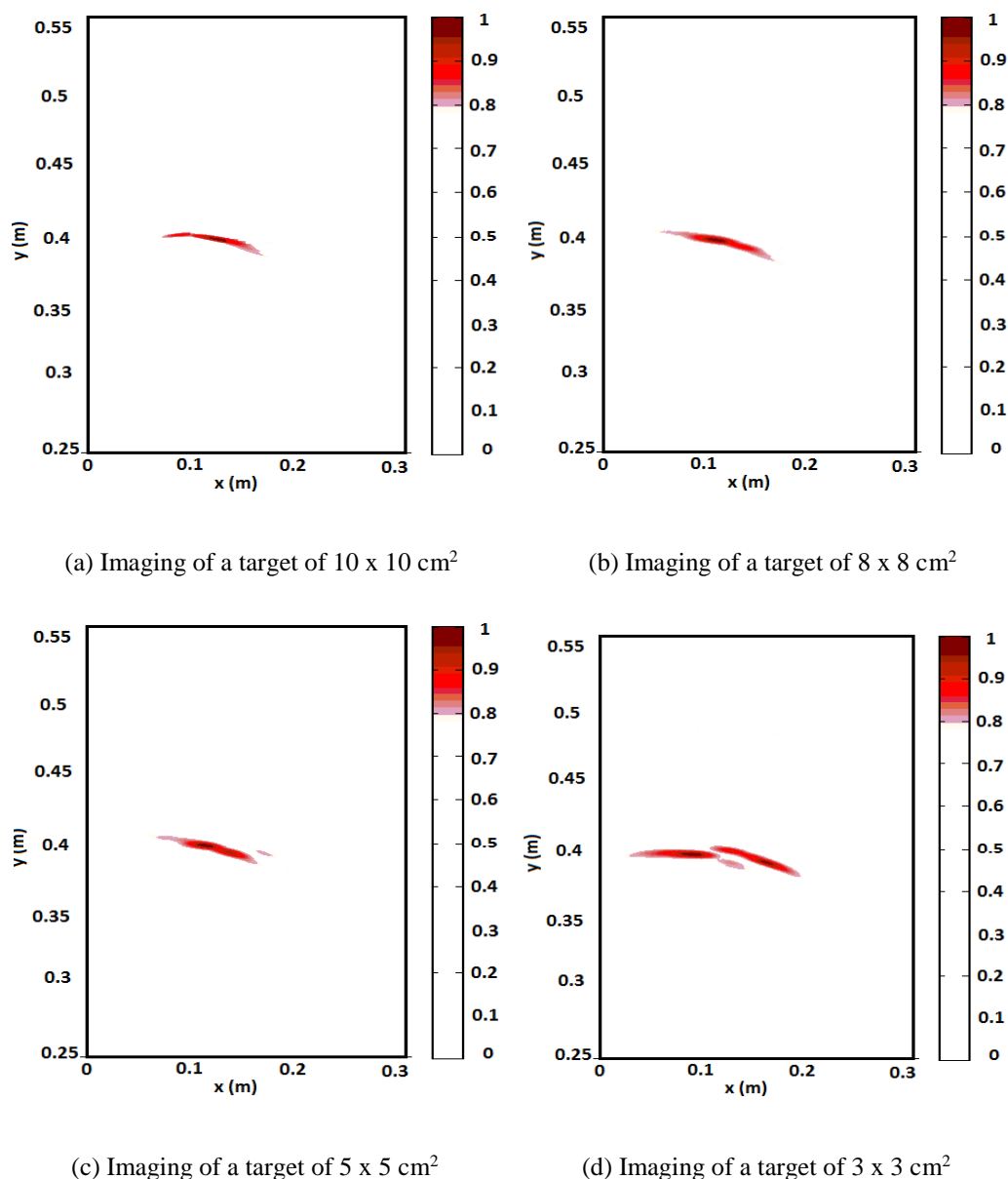
Figure 3-8 Images of a single target of decreasing size

In Figure 3.7, when the target becomes smaller, the peak value of the reflected signal is reduced. Take S_{31} for example, the amplitude of the received signal drops by 8.6%, 18.6% and 19.2% respectively, when the target size is reduced from 10 x 10 cm^2, 8 x 8 cm^2, 5 x 5 cm^2 and 3 x 3 cm^2. The other issue is that the wave-form of received signals is deformed as the target size is reduced.

As shown in Figures 3.8(a), (b) and (c), a single target of 5 x 5 cm^2 can be imaged adequately. However, when the size of the target drops to 3 x 3 cm^2, as indicated in Figure 3.8(d), the image is split and could be easily mistaken as two targets partly overlapping. The error rate study is

given in Table 3-2. As the target size is 3 x 3 cm^2, the cross range error rate increases dramatically up to 500%. This indicates that the smallest detectable target size is 5 x 5 cm^2.

Table 3.2 Error rate of range and cross range estimations

	Range (Reference: 40cm)			Cross Range	
Target size (cm^2)	Estimated Range (cm)	Error rate (%)	Changing rate (%)	Estimated Cross Range (cm)	Error rate (%)
10x10	40	0	-	9.5	5
8x8	39.9	0.25	-0.25	9	12.5
5x5	40	0	+0.25	5.5	10
3x3	40/39.5	0/1.25	0/+1.25	18	500

After the discussion of one target's detection and imaging, the next topic focuses on two targets. Generally, down-range resolution and cross-range resolution are the most relevant parameters.

Down-range resolution is a metric that is used to describe the ability to detect targets in close proximity as distinct targets along the vertical direction. Assuming there is a transmitting pulse towards two targets in the space, in theory, the returned pulse should be composed of two sets of signals from both targets. However, if the width of the pulse is too wide or the trail of each wave starts to overlap, these two signals cannot be separated by distinguishable distance. Down-range resolution is not wavelength dependent. It is a function of the pulse width divided by the speed of waves and can be expressed in the formation of pulse bandwidth and velocity of light. With the knowledge of the operating wideband of 1GHz in the proposed system, it can be deduced that the theoretical down-range resolution is 15cm.

In simulation, the smaller target with the size of 8 x 8 cm^2 is placed behind a bigger target with the size of 10 x 10 cm^2. The bigger target is fixed at the location 20cm away from the antenna array. The transmitting pulse width is 1ns, which determines a theoretical down range resolution value of 15cm. So the inter distance "d_y" between two targets is set as 5cm, 10cm, 15cm and 20cm respectively. The antenna set-up is the same as the previous one, with one transmitting antenna and four receiving antennas. The images for four different inter-distances are shown in Figure 3.9.
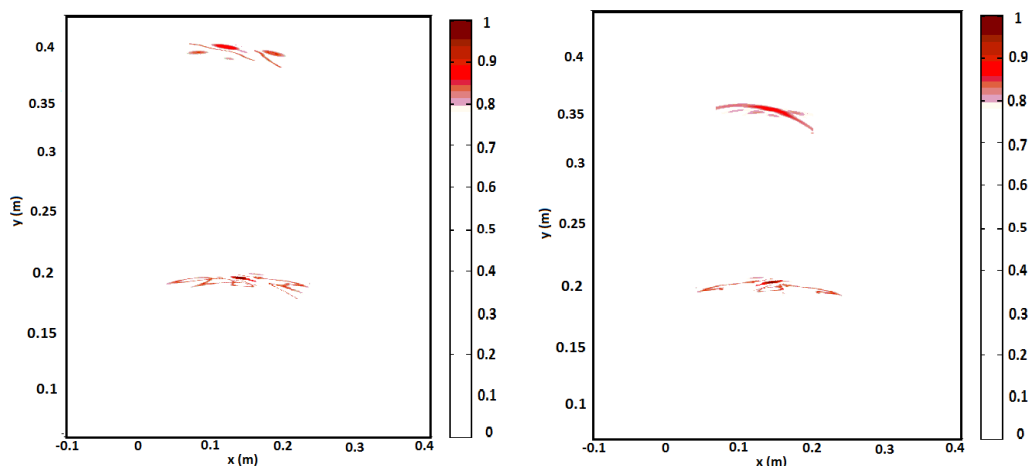
(a) Two targets with a vertical distance d_y of 20cm;   (b) Two targets with a vertical distance d_y of 15cm
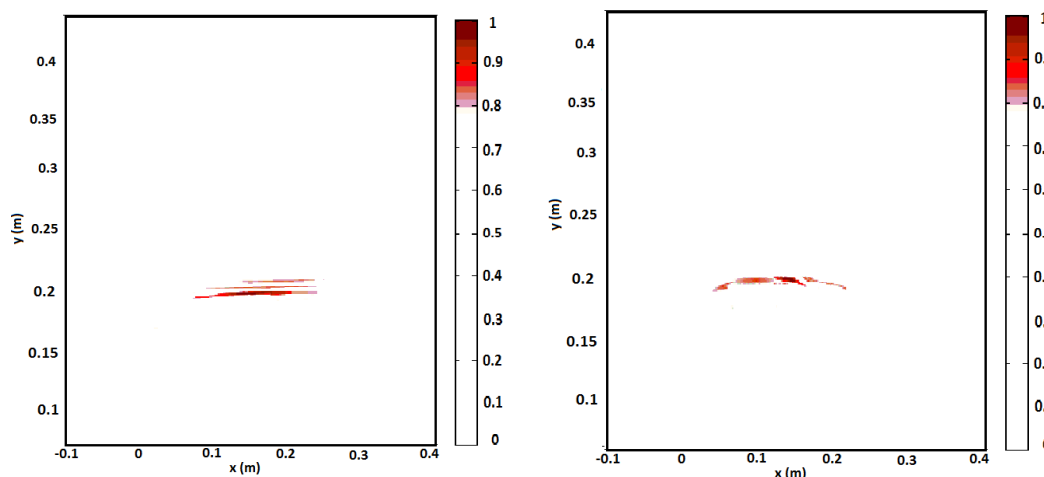
(c) Two targets with a vertical distance d_y of 10cm;   (d) Two targets with a vertical distance d_y of 5cm

Figure 3-9 Images of two targets with vertical distance d_y of 20cm, 15cm, 10cm and 5cm

It is shown that two square metal targets with vertical distances of 20cm and 15cm are successfully imaged by the DAS algorithm. The down range estimation is accurate. However,

the cross range estimation differs. When the vertical distance is 20cm, the image of the nearer target can recover 18cm in cross range; when the vertical distance is 15cm, that value is 2cm higher. The observation is that when the vertical distance is getting smaller, the error of the cross range estimation is getting larger. When the vertical inner distance is reduced to 10cm and 5cm, two targets cannot be separated. This means that these distances are even smaller than the range resolution.

Signal processing for two targets is a little more complicated than that for only one target. The target placed further away from the array generates a smaller reflection, compared to the nearer one. So the image of the nearer target is processed based on the 1st signal peak at first. Then, the first received signal peak is filtered out and the location of the second target is determined based on the 2nd signal peak. Both steps need normalisation to their own peak values and the final imaging results can be plotted onto the same graph. However, the filtering function needs to at least separate the two strongest reflection peak values. When the inner distance becomes smaller than the range resolution, this step is no longer effective and the information of the further target will be lost.

The other arrangement of two targets is to place them side by side in a row with the same vertical distance away from the antenna array. This is to test if the theoretical cross-range resolution can be achieved.

Cross-range resolution is used to distinguish the targets along the horizontal direction, which is related to the beam width of the antenna array, or, more specifically, the effective aperture of the antenna array. It is a function of the product of wavelength and range, divided by effective antenna aperture. The antenna used in experiment is the corrugated "Balanced Antipodal Vivaldi Antenna (BAVA)" with a 3dB beam width of 18-20 degrees from frequency 4GHz to 5GHz.[82]. Therefore, the estimated theoretical cross range resolution is around 6cm.

In simulation, the antenna array set-up is the same as before. Two targets are placed 20cm away from the array, and the inter distance "d_x" is 15cm, 8cm, 6cm and 4cm respectively. The images are given in Figure 3.10.
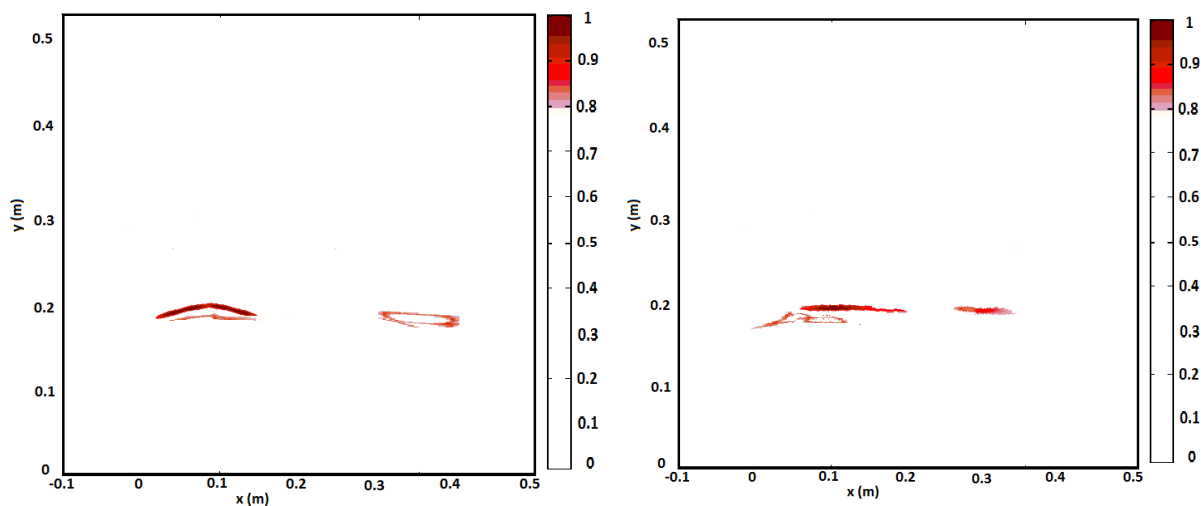
(a) Two targets with a horizontal distance d_x of 15cm;   (b) Two targets with a horizontal distance d_x of 8cm
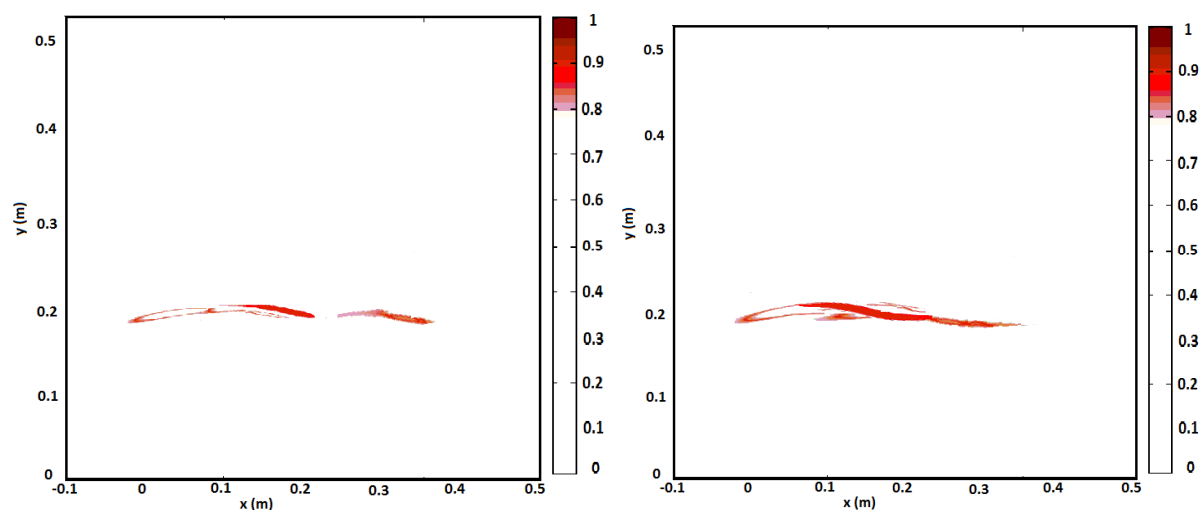
(c) Two targets with a horizontal distance d_x of 6cm;   (d) Two targets with a horizontal distance d_x of 4cm

Figure 3-10 Images of two targets with horizontal inter-distance d_x of 15cm, 8cm, 6cm and 4cm

As shown in Figure 3.10, two metal targets are detectable with a reasonable horizontal inter distance. When the distances are 15cm, 8cm, 6cm, the two targets are easily distinguishable with one image bigger and the other one smaller. When the distance is as small as 4cm, the two targets start to overlap and become indistinguishable, as indicated in Figure 3.10(d).

Both simulations of down-range resolution and cross-range resolution in free space have shown that the theoretical resolution values can be satisfied by the DAS algorithm.

3.2.3 DAS beam-forming in a multipath environment

In any "see-through" situation, the EM wave propagating through a different medium has to be accounted for in order to generate accurate images of the target. The EM wave encounters multiple reflections and refractions at the interface between different media.

The model of the EM wave penetrating through one homogeneous layer is presented in Figure 3.11. The probing space under investigation is discretised into multiple pixels by using range parameter "R" and angle parameter "θ". The equivalent electrical propagation length between the selected pixel and some observation point is $L = L_1 + \sqrt{\varepsilon_r}L_2 + L_3$. The lossless layer has a thickness of "t" and a relative permittivity of "ε_r". The detection range has a standoff distance of "d" from the wall. "θ_1" is the incidence angle and "θ_2" the refraction one. Their relationship is written as below:

$$sin\theta_1 = \sqrt{\varepsilon_r}sin\theta_2 \qquad (3-9)$$

$$(Rcos\theta - t - d) * tan\theta_1 + t * tan\theta_2 + d * tan\theta_1 = Rsin\theta \qquad (3-10)$$

Next, the equivalent electrical length propagation *"L"* can be written as:

$$L = L_1 + \sqrt{\varepsilon_r}L_2 + L_3 = \frac{Rcos\theta - t - d}{cos\theta_1} + \sqrt{\varepsilon_r} * \frac{t}{cos\theta_2} + \frac{d}{cos\theta_1} \qquad (3-11)$$
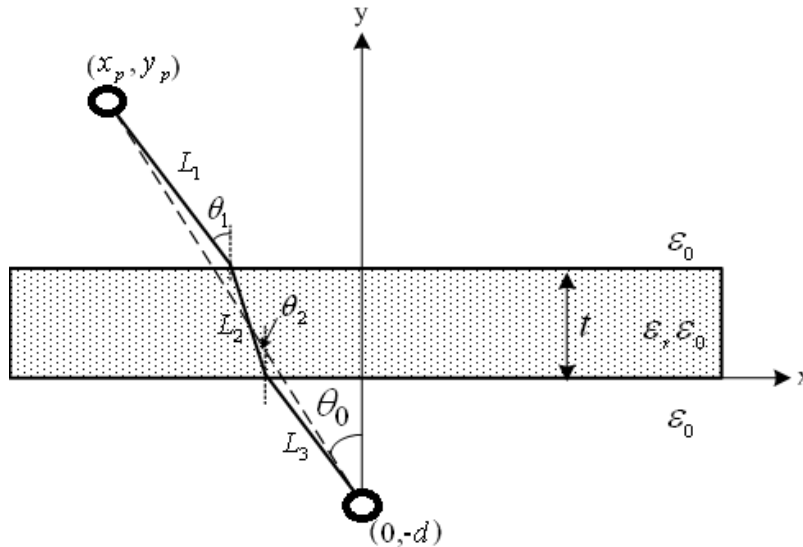
Figure 3-11 The model of an EM wave penetrating through a homogeneous substrate

The performance of DAS has been assessed in this see-through scenario in simulation. There is one transmitting antenna, four receiving antennas, and one metal target placed behind one substrate with the permittivity of 3. The dimension of the substrate is 58 x 21.5 x 1.7 cm^3 and it is placed 10cm away from the array. The target size is 10 x10 x 1 cm^3 and it is placed 20cm away from the array. The substrate is meant to block line-of-sight signal propagation between antennas and the metal target and to cause multipath effect on the signals.

The initial image is shown in Figure 3.12(a). There are two highlights in the investigated space. The first reflection happens at the position of the substrate and the second reflection occurs at the location of the metal target, but is over-stretched. After extracting only the top 20% of the energy level, the image becomes unclear with many reflections as shown in Figure 3.12 (b).
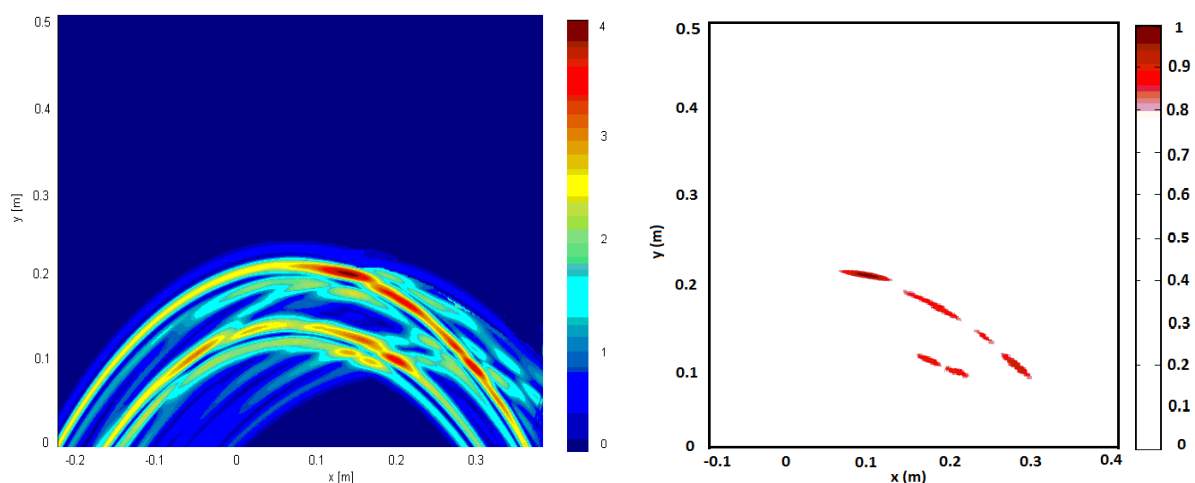
(a) Initial image of the target behind a substrate;   (b) Processed image of the target behind a substrate

Figure 3-12 Image of one metal target behind a substrate

Another scenario with a sealed box is introduced in the model. The box has the same substrate as the one used above with an extra five walls. The dimension of the box is 58 x 58 x 21.5 cm^3. The thickness of the walls remains at 1.7cm for consistency. The nearer surface of the box is 10cm away from the array and the metal target is placed inside with a range distance of 20cm away from the array.

In theory, the box constitutes more interference in the testing environment than just one wall, so it is expected to generate more reflections and make the detection of the target more challenging. The simulated images show that, the back wall of the box and the vertical layers

of the box have little impact on the finalized images. In general, all the walls have generated multipath signals, which worsen the image of the target, as shown in Figure 3.13(a) and the processed image in Figure 3.13(b).
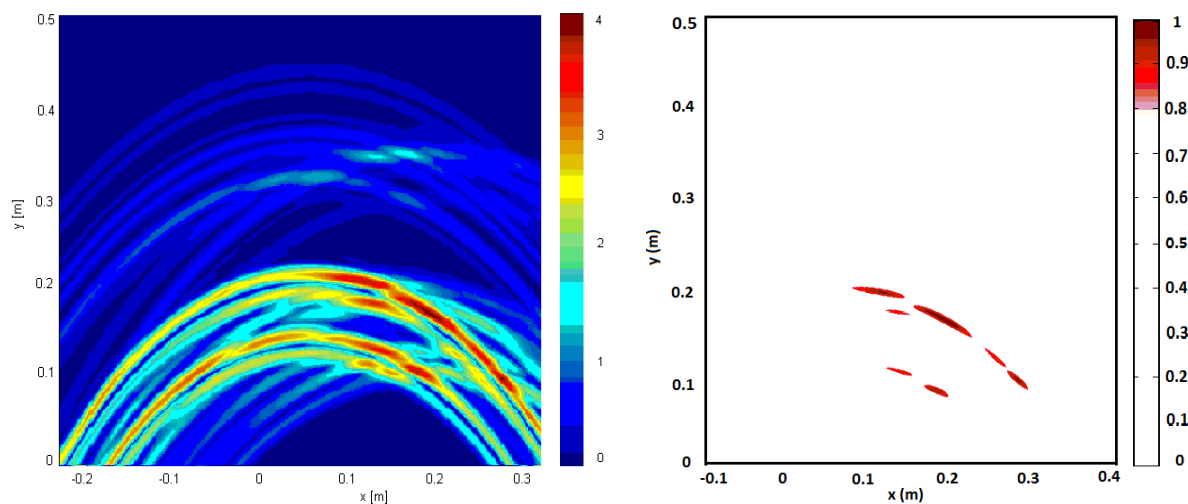
(a) Initial image of the target in a box;   (b) Processed image of the target in a box

Figure 3-13 Image of one metal target inside a sealed box

It is demonstrated in these two simulations that multipath signals will cause the blurring and ghosting of the target image in the DAS beam forming, even in the scenario of a single target. Therefore, there is a need to find a way to improve the DAS method in multipath environments.

One way to improve the DAS approach in multipath environments is to employ a "differential method". This method needs to do imaging in two rounds. The first round of imaging is done with the environment (substrate/box) only; while the second round is conducted with the introduction of the target. The impact of the multipath can be filtered by differentiating the first round of image with the second round one. A much more accurate image of the target can be obtained, as shown in Figure 3-14(a) and (b), even though there are still a few blurring in the images.
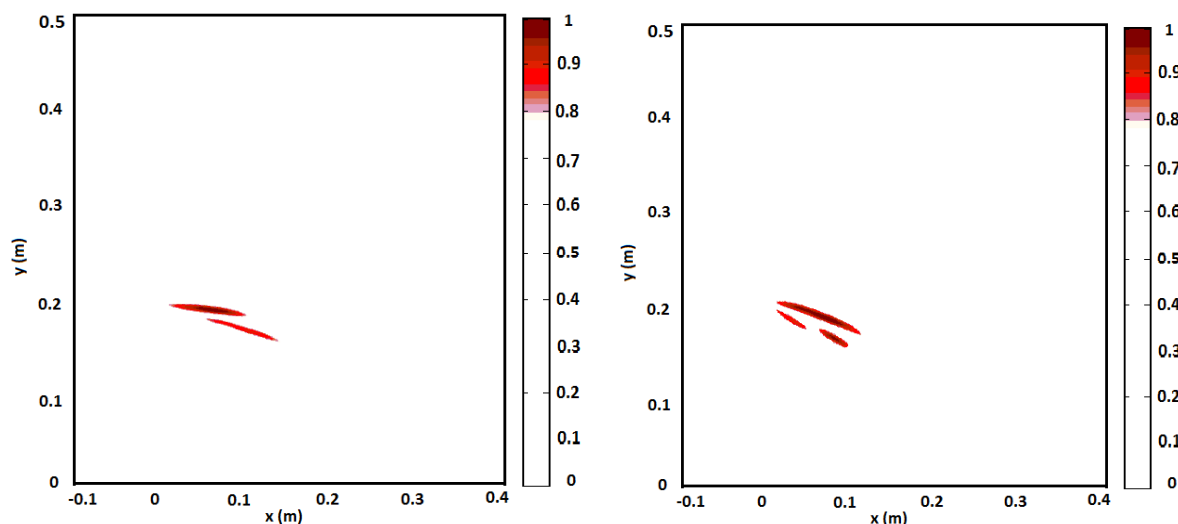
(a) Image of the target behind a substrate;   (b) Image of the target in a box

Figure 3-14 Image of one target behind a substrate and in a box after the differential method

3.2.4 3-D DAS beam-forming

The 3-D DAS beam-forming method is an extension of the 2-D method. It requires range estimation and cross range estimation in both perpendicular directions on multiple planes vertical to the ground. The geometry of the model is depicted in Figure 3.15. Due to an additional dimension, a model consists of a planar antenna array. One substrate with a thickness of "d" and dielectric constant "ε" is placed in front of the planar array. The domain behind the wall is divided into multiple voxels, denoted in 3-D co-ordinates (x, y, z) [79].
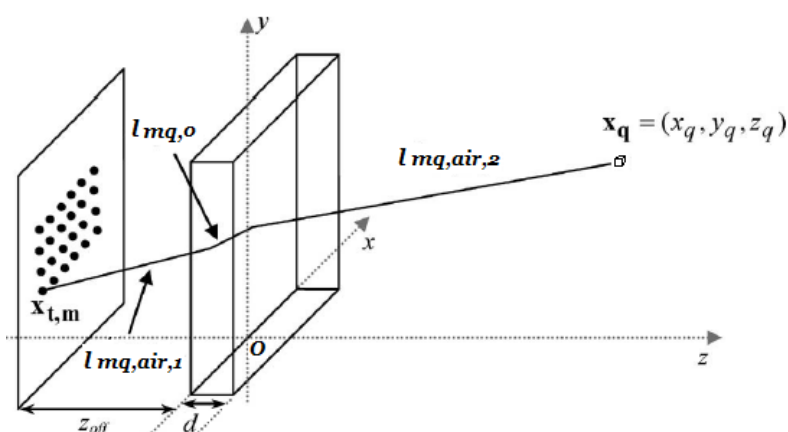
Figure 3-15 Geometry for 3-D DAS imaging [79]

Assuming "a" elements in a transmitting planar array, "b" elements in a receiving array, "c" voxels in the probed region, a complete 3-D DAS imaging calculation shall repeat "a x b x c" times to finish the scanning of the whole area.

To achieve good quality 3D images, it is preferable to have a bigger planar array with more antenna elements, which means a more complicated and expensive imaging system. In order to develop a low-cost and compact 3D imaging system, a rotating arm of antenna array is adopted, as illustrated in Figure 3.16 (a) and (b).
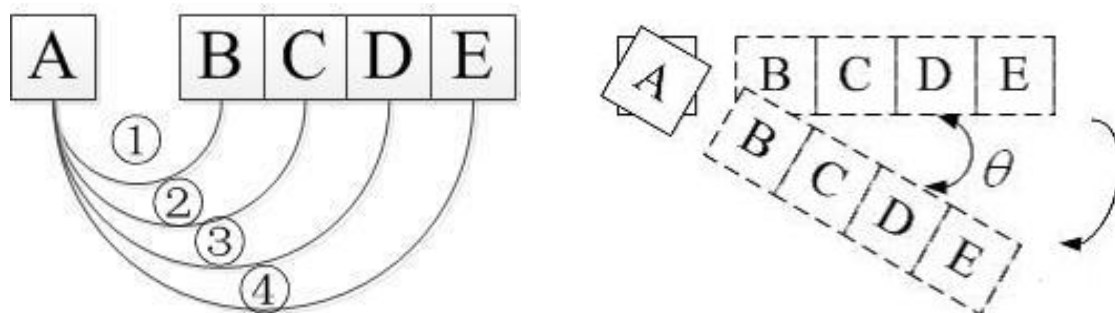
(a) Four measurements in a sequence at one rotating position; (b) The rotation of the antenna array

Figure 3-16 Illustration of the rotating arm of antenna array

The rotary arm of antenna array has one transmitting antenna in the centre and four closely-attached receiving antennas placed at the end. The rotation covers a full circle to maximise receiving data. The angular increment determines the amount of collectable data and is dependent on the gear match in the motor system. Most of the step motors in the market adopts angular increments as small as 0.9degree. However, a 0.9degree increment translates into a high sampling rate, thus making the measurements time-consuming. In practice, 5 or 6 angular degrees are used to form reliable 3D imaging results with the assistance of the right gear match. The receiving antennas work in a synthetic manner and all connected to a RF switch unit. For each link, there is only one receiving antenna in operation. By controlling the RF switch, the imaging data can be picked up on four receiving antennas in sequence, as illustrated in Figure 3.16.

In simulation, it is inconvenient to rotate antenna models due to the port's set-up and meshing issues. So the rotation is accomplished by rotating the target instead. For illustration purpose, eight angles are chosen to create eight images of the target, as shown in Figure 3.17. The angles

of 0, 45, 90, 135,180, 225, 270 and 315 degrees are designated to produce their own images of the target. By adding them all together for each scenario and rescaling the energy threshold, a complete cross range image of the target can be produced.
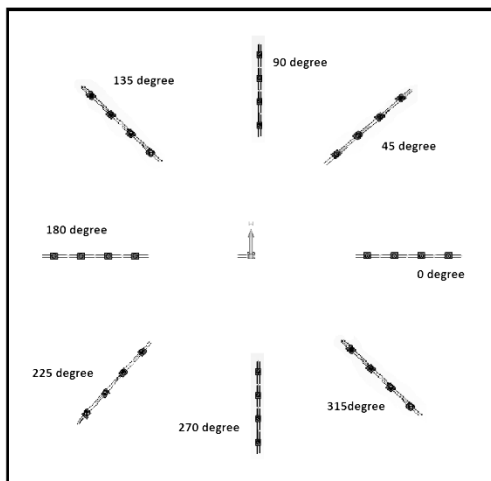
Figure 3-17 Rotation of the array with eight angular stops in simulation

The first series of testing scenarios is to image one metal target in free space. The DAS algorithm has been applied. In simulation, the antenna arrangement is the same as that used in the previous models. One target with a size of 10 x 10 cm^2 is placed 40cm away from the array. The range and cross range images after superposition for single target detection are shown in Figure 3.18.
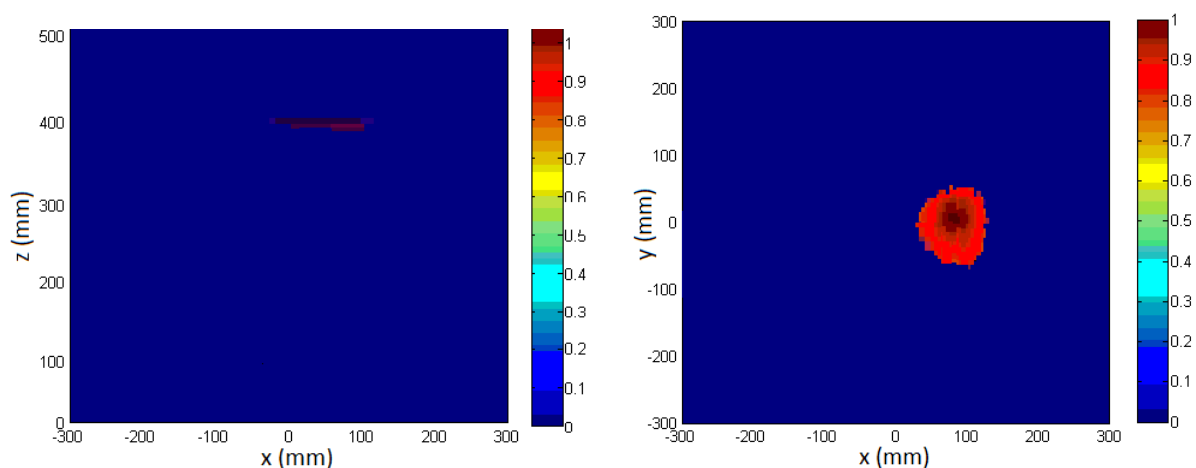
(a) Range image of one metal target in free space; (b) Cross-range image of one metal target in free space

Figure 3-18 Range and cross-range images of one metal target in free space

The second model in free space is to image a pair of metal targets. It is based on the first model, with one additional metal target with a size of 8 x 8 cm^2. First of all, two metal targets are placed one behind the other in a column. The first target is 20cm away from the antenna array and the second one 35cm. So the inner distance between them is 15cm. The range and cross range images are illustrated in Figure 3.19. It is shown that these two images have a good estimation of the targets. The range image and the cross-range images give good indication of the targets' sizes and positions.
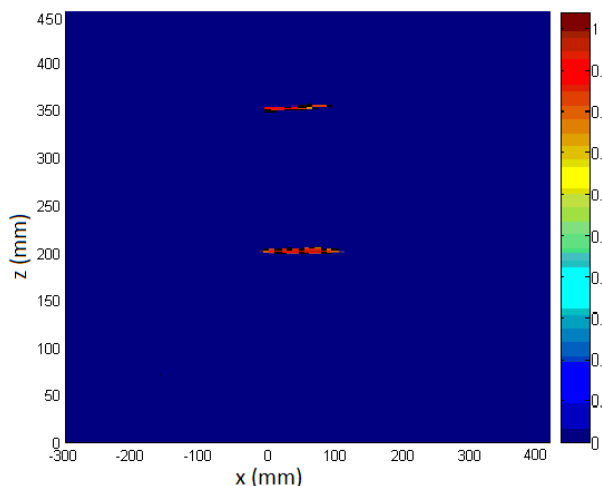
(a) Range image of two metal targets in free space
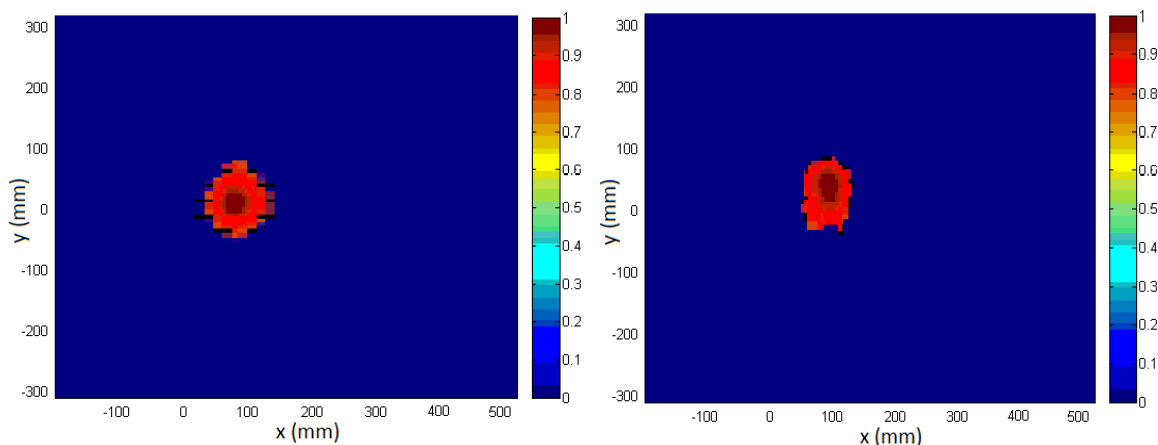
(b) Cross-range image of the 1st target in free space;   (c) Cross-range image of the 2nd target in free space

Figure 3-19 Range and cross-range images of two metal targets with d_y of 15cm in free space

The other arrangement is to place two targets in a row in front of the antenna array. They have an inner distance of 6cm and both have the same distance of 20cm away from the antenna array. The range and cross range images are given in Figure 3.20.
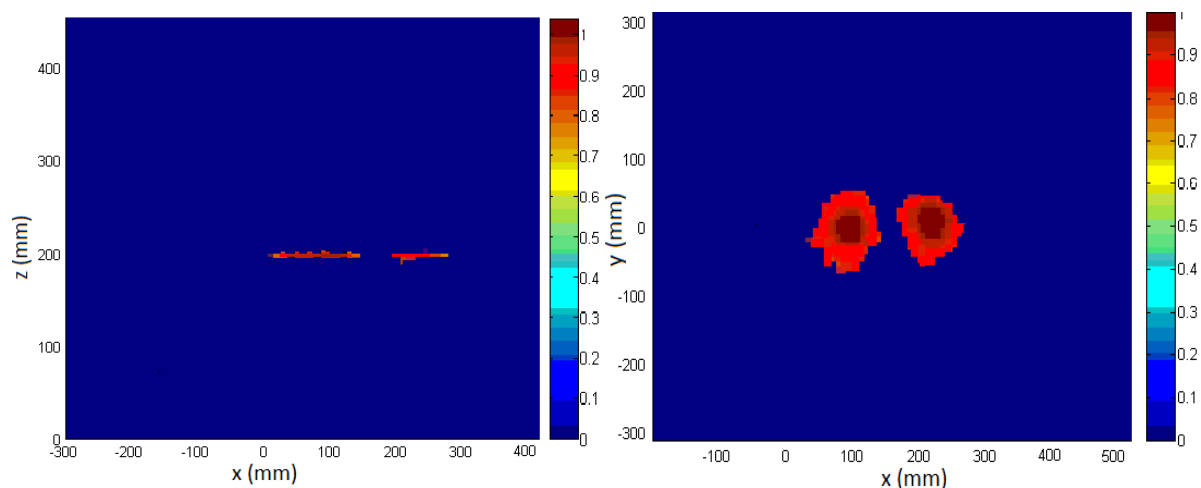
(a) Range image of two metal targets in free space;   (b) Cross-range image of two targets in free space

Figure 3-20 Range and cross-range images of two metal targets with d_x of 6cm in free space

The second testing scenario is to introduce a substrate with a dimension of 58 x 21.5 x 1.7 cm^3 and a permittivity of the 3. The Antenna set-up is the same as the one used above. One metal target with a size of 10 x 10 cm^2 is placed 40cm away from the array but behind the substrate. The range and cross-range images are given in Figure 3.21.
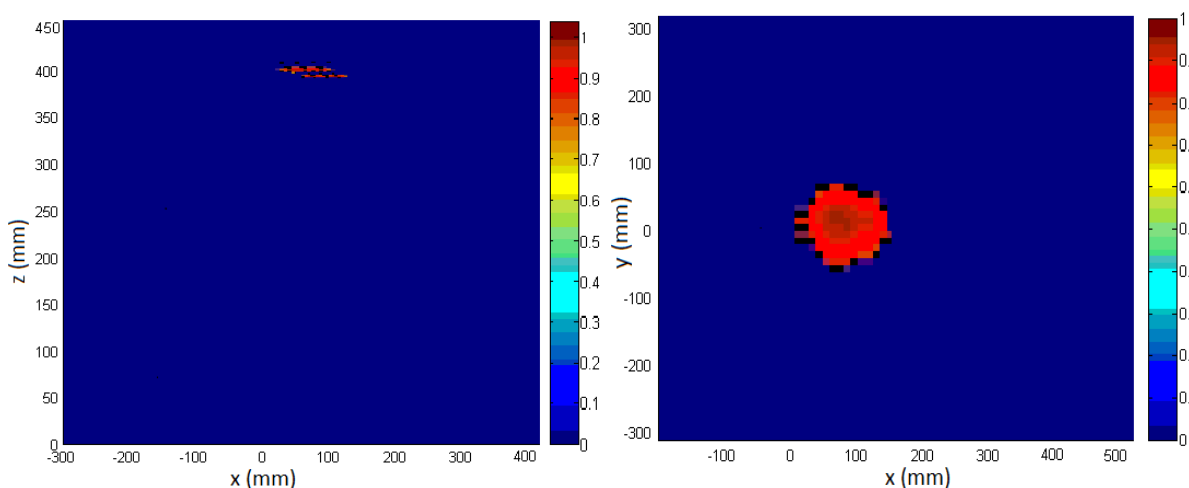
(a) Range image of one target behind the substrate; (b) Cross-range image of one target behind the substrate

Figure 3-21 Range and cross-range images of one metal target behind a substrate

After the signal target imaging, two targets are adopted. First, two metal targets are placed behind the substrate with a 15cm vertical gap between them. The target nearer to the antenna array has a distance of 20cm away from it and the second target 35cm. Then, two targets are placed in a row behind the substrate with a 6cm horizontal gap. Both targets are the same 20cm distance away from the antenna array.

The simulations on these two cases have been conducted and the images are shown in Figures 2.22 and Figure 2.23 respectively, where the differential method is applied. When there is only one target behind the substrate, the influence of the substrate can be mostly filtered, though the images blur slightly compared to those in free space. However, the blurring gets worse in the two-target images.
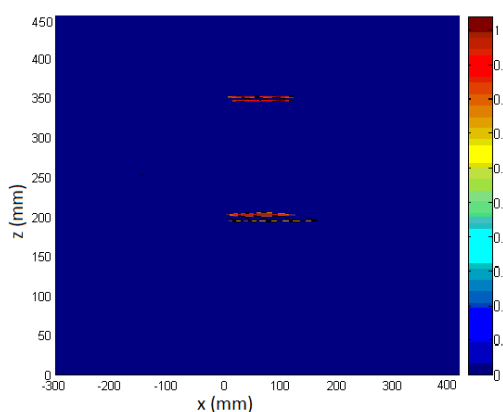
(a) Range image of two metal targets behind the substrate
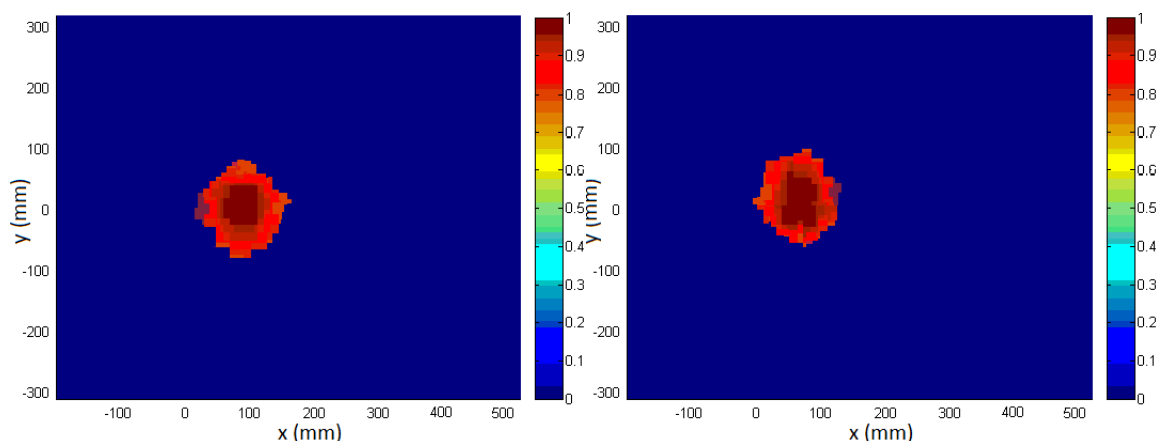
(b) Cross-range image of the 1st target behind the substrate; (c) Cross-range image of the 2nd target behind the substrate

Figure 3-22 Range and cross-range images of two metal targets with d_y of 15cm behind a substrate
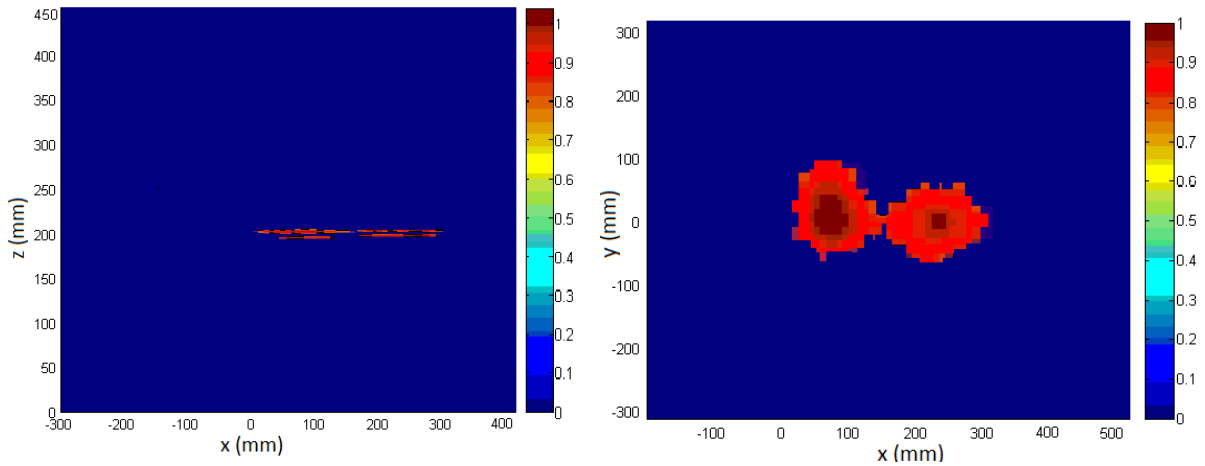
(a) Range image of two targets behind the substrate;   (b) Cross-range image of two targets behind the substrate

Figure 3-23 Range and cross-range images of two metal targets with d_x of 6cm behind a substrate

3.2.5 Limitations of DAS Beam-forming

The DAS beam-forming method depends on the effective capture of the peak value of the received signal. A window function is used to control the extent of capturing, as shown in Figure 3.24(a). When there are more targets, the second window function is used in the same way, as shown in Figure 3.24(b). This would work perfectly when the propagation happens in free space or an environment without much interference.
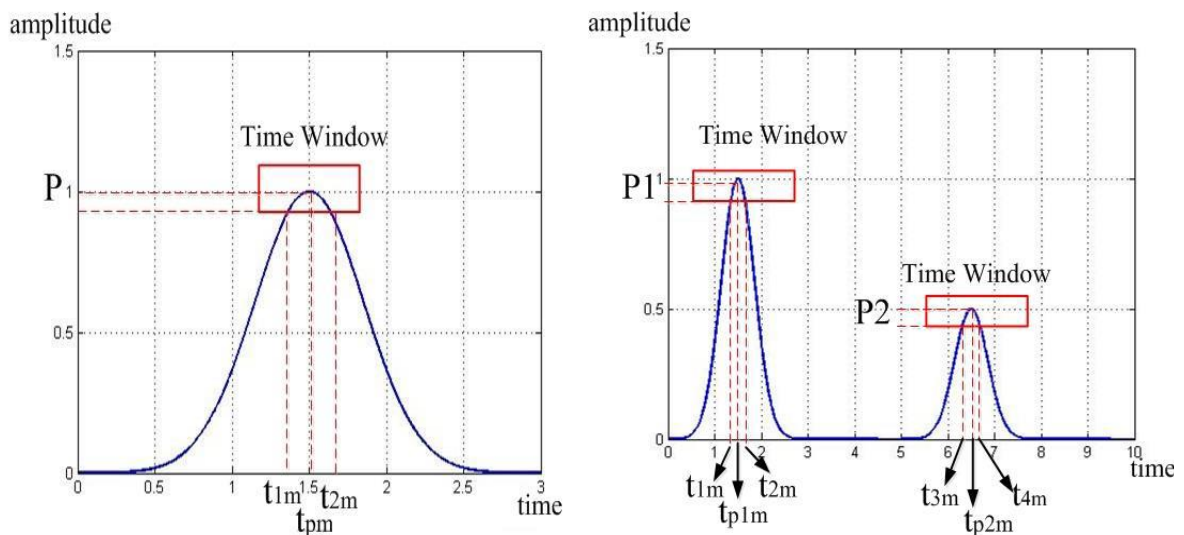
(a) One time window;   (b) Two time windows

Figure 3-24 Illustration of the time window

The time window function "*TW*" can be written as:

$$\{t_{1m} \leq TW_m \leq t_{2m};\ \frac{t_{1m} + t_{2m}}{2} = t_{Pm}\} \tag{3-12}$$

Here, t_{Pm} is the time of peak value for P_m for $b_m(t)$. t_{1m} and t_{2m} are determined as below:

$$\begin{cases} t_{1m} \parallel (p(t_1) = \alpha * P_m) \wedge (t_1 < t_{Pm}) \\ t_{2m} \parallel (p(t_2) = \alpha * P_m) \wedge (t_2 > t_{Pm}) \end{cases} \tag{3-13}$$

Here, $p(t_1)$ and $p(t_2)$ are amplitude for t_{1m} and t_{2m} respectively. α is the relative ratio in percentage, calculated by the division of the chosen signal value by the peak value. The choice of α is important because it will decide the brightness in the final images. In order to investigate the effectiveness of α parameters, simulation results of two targets in free space are used to demonstrate.

The first simulation model is two targets placed in a column in front of the antenna array. The distance between the targets is set as 10cm, 15cm and 20cm, respectively. All the imaging results show successful detection of both targets. By choosing different top energy ratios, such as 10%, 20%, 30% and 40%, the cross-range information of both targets is estimated. The error rate is calculated based on the true dimension of the target and the estimated one. The results are given in Figure 3.25. It is found as the energy ratio increases, the cross-range error increases.
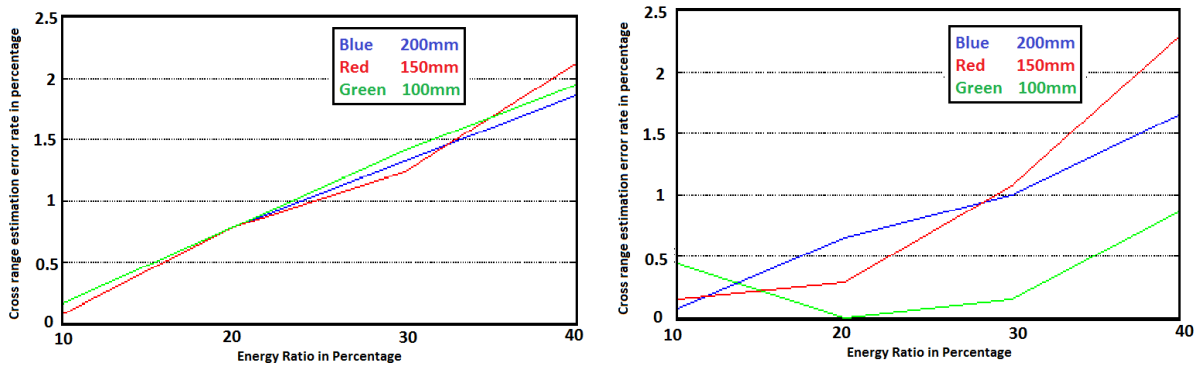
(a) Error of cross-range estimation of the 1st target   (b) Error of cross-range estimation of the 2nd target

Figure 3-25 Error of cross-range estimation with energy ratios of 10%, 20%, 30% and 40%
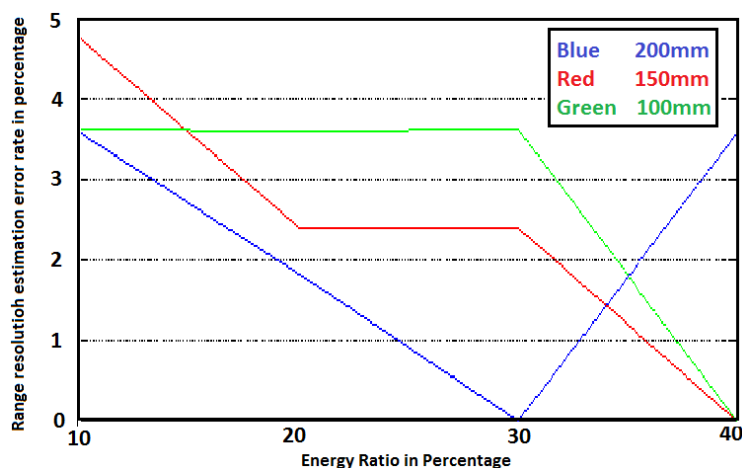
Figure 3-26 Error of down-range resolution estimation with energy ratios of 10%, 20%, 30% and 40%

The error of the down-range resolution estimation based on top energy ratios of 10%, 20%, 30% and 40% is shown in Figure 3.26. Generally, the impact varies depending on different inter-space between two targets. The error rates are less than 5 percentages in all cases, so it means that various energy ratios have little impact on the down range resolution estimation.

The second simulation model includes two targets placed in a row in front of the array. The inter distance is set as 15cm, 8cm to 6cm respectively. Four different energy ratios of 10%, 20%, 30% and 40% are chosen to create the images. As shown in Figure 3.27, when 30% and 40% are used, the images spread out too much to clearly distinguish two targets.

(a) Two targets image with top energy ratio of 30%　　(b) Two targets image with top energy ratio of 40%
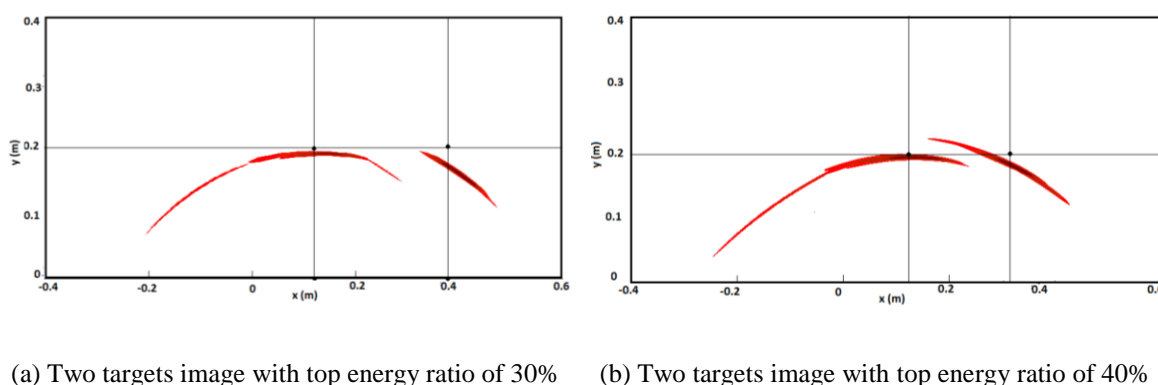
Figure 3-27 Images of two targets in a row with top energy ratios of 30% and 40%

It is clear that top energy ratios of 30% and 40% are not suitable for effective image recovery, so only 10% and 20% are selected to be analysed in terms of cross range estimation and cross range resolution estimation. The error rate of cross range estimation of two targets is given in Figure 3.28, while the error of cross range resolution estimation is given in Figure 3.29.

Images by both 10% and 20% top energy ratios can focus precisely on the first target, but the 20% value shows a better effect over 10% on the second target, as shown in Figure 3.28 (b). The error of the cross-range estimation drops from 0.8% to 0.3% when two targets are distanced 15cm apart in a row. This value drops even further from 0.8% to 0.15% when two targets are 8cm and 6cm apart in a row.

When two targets are placed 15cm and 8cm apart, 10% and 20% top energy ratios have the same effect on the error of cross range resolutions. When two targets get as close as 6cm, the error rate increases from 1% to 1.4% when the top energy ratio changes from 10% to 20%. In conclusion, top 10% and 20% energy ratios are both good thresholds to image two targets. The 10% top energy ratio is better at differentiating two closely-placed targets, while the 20% top energy ratio can reveal better cross range information of the two targets.
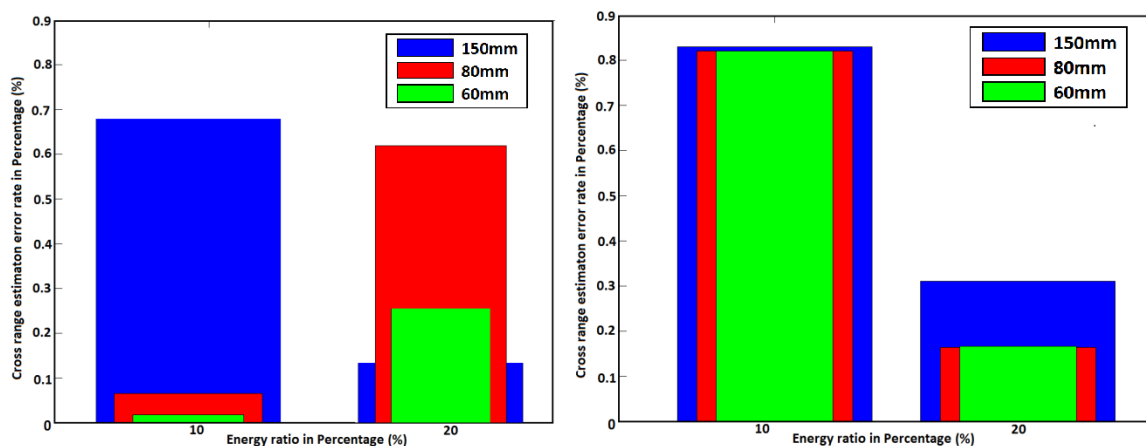
(a) Error of cross range estimation of the first target   (b) Error of cross range estimation of the second target

Figure 3-28 Error of cross range estimation of two targets with the top energy ratios of 10% and 20%
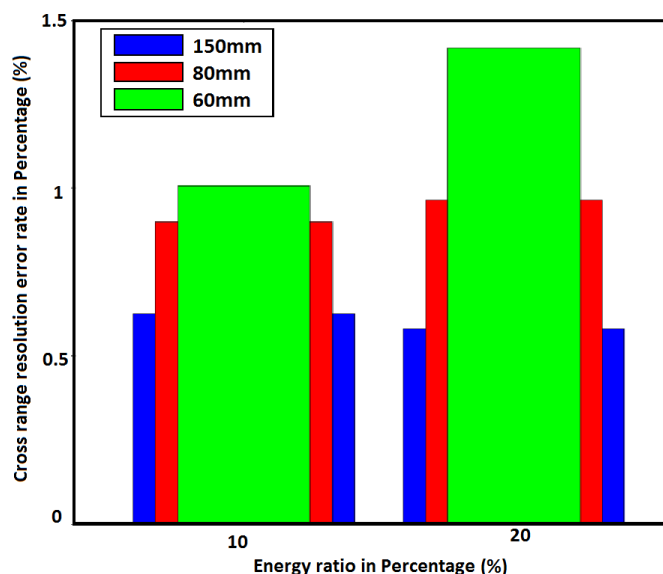
Figure 3-29 Error of cross range resolution estimation based on top energy ratios of 10% and 20%

However, there is a limitation in the use of window functions. When unwanted interference signals are very strong and the energy level is comparable to the target signature in the testing environment, the adoption of one window function to capture the peak signal values could compromise the images. It may capture multiple maximum values, including local ones which interfere with the useful value. The target signal can be masked in the noise and multipath signals, leading to imaging errors. In one typical case, as shown in Figure 3.30(a), there are three peak values selected by one window function, so DAS method produces three hot spots of brightness, as shown in Figure 3.30(b). It is difficult to determine the real target's location.
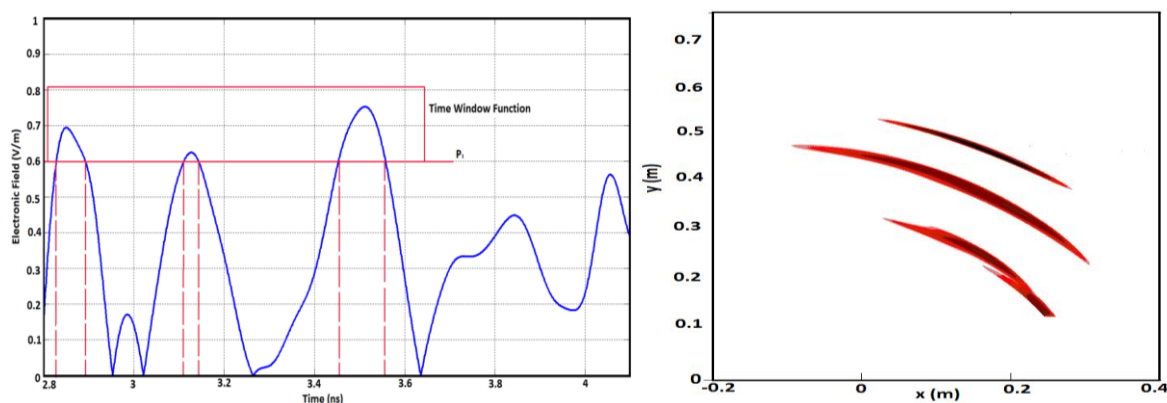
(a) Time window to capture three peaks   (b) Image reflecting three peaks with strong signal interference

Figure 3-30 The image with strong signal interference under one time window

3.3 The Time Reversal imaging method

The "Time-Reversal (TR)" method reverses the received signals in time sequence and re-transmits them. The first in-coming signals would be the last to be re-transmitted out. Later study has shown that signal reversal in time domain is equivalent to signal phase conjugation in frequency domain. The most prominent feature of the TR method lies in its ability to focus simultaneously in time and in space [80]. The temporal focusing represents the capability of maximum energy concentration of all the time-reversed signals at the same time from the receivers. This is especially beneficial when it comes to non-uniform and complex testing media, where the signal propagation is severely interfered by multipath signals. The spatial focusing means that the time-reversed signals are able to self-adaptively trace back to the location of the strongest source, no matter if it is an active source, such as a transmitting antenna, or a passive one such as metal targets with strong reflectivity. In theory, both focuses don't need the knowledge of the propagation environment, provided that it is time-invariant or with very minor changes during the period of TR calculation.

3.3.1 Standard Time-Reversal method

Ideally in the standard TR method the target is surrounded by a spherical array. This cavity creates a complete coverage of the target and all the signal information can be retained. In essence, two steps in TR operation are given below, also shown in Figure 3.31:
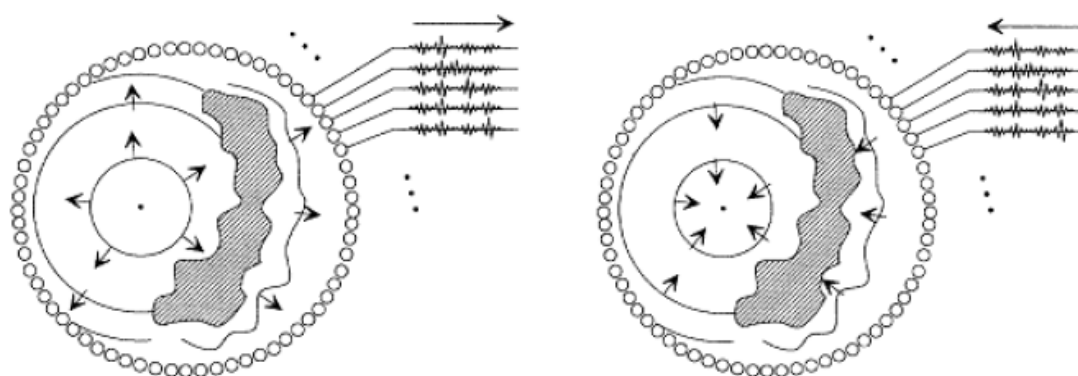
(a) The step of transmitting and recording;   (b) The step of time-reversal, re-transmission and focusing

Figure 3-31 Model of the TR cavity [81]

1) Step one: A point source generates a wave front and emits outwards, which is distorted by the time-invariant heterogeneity in the cavity. The distorted field is recorded by the cavity antenna elements;

2) Step two: The recorded signals are time-reversed and re-emitted by those elements. The time-reversed field back-propagates and tends to focus on the initial illuminating source.

In practice, it is impossible to place a dense circle of receivers as a cavity around the target. Instead, it makes more sense to apply a certain number of antennas at a specific position to cover a partial area. These receivers are called a "Time Reversal Mirror (TRM)". This compromise would necessarily lose some part of the target information. However, by transforming the prevalent multipath signal in the real testing environment into something useful for imaging, TR can produce better images with sharper resolution, with the additional help of alternatively increasing the effective array aperture. This phenomenon works best with more multipath signals, which at their best are the signals related to the interaction between the target and other obscurities. Three scenarios are illustrated in Figure 3.32.

(a) TR in free space   (b) TR with one dielectric suitcase   (c) TR with discrete scatterers
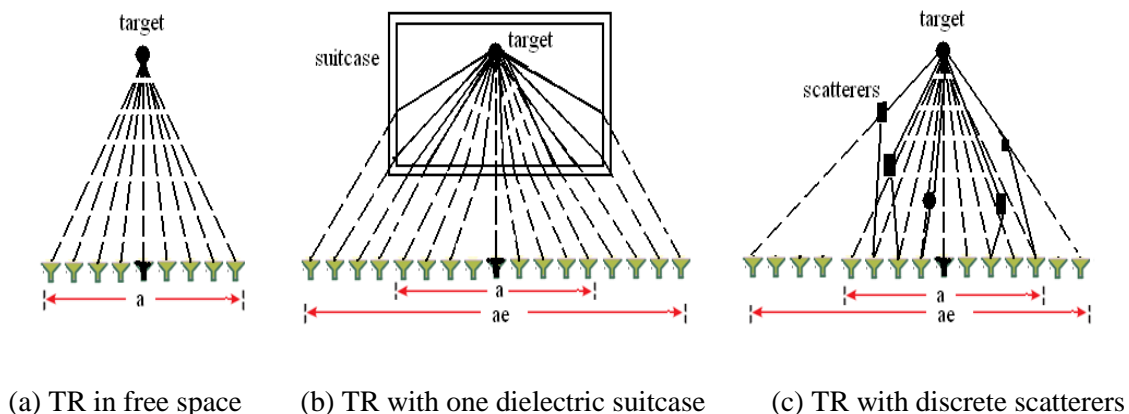
Figure 3-32 Different effective antenna apertures in imaging applications with and without multipath

In free space, the effective array aperture is certain once the type of antenna and the array configuration are determined, as shown in Figure 3.32(a). When multipath is introduced by a dielectric suitcase, shown in Figure 3.32(b) or multiple scatterers, shown in Figure 3.34(c), the effective antenna aperture is artificially enlarged to some extent. The fictional antennas on both sides of the real array, shown in Figure 3.32(b) and (c), indicate this enlargement. The significance of this phenomenon lies in the imaging application. The cross range resolution can be influenced greatly by the effective antenna array aperture. What makes TR stand out is that

when multipath effect fails or compromises the conventional imaging methods, the TR method can otherwise make use of it and turn it into a useful factor to achieve a better cross range resolution in imaging of multiple targets.

In simulation, the standard TR method is very straight-forward in its expression in time domain. The procedures of signal reversal are given below:

1. A short UWB pulse is transmitted from one of the transceivers towards the probed domain and one target is placed in front, as shown in Figure 3.33.
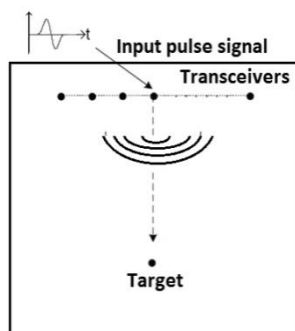
Figure 3-33 A UWB signal transmitted from one of the transceivers to the target

2. The transmitting signal propagates through the medium and meets the target, as shown in Figure 3.34. The medium could be homogeneous / heterogeneous, so the received signals may contain not only target signature but also interferences.
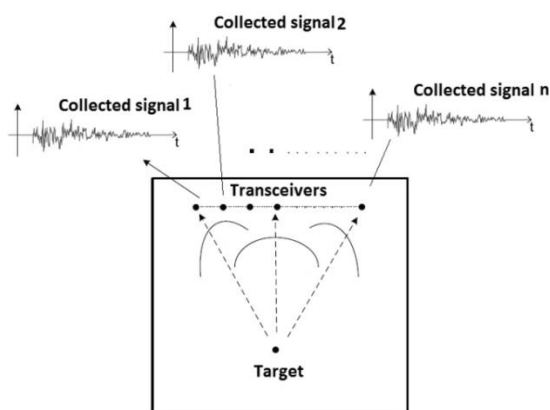
Figure 3-34 Signal reflected by a target in the unknown medium with noise and interference

3. For a pre-defined period of propagation time, received signals are collected and saved at the receiving end. A cut-off time parameter is used to stop the receiving at a certain point. Then all the received signals are truncated and reversed in time sequence, as illustrated in Figure 3.35.
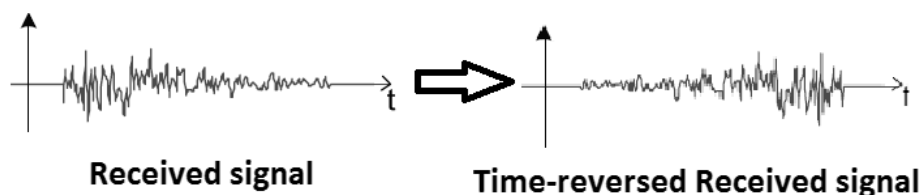
Figure 3-35 One received signal and its time-reversal

4. The time-reversed signals are re-transmitted back to the same domain. In theory, the re-transmissions of time-reversed signals tend to create a focus at the original target's position. The convergence is shown in Figure 3.36.
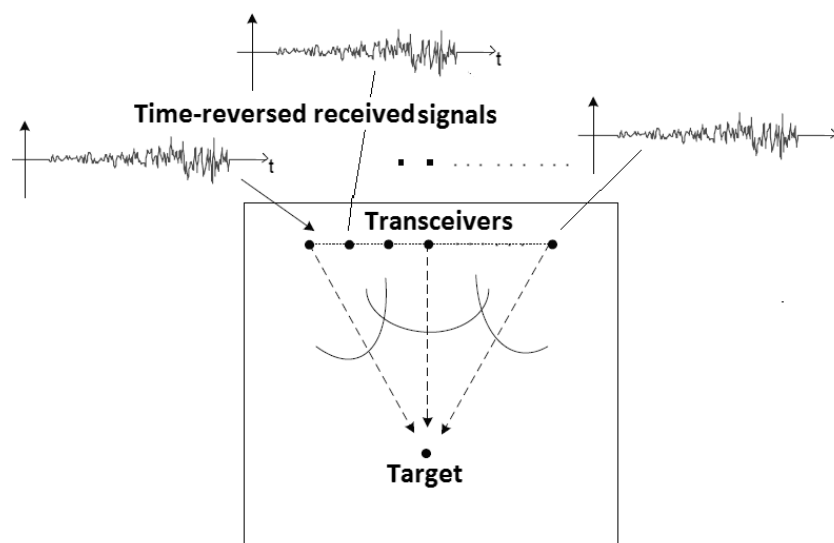
Figure 3-36 Convergence of the re-transmitted time-reversed signals at the target's position

3.3.2 Re-focusing of the transmitted Gaussian pulse by TR

This example in simulation re-focuses an active Gaussian pulse in a multipath environment by TR method, in comparison with original one in free space. As shown in Figure 3.37, the model consists of a pair of parallel metal slabs and two identical horn antennas. The dimensions of the waveguide feeding structure for the horns are 28.5 x 12.6 x 100 mm^3. Horn antennas are

taper-extruded from the waveguides at 30 degree angles and the length is 40mm. The operating frequency is defined from 6.5 to 10GHz. The distance between these two antennas is noted as "L_3", which is 800mm.
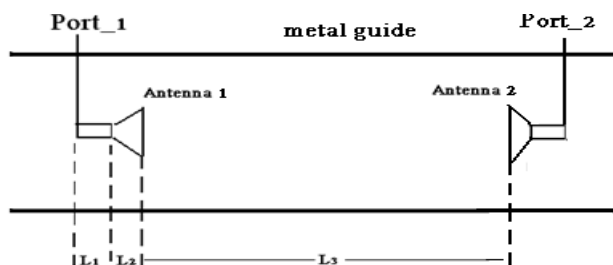
Figure 3-37 The bi-static horn set-up with a pair of parallel metal slabs

From the figure above, "Antenna 2" acts as a receiver while a Gaussian pulse is transmitted from "Antenna 1", which is regarded as the active source. Received signal should arrive at 4.6ns in free space, however, metal slabs create multipath signals and blurred the line-of-sight propagation. The transmitted Gaussian Pulse is shown in Figure 3.38 (a) and the received signal is shown in Figure 3.38 (b). The observation time of 40ns is used to record the received signal.
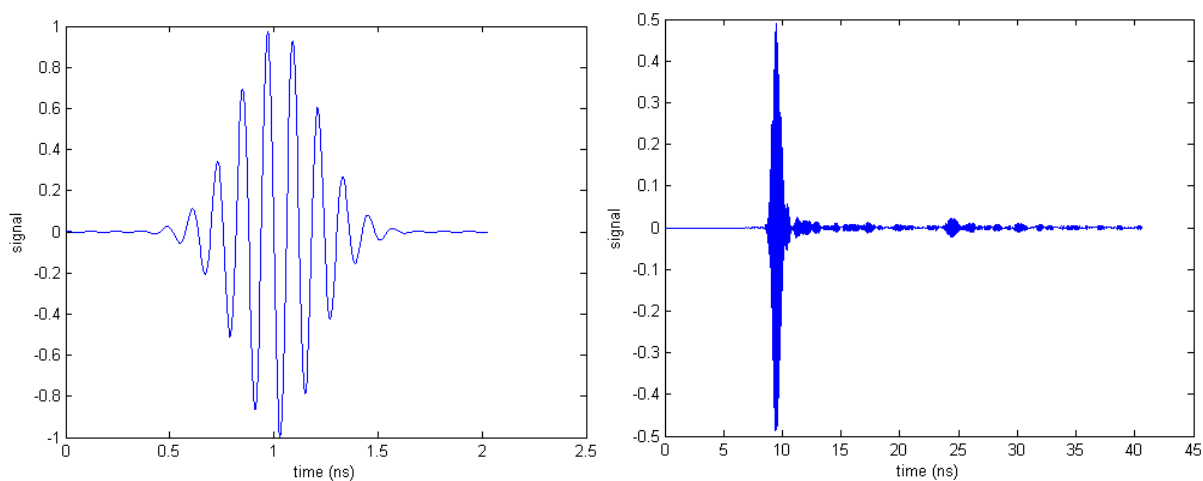
(a) The transmitted Gaussian pulse;   (b) The received signal

Figure 3-38 Transmitted and received signals

Three following procedures are implemented in the TR method. The first step is to reverse the received signal in time sequence. Inevitably, the time-reversed signal falls into the negative time zone. So the second step is to delay the time-reversed signal till it is within the positive time zone only. This delay is 40ns. The last step is to normalise the time-reversed signal. After

these three steps, the adjusted signal is ready for re-transmission from the "Antenna 2" to "Antenna 1", as shown in Figure 3.39(a). The received signal is shown in Figure 3.39(b).
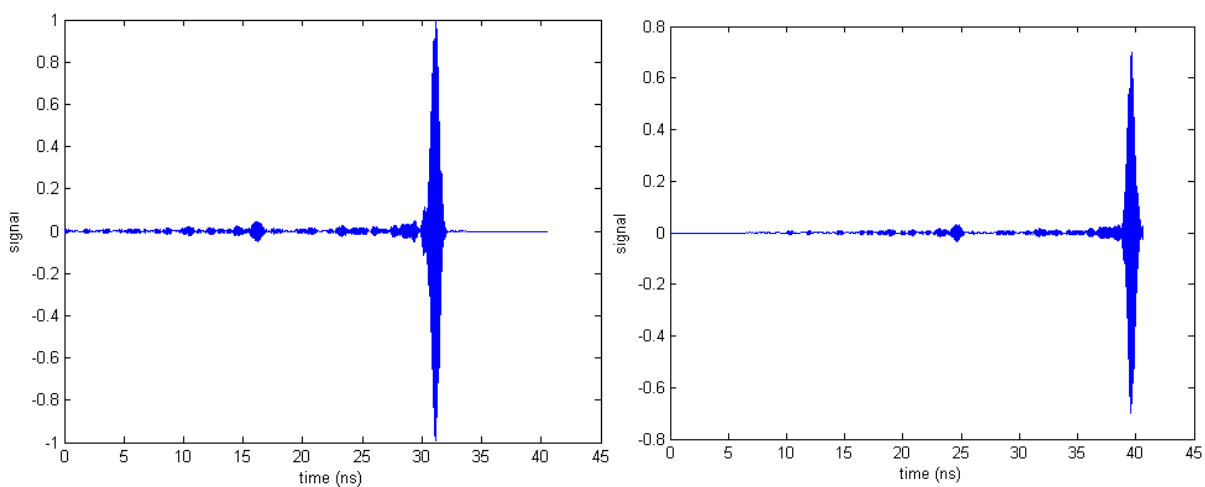
(a) The re-transmitted TR signal;   (b) The received TR signal

Figure 3-39 Re-transmitted and received TR signals
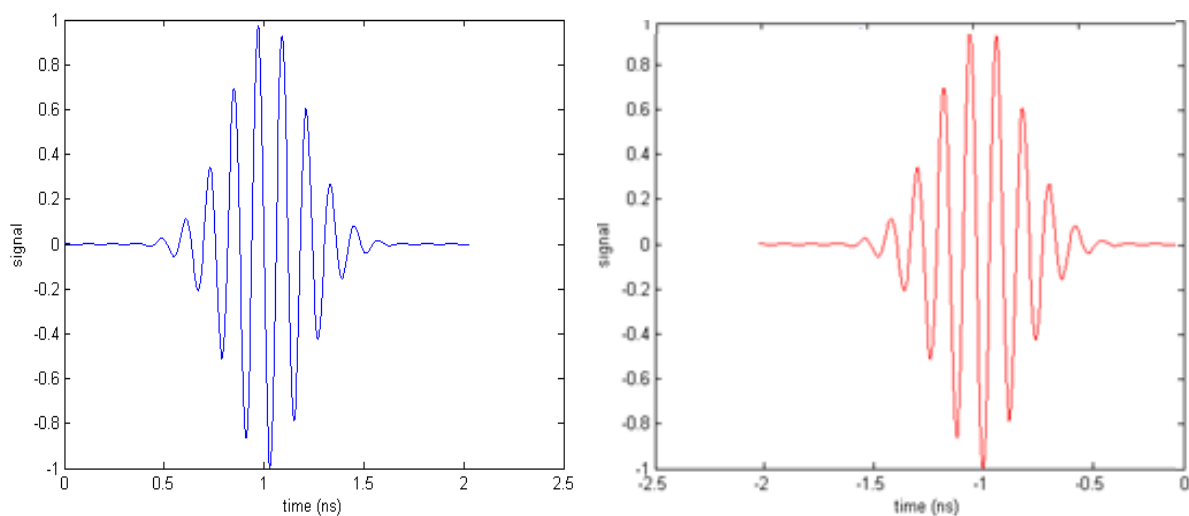
(a) Original transmitted Gaussian pulse   (b) Recovered TR pulse

Figure 3-40 The Gaussian pulse and its time reversed version

Due to the time delay of 40ns introduced in the previous step, the original received TR signal needs to compensate it by stepping back into the negative time zone. Note that the peak value of the original Gaussian pulse in Figure 3.38(a) occurs at 0.97ns. The peak value of the received TR signal is at -0.97ns. This symmetry indicates that TR method has achieved the temporal re-

focusing. By truncating a time window of 2.5ns and signal amplitude normalization, the comparison of the original Gaussian pulse and the recovered one can be shown in Figure 3.40.

Rise time and pulse width are used as the indicators to show the resemblance between the original Gaussian pulse and the recovered one by TR. Rise time "t_{rise}" is the time when the Gaussian pulse reaches its 90% of the peak amplitude from 10%. Pulse width is defined as "t_p", which is the time duration between 50% of peak amplitude in the ascending and trailing edges of the pulse. In comparison between the original Gaussian pulse and the recovered one, rise time has increased from 0.4ns to 0.6ns and pulse width has increased from 0.43ns to 0.6ns. Above all, the pulse under the TR process has successfully recovered the original Gaussian pulse.

3.3.3 TR imaging in free space

In simulation, one target with the dimension of 10 x 10 cm^2 is placed 40cm away from one transmitter and four receivers. The propagation time is defined as 40ns. The first step is to transmit a UWB pulse towards the target by the transmitting antenna and to obtain four received signals on the receiving antennas. After reversing the signals in time sequence, they are re-transmitted by the receiving antennas towards the same environment. A comparative algorithm is designed and applied to capture each maximum electrical field in the area at each moment, as shown in Figure 3.41, where the most maximum peak value occurs at the moment of 19.84ns. The E-field is mapped out at this particular moment to reveal the information of the target.
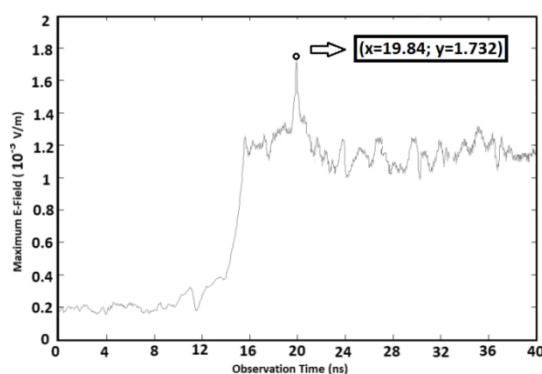
Figure 3-41 Recorded maximum E-field along the observation time

In order to compare with the DAS imaging method, the same eight angles are used to imitate the rotation of the array in the simulation of TR imaging. The 3D images of the target have

been generated by integrating the target data collected at these angles step by step to see the effect of superposition.

The breakdown of the TR method can be described in the following steps. First, the UWB signal is launched from the transmitting antenna and is received by four receivers with a pre-defined time window when the target is not present. Then, the same set-up is simulated again with the presence of the target. The longer the period of this time window is, the more received data can be collected, but it takes more time for its collection. The subtraction produces the target signature signal as well as the multipath residue left between the target and the surroundings. The differential procedure is useful to detect a moving target with time-invariant environments. Before the measurement of the target, the environment first needs to be tested. This value can be saved and subtracted from each measured component of the target signal. When the target is moving, the subtracted signals indicate different target signals related to their corresponding locations.

When the time window expires, the four extracted signals (after the subtraction) are time-reversed, time-delayed and re-transmitted back into the domain from the four receivers. Multiple field monitors, such as far-field monitors, E-field monitors, and probes are employed in the investigated areas with pre-defined space and time step. The use of these can monitor and capture the field fluctuation while the time-reversed signals are propagating into the area of interest. The recording of this field data can reveal the key information of the target and the corresponding data are saved and transferred to PC for imaging processing.

The strategy of presenting the processed images is that two angles with 180 degrees difference are chosen to integrate one image first. Then eight angles can produce four integrations. The first integration of 0 degree and 180 degrees creates one added image, as shown in Figure 3.42(a). 45 degrees and 225 degrees are added on to it and create another image result, as shown in Figure 3.42(b). The same is applied to 90 degrees and 270 degrees, and 135 degrees and 315 degrees to produce Figures 3.42(c) and (d). All the images are normalised to their own peak values respectively. The range images seem to be consistent throughout the angle integrating process.

(a) 0 and 180 degrees;

(b) 0,180,45 and 225 degrees

(c) 0,180,45,225,90 and 270 degrees;

(d) 0,180,45,225,90,270,135 and 315 degrees
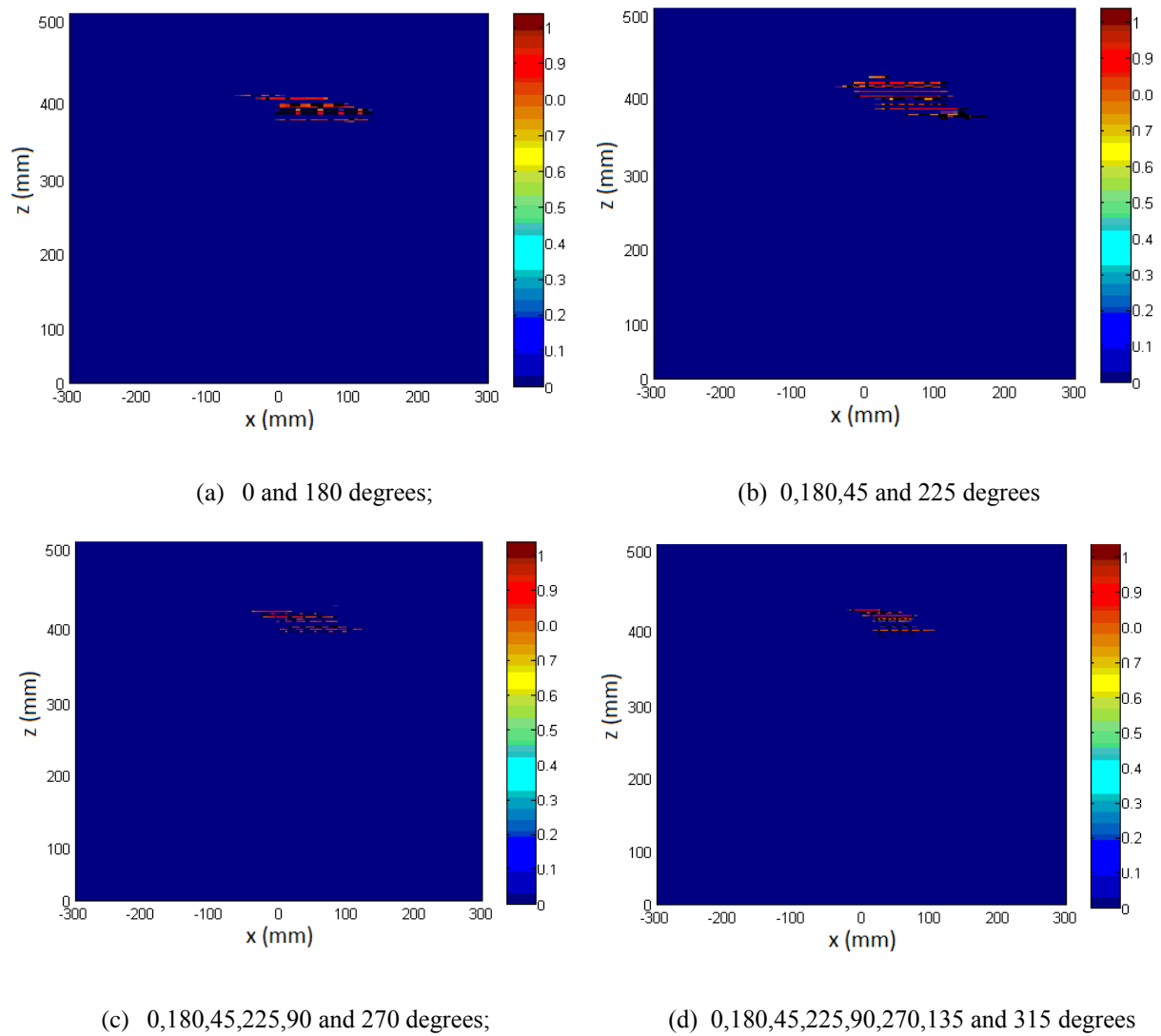
Figure 3-42 Range images of one target at different integration of angles in free space

The same angle integration procedure is used to create the cross-range images, as shown in Figure 3.43. It is evident that this procedure can re-create a much more focused image of the target when adding the 3D cross range information.

(a) 0 and 180 degrees;

(b) 0,180,45 and 225 degrees

(c) 0,180,45,225,90 and 270 degrees;

(d) 0,180,45,225,90,270,135 and 315 degrees
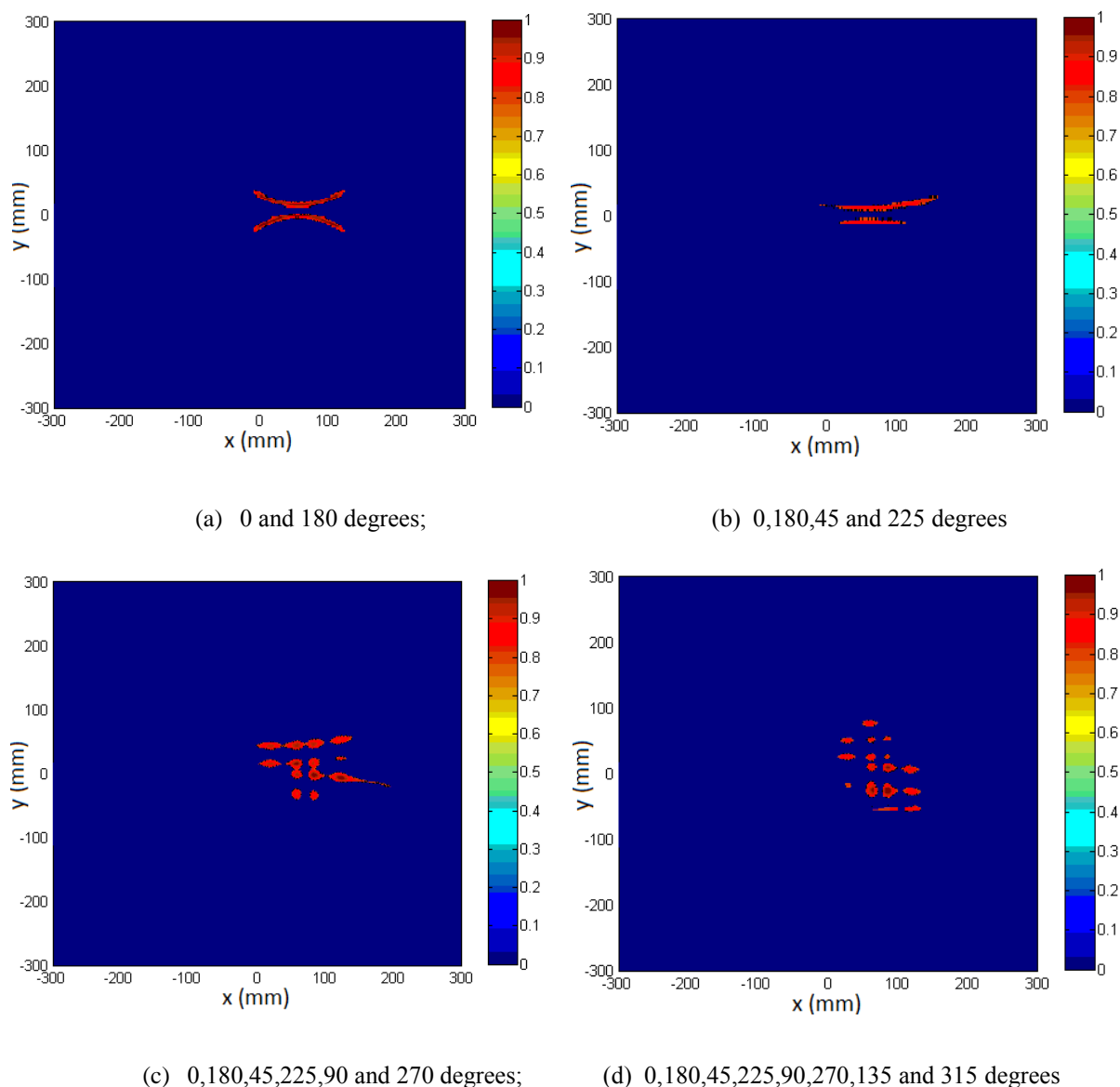
Figure 3-43 Cross-range images of one target at different integration of angles in free space

Two targets are also considered in simulation. The sizes of the two targets are 10 x 10 cm^2 and 8 x 8 cm^2 respectively. The vertical inter-distance of two targets is denoted as "d_y" and the value is set as 15cm in the simulation. The first target nearer the antenna array is 20cm away. Eight rotation angles are used to add up images and the range images are given in Figure 3.44. It is observed that when more images are added, the image of the two targets becomes clearer and the focus is more concentrated. The cross-range images of two targets after the integration of eight rotation angles are given in Figure 3.45(a) and (b).

(a) 0 and 180 degrees;   (b) 0,180,45 and 225 degrees

(c) 0,180,45,225,90 and 270 degrees;   (d) 0,180,45,225,90,270,135 and 315 degrees
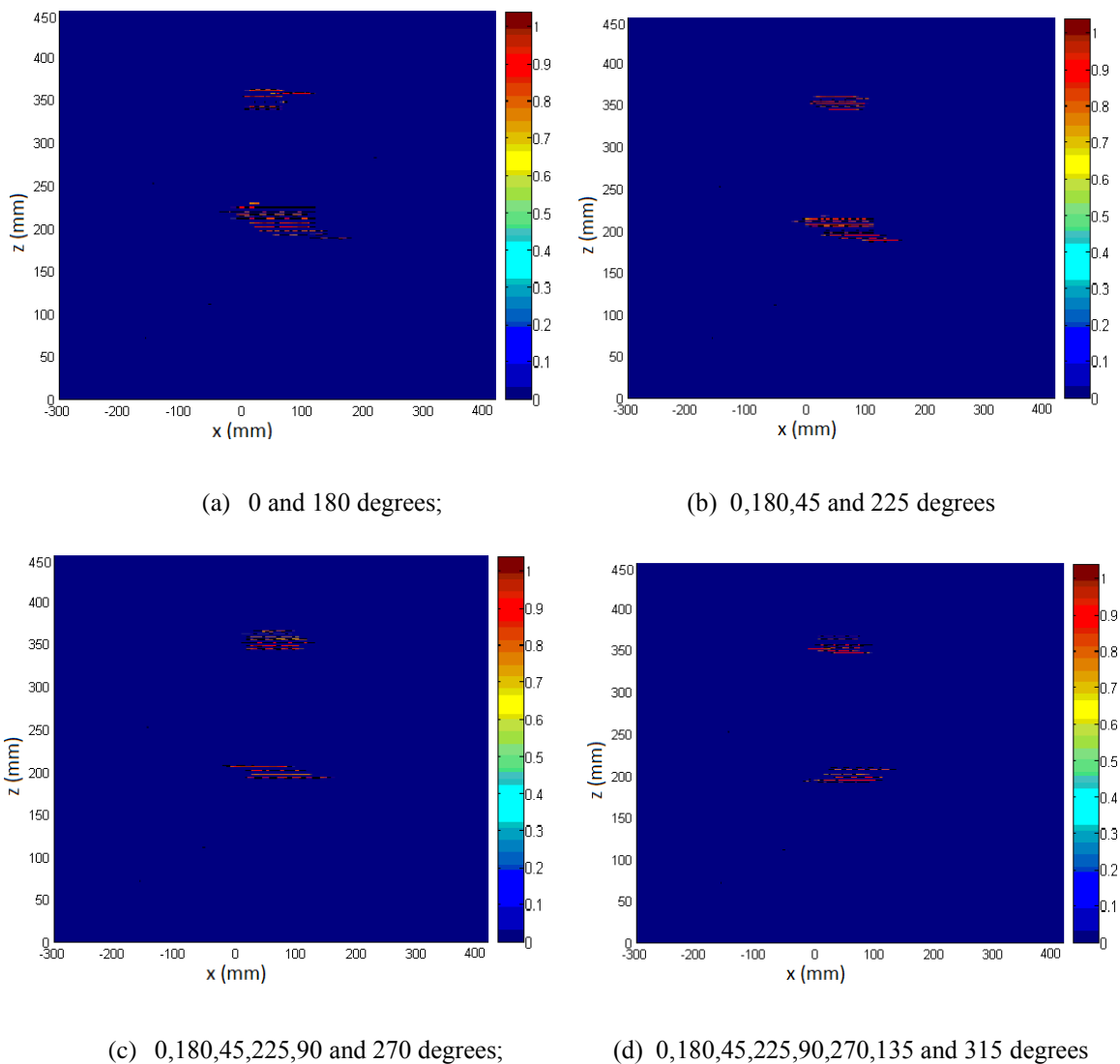
Figure 3-44 Range images of two targets at different integration of angles in free space

(a) Cross-range image of the 1st target;   (b) Cross-range image of the 2nd target
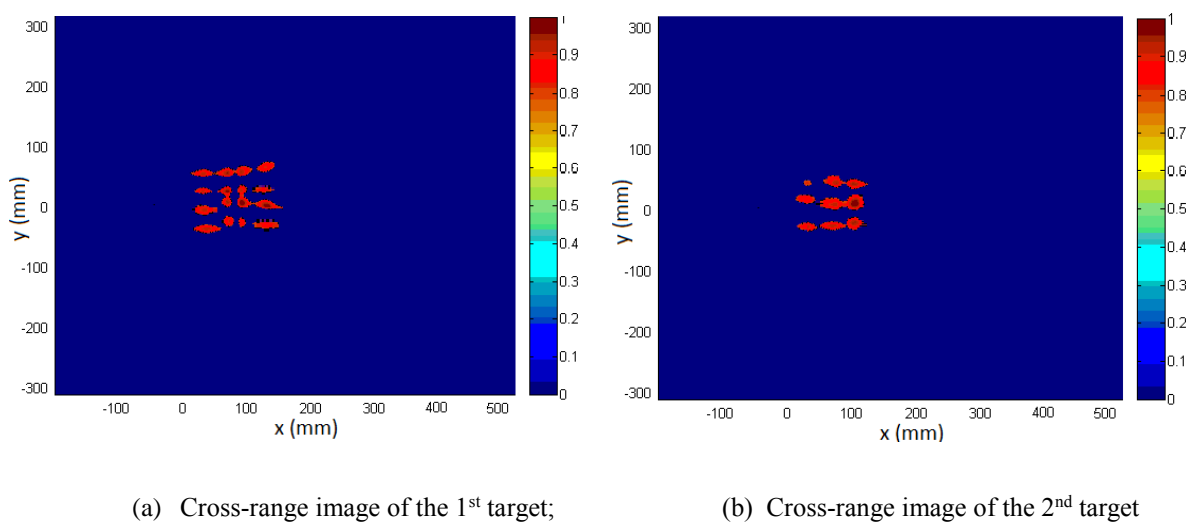
Figure 3-45 Cross-range images of two targets after integration of eight rotation angles in free space

In Figures 3.44 and 3.45, it is shown that two targets are imaged successfully in range estimation. There is a slight decline in energy concentration of the 2nd target image, because the second target is placed further away compared to the first one. A weaker target signature signal results in a poorer convergence.

The same two targets are re-arranged in a row with an inter-distance of 6cm, denoted as "d_x" Both targets have the same distance of 20cm away from the antenna array. After the adoption of four different integrations, the range images are given in Figure 3.46 and the cross-range images in Figure 3.47.

(a) 0 and 180 degrees;   (b) 0,180,45 and 225 degrees

(c) 0,180,45,225,90 and 270 degrees;   (d) 0,180,45,225,90,270,135 and 315 degrees
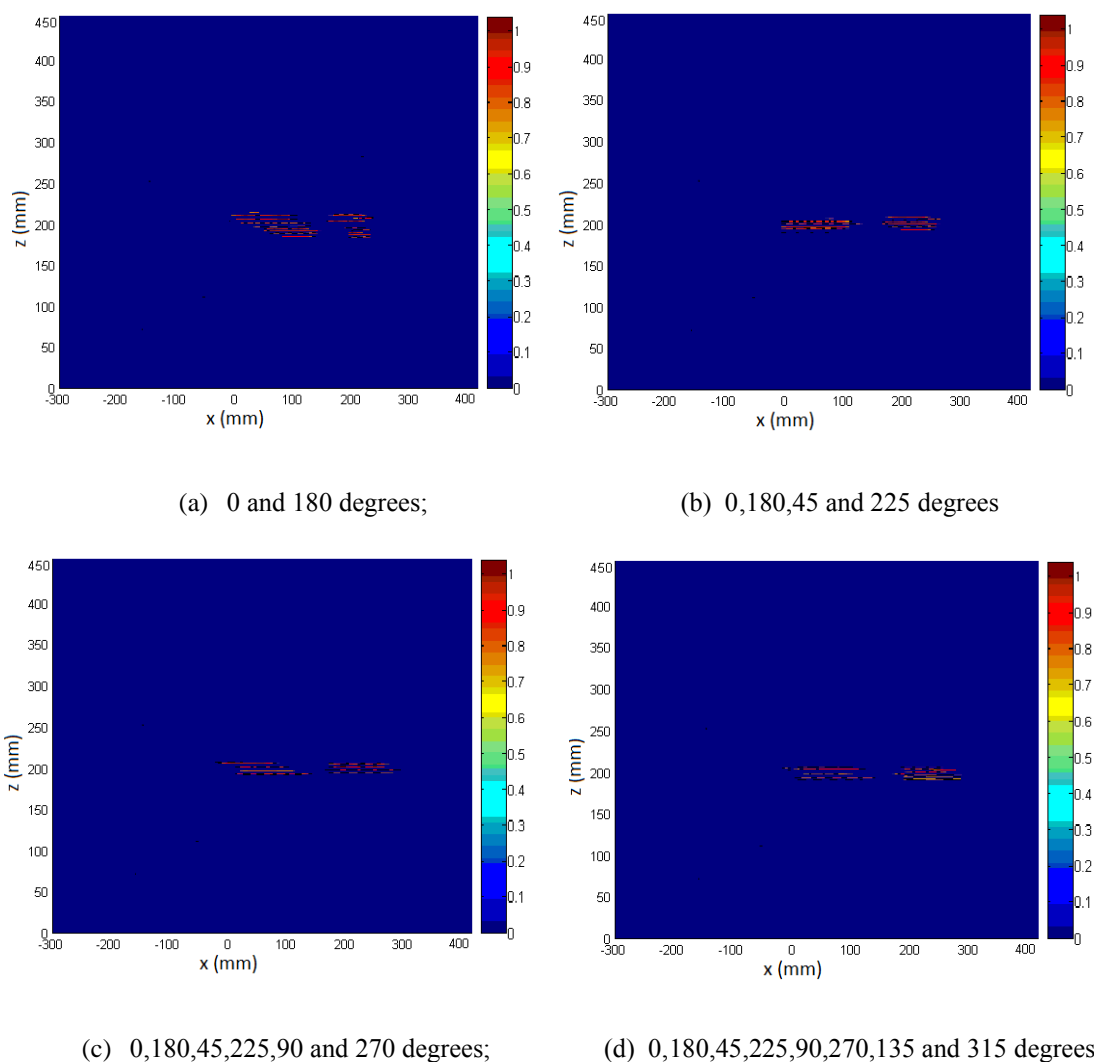
Figure 3-46 Range images of two targets at different integration of angles in free space

In Figure 3.46, it shows that two targets in a row can be separated. When only two angle positions are added, the range images are wider. When more angle positions are integrated, the

range images get sharper on both targets. The difference in the range images generated by DAS and TR methods is that the latter usually show more ripples. This will cause a difficulty in deciding the exact x-o-y plane for cross-range imaging. However, the recovered range images seem to be around the true value of the target position. Therefore, the chosen range is 20cm for its cross-range imaging process below.
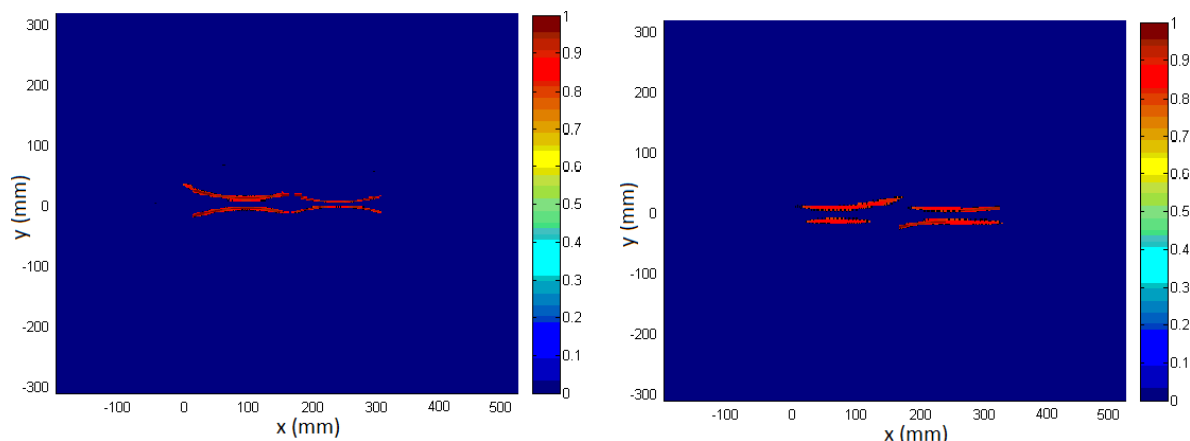
(a) 0 and 180 degrees;   (b) 0,180,45 and 225 degrees
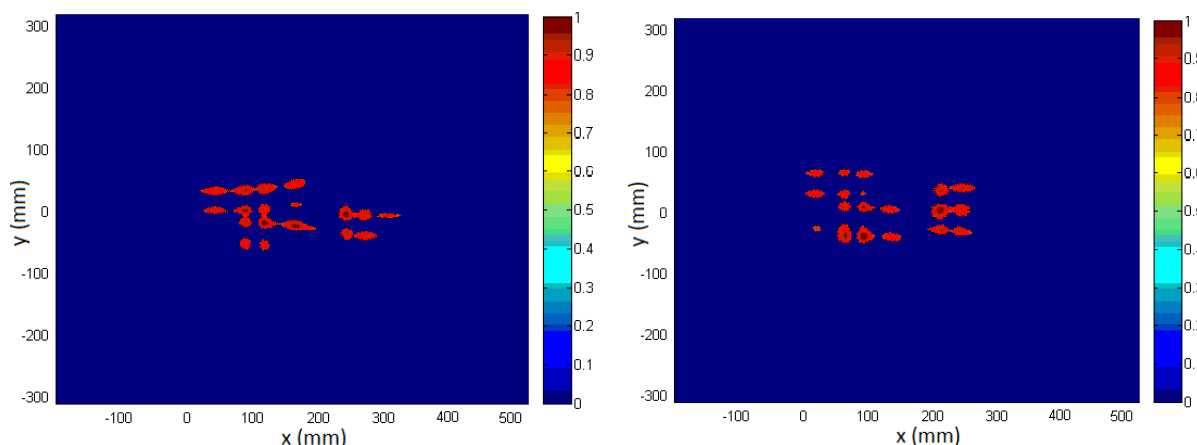
(b) 0,180,45,225,90 and 270 degrees;   (d) 0,180,45,225,90,270,135 and 315 degrees

Figure 3-47 Cross-range images of two targets at different integration of rotation angles in free space

In Figure 3.47, cross-range images have shown that integrating more imaging data at different rotating angles can produce better images. When only the data at 0 degree and 180 degrees are used, the energy concentration is not clear and two targets are not effectively separable. After the introduction of the data at 45 degrees and 225 degrees, the new wavefront energy becomes sharper and the trailing edges fade away. In Figure 3.47(c) and (d), the data at 90, 270, 135 and

315 degrees can provide more energy concentration. Thus the shapes of the recovered target images become clearer.

However, in comparison with DAS imaging results, the TR imaging method shows little improvement in terms of metal targets detection in free space. The error analysis of one target detection is shown in Table 3.3 and two targets in Tables 3.4 and 3.5. The analysis shows that the DAS imaging method is better at imaging one and two metal targets in free space. The error rate is smaller for recovered images by the DAS method. In general, both methods can reconstruct the image of the true targets satisfactorily.

Table 3.3 Error analysis of one target detection in free space by DAS and TR

	DAS	TR
Real target's 2D dimension (cm^2)	10 x 10	10 x 10
Real target's range (cm)	40	40
Recovered target's 2D dimension (cm^2)	11 x 13	12 x 17
Recovered target's range (cm)	40	38-42
2D dimension error (%)	43	104
Range error (%)	0	0-5

Table 3.4 Error analysis of two targets images in free space with an inter-distance d_y of 15cm by DAS and TR

DAS (d_y=15cm)						TR (d_y=15cm)					
Ist target's length			2rd target's length			Ist target's length			2rd target's length		
real	recovered	error	real	recovered	error	real	recovered	error	Real	recovered	error
10cm	15cm	50%	8cm	12cm	50%	10cm	13cm	30%	8cm	10cm	25%
Ist target's width			2rd target's width			Ist target's width			2rd target's width		
real	recovered	error	real	recovered	error	real	recovered	error	Real	recovered	error
10cm	16cm	60%	8cm	15cm	87.5%	10cm	10cm	0%	8cm	9cm	12.5%
Ist target's range			2rd target's range			Ist target's range			2rd target's range		
real	recovered	error	real	recovered	error	real	recovered	error	Real	recovered	error
20cm	20cm	0%	35cm	36cm	2.9%	20cm	17-22cm	0-15%	35cm	35-36cm	0-2.9%
Vertical distance (d_y=15cm)						Vertical distance (d_y=15cm)					
real		recovered		error		real		Recovered		error	
15cm		16cm		6.7%		15cm		14-19cm		0-26.7%	

Table 3.5 Error analysis of two targets images in free space with an inter-distance d_x of 6cm by DAS and TR

DAS (d_x=6cm)						TR (d_x=6cm)					
Ist target's length			2rd target's length			Ist target's length			2rd target's length		
real	recovered	error	real	recovered	error	real	recovered	error	real	recovered	error
10cm	15cm	50%	8cm	13cm	62.5%	10cm	13cm	30%	8cm	7cm	12.5%
Ist target's width			2rd target's width			Ist target's width			2rd target's width		
real	recovered	error	real	recovered	error	real	recovered	error	real	recovered	error
10cm	18cm	80%	8cm	12cm	50%	10cm	15cm	50%	8cm	10cm	25%
Ist target's range			2rd target's range			Ist target's range			2rd target's range		
real	recovered	error	real	recovered	error	real	recovered	error	real	recovered	error
20cm	20cm	0%	20cm	20cm	0%	20cm	18-21cm	0-10%	20cm	17-21cm	0-15%
Horizontal distance (d_x=6cm)						Horizontal distance (d_x=6cm)					
real		recovered		error		real		Recovered		error	
6cm		3cm		50%		6cm		5cm		16.7%	

3.3.4 TR imaging in a multipath environment

In order to test the TR method in its re-focusing ability in a multipath testing environment, a substrate is introduced in the model construction. All the parameters of the substrate are kept the same as those used in the DAS signal processing method for comparison purposes. TR procedures are applied to this scenario with all the eight rotation angles (0, 45, 90, 135, 180, 225, 270 and 315 degrees) involved in calculation. The down-range and cross-range images for one target with the size of 10 x 10 cm^2 placed 40cm away from antenna array and behind the substrate are given in Figure 3.48. Two targets images placed with a d_x distance of 6cm and d_y of 15cm behind the substrate are given in Figures 3.49 and 3.50.
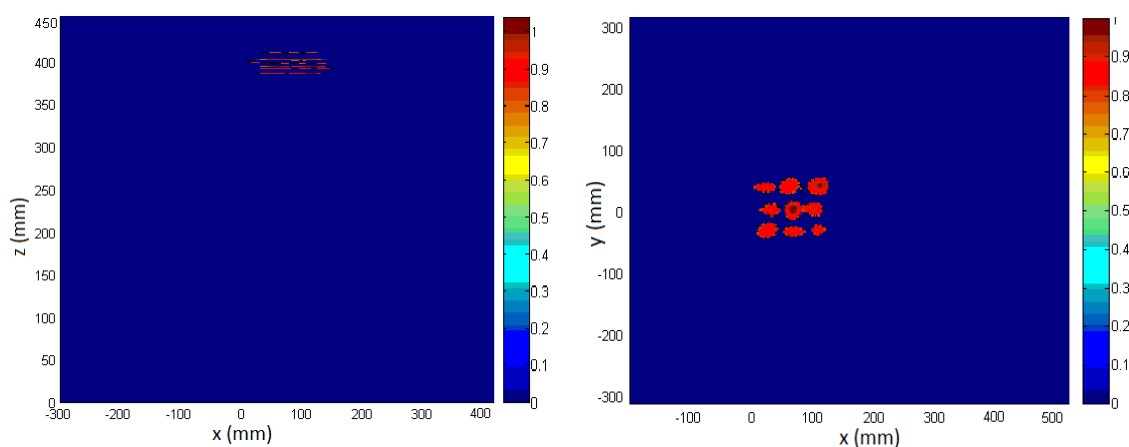
(a)   Range image of one target behind the substrate;   (b) Cross-range image of one target behind the substrate

Figure 3-48 Images of one target behind the substrate by the TR method
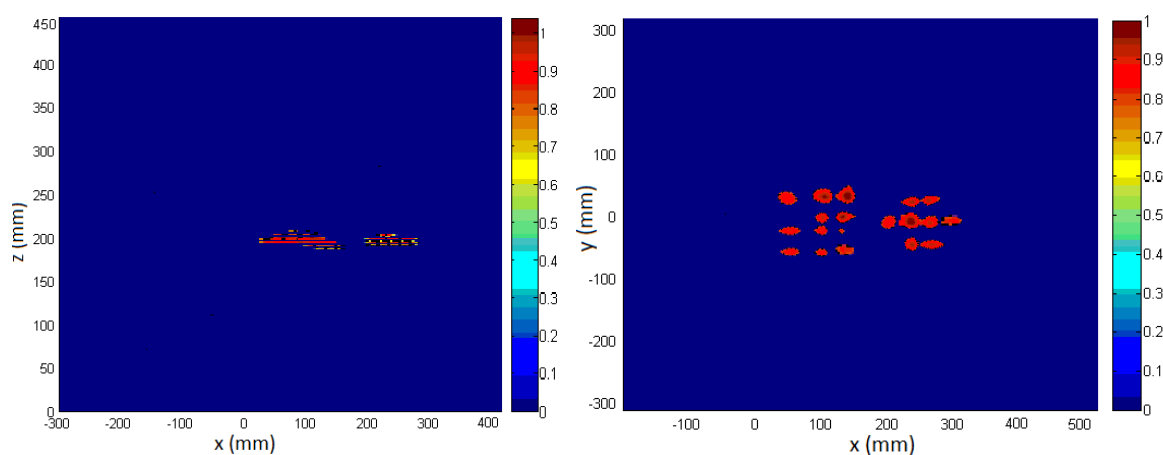
(a)   Range image of two targets behind the substrate;   (b) Cross-range image of two targets behind the substrate

Figure 3-49 Images of two targets with a distance d_x of 6cm behind the substrate by the TR method
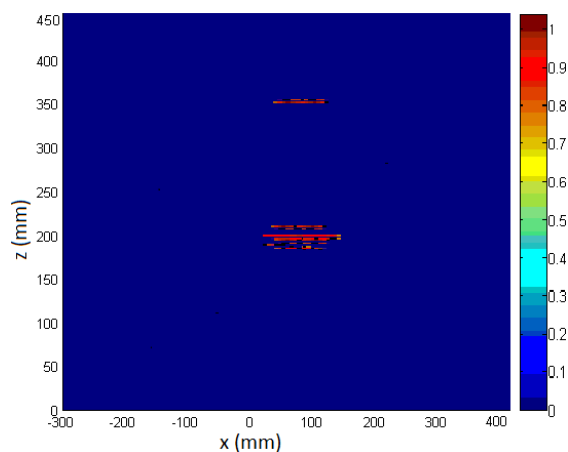
(a) Range image of two targets behind the substrate;
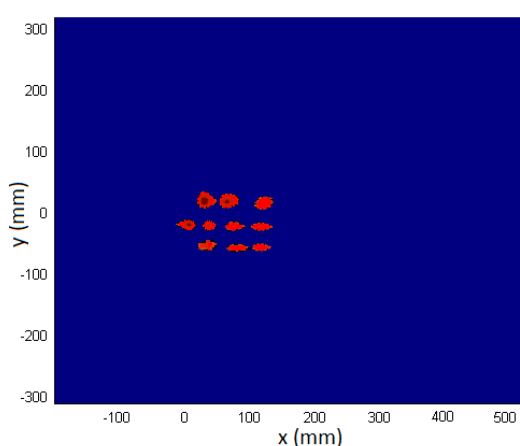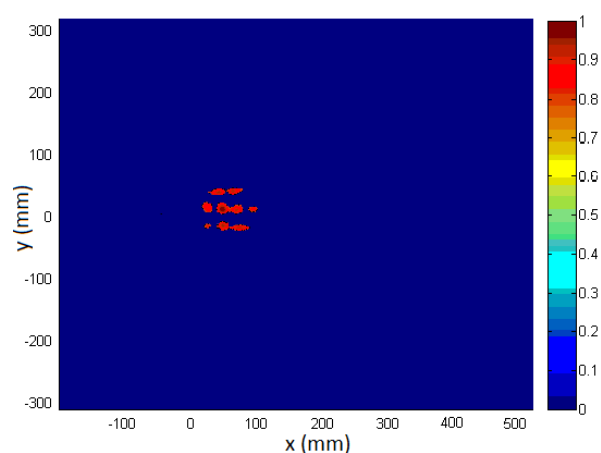
(b) Cross-range image of the 1st target;   (c) Cross-range image of the 2nd target

Figure 3-50 Images of two targets with a distance d_y of 15cm behind the substrate by the TR method

In both cases, one target and two targets behind the substrate can be imaged satisfactorily by the TR method. The comparison of range image with the substrate and without shows no obvious distortion. As for cross-range image, two targets can be separated in the imaging results. The advantage of the TR method is that it can distinguish two targets better than DAS. The error analysis in DAS and TR for one target detection is shown in Table 3.6 and for two targets in Table 3.7 and 3.8.

The error analysis has shown that in two target imaging behind the substrate, the TR method has better cross-range images than the DAS method. The error of the horizontal distance has decreased from 83.3% (DAS) to 16.7% (TR). This observation is very important in order to distinguish two targets placed together, particularly when they are placed side by side in a row.

Table 3.6 Error analysis of one target image behind the substrate by DAS and TR

	DAS	TR
Real target's 2D dimension (cm^2)	10 x 10	10 x 10
Real target's range (cm)	40	40
Recovered target's 2D dimension (cm^2)	12 x 15	10 x 12
Recovered target's range (cm)	40	38-43
2D dimension error (%)	80	20
Range error (%)	0	0-7.5

Table 3.7 Error analysis of two targets images behind the substrate with an inter-distance d_y of 15cm by DAS and TR

DAS (d_y=15cm)						TR (d_y=15cm)					
Ist target's length			2rd target's length			Ist target's length			2rd target's length		
real	recovered	error	real	recovered	error	real	recovered	error	Real	recovered	error
10cm	12cm	20%	8cm	10cm	25%	10cm	13cm	30%	8cm	10cm	25%
Ist target's width			2rd target's width			Ist target's width			2rd target's width		
real	recovered	error	real	recovered	error	real	recovered	error	Real	recovered	error
10cm	15cm	50%	8cm	13cm	62.5%	10cm	12cm	20%	8cm	10cm	25%
Ist target's range			2rd target's range			Ist target's range			2rd target's range		
real	recovered	error	real	recovered	error	real	recovered	error	Real	recovered	error
20cm	20cm	0%	35cm	35cm	0%	20cm	18-22cm	0-10%	35cm	34-37cm	0-5.7%
Vertical distance (d_y=15cm)						Vertical distance (d_y=15cm)					
real		recovered		error		real		Recovered		error	
15cm		15cm		0%		15cm		12cm		20%	

Table 3.8 Error analysis of two targets images behind the substrate with an inter-distance d_x of 6cm by DAS and TR

DAS (d_x=6cm)						TR (d_x=6cm)					
Ist target's length			2rd target's length			Ist target's length			2rd target's length		
real	recovered	error	real	recovered	error	real	recovered	error	real	recovered	error
10cm	15cm	50%	8cm	13cm	62.5%	10cm	12cm	20%	8cm	10cm	25%
Ist target's width			2rd target's width			Ist target's width			2rd target's width		
real	recovered	error	real	recovered	error	real	recovered	error	real	recovered	error
10cm	15cm	50%	8cm	12cm	50%	10cm	12cm	20%	8cm	8cm	0%
Ist target's range			2rd target's range			Ist target's range			2rd target's range		
real	recovered	error	real	recovered	error	real	recovered	error	real	recovered	error
20cm	20cm	0%	20cm	20cm	0%	20cm	18-22cm	0-10%	20cm	19-21cm	0-10%
Horizontal distance (d_x=6cm)						Horizontal distance (d_x=6cm)					
real		recovered		error		real		Recovered		error	
6cm		1cm		83.3%		6cm		5cm		16.7%	

3.4 Summary

In this chapter, the study of DAS and TR imaging methods has been carried out in simulation. Both methods are used to recover the image of targets in varied scenarios, such as a single target and a pair of targets in free space and behind a wooden board. Positive results have demonstrated their ability for image reconstruction. The differential method is needed to overcome the multipath effect to some extent. In comparison, the TR method has been applied to the same scenarios and it shows a superior focusing ability for two targets detection in a multipath environment.

Reference

[1] Chris Oliver, Shaun Quegan, "Understanding Synthetic Aperture Radar Images", Published in 1998

[2] Armin W. Doerry, "Basics of Polar-Format Algorithm for Processing Synthetic Aperture Radar Images", Prepared by Sandia National Laboratories, May, 2012

[3] Samiur Rahman, "Focusing Moving Targets Using Range Migration Algorithm in Ultra Wideband Low Frequency Synthetic Aperture Radar", Blekinge Institute of Technology, June 2010

[4] Alberto Moreira, Yonghong Huang, "Chirp scaling algorithm for processing SAR data with high squint angle and motion error", SPIE Vol. 2316 SAR Data Processing for Remote Sensing, 1994

[5] R. Stolt, "Migration by Fourier transform techniques," Geophys., no. 43, pp. 49–76, 1978.

[6] R. K. Raney, H. Runge, R. Bamler, I. G. Cumming, and F. H. Wong, "Precision SAR processing using chirp scaling," IEEE Trans. Geosci. Remote Sensing, vol. 32, pp. 786–799, July 1994.

[7] LARS M. H. ULANDER,HANS HELLSTEN, GUNNAR STENSTRO, "M Synthetic-Aperture Radar Processing Using Fast Factorized Back-Projection", IEEE TRANSACTIONS ON AEROSPACE AND ELECTRONIC SYSTEMS VOL. 39, NO. 3 JULY 2003

[8] W. Shao, B. Zhou, Z. Zheng, and G. Wang, "UWB microwave imaging for breast tumor detection in inhomogeneous tissue", in Proceedings of the 27th IEEE Annual International Conference of the Engineering in Medicine and Biology Society (EMBS '05), pp. 1496–1499, Shanghai, China, September 2005.

[9] Z. Wang, J. Li and R. Wu, "Time-delay- and time-reversal-based robust Capon beamformers for ultrasound imaging", IEEE Transactions on Medical Imaging, vol. 24, no. 10, pp. 1308–1322, 2005.

[10] M. Fink, C. Prada, F. Wu, and D. Cassereau, "Self focusing in inhomogeneous media with time-reversal acoustic mirrors," IEEE Ultrason. Symp, vol. 1, pp. 681–686, 1989. 4

[11] M. Fink, "Time-reversal of ultrasonic fields 1. basic principles," IEEE Trans. Ultrason., Ferroelect., Freq. Contr., vol. 39, no. 5, pp. 555–566, 1992. 4

[12] "Time reversal mirrors," J. Phys. D.: Appl. Phys., vol. 26, no. 9, pp. 1333–1350, 1993. 4

[13] "Time-reversed acoustics," Physics Today, vol. 50, no. 3, pp. 34–40, Mar 1997. 4

[14] D. R. Dowling and D. R. Jackson, "Phase conjugation in underwater acoustics," J. Acoust. Soc. Am., vol. 89, pp. 171–181, 1990. 4

[15] W. A. Kuperman, W. S. Hodgkiss, H. C. Song, T. Akal, C. Ferla, and D. R. Jackson, "Phase conjugation in the ocean: Experimental demonstration of a time-reversal mirror," J. Acoust. Soc. Am., vol. 103, pp. 25–40, 1998. 4

[16] M. Fink and C. Prada, "Acoustics time-reversal mirrors," Inverse Prob., vol. 17, no. 1, pp. R1–R38, 2001. 4

[17] G. F. Edelmann, T. Akal, W. S. Hodgkiss, S. Kim, W. A. Kuperman, and H. C. Song, "An initial demonstration of underwater acoustic communications using time reversal," IEEE Jour. of Oceanic Eng., vol. 27, pp. 602–609, July 2002. 4, 5

[18] S. Kim, W. A. Kuperman, W. S. Hodgkiss, H. C. Song, G. F. Edelman, and T. Akal, "Robust time reversal focusing in the ocean," J. Acoust. Soc. Am., vol. 114, no. 1, pp. 145–157, Jul 2003. 4

[19] C. Prada, F. Wu, and M. Fink, "The iterative time reversal mirror: A solution to self-focusing in the pulse echo mode," J. Acoust. Soc. Am., vol. 90, no. 2, pp. 1119–1129, 1991. 4

[20] C. Prada and M. Fink, "Eigenmodes of the time reversal operator: A solution to selective focusing in multiple-target media," Wave Motion, vol. 20, pp. 151–163, 1994. 4, 5, 32, 33, 95

[21] C. Prada, J.-L. Thomas, and M. Fink, "The iterative time reversal process: Analysis of the convergence," J. Acoust. Soc. Am., vol. 97, pp. 62–71, 1995. 4, 32, 55

[22] A. Derode, P. Roux, and M. Fink, "Robust acoustic time reversal with high order multiple scattering," Phys. Rev. Lett., vol. 75, no. 23, pp. 4206–4209, 1995. 4

[23] C. Prada, S. Manneville, D. Spoliansky, and M. Fink, "Decomposition of the time reversal operator: Detection and selective focusing on two scatterers," J. Acoust. Soc. Am., vol. 99, pp. 2067–2076, 1996. 4, 5, 32, 33, 40, 80, 95, 98

[24] E. Kerbrat, C. Prada, and D. Cassereau, "Ultrasonic nondestructive testing of scattering media using the decomposition of the time-reversal operator," IEEE Trans. Ultrason., Ferroelect., Freq. Contr., vol. 49, no. 8, pp. 1103–1112, 2002. 4, 5

[25] D. R. Dowling and D. R. Jackson, "Narrowband performance of phase conjugate arrays in dynamic random media," J. Acoust. Soc. Am., vol. 91, pp. 3257–3277, 1992. 4

[26] J. F. Clouet and J. P. Fouque, "A time reversal method for an acoustical pulse propagating in randomly layered media," Wave Motion, vol. 25, pp. 361–368, 1997. 4

[27] M. Asch, W. Kohler, G. Papanicolaou, M. Postel, and B. White, "Frequency content of randomly scattered signals," SIAM Review, vol. 33, pp. 519–62, 1991.4

[28] W. Kohler, G. Papanicolaou, and B. White, "Localization and mode conversion for elastic waves in randomly layered media," Wave Motion, vol. 23, pp. 1–22 and 181–201, 1996. 4

[29] J. G. Berryman, L. Borcea, G. Papanicolaou, and C. Tsogka, "Statistically stable ultrasonic imaging in random media," J. Acoust. Soc. Am., vol. 112, no. 4, pp. 1509–1522, 2002. 4, 44, 96, 134, 136

[30] L. Borcea, G. Papanicolaou, C. Tsogka, and J. Berryman, "Imaging and time reversal in random media," Inverse Prob., vol. 18, no. 5, pp. 1247–1279, 2002. 4, 44, 96, 99

[31] C. Tsogka and G. Papanicolaou, "Time reversal through a solid-liquid interface and super-resolution," Inverse Prob., vol. 18, no. 6, pp. 1639–1657, 2002. 4, 41, 48, 54

[32] G. Papanicolaou, L. Ryzhik, and K. Solna, "Statistical stability in time reversal," SIAM J. Appl. Math., vol. 64, no. 4, pp. 1133–55, 2004. 4

[33] P. Blomgren, G. Papanicolaou, C. Tsogka, and J. Berryman, "Super resolution in time-reversal acoustics," J. Acoust. Soc. Am., vol. 111, no. 1, pp. 230–48, 2002. 4, 101

[34] G. Lerosey, J. de Rosny, A. Tourin, A. Derode, G. Montaldo, and M. Fink, "Time reversal of electromagnetic waves," Phys. Rev. Lett., vol. 92, p. 193904, 2004. 5

[35] G. Lerosey, J. de Rosny, A. Tourin, A. Derode, and M. Fink, "Time reversal of wideband microwaves," Applied Phys. Lett., vol. 88, no. 15, p. Art. No. 154101, April 2006. 5

[36] D. M. Pepper, "Nonlinear optical phase conjugation," Optical Engineering, vol. 21, no. 2, p. 156, March/April 1982. 4

[37] J. L. Thomas, F. Wu, and M. Fink, "Time reversal focusing applied to lithotripsy," Ultrason. Imag., vol. 18, no. 2, pp. 106–121, April 1996. 4, 96

[38] G. Montaldo, P. Roux, A. Derode, C. Negreira, and M. Fink, "Ultrasonic shock wave generator using 1-bit time-reversal in a dispersive medium : application to lithotripsy," Appl. Phys. Lett., vol. 80, no. 5, pp. 897–899, 2002. 4

[39] C. L. Floch, M. Tanter, and M. Fink, "Self defocusing in ultrasonic hyperthermia: Experiment and simulation," Appl. Phys. Lett., vol. 74, no. 20, pp. 3062–3064, May 1999. 4

[40] P. Kosmas and C. M. Rappaport, "Time reversal with the fdtd method for microwave breast cancer detection," IEEE Trans. Microwave Theory Tech., vol. 53, pp. 2317–2323, July 2005. 5, 6, 65, 66, 90

[41] A. G. Cepni and D. D. Stancil, "Single antenna microwave nulling using time reversal techniques," Microwave Symp. Digest, IEEE MTT-S International, pp. 1723–1726, 2005. 6, 128, 158

[42] A. G. Cepni, D. D. Stancil, J. Zhu, and Y. Jiang, "Experimental results on target detection in cluttered medium using electromagnetic time-reversal techniques," Proc. of the IEEE Antennas Prop. Symp., vol. 4B, pp. 139–142, 2005. 6, 158

[43] J. M. F. Moura and Y. Jin, "Detection by time reversal: Single antenna," IEEE Trans. Signal Process., vol. 55, no. 1, pp. 187–201, Jan. 2007. 6

[44] H. T. Nguyen, J. B. Andersen, G. F. Pedersen, P. Kyritsi, and P. C. F. Eggers, "Time reversal in wireless communications: A measurement-based investigation," IEEE Trans. Wireless Comm., vol. 5, no. 8, pp. 2242–2252, 2006. 6

[45] A. G. Cepni, Experimental Investigation of Time-Reversal Techniques using Electromagnetic Waves. Ph. D. Dissertation: Carnegie Mellon University, Dec 2005. 6

[46] T. Leutenegger and J. Dual, "Non-destructive testing of tubes using a time reverse numerical simulation (trns) method," Ultrasonics, vol. 41, no. 10, pp. 811–822, May 2004. 5

[47] "Detection of defects in cylindrical structures using a time reverse method and a finite-difference approach," Ultrasonics, vol. 40, no. 1-8, pp. 721–725, May 2002. 5

[48] N. Chakroun, M. Fink, and F. Wu, "Time reversal processing in ultrasonic non-destructive testing," IEEE Trans. Ultrason., Ferroelect., Freq. Contr., vol. 42, no. 6, pp. 1087–1098, 1995. 5

[49] M. Saillard, P. Vincent, and G. Micolau, "Reconstruction of buried objects surrounded by small inhomogeneities," Inverse Prob., vol. 16, no. 5, pp. 1195– 1208, Oct 2000. 5, 33, 62, 65, 99

[50] G. Micolau, M. Saillard, and P. Borderies, "DORT method as applied to ultrawideband signals for detection of buried objects," IEEE Trans. Geosci. Remote Sensing, vol. 41, no. 8, pp. 1813–1820, Aug 2003. 5, 6, 33, 34, 81, 105

[51] G. F. Edelmann, H. C. Song, S. Kim, T. Akal, W. S. Hodgkiss, and W. A. Kuperman, "Underwater acoustic communications using time reversal," IEEE Jour. of Oceanic Eng., vol. 30, no. 4, pp. 852–864, Oct 2005. 5

[52] W. J. Higley, P. Roux, W. A. Kuperman, W. S. Hodgkiss, H. C. Song, T. Akal, and M. Stevenson, "Synthetic aperture time-reversal communications in shallow water: Experimental demonstration at sea," J. Acoust. Soc. Am., vol. 118, no. 4, pp. 2365–2372, Oct 2005. 5

[53] H. Lev-Ari and A. J. Devaney, "The time reversal techniques re-interpreted: Subspace-based signal processing for multistatic target location," Proc. IEEE Sensor Array Multichannel Signal Proc. Workshop, pp. 509–513, March 2000. 5, 56, 95, 96, 101, 102

[54] S. K. Lehman and A. J. Devaney, "Transmission mode time-reversal superresolution imaging," J. Acoust. Soc. Am., vol. 113, pp. 2742–2753, 2003. 5, 96

[55] S. Hou, K. Solna, and H. Zhao, "Imaging of location and geometry for extended targets using the response matrix," J. Comp. Phys., vol. 199, no. 1, pp. 317–338, 2004. 5

[56] K. Sarabandi, I. Koh, and M. D. Casciato, "Demonstration of time reversal methods in a multi-path environment," Proc. of the IEEE Antennas Prop. So- ciety Int. Symp., vol. 4, pp. 4436–4439, 20-25 June 2004. 6

[57] Y. Jiang, J. Zhu, D. D. Stancil, and M. J. Chabalko, "Polarization sensitive time-reversal sar imaging in an environment filled with trees," Proc. of the IEEE Antennas Propagat. Symp., vol. 1, pp. 4000–4003, 2007. 6

[58] P. Kyritsi, G. Papanicolaou, P. Eggers, and A. Oprea, "MISO time reversal and delay-spread compression for FWA channels at 5 GHz," IEEE Antennas Wireless Prop. Lett., vol. 3, pp. 96–99, 2004. 6

[59] S. M. Emami, J. Hansen, A. D. Kim, G. Papanicolaou, A. J. Paulraj, D. Cheung, and C. Prettie, "Predicted time reversal performance in wireless communications using channel measurements," IEEE Commun. Lett., 2007

[60] P. Kyritsi and G. Papanicolaou, "One-bit time reversal for wlan applications," IEEE 16th Int. Symp. Personal, Indoor, Mobile Radio Comm., PIMRC 2005, vol. 1, pp. 532–536, 2005. 6

[61] P. Kyritsi, P. Stoica, G. Papanicolaou, P. Eggers, and A. Oprea, "Time reversal and zero-forcing equalization for fized wireless access channels," 2005 Conf. Record of the Thirty-Ninth Asilomar Conf. on Signals, Systems, Computers, pp. 1297–1301, Oct 28- Nov 1, 2005. 6

[62] G. Lerosey, J. de Rosny, A. Tourin, A. Derode, G. Montaldo, and M. Fink, "Time reversal of electromagnetic waves and telecommunication," Radio Sci., vol. 40, no. 6, p. Art. No. RS6S12, Sep. 2005. 6

[63] G. Montaldo, G. Lerosey, A. Derode, A. Tourin, J. de Rosny, and M. Fink, "Telecommunication in a disordered environment with iterative time reversal," Waves in Random Media, vol. 14, no. 3, pp. 287–302, Jul. 2004. 6

[64] F. Coppinger, A. S. Bhushan, and B. Jalali, "Time reversal of broadband microwave signals," Electron. Lett., vol. 35, no. 15, pp. 1230–1232, July 1999.6

[65] D. H. Chambers and J. G. Berryman, "Analysis of the time-reversal operator for a small spherical scatterer in an electromagnetic field," IEEE Trans. Antennas Propagat., vol. 52, no. 7, pp. 1729–1738, July 2004. 6, 33, 40, 49, 98

[66] P. Kosmas, FDTD modeling for forward and linear inverse electromagnetic prob- lems in lossy, dispersive media. Ph. D. Dissertation: Northeastern University, Jan 2005. 6

[67] P. Kosmas and C. M. Rappaport, "FDTD-based time reversal for microwave breast cancer detection - localization in three dimensions," IEEE Trans. Microwave Theory Tech., vol. 54, no. 4, pp. 1921–1927, Apr 2006. 6

[68] "A matched-filter FDTD-based time reversal approach for microwave breast cancer detection," IEEE Trans. Antennas Propagat., vol. 54, no. 4, pp. 1257–1264, Apr 2006. 6

[69] N. Mordant, C. Prada, and M. Fink, "Highly resolved detection and selective focusing in a waveguide," J. Acoust. Soc. Am., vol. 105, no. 5, pp. 2634–2642, May 1999. 5

[70] C. Prada and J. L. Thomas, "Experimental subwavelength localization of scatterers by decomposition of the time reversal operator interpreted as a covariance matrix," J. Acoust. Soc. Am., vol. 114, no. 1, pp. 235–243, July 2003. 5

[71] G. Micolau and M. Saillard, "DORT method as applied to electromagnetic sensing of buried objects," Radio Sci., vol. 38, no. 3, pp. 4–1–12, 2003. 5, 6, 33, 40, 49, 81, 98, 99

[72] G. Montaldo, M. Tanter, and M. Fink, "Real time inverse filter focusing through iterative time reversal," J. Acoust. Soc. Am., vol. 115, no. 2, pp. 768–775, Feb. 2004. 5

[73] "Revisiting iterative time reversal processing: Application to detection of multiple targets," J. Acoust. Soc. Am., vol. 115, no. 2, pp. 776–784, Feb. 2004. 5

[74] H. Tortel, G. Micolau, and M. Saillard, "Decomposition of the time reversal operator for electromagnetic scattering," J. Electromagn. Waves Appl., vol. 13, pp. 687–719, 1999. 6, 33, 34, 40, 49, 98, 99

[75] A. J. Devaney, "Super-resolution processing of multistatic data using time reversal and music," Unpublished paper, preprint available on the author's web site, http://www.ece.neu.edu/faculty/devaney/. 5, 96, 100, 101, 102

[76] F. K. Gruber, E. A. Marengo, and A. J. Devaney, "Time-reversal imaging with multiple signal classification considering multiple scattering between the targets," J. Acoust. Soc. Am., vol. 115, pp. 3042–3047, 2004. 5, 56, 96

[77] A. J. Devaney, E. A. Marengo, and F. K. Gruber, "Time-reversal-based imaging and inverse scattering of multiply scattering point targets," J. Acoust. Soc. Am., vol. 118, pp. 3129–3138, 2005. 5, 96, 101

[78] E. A. Marengo and F. K. Gruber, "Single-snapshot time-reversal music and maximum likelihood estimation for active target location including multiple scattering," IEEE Trans. Antennas Propagation, 2008, under review. 5, 96

[79] Y. Wang, Y. Yang and A.E. Fathy, "Three dimension through wall imaging using an UWB SAR," IEEE AP-S Int. Symp. on Antennas and Propagation., Toronto, Canada, July 2010.

[80] M.Fink. "Time-reversal of ultrasonic fields I:basic principles". IEEE Transaction on Ultrasonics, Ferroelectrics and Frequency Control, Vol.9, No.5: 555-666, September 1992

[81] Didier Cassereau, Mathias Fink. "Time-Reversal of Ultrasonic Fields-Part Three: Theory of the Closed Time-Reversal Cavity". IEEE Transaction on Ultrasonics, Ferroelectrics and Frequency Control, Vol.9, No.5: 579-592, September 1992

[82] Min Zhou, "Design and Time-domain Analysis of Antenna Array for UWB Imaging Application", PhD thesis, Queen Mary College, University of London, June 2014

Chapter 4 UWB Imaging Radar System

The prevalent use of UWB technology has been for localisation and imaging purposes. Microwave imaging has achieved encouraging results in these applications, such as the penetration of walls for human detection, and the scanning of bags and luggage in airport and railway stations for security issues. The project aims to detect hidden metallic targets for security purpose.

In the beginning of this chapter, the proposed time-domain based UWB imaging radar system is illustrated, together with a system level simulation. The implementation of the system is explained by introduction of all the active and passive components in the set-up, which would support and establish the link budget and dynamic range analysis. The computer-aided LabVIEW from NI further reduces the complexity of the rotating structure and paves the way for future minimisation of the system. Systemic simulation work is accompanied by an initial measurement.

4.1 Design of the proposed UWB imaging radar system

It is useful and necessary to simulate the performance of the UWB radar system before fabrication. Proper simulation work can help researchers avoid some overlooked flaws and optimise the system design. In addition, a system-level simulation can estimate the impact from each sub-system on the holistic system performance. A UWB imaging radar system can be divided into several sub-systems, as shown in Figure 4.1. This flow diagram illustrates experimental testing or computer simulation required in each design procedure.
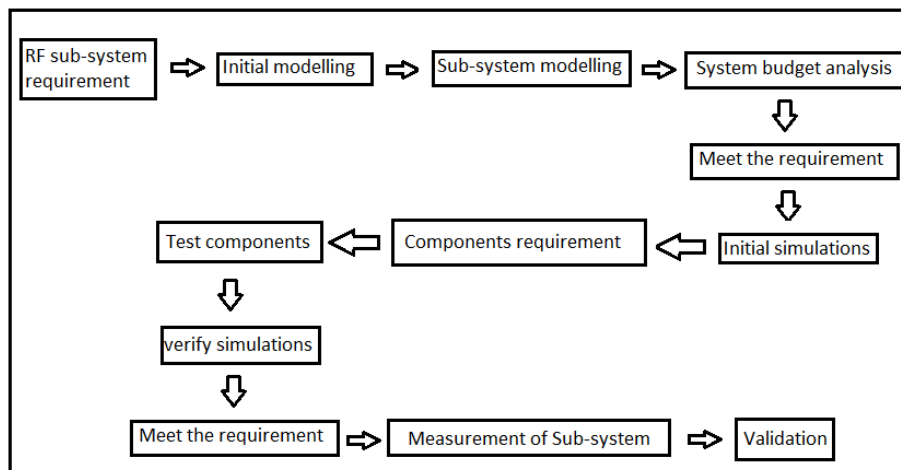
Figure 4-1 Design of RF sub-systems in simulation and measurement

For a UWB imaging radar system, there are six steps to complete the simulation work, as shown in Figure 4.2. This flow chart follows the signal propagation in each stage.
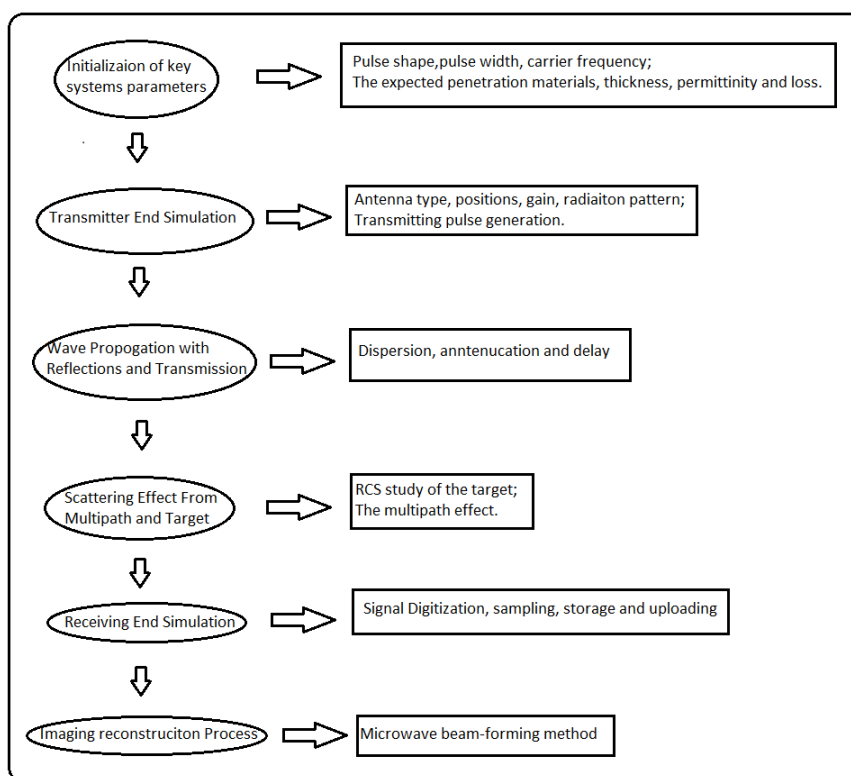
Figure 4-2 Steps of System level simulation

Initially, some key parameters need to be specified, such as the antenna gain, antenna positions, permittivity and thicknesses of the obstructions. Then, models are built in the commercial

software Agilent ADS Circuit Design Tool to simulate some parts of the transmitter sub-system. At the transmitting end, the RF signal propagates across the obstruction and reaches the target. The transmission and multiple reflections are analysed by the MATLAB Tool. A fraction of the signal is reflected by the target and this is related to the RCS of the target.

At the receiving end, the scattered signals penetrate back through the wall and reach the receiving antennas. These signals are amplified, down-converted, filtered, digitised, transferred and stored in PC. Microwave beam-forming algorithms are applied to recover the images of the targets based on the received signals.

4.1.1 The transmitting sub-system

The transmitting sub-system is essentially a cascaded system, which determines the main characteristics of the active components, such as gain, Noise Figure, 1dB compression point and third-order intercept point. Ideally, the cascade gain is the summation of the gain of each component at every stage. In experimental measurements, however, the mismatch between adjacent components should be taken into account in the calculation. The noise factor is the ratio of the noise at the output of a practical linear component to the noise at the input of an ideal component with the same overall gain and bandwidth at standard noise temperature. It is a measure of the degradation of SNR. All the insertion loss preceding the power amplifier would have an adverse effect on the noise factor.

Furthermore, the 1dB compression point is defined as the input power when the gain is 1dB less than the small signal gain, as shown in Figure 4.3. Normally the input 1dB compression point is relevant for a receiver and the output 1dB compression point is relevant for a transmitter [1].
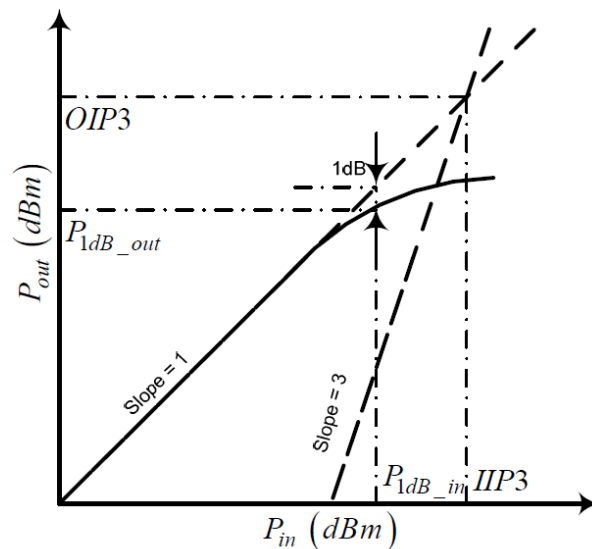
Figure 4-3 Definition of 1dB compression point and third-order intercept point [1]

A simplified block diagram of a transmitting sub-system is shown in Figure 4.4. A user-defined waveform is generated in the beginning. Then, the IF signal is up-converted to the desired RF signal. The filtering and pre-amplification are performed in the end. The typical schematic of the up-conversion is shown in Figure 4.5.
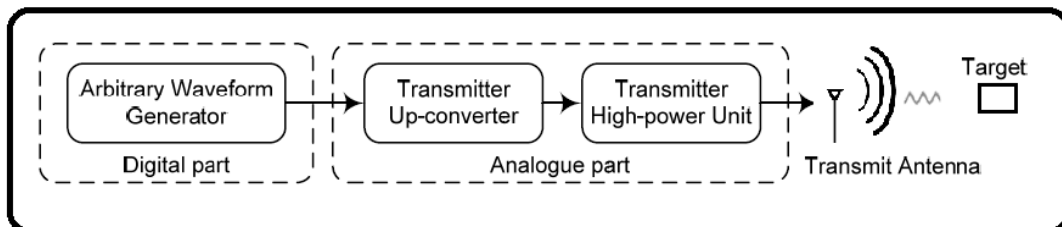
Figure 4-4 Block diagram of a transmitting sub-system [1]
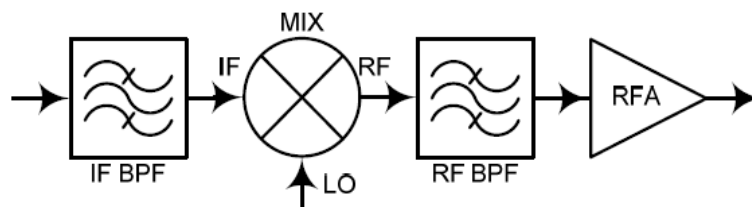
Figure 4-5 Structure of transmitting up-conversion [1]

In MATLAB simulation, the first step is to generate a Nano-second UWB pulse waveform. The UWB signal source can be simulated by the equation 4.1:

$$Gp(t) = \frac{i}{[i + 2\pi f(t - t_0)/4]^5} \qquad (4-1)$$

The centre frequency f is 4.5GHz. i is the imaginary unit. The frequency band is designed from 4 to 5GHz with a bandwidth of 1GHz. The UWB signal is expected to be a modified first derivative Gaussian signal with one positive peak. The simulated results in time domain and frequency domain are completed in MATLAB, as shown in Figure 4.6(a) and (b). This waveform function can be embedded as the first step in the whole Simulink simulation package.
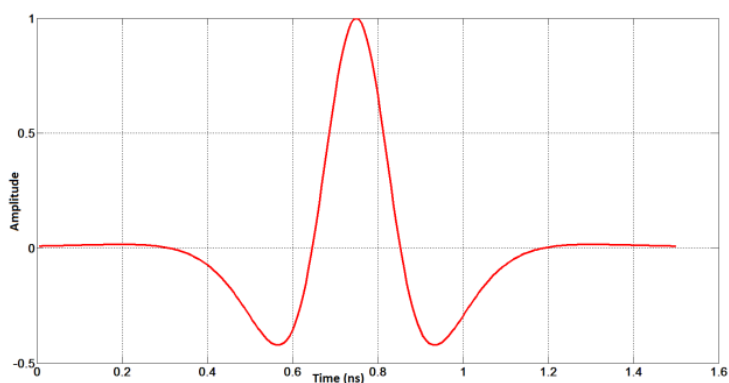
(a) Gaussian Pulse in time domain
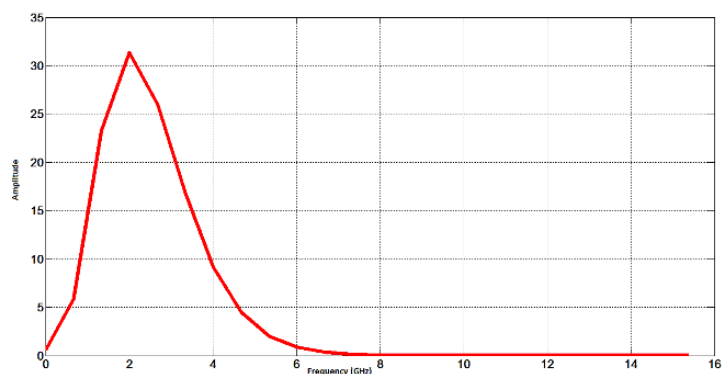
(b) Gaussian Pulse in frequency domain

Figure 4-6 The first derivative modified Gaussian Pulse in time domain and frequency domain

Additionally, an alternative model can be constructed with the aid of the ADS Ptolemy simulation tool. The short pulses can be generated by using "Step Recovery Diodes (SRDs)" and shorted transmission lines [2]. SRDs present the characteristic that when they are forward biased but suddenly reversed biased, a low impedance would show up until the charge in the junction is depleted. This means that after the biasing moves from a positive voltage to a

negative one, the diode will conduct during a short period, thus inducing a small negative pulse on the output, as shown in Figure 4.7.

(a)   (b)
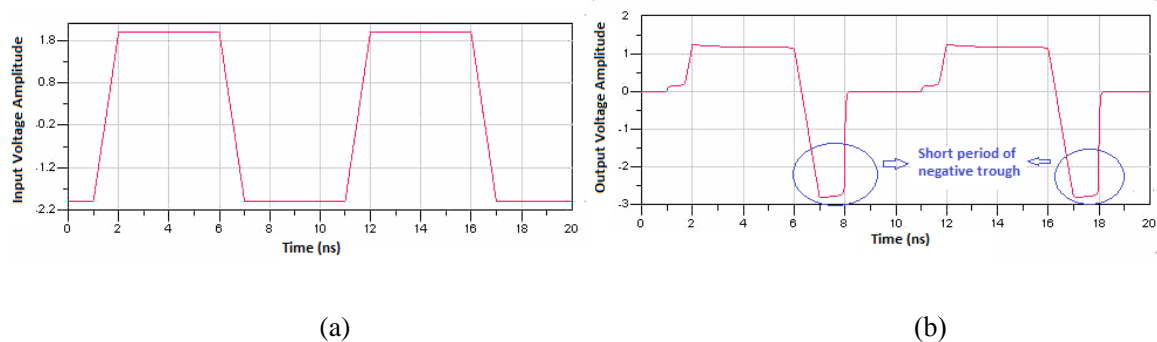
Figure 4-7 (a) The input signals before the diodes; (b) the output signal after the diodes [2]

The signal polarity, highlighted in Figure 4.7 and the width of the pulse are controlled by a shorted transmission line. This requires careful design of impedance matching to avoid undesired signal reflections. As shown in Figure 4.8, two transmission line modules are added in TLIN simulation,
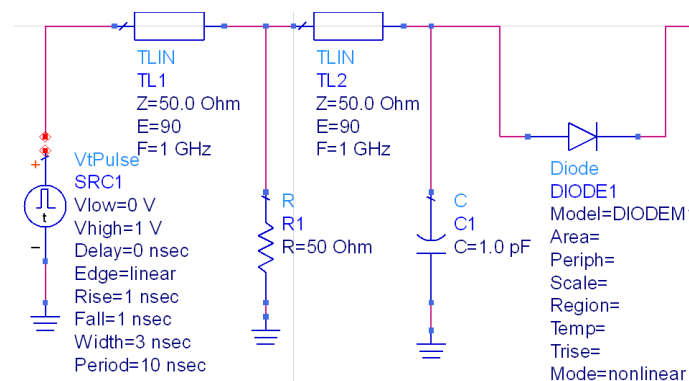
Figure 4-8 The integration of transmission line modules in the ADS simulation

The pulse travels through both the load and the transmission lines and is reflected with its shape inverted. After the reflection, the pulse received on the load goes through double routes. The input impedance seen from the transmission line is equivalent to the parallel of the generator and load impedances. Therefore, the impedance of the transmission line should be equal to the parallel of the impedance of the generator and the load in order to match with minimal ringing. The voltage signal seen on the load is equal to the addition of the voltage signal coming from the generator and the voltage signal that is reflected from the transmission line. On the load, the output signal would contain a short pulse with a width equal to the second round delay. In order to

generate a mono-cycle first derivative Gaussian pulse, some modification needs to be applied to the design mentioned above. Therefore, more shorted transmission lines are needed to test the effect. The spectrum characteristics are within the frequency range of 3.1-10.6GHz and the corresponding shorted stubs are dimensioned. In the ADS simulation, the lengths of the shorted stubs are tuned until the signal pulse reaches 1 Nano-second. The mono-cycle Gaussian pulse model in ADS is shown in Figure 4.9. The simulation result is given in Figure 4.10.
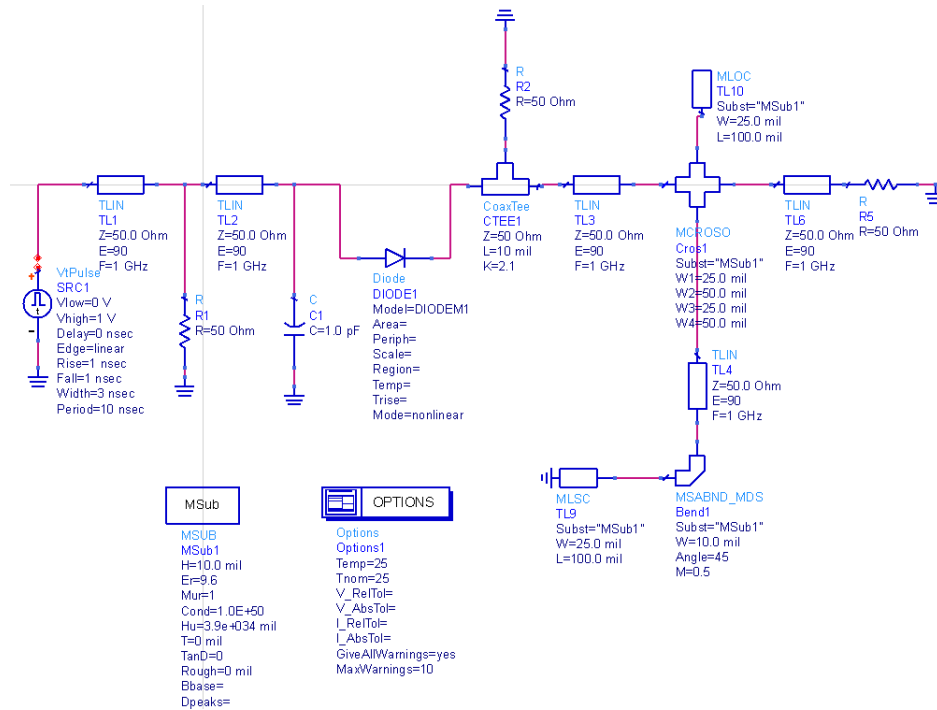
Figure 4-9 Mono-cycle Gaussian pulse model [3]
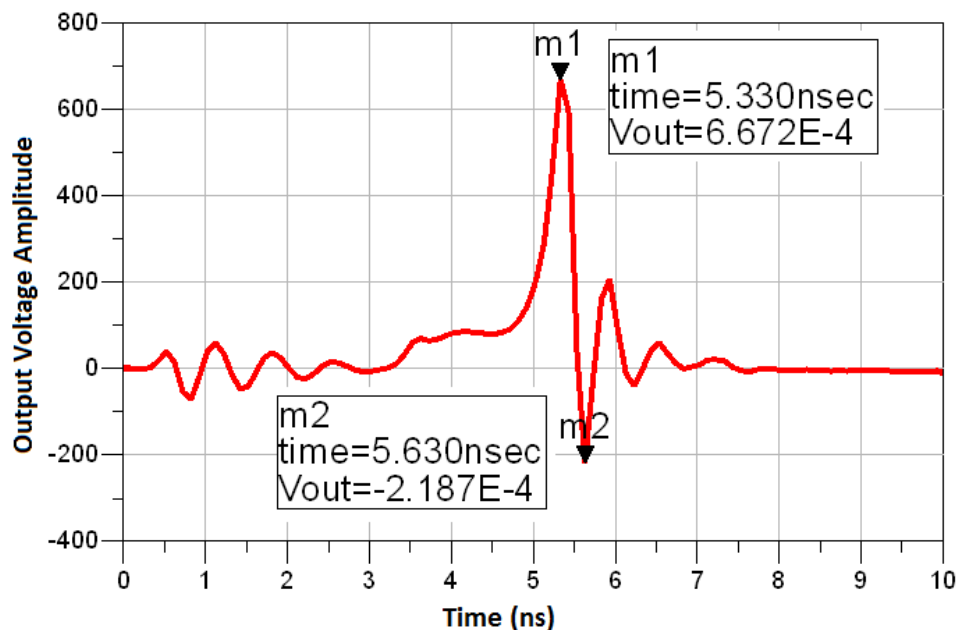
Figure 4-10 Simulation result of the UWB Gaussian Pulse

Next, the UWB pulse signal is mixed with the LO signal generated by a VCO device. In order to match the specifications of the proposed UWB system in experiment, a 4.5GHz sinusoid signal is simulated in MATLAB.

A mixer is acting as a key component in up-conversion in the transmitting link. The conventional Gilbert cell mixer consists of three stages: the trans-conductance stage, the mixing stage and the load stage. The RF input signal is given to the trans-conductance stage acting in the saturation region where the RF voltage is converted into RF current. The mixing stage is acting in the triode region that performs switching by LO signal [1].

In simulation, the modelling of a proper mixer operating within an ultra-wide band is difficult and time-consuming. As there are no existing RF mixers models suitable enough in the libraries, a search of the available commercial components is required. "Marki" double-balanced mixers are found to meet the demand. They can offer a broad band frequency range of 2-12GHz, good conversion loss of 6dB and a high isolation level of 35dB between LO and RF. All the useful parameters are chosen to facilitate the model construction and the module is embedded in the simulation.

In terms of power amplifier, an effective search results in a good choice, the "AAREN" AT26A-E114-KF Power Amplifier. It has a typical gain of 34dB and 1dB output level of

29dBm. These features are also used in another module construction, which is integrated in the whole simulation package.

The ADS Ptolemy based simulation model is given in Figure 4.11. At first, the "Timed-Source" module generates the UWB pulse signal and is embedded at the front. Then, the signal is mixed with a sinusoid signal with a centre frequency of 4.5GHz to realise the up-conversion via a module named as "Multiplier-RF". The mixer is set to produce both the lower and upper sides of the converted signals. A "Butterworth-Timed" filter module is followed and ensures that only the upper signal is chosen. Afterwards, a "Gain-RF" module is used to offer a 34dB gain to amplify the signal. In the end, a "PackCx_M" module is used to collect the output signal. The saved data is transferred to the embedded "MATLAB-Sink" interface unit, which bridges the signals processing between ADS and MATLAB environments.
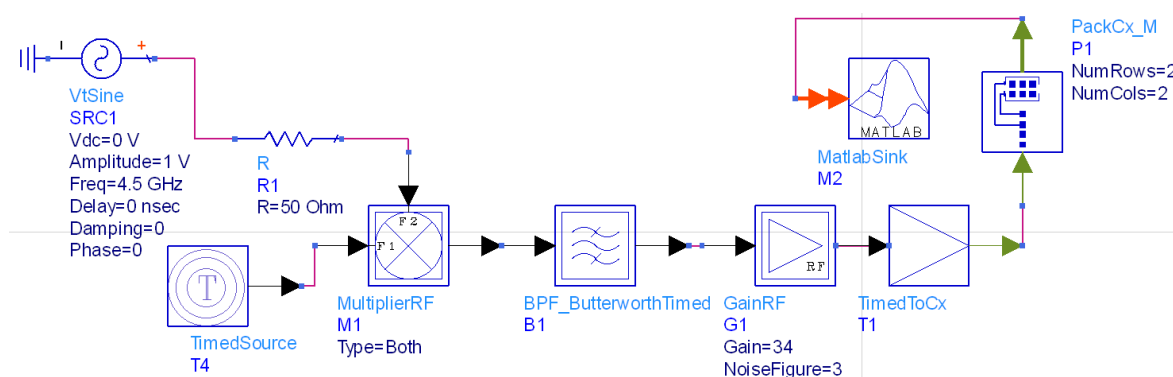
Figure 4-11 ADS Ptolemy simulation of the UWB radar transmitting sub-system [3]

In practice, digital waveform generators are constructed by linking a digital signal source with a "Digital to Analog (D/A)" converter. Digital memories are used to store the signal waveform and the memory is read out based on the timing characteristics of the desired waveform. The choice of a proper waveform is mainly determined by these factors: the detection purpose of the radar, the expected characteristics of the targets, the demand of moving target tracing and the electromagnetic compatibility requirement.

In measurement, the rectangular waveform signal is used instead due to the unavailability of the Gaussian pulse generator with required UWB bandwidth. The signal is generated by "Picosecond Pulse Generator Model 10060A" available in the lab with the amplitude of 1V and the bandwidth of less than 1 Nano-second, as shown in Figure 4.12.
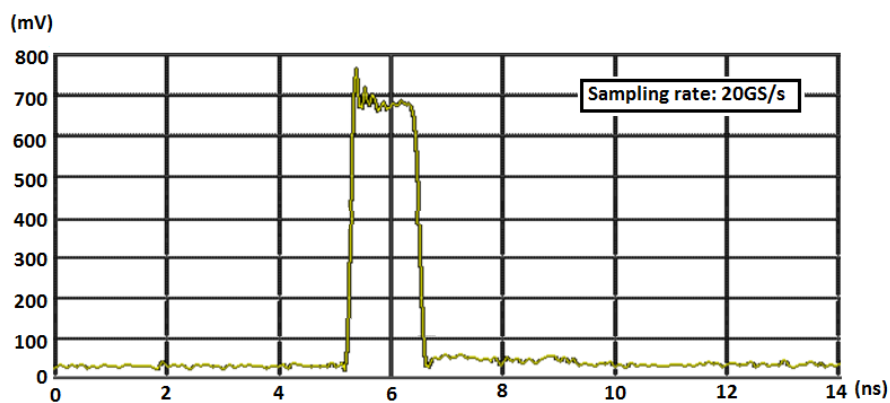
Figure 4-12 A single step signal with a pulse-width of 1ns

The modulated rectangular signal can also be extracted from the Equation 4.2:

$$
f(t) = \begin{cases} sin2\pi f_c t & qT \le t \le qT + \tau \\ 0 & qT + \tau \le t \le (q+1)T \end{cases} \tag{4-2}
$$

Here, q is the period of time. T is the signal repetition period of 10μs. τ is the signal duration of 1ns. f_c is the center frequency of 4.5GHz. One period of the modulated rectangular signal is a pulse train of sine signal in rectangular envelope.

The "Power Spectral Density (PSD)" of the modulated rectangular signal is considered next, because it should satisfy the FCC's regulation across the UWB frequency range. The calculation shows that the PSD of the modulated signal is below -41.3dBm/MHz across the whole UWB frequency band from 0 to 12GHz, matching well with the FCC's regulation, as shown in Figure 4.13.
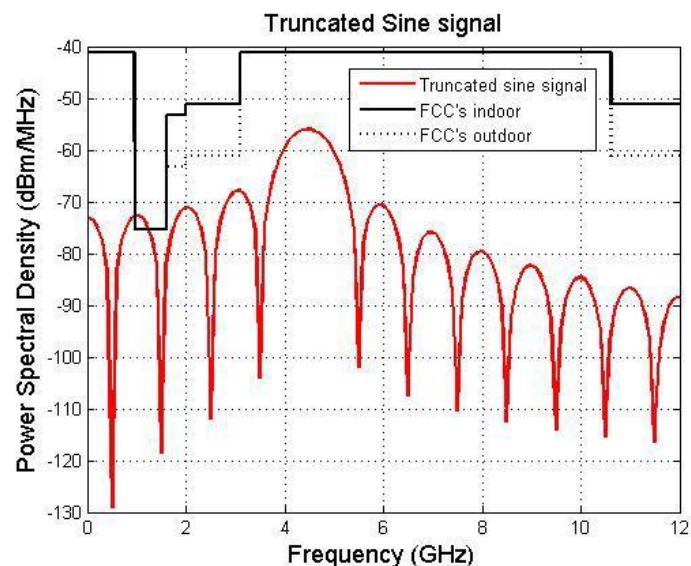
Figure 4-13 PSD of the modulated rectangular signal
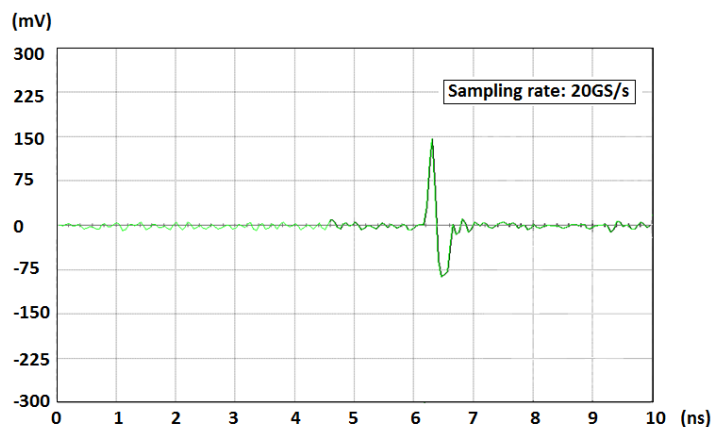
Figure 4-14 A Gaussian pulse generated via an IFN component

One attempt at creating the Gaussian pulse is to use a passive component "Impulse Forming Network (IFN)". An IFN produces an output signal that is approximately one derivative of the input signal. When the input is a step signal, the output will be an impulse; when the input is an impulse, the output will be a monocycle. The amplitude of the output signal is about 1/3 of the input one. The negative trough of the derivative pulse is wider than the positive peak and also has smaller amplitude because the trailing edge of the generator is slower. In experiment, by shortening the time duration of the step signal to 50ps, the output waveform becomes a quasi-Gaussian pulse with a pulse-width of as short as 1ns. However, the insertion loss of IFN makes the amplitude of the output signal level down to 150mv, as shown in Figure 4.14. It is

-137-

impossible to take advantage of this output signal because it is too weak for the receiver to effectively capture the target reflections from the noise and other interferences.

In fact, it is not strictly necessary to restrict the Gaussian pulse as transmitting signal. As long as the amplitude of the pulse satisfies the system requirement and the tail vibration is small enough, a square waveform signal can be accepted in the measurement. Besides, the antennas act as filters, inevitably bringing distortions to the transmitting signal.

In order to match the broadband feature of the system, one off-the-shelf VCO product "Mini Circuits ZX95-5400+" is chosen. It has a liner tuning frequency range from 4.3 to 5.4GHz and the output signal frequency of 4.5GHz is finely tuned.

After the up-conversion, the determinant factor in the transmitting sub-system is the functionality of "Power Amplifiers (PA)". In the past, tube amplifiers, such as grid controlled tubes, magnetrons, klystrons, traveling-wave tubes (TWTs), and crossed field amplifiers (CFAs) have been used as PAs for radar transmitters. These amplifiers generate high power, but usually operate with a low duty cycle. The klystron PA offers higher power than the magnetron at microwave frequencies, and also allows the use of more complex waveforms. The TWT is similar to the klystron, but with wider bandwidth. CFAs are characterised by wide bandwidth, modest gain, and compactness. Solid State Power Amplifiers (SSPAs) support long pulses and high duty cycle waveforms.

The ideal PA in the proposed UWB radar system needs to have more than 30dB Gain over a broad frequency band from 3 to 10GHz. Furthermore, the plan to build up a stand-alone compact system requires a minimal size of PA. One off-the-shelf product "AAREN AT26A-E114-KF" meets the requirement and is adopted in the systemic construction.
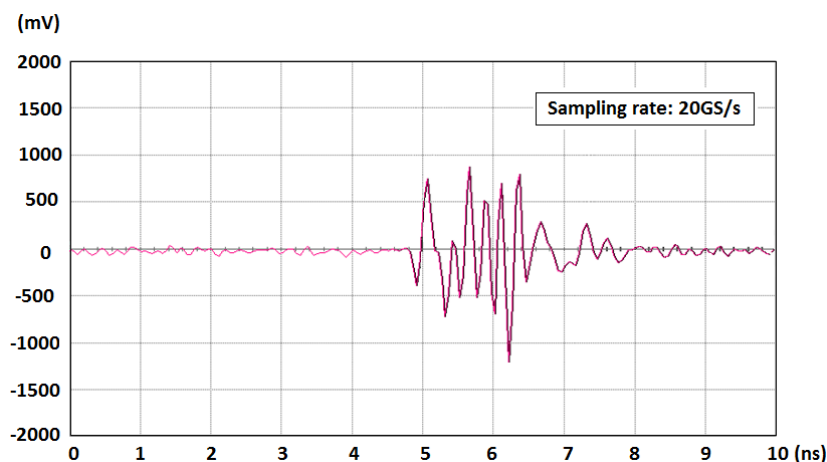
Figure 4-15 The transmitting signal after PA

The transmitting signal after PA is captured in experiment and shown in Figure 4.15. Two major changes occur in terms of the signal propagation: the first is that the transmitting square waveform is distorted. The derivative and non-linear distortion starts to occupy more than 2ns time space and affect the integrity of the pulse width; the second is that the signal level is powered up to 900mV, enabling the effective signal reception later in the receiving sub-system.

4.1.2 Wave propagation analysis in "see-through" scenarios

The choice of operating frequency band for UWB radars depends on what materials they are intended to penetrate. In theory, a longer wavelength would lead to better penetration, but worse imaging resolutions. Therefore, the upper UWB frequency range is preferably used to penetrate lower loss materials and the lower range is a better candidate for higher loss objects. In conclusion, the dilemma is that high penetration ability is contrary to high imaging resolutions. The research work from Hughes Advanced Electromagnetic Technologies Centre shows that there is limited EM signal attenuation penetrating a concrete wall within the frequency range from 1 to 10GHz. The lower the frequency is, the less the attenuation is observed. The typical value of attenuation at 8GHz is around 10dB but would drop to 5dB at 2GHz. So it is reasonable to conclude that the usable frequency range for "see-through" applications should be between 2 and 10GHz.

Instead of splitting the UWB frequency band into lower band and higher band, the proposed UWB radar system focuses on the middle frequency range from 4 to 5 GHz. There are two

reasons for this: the first lies in the application of the imaging system, which is to scan luggage/suitcases for metal target detection and imaging. The chosen operating frequency band can promise good penetration capability. The second reason is that the achievable bandwidth is restrained by the VCO and the pulse generator. Current products and equipment in the lab cannot generate a shorter pulse-width. Nevertheless, the existing components for this proposed system are adequate for the proposed UWB imaging system. The expansion of the workable frequency band for other applications can be explored in the design of the next generation of UWB imaging system.

The analysis of homogeneous obstruction penetration is made based on microwave signal reflection behaviour. First, the speed of propagation in the medium of EM waves can be calculated by using Equation 4.3 [1].

$$c = \frac{1}{\sqrt{\frac{\mu\varepsilon}{2}\left[\sqrt{\left(\frac{\sigma}{\omega\varepsilon}\right)^2+1}+1\right]}}$$
(4-3)

An illustration of the signals propagation through one layer is given in Figure 4.16. In it, "A" is the transmitting signal; "B" is the reflected signal from the first surface; "C" is the penetrating signal; "D" is the initial reflected signal from the target; and "E" is the final received signal from the target.
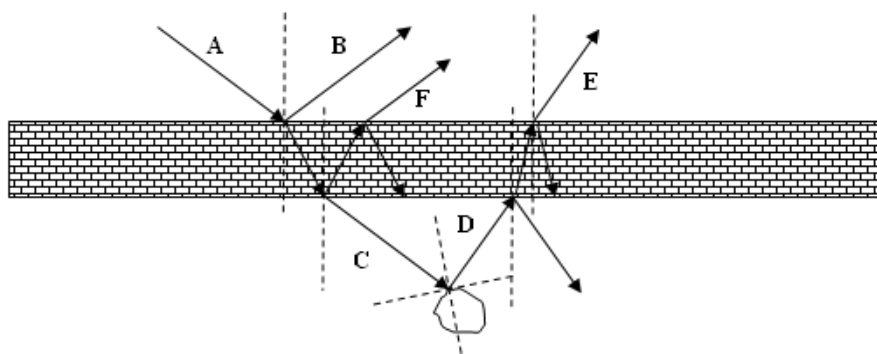
Figure 4-16 An illustration of EM wave penetration through one homogeneous layer [1]

The angles for signal transmit, reflection and refraction are "$\theta_I,\theta_R,\theta_D$".The EM characteristics of the layer are "$\varepsilon_W, \sigma_W, \mu_W$". According to the law of reflection: $\theta_I = \theta_R$. Therefore, their relationships can be written in Equation (4-4):

$$\frac{sin\theta_D}{sin\theta_I} = \sqrt{\frac{\mu_0\varepsilon_0}{\mu_W\varepsilon_E}} = \sqrt{\frac{\varepsilon_0}{\varepsilon_W - j\frac{\sigma_W}{\omega}}}; \quad where \ \varepsilon_E = \varepsilon_W - j\frac{\sigma_W}{\omega} \ and \ \mu_W \approx \mu_0 \qquad (4-4)$$

The impedance η_0 in the air is $\sqrt{\mu_0/\varepsilon_0}$ and the impedance η_W in the layer is $\sqrt{\mu_W \Big/ (\varepsilon_W + j\frac{\sigma_W}{\omega})}$.

Assuming the interface is continuously smooth, according to Fresnel Equations, the parallel polarised and vertically polarised waves can be written as below [1]:

$$R_{//} = \frac{\eta_A cos\theta_I - \eta_W cos\theta_D}{\eta_A cos\theta_I + \eta_W cos\theta_D}, \qquad (4-5)$$

$$\Gamma_{//} = \frac{2\eta_W cos\theta_I}{\eta_A cos\theta_1 + \eta_W cos\theta_D}, \qquad (4-6)$$

$$R_\perp = \frac{\eta_W cos\theta_I - \eta_A cos\theta_D}{\eta_W cos\theta_I + \eta_A cos\theta_D}, \qquad (4-7)$$

$$\Gamma_\perp = \frac{2\eta_W cos\theta_I}{\eta_W cos\theta_1 + \eta_A cos\theta_D}. \qquad (4-8)$$

The equations above are helpful for checking the attenuation and time delay in simulation. In Simulink, delay lines and delay blocks are used to model the delay effect. For example: as the transmitted wave passes the first delay block, one delay is introduced in the signal. The output is connected to an adder block and the same output is connected to the second delay block which further introduces a second delay. The Simulink model is given in Figure 4.17.
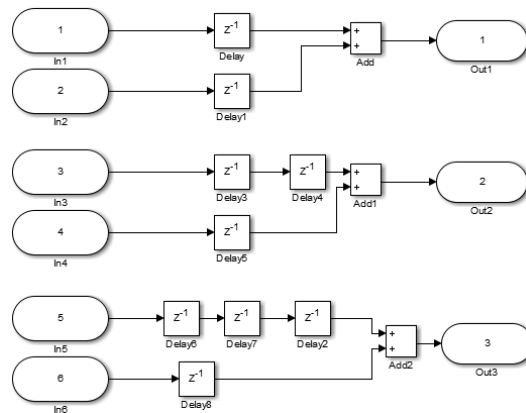
Figure 4-17 Target model using delay block
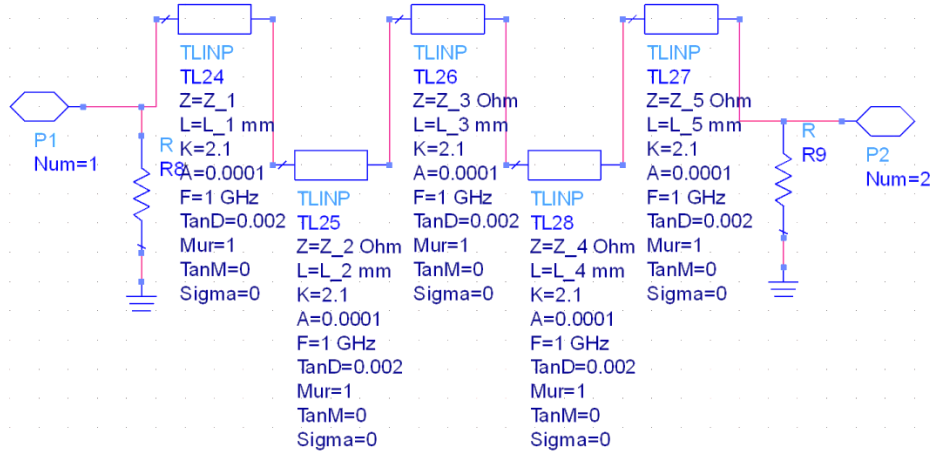
Figure 4-18 ADS simulation of the signal propagation through homogeneous obstructions

An ADS model is constructed to simulate the "see-through" scenario, as shown in Figure 4.18. The slabs of obstruction and propagation in the air are represented by transmission-line modules.

4.1.3 Analysis of EM scattering effect of the metallic target

The EM scattering of the target refers to the definition of "Radar Cross Section (RCS)". RCS is the measure of the scattering properties of a target at a certain fixed incident radiation angle. For a single target at a single frequency, the power backscattered from the target can be calculated from the classic Radar Equation, as shown in Equation (4-9) [1]:

$$P_{backscattered} = \frac{P_t \cdot G_t \cdot G_r \cdot \lambda^2 \cdot \sigma}{(4\pi)^3 \cdot r_t^2 \cdot r_r^2} \qquad (4-9)$$

Here, P_t is the transmitting power; G_t, G_r are the gains of the transmitting antenna and the receiving antenna, respectively; λ is the operating wavelength; σ is the RCS of the target; r_t, r_r are the ranges from transmitter to target and from target to transmitter respectively. Assuming $G_t = G_r$ and $r_t = r_r$, RCS of the target can be written as the function of the return loss:

$$|S_{11}|^2 = \frac{P_{backscattered}}{P_t} = \frac{G_t \cdot G_r \cdot \lambda^2 \cdot \sigma}{(4\pi)^3 \cdot r_t^2 \cdot r_r^2} \qquad (4-10)$$

$$\sigma = |S_{11}|^2 \cdot \frac{(4\pi)^3 \cdot r_t^2 \cdot r_r^2}{G_t \cdot G_r \cdot \lambda^2} \qquad (4-11)$$

Furthermore, RCS can be rewritten in dB format as:

$$\sigma \ (dBm^2) = |S_{11}|^2 + 33 + r_t{}^4 - G_t - G_r - \lambda^2 \qquad (4-12)$$

The estimation of RCS can vary depending on the electrical length of the target. For targets much larger than the operating wavelength, RCS is about the same size as the true size of the target; For targets comparable to the wavelength, RCS varies greatly and may be much bigger or smaller than the true size value; For targets smaller than the wavelength, $RCS \propto \lambda^{-4}$.

The methods mentioned above assume that the radiation incident angle is normal to the target. RCS values will change when the incident angle varies. In order to visualise the changes in signal propagation, a multi-static model is built in CST Microwave Studio and Wireless Insite. Three antennas are used to radiate towards a square metallic target. The inter-space between each antenna is 100mm. The size of the target is 100 x 100 mm². In order to investigate the models in Wireless Insite correctly, some modifications need to be done beforehand.

Wireless Insite is based on a frequency-domain ray-tracing technology and limited to single frequency simulation. That is why Wireless Insite can exhibit such superfast computation time. A full simulation, consisting of five antennas and targets in CST Microwave Studios, cans last five hours. However, the same set-up can be completed within 15 minutes in Wireless Insite based on single frequency calculation. It would not contain as much information compared with CST simulation results, but some interface connection techniques can be adopted to take advantage of the merits of both.

For the UWB imaging system, if performing the simulation on the single frequency basis, different frequency points will require related radiation patterns and new simulations. The UWB antenna in the system is a modified corrugated "Balance Antipodal Vivaldi Antenna (BAVA)" with an operating band from 2 to 10GHz. By dividing the frequency band with a step of 1GHz, there are 9 different radiation patterns at 9 different frequency points.

The simulation results of radiation patterns of the UWB antenna from CST Studios at these 9 frequency points are saved first. The pattern data is re-formatted and transferred as a user defined function in Wireless Insite. In theory, each frequency needs a new run with a related pattern. All the simulations have shown the similar trend in terms of multiple propagation paths and 5GHz is chosen for demonstration below. The propagation paths between the antenna and

the target are illustrated in Figure 4.19. The change in colour of the propagation paths reflects the varying energy level.
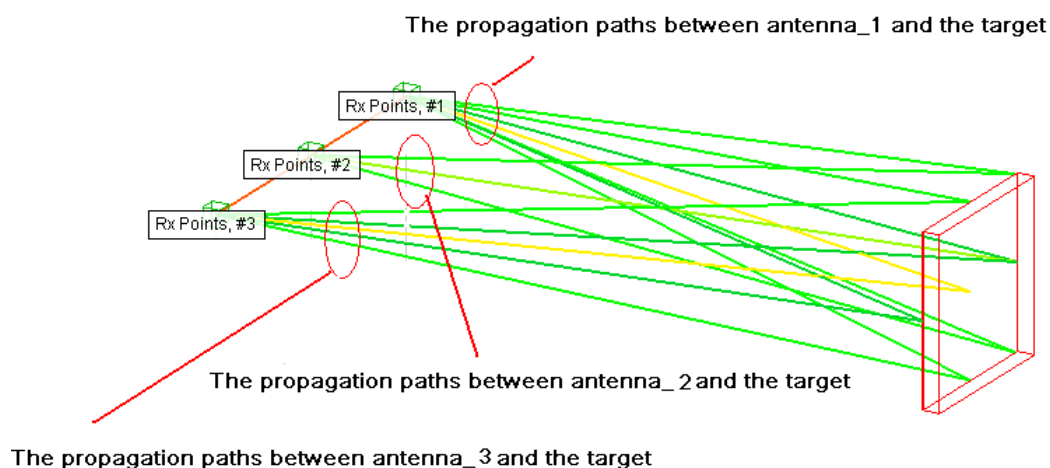
Figure 4-19 A multi-static set-up for square metallic target detection

(a) Two propagating paths;   (b) Four propagating paths

(c) Five propagating paths
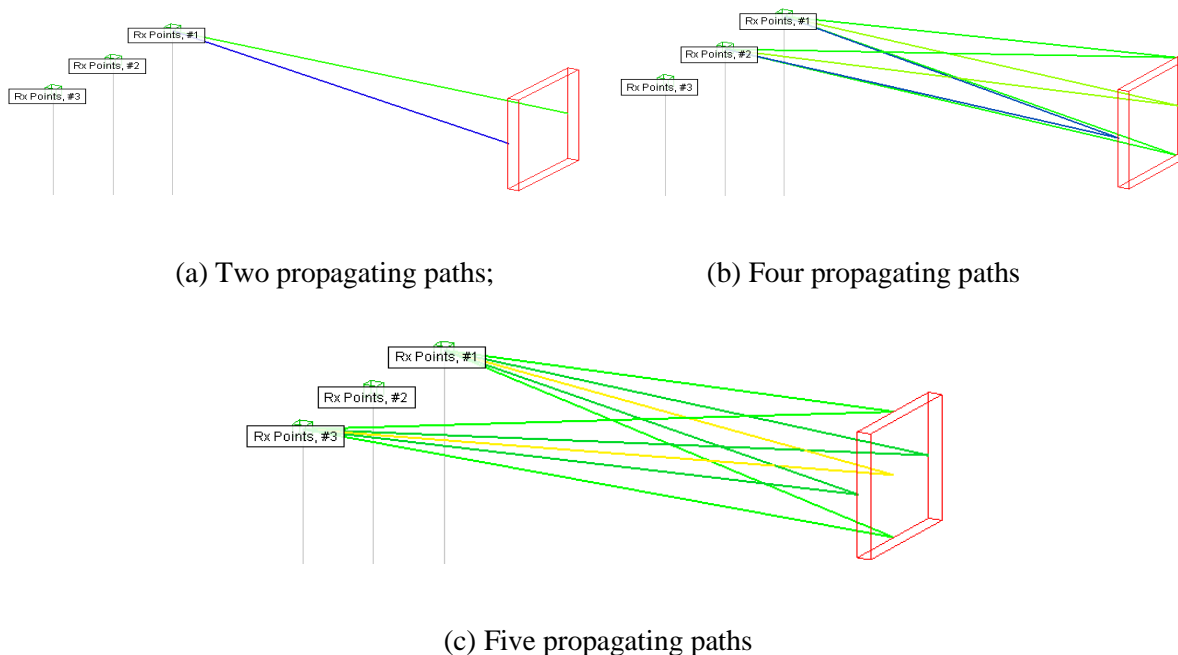
Figure 4-20 Multiple propagating paths between antennas and one metallic target

A more specific illustration has been given in Figure 4-20(a), (b) and (c). In Figure 4-20(a), "Rx Points 1" is used as a transceiver. Simulation in Wireless Insite shows that there are two major propagation paths between the antenna and the target. In Figure 4-20(b) and (c), "Rx

Points 1" acts as the transmitter and "Rx Points 2 and 3" are acting as receivers respectively. The simulation results show four and five major propagation paths.

The energy level of each path is recorded in Table 4-1. It shows that when only one antenna is operating as the transceiver, there are two major propagation paths with the energy levels of -52.15dBm and -65.54dBm; when the second antenna is introduced as one receiver, the number of effective propagation paths increases to four with the strongest energy level up to -47.64dBm; when the third antenna is used, there are five major propagation paths with the strongest energy level up to -42.41dBm.

Table 4-1 Illustrations of energy levels of different propagation paths when the incident angle is 90 degrees

Energy (dBm)	Number 1	Number 2	Number 3	Number 4	Number 5
Rx Point_1	-52.15	-65.54	-	-	-
Rx Point_2	-47.64	-53.3	-53.3	-60.8	-
Rx Point_3	-42.41	-53.45	-53.45	-55.18	-55.22

The second scenario in simulation is to tilt the same metal target with 45 degrees in front of the antenna array. Similar procedures have been taken and the corresponding simulation results of the energy levels of multiple propagation paths are given in Table 4-2. The results show that when one antenna is used, there is only one major propagation path with the energy level of -63.45dBm; two antennas have generated three propagation paths with the strongest energy level up to -57.32dBm; the third antenna helps to creates four major propagation paths with the strongest energy level up to -54.77dBm.

Table 4-2 Illustrations of energy levels of different propagation paths when the incident angle is 45 degrees

Energy (dBm)	Number 1	Number 2	Number 3	Number 4	Number 5
Rx Point_1	-63.45	-	-	-	-
Rx Point_2	-57.32	-65.12	-65.19	-	-
Rx Point_3	-54.77	-65.33	-65.33	-69.25	-

By comparison, the impact of the change of the incident angle is evident. The energy of propagation paths has dropped by 20% to 25% and the number of significant propagation paths has decreased by 1 for each scenario. In imaging, the different incident angles inevitably change the RCS of the target. Less effective propagation paths and lower received energy would lead to a less precise localisation and worse imaging results.

There are two procedures worth mentioning in the simulation and calculation. First, the direct propagations between antennas are excluded in the analysis. They contribute to mutual coupling and are irrelevant information, though their energy levels are prominently higher than the target signature. Secondly, the discussion above is based on the simulation in CST Studio and Wireless Insite with the approximation. The qualitative analysis aims to visualise the signal propagation with one target in mono-static and bi-static set-up, rather than exploring the full information of the whole domain.

4.1.4 The receiving sub-system

The major function of the radar receiving sub-system can be described as follows: the RF front-end is used to collect the scattered signals from the target via the receiving antenna and preform RF filtering and low noise amplification; the down-converter converts the input RF signals to the desired IF signals and performs IF filtering and amplification to a certain level; then ADC undertakes digital sampling work and passes on the digitalised data to PC/Microprocessor for

the imaging process. The block diagram of a digital receiving sub-system is shown in Figure 4.21.
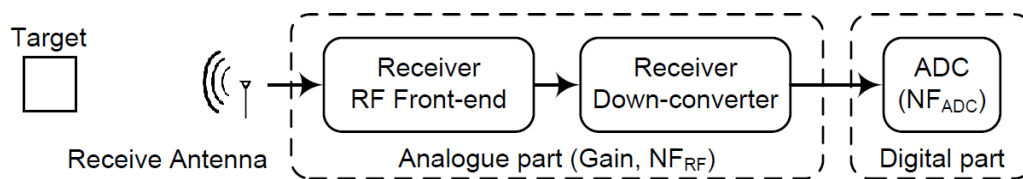
Figure 4-21 The block diagram of a typical receiving sub-system [1]

Most modern radar receiving sub-systems start with a LNA and end with an ADC. It is necessary to understand not only the limitations of the input power and noise at the receiver end, but also to consider the requirements and limitations of the ADC.

The purpose of an LNA is to boost the desired signal power while adding as little noise and distortion as possible, so that the retrieval of the target signal can be maintained and is well distinguishable from noise and other unwanted interferences. LNAs usually need to have a low "Noise Figure (NF)", which is defined as the input "Signal to Noise Ratio (SNR)" divided by the output *SNR*. LNAs are used at the front end of the radar receiver.

In addition to NF, there are other important parameters. First, the receiver should have a reasonable dynamic range. A large dynamic range allows for detection of small targets while strong interferences are present. Secondly, the receiver should have a high sensitivity in order to achieve the maximum detection range. However, there is always a trade-off between dynamic range and sensitivity. For a given bandwidth, the cascade NF defines the sensitivity of the receiver and determines the lowest input RF power that can be detected by the receiver. The highest sensitivity can be realised by using a LNA with the lowest NF and highest available gain in order to minimise the impact of a high NF of succeeding stages in the receiver chain. The dynamic range of the receiver is a measure of the receiver's ability to handle the range of signal strengths, from the weakest to the strongest. The largest dynamic range can be realised by using a LNA with the largest third-order intercept point at the input. This maximum IIP3can be obtained by a LNA with the highest third-order intercept point at the output and a moderate gain. This means that there is a contradiction in obtaining the LNA with the lowest NF and the largest sensitivity.

Thirdly, the receiver should have high frequency stability in order to meet the requirements for advanced digital signal processing. The LO, all the clocks and reference signals need to be produced by a highly stable oscillator to guarantee the stability and coherency of the radar system. Complex algorithms with reliable performance can then be implemented in the radar. Budget link analysis is needed to estimate all the useful parameters in radar designing. An initial model is built in ADS to simulate a simplified receiver end, as shown in Figure 4.22 [3]. The recovered pulse signal in simulation is given in Figure 4.23.
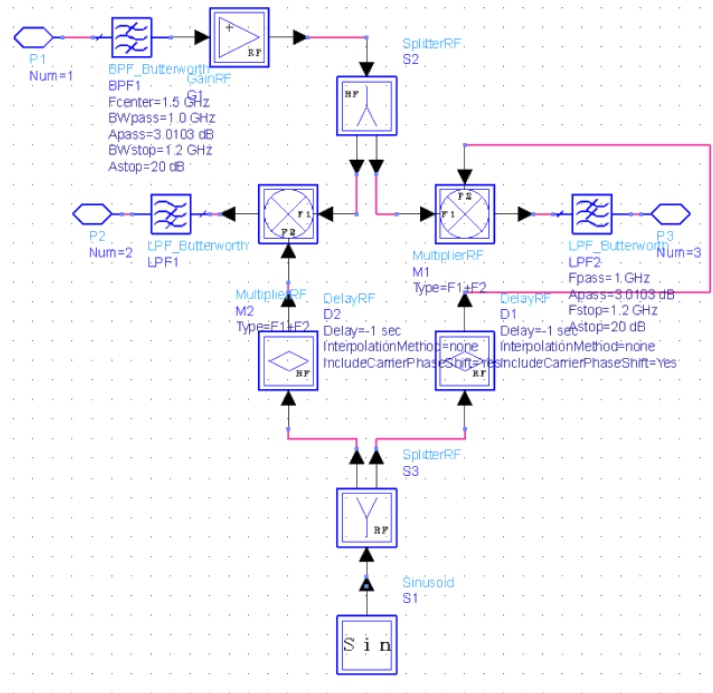
Figure 4-22 Block diagram of the radar receiver in ADS simulation [3]
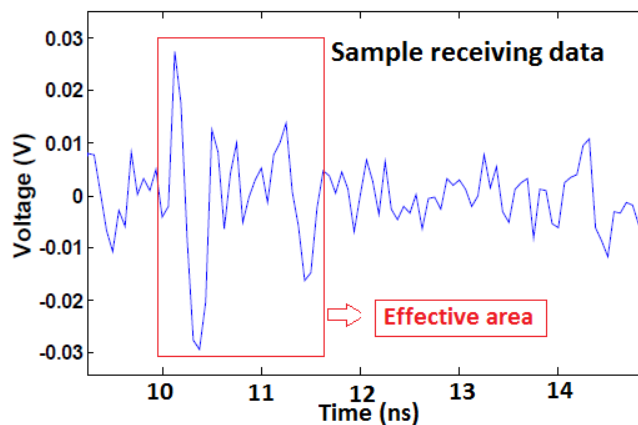
Figure 4-23 Recovered sample of a UWB Square wave pulse

4.2 Link budget and dynamic range analysis

The theoretical link budget analysis is mainly concerned with the investigation of the relationship between the antenna gain and *SNR*. This can help researchers to further understand the practicability of the proposed UWB imaging system. The *SNR* can be written as the equation (4-13) [1]:

$$\text{SNR} = \frac{P_t G_t G_r \sigma \lambda^2}{(4\pi)^3 R^4 k T_0 FBL_s} \tag{4-13}$$

RCS σ of the square flat metal target can be written as $4\pi A^2 / \lambda^2$. A is defined as the surface area of the target. In this case, The *SNR* can be rewritten as the equation (4-14):

$$\text{SNR} = \frac{P_t G_t G_r A^2}{(4\pi)^2 R^4 k T_0 FBL_s} \tag{4-14}$$

Calculation of the thermal noise floor is carried out. k=1.38x10⁻²³JK⁻¹ is the Boltzmann's constant and can be converted to -228.6dBW/k/Hz. T_0 is the system temperature and usually regarded as 290K, which is 24.6dBk. B is the bandwidth of the signal as 1GHz, which is 90dBHz. So the thermal noise floor is -113.97dBW, which is -83.97dBm. Additionally, NF is commonly assumed to be 3dB.

In the proposed UWB imaging system, the maximum transmitting power to the transmitting antenna is 29dBm, which is determined by the maximum output power of PA. The power of the minimum noise level is about 0.1mW (-10dBm) according to the measurement and the minimum power of identified received signal is no less than 0.2mW (-7dBm). Thus, *SNR* is considered to be above 3dB. Considering that PA works below the saturation state, a more cautious estimation of the transmitting signal power should be more practical. So the input power of the signal in the system is revised as 250mW (24dBm). The system loss is assumed as a figure between 40dB and 50dB based on the measurement.

The complexities of different testing scenarios result in varying path loss. For illustration purpose, the pass loss is fixed as 50dB. Thus, *SNR* is mathematically related to the testing ranges, the size of the target and the antenna Gains.
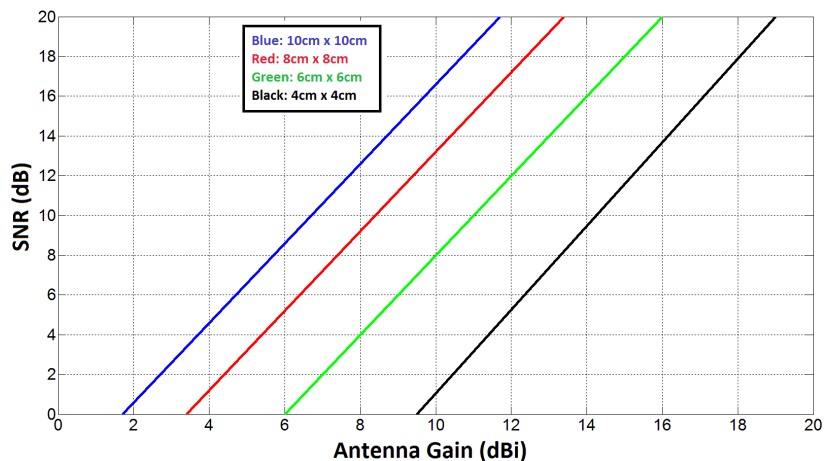
Figure 4-24 The relationship between antenna gain and SNR for different sizes of the detected target at the distance of 40cm
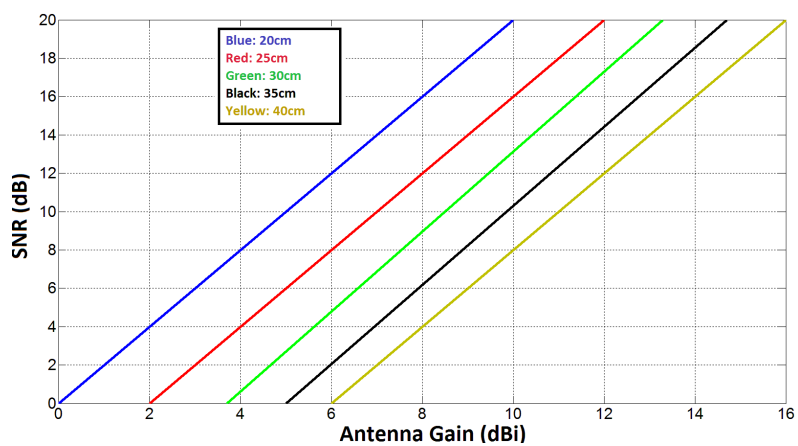
(a) Target size of 6×6 cm^2;
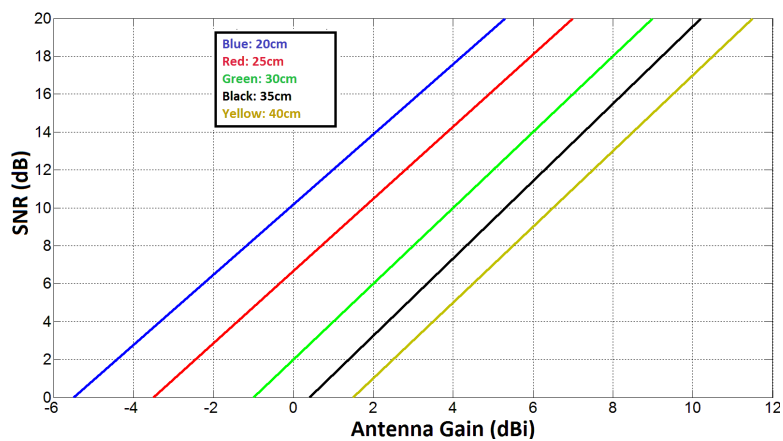
(b) Target size of 10×10 cm^2

Figure 4-25 The relationship between the antenna gain and *SNR* for the target at detection ranges of 20cm, 25cm, 30cm, 35cm and 40cm

First, assuming the testing range is 40cm, the relationship between *SNR* and antenna gains can be illustrated in Figure 4.24 for targets with different sizes. Secondly, when the sizes of target are 6 x 6 cm^2 and 10 x 10 cm^2 respectively, the relationship between *SNR* and antenna gains is given in Figure 4.25(a) and (b).

It can be concluded that *SNR* is linear proportional to the antenna gains. In experiment, the transmitting and the receiving antennas are the same and the gain varies around 5.5dBi to 7dBi from 3 to 10GHz, which can guarantee a reliable SNR for the purpose of the measurement at the maximum detection range of 40cm.

The dynamic range is related to the active and passive components in the proposed system. The proposed UWB imaging system consists of the RF circuit, the rotating antenna array and the signal-processing unit. The flow chart of the imaging system is given in Figure 4.26 [4].
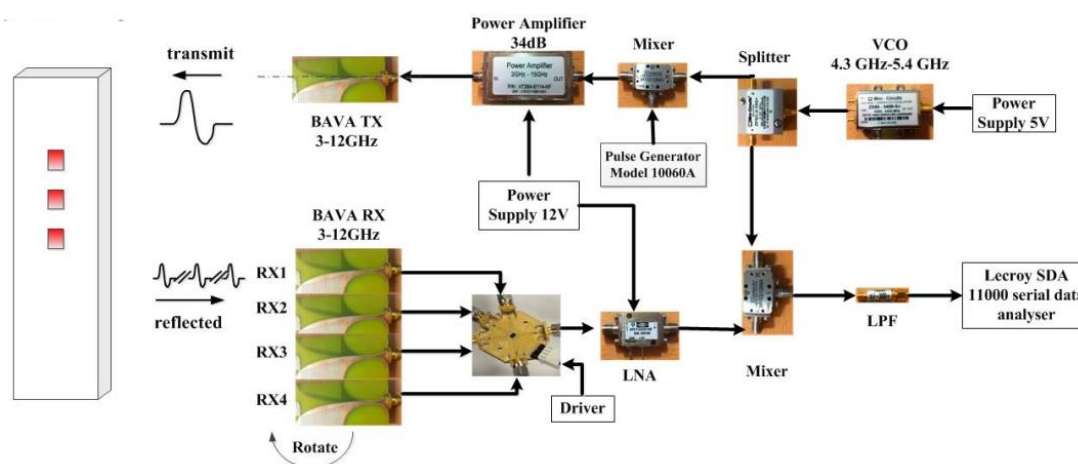
Figure 4-26 The proposed UWB imaging system architecture [4]

The modulated rectangular signal goes through an RF transmitting path and is radiated by the transmitting antenna. It penetrates through the testing area, and is reflected by the target. The reflected signals propagate back and are received by the receiving antenna array. The received data is collected and shown in Lecroy SDA 11000 serial data analyser. Discretised data is transferred to PC for the image reconstruction.

The signal generated from the Picosecond Pulse Generator Model 10060A is a periodic rectangular pulse. The time period is 10μs and time duration is 1ns. The LO (Local Oscillator) signal generated from VCO is a sinusoid signal with the time period of 0.22ns and the operating frequency of 4.5GHz. Two signals are mixed by Marki mixer M1-0212 and then powered up

by PA. The transmitting power level of the system is mainly determined by PA, which provides a maximum output power of 29dBm. Considering the inevitable loss from the cables and connectors, an output power of 24dBm is a reasonable estimation of the transmitted signal power to the transmitting antenna.

From the receiving link, LNA has a minimum 1dB output compression of 13dBm and gain of 22dB, so that the theoretical minimum received power at LNA is -9dBm. The estimated antenna isolation between Tx and Rx is around 33dB.

The thermal noise floor of the receiver is -84dBm and the NF is 3dB. Meanwhile, the minimum *SNR* would be well above 3dB. Therefore, the receiver sensitivity is -78dBm. Because the minimum received power is -9dBm, the dynamic range of this UWB imaging system is 69dB. The dynamic range analysis of the proposed system is listed in Table 4.3.

Table 4-3 Dynamic range analysis of the proposed UWB imaging system

Dynamic range analysis	Values
Transmitter total power (dBm)	24 (Max:29)
Tx-Rx isolation (dB)	33
Thermal noise floor (dBm)	-84
Noise figure (dB)	3
Required minimal *SNR*	3
Receiver sensitivity (dBm)	-78
Receiver minimum received power (dBm)	-9
Receiver dynamic range (dB)	69

4.3 Automation design of antenna sub-system

The previous generation of the developed UWB imaging system is bulky and complicated [4]. It encompasses four independent power supplies to power up active components, a heavy 15 x 30 x 13 cm^3 motor device fixed onto the table and a 40 x 40 x 15 cm^3 driver system to activate and control the motor. It is impossible to make the imaging system portable and compact enough for the intended applications. This section shows the procedures taken to slim down the system architecture with the final goal being to make the proposed system a stand-alone portable unit.

4.3.1 The Antenna positioning sub-system

The two common methods for achieving more data and wider array aperture in antenna deployment are either to add as many receiving elements as possible, or to move the fixed-numbered array in horizontal/vertical direction. But the number of elements in the receiving array cannot be expanded without limit. The intrinsic mutual coupling effect between the neighboring antennas cannot be ignored either. Horizontal and vertical movement of the receiving array needs careful mechanical design and a precise controlling unit. In the proposed system designing, a rotary array is employed, as shown in Figure 4.27.
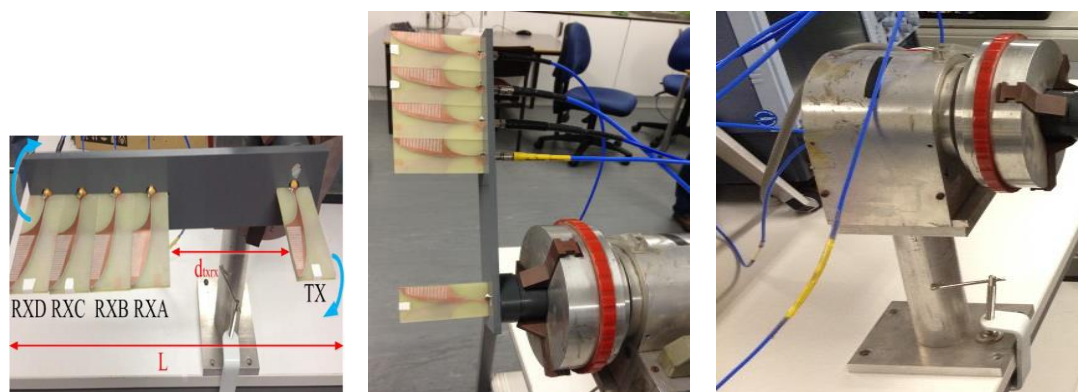
(a) Antennas array arm; (b) Array mounted on the motor shaft; (c) Motor body fixed onto the table

Figure 4-27 The rotary array and the original motor in the previous experimental set-up

The antenna array straight arm includes one transmitting antenna and four receiving antennas side-by-side. The inter distance d_{txrx} between the transmitting antenna and the first receiving

antenna is 11.5cm. The width of the corrugated BAVA is 3.5cm and the receiving antenna elements are placed together. Therefore, the total length *L* of the rotating antenna array is 29cm.

While powered by the motor placed behind, the arm of array rotates in a circle around the single transmitting antenna at an angular increment. The four receiving elements do not work at the same time. Each of them is chosen by a RF switch to work individually in a synthetic manner. The mutual coupling between the transmitting antenna to the receiving antenna is well below -30dB.

One issue of the mechanical configuration is that the motor should not attach itself onto any platform. This will greatly limit the portability of the imaging system. The other one is that the existing motor and driver system are too big and heavy. The programming of the driver is complex and slow. All in all, an alternative portable and compact motor positioning sub-system is needed to replace the previous one. One small step motor "RS191-8356" is a good candidate, as shown in Figure 4-28 (a). The frontal shaft of the motor is connected to a smaller black metal gear, which is matched up with a blue plastic bigger gear. The transmitting antenna is fixed onto the center of the bigger gear, as shown in Figure 4-28 (b).
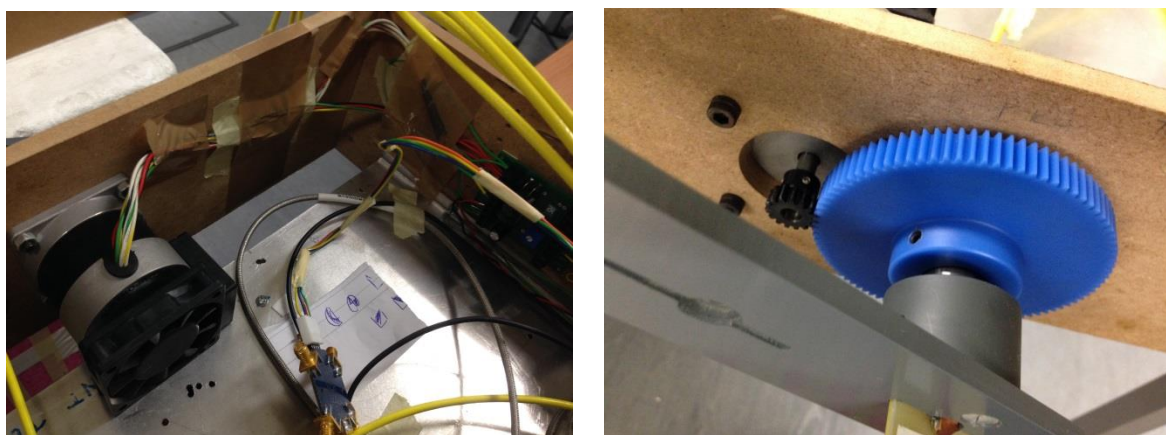
(a) Step motor RS191-8356 fixed inside the box;   (b) A pair of gears fixed to the shaft

Figure 4-28 The step motor and a pair of gears in the antenna positioning design

There are many benefits in using a proper step motor for the project. First of all, the rotation angle of the motor is proportional to the input pulse. This means that if the input signal pulses are electronically controlled, the movement of the motor can be computerised. Secondly, when the winding is energised, the motor can provide full torque at stand-still positions, which means

that when the rotation stops at a certain position, the motor can reliably support the stay. Lastly, step motors can usually offer very precise positioning and repeatability of movement with a recognised accuracy error rate of 3% to 5% for each step. This minor error is also of non-cumulative nature from one step to the next.

The foreseeable disadvantages may include unwanted resonance if the motor is not properly wired and controlled and difficulty in performing extreme high speed rotation. However, in experiment, the data collection is carried out in the synthetic fashion. This means that the motor needs to stop at each angular step for a little while and then carry on to the next step. The rotation is not continuous, thus there is no need for high speed movement.

The step motor "RS191-8356" is an 8-wire structure, allowing for multiple wiring configurations depending on whether the motor's speed or torque is more important. The driver card for the chosen motor is a commercial product "RS240-7920". It is designed to drive a step motor in unipolar mode, either with or without forcing resistors connected between motor commons and "+" volts. Full, half or wave mode, is selected, as is direction and speed external clock via the logic connections. Speed can be derived from an adjustable clock on board. "Enable" and "Disable" inputs allow for a variety of start/stop control options to be implemented. The "RS240-7920" driver card has two terminal blocks, and a trimmer pot. The first block is for connection of the motor and power supplies and the second one is for logic connection. The trimmer pot adjusts the speed via the on-board clock. The logic inputs, outputs are generally TTL LS and CMOS (12 Volt max) compatible and are fitted with various series and pull up, or down resistors. The phase outputs are open drain power MOSFET (source to 0VM) with a fast diode between drain and +VM. The connections of the driver board are given in Figure 4.29. The step motor operating at the maximum rated current will be very hot. Two sided fans can effectively cool it down. Some connections in the lab are shown in Figure 4.30.
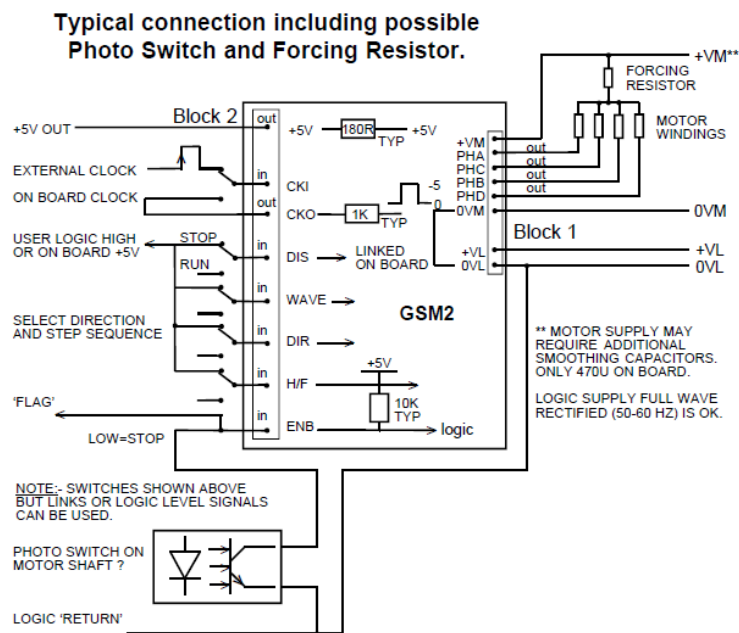
Figure 4-29 Typical connections for the driver card including photo switch and forcing resistor
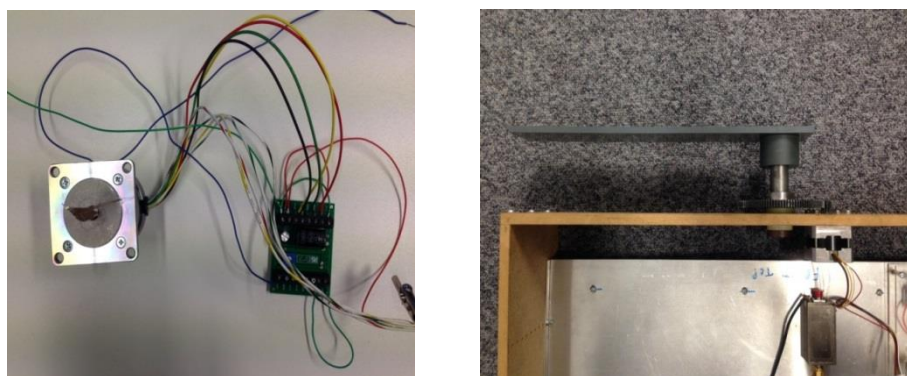
(a) Connections between the step motor and the driver card; (b) The step motor and gears

embedded behind the antenna array arm

Figure 4-30 Positioning configurations with a step motor, a driver card, gears and an antenna array

4.3.2 Automotive control design in LabVIEW with NI DAQ

With the step motor, the driver card and the RF switch in place, one interface device is needed to achieve an automated control. National Instrument USB-6009 is a USB based data acquisition and control device with multiple analog inputs and outputs, and digital inputs and outputs. This device is able to interact with LabVIEW and make the control computerised.

In general, there are three tasks. The first is to use one analog output of NI "Data Acquisition (DAQ)" to transfer the periodic signal produced from LabVIEW to the driver card. The second is to use two analog outputs to determine the minimal angular angle and the arrangement of a "direction" key. The last one is to use the "Measurement & Automation Explorer" testing panel to control the digital output to control the RF switch, which is the key to collecting signals in a synthetic manner in experiment. The model to tackle the first task is shown in Figure 4.31(a) and (b).
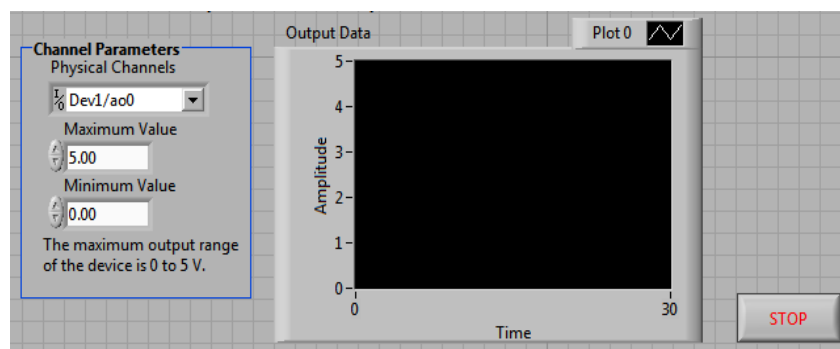
(a) The front panel program in LabVIEW;
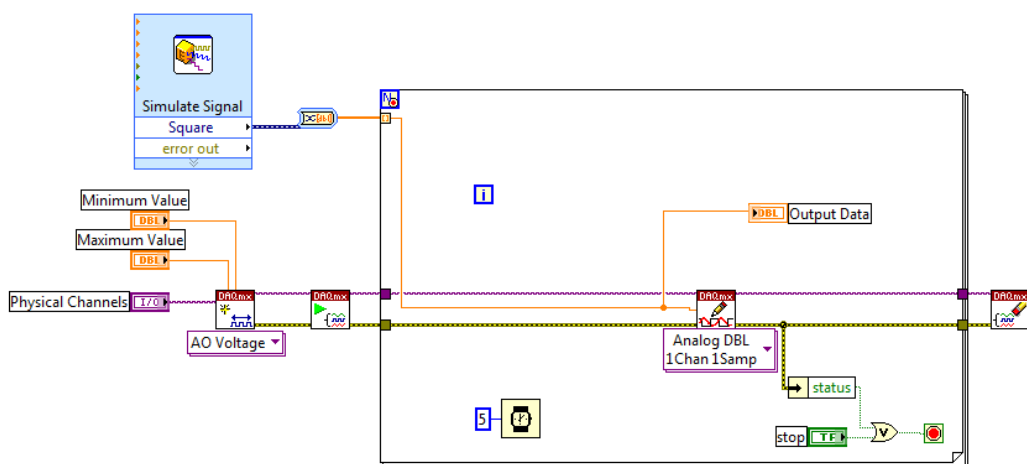
(b)   The block diagram program in LabVIEW

Figure 4-31 Programs to generate the periodic signal to activate step motor in LabVIEW

The LabVIEW program provides two interfaces. One is the front panel, as shown in Figure 4.31(a) and the other one is the block diagram, as shown in Figure 4.31(b). Among the channel parameters, the "Dev1/ao0" means that the first DAQ device is chosen and the number "0"

analog port is selected. The maximum and minimum values refer to the voltage amplitude of the square wave generated in the window. In the block diagram, "Simulate Signal" block is used to transfer the square wave signals from the NI DAQ device to the step motor.

The second task is to use two DAQ assistant components in the LabVIEW program to give the order to the driver card, as shown in Figure 4.32. The front panel is shown in Figure 4.32(a) and the block diagram is shown in Figure 4.32(b). Both DAQ assistant components can produce a voltage level of 0 to 5V, but have different purposes. The first DAQ assistant is to control the minimal rotary angle. This is realised by connecting one analog output of the DAQ to the "H/F" port. When the voltage level is turned from 0V (Low) to 5V (High), the rotation angle is halved. The other DAQ assistant is to control the direction of the rotation. When the voltage level is High, the rotation is clockwise. When it is Low, the rotation is immediately reversed.
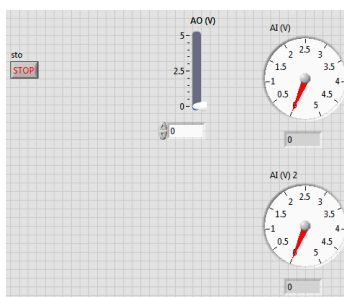
(a) The front panel program in LabVIEW;
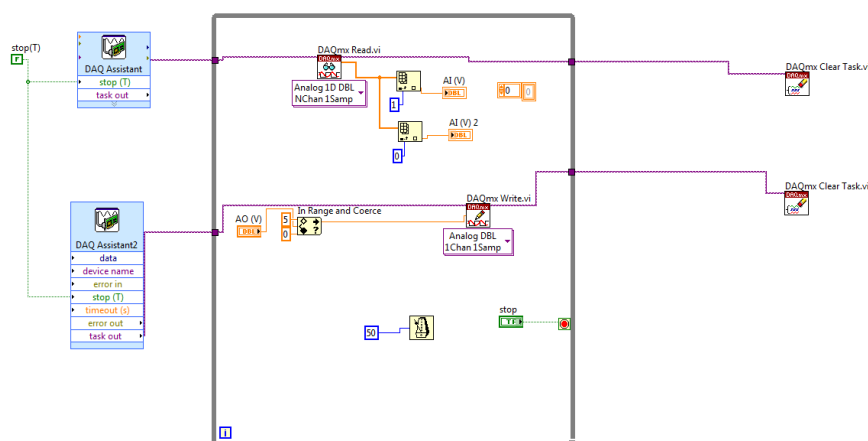
(b) The block diagram program in LabVIEW

Figure 4-32 Programs to generate voltage range of 0 to 5V to control the angular step and the rotation direction in LabVIEW
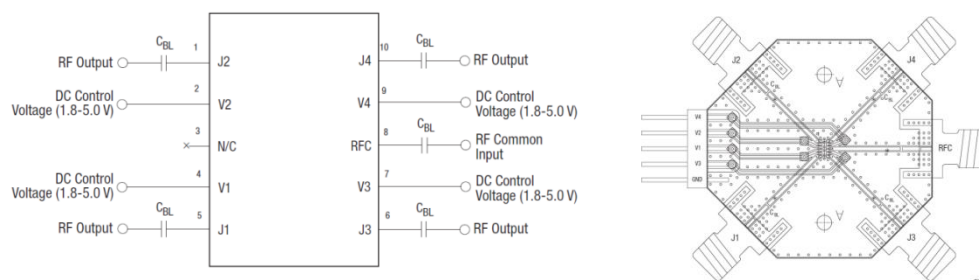
(a) Evaluation board schematic;   (b) Evaluation board assembly diagram

Figure 4-33 RF switch "SKY13322-375LF" configurations [5]

Table 4-4 Truth Table of RF switch "SKY13322-375LF" [5]

V1 (Pin 4)	V2 (Pin 2)	V3 (Pin 7)	V4 (Pin 9)	RFC to J1	RFC to J2	RFC to J3	RFC to J4
1	0	0	0	Insertion loss	Isolation	Isolation	Isolation
0	1	0	0	Isolation	Insertion loss	Isolation	Isolation
0	0	1	0	Isolation	Isolation	Insertion loss	Isolation
0	0	0	1	Isolation	Isolation	Isolation	Insertion loss

The last task is to electrically select the right receiving antenna in the synthetic way. One RF switch "SKY13322-375LF" from the SKYWORKS Company is used, as shown in Figure 4.33. The frequency range of the switch is from 20MHz to 6GHz and the insertion loss is as low as 0.45dB per 1GHz. The truth table of the switch is given in Table 4.4. "1" represents a voltage value from +1.8V to +5V, while "0" refers to the voltage from 0V to +0.2V.

The initial attempt to make the switch was an independent soldering piece, as shown in Figure 4.34. A pair of AAA batteries is used to offer high voltage. Four pull/push switches are embedded physically into a transparent plastic board to represent each RF switch channel.
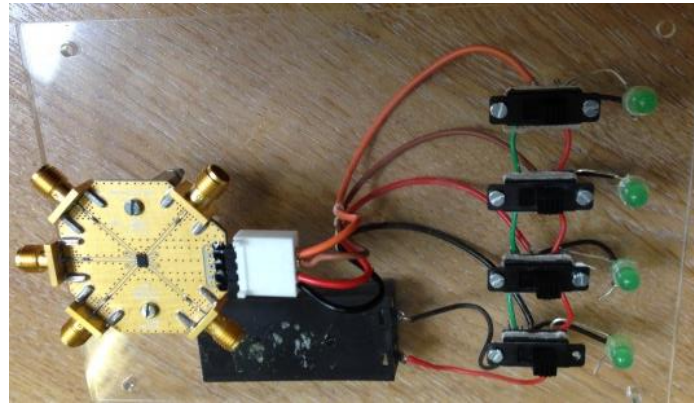
Figure 4-34 Physical RF switch board with pull/push switches
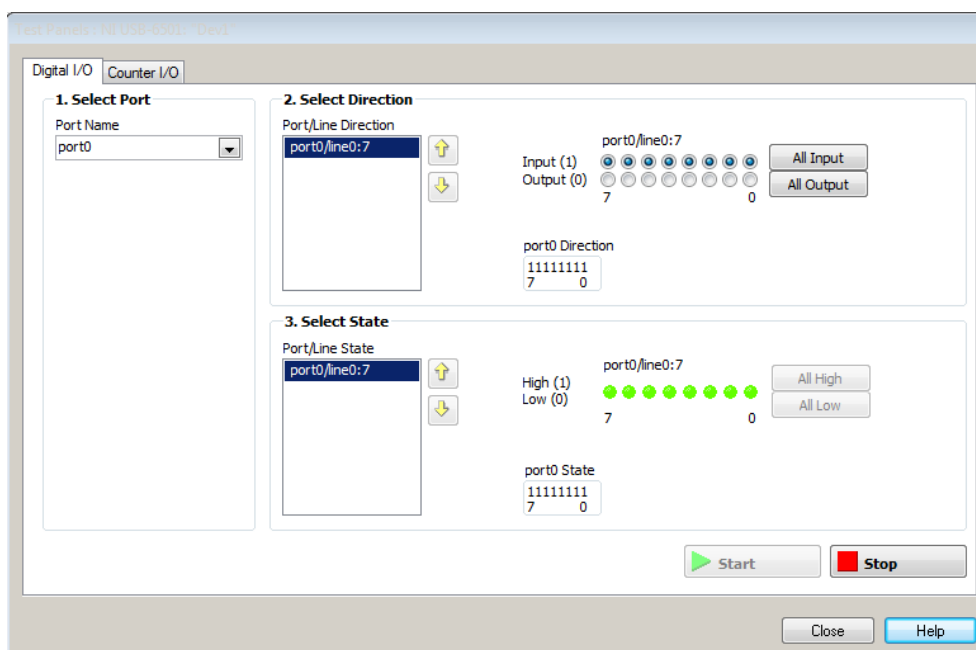
Figure 4-35 Digital outputs in "Measurement & Automation Explorer" testing panel to electrically control the RF switch

The physical board has soon been replaced by the use of four digital outputs in the NI DAQ device. Four RF switch ports are connected to the four digital outputs and the voltage values can be easily controlled in the "Measurement & Automation Explorer" testing panel, as shown in Figure 4.35. When a single switch is pushed up to "Green", one particular RF switch is

turned on and one channel is chosen to carry on the measurement, while the rest are off. This can be repeatedly performed during the experiment to choose the wanted channel to collect signals and dramatically save time and energy in experiments. Four switches are used sequentially until all the signal data at all the required angular stops are received and stored.

4.4 Summary

In this chapter, the architecture of the proposed UWB system is investigated in detail. Simulation work and some initial experimental results have validated the feasibility and practicality of the proposed UWB imaging system. Studies of the transmitting sub-system, wave propagation of the layer penetration, scattering of the target and the receiving sub-system are introduced. The link budget and dynamic range study show that the proposed UWB imaging system has a receiving dynamic range of 69dB and a receiving sensitivity of -78dBm. In order to build a portable UWB imaging system, the LabVIEW and two NI DAQ devices are used to form a computer-aided platform with a user-friendly interface. Therefore, a small step motor, driver card and one 5 ports RF switch can be controlled electronically.

Reference

[1] Kingsley, S. Quegan, "Understanding Radar Systems", McGraw-Hill, 1992.

[2] A. Kuthi, M. Behrend, T. Vernier,M. Gundersen, "Bipolar Nanosecond Pulse Generation using Transmission Lines for cell electro-manipulation," 26th International Power Modulator Symposium, May 23, 2004.

[3] Y. Wang, A.E. Fathy, "Advanced System Level Simulation Platform for Three-Dimensional UWB Through-Wall Imaging SAR Using Time-Domain Approach", IEEE Transactions on Geoscience and Remote Sensing, Vol: 50, No: 5, Page(s): 1986-2000, May 2012.

[4] Min Zhou, "Design and Time-domain Analysis of Antenna Array for UWB Imaging Application", PhD thesis, Queen Mary College, University of London, June 2014.

[5] http://www.skyworksinc.com/uploads/documents/201098D.pdf

Chapter 5 Experimental Evaluation of the proposed UWB imaging system

The aim of this project is to build a compact UWB imaging system with a rotating antenna array and with the minimal structural complexity. In experiment, the target is chosen to be metallic rectangular plates, because these are the main constituent for most contraband and dangerous weapons. Usually, target objects are concealed by being hidden in bags/luggage or behind obstructions like walls and cases/chests. In practice, targets may be mixed with other items, such as clothes, plastics and toiletries, which would introduce interferences.

In this chapter, several scenarios have been investigated in experiment to detect and image one and two metallic targets by using both DAS and TR methods. The targets are placed in free space, behind wooden boards, surrounded by multiple rods and inside a fully packed sport bag. A comparison between the DAS and TR images is made to show the advantages and disadvantages of both methods.

5.1 The UWB imaging system and calibration procedure

The developed UWB imaging system is shown in Figure 4.26 and needs to be carefully calibrated before conducting the imaging studies. One important calibration procedure is to eliminate the mutual coupling between the transmitting and receiving antennas since there is no decoupling arrangement between them.

This calibration procedure is done without the presence of the metallic target and any obstruction in free space. The modulated square signal with time duration of 1ns and a repetition period of 10μs is transmitted by the transmitting antenna, as shown in Figure 5.1. Correspondingly, four mutual coupling signals are received on the four receiving antennas as plotted in Figure 5.2, representing as S_{t1}, S_{t2}, S_{t3} and S_{t4}, respectively.
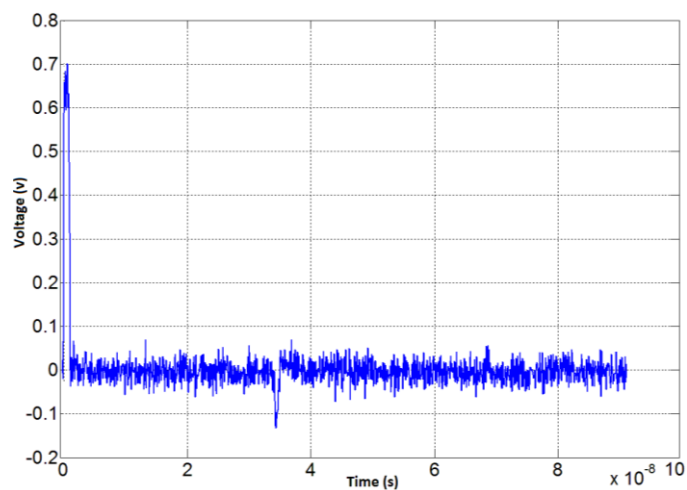
Figure 5-1 1ns UWB square-wave transmitting signal at the source
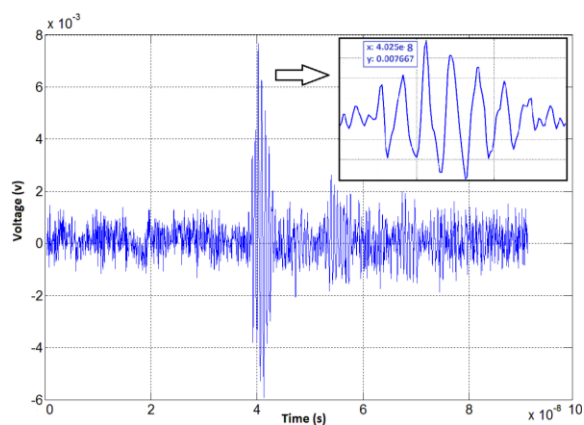
(a) Received signal at receiving antenna one;   (b) Received signal at receiving antenna two
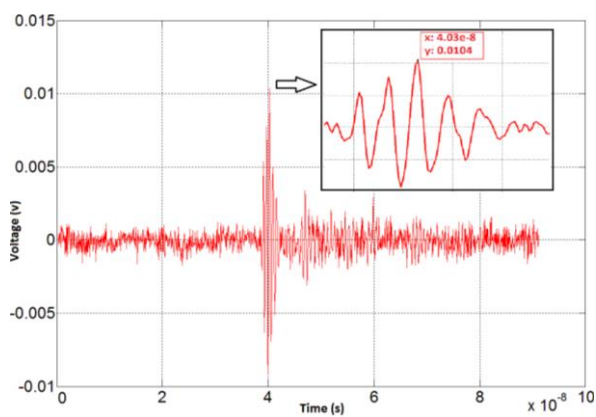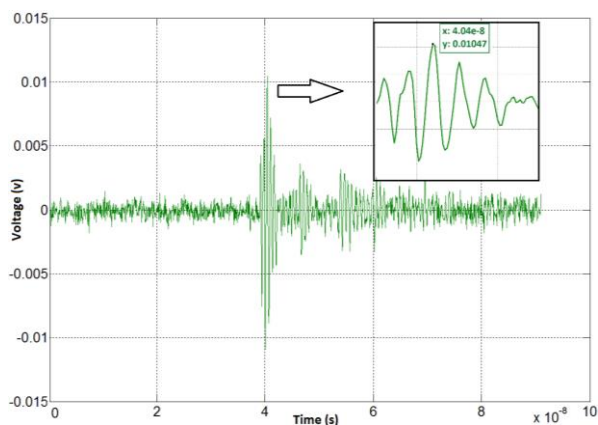
(c) Received signal at receiving antenna three;   (d) Received signal at receiving antenna four
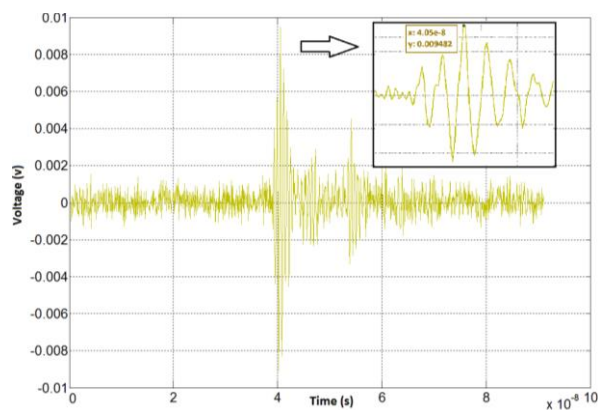
Figure 5-2 Received signals at four receiving antennas in experiment for calibration

Figure 5.2 shows that the mutual coupling signals picked up on the receiving antennas have a ringing effect, which will interfere with the target signals. Therefore, these mutual coupling signals need to be eliminated from the received target signals on each receiver when imaging the targets.

5.2 Test of the metallic targets imaging in free space

The first scenario in experiment is to detect metallic targets in free space. One metallic square piece is placed at a distance away from the antenna array, as shown in Figure 5.3. The experiment is carried out in an office room and there is no major obstruction within 3 meters around the UWB image system. Free space offers an ideal environment for potentially the longest detection range because of the minimal interference with the target signature.

Figure 5-3 One metallic target placed at a certain distance away from the array in experiment

5.2.1 Single target imaging in free space

The size of the single target is changed from 10 x 10 cm^2, to 8 x 8 cm^2, to 5 x 5 cm^2. The thickness of the target is 1cm. The testing area is limited within 50 x 50 cm^2 in front of the transmitting antenna and receiving antenna array.

For the target with the size of 10 x10 cm^2, the farthest detectable down range can be as far as 50cm. The measurements at different locations have been accomplished. For illustration purpose, the results of received signals with the down range of 20cm are given in Figure 5.4.

(a) Extracted received signal from antenna one;   (b) Extracted received signal from antenna two

(c) Extracted received signal from antenna three;   (d) Extracted received signal from antenna four
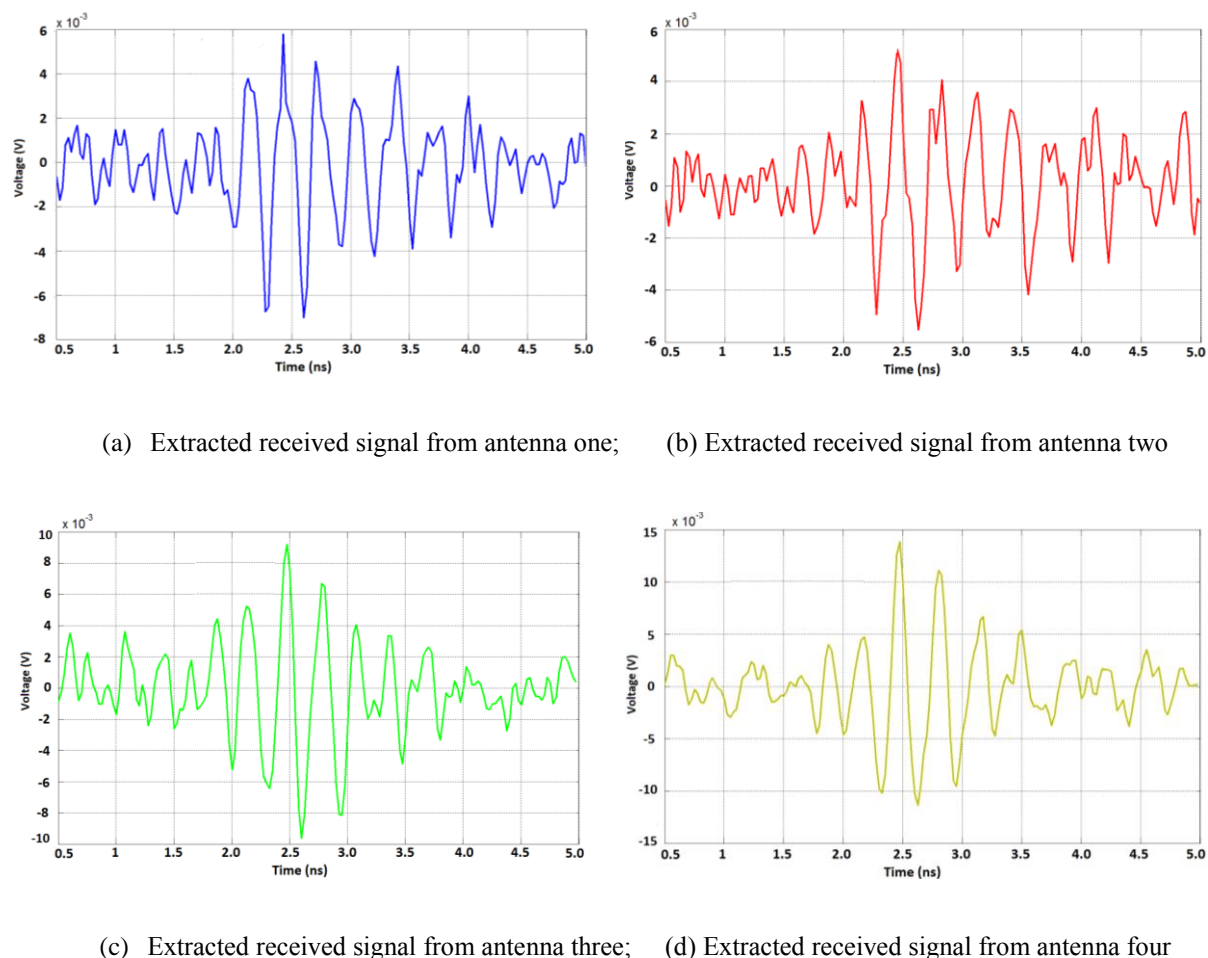
Figure 5-4 Extracted received signals at four receiving antennas from the single metallic target with the size of 10 x 10 cm^2 at the down range of 20cm

First, the signal target is imaged at different distances as shown in Figures 5-5, 5-6, 5-7 and 5-8. The results are presented in two parts: one illustrating the 2D cross range image of the target; the other showing the range estimation, as shown in all sub-figures (a) and (b), (c) and (d). In addition, comparisons between DAS and TR images are made with each pair of figures.

All the images have shown that the range of the target can be clearly recovered. When the target moves away from the antenna array, the received signal level starts to drop. Hence, with both DAS and TR images, the length of the highlighted range begins to shrink. In comparison, the DAS method can maintain better range estimation accuracy, while the TR images tend to be spread more in range estimation.

In terms of cross range estimation, the DAS images are better at recovering the target's real size. The summed-up ellipses have not achieved the perfect rectangular shape of the real target. However, in general, the DAS images have very accurate down range and cross range estimation. Because the target is imaged in free space, the image is prominently determined by signals directly reflected from the target. When the arm of the antenna array starts to rotate in front of the target, more received data in each scanning position would enhance the accuracy of cross-range images. The one exception to this is that when the target is placed 50cm away from the array, the DAS cross-range image becomes smaller. When the target is moved further than 50cm from the array, the target signal is buried in the noise below the detection threshold.

In contrast, TR images have a more flattened recovered shape of the target. They have shown a consistent imaging capability, even when the testing range distance is as far as 50cm.

Both methods have demonstrated that one metallic rectangular target with a size of 10 x 10 cm^2 is detectable. The furthest range of detection is 50cm in the experiment.
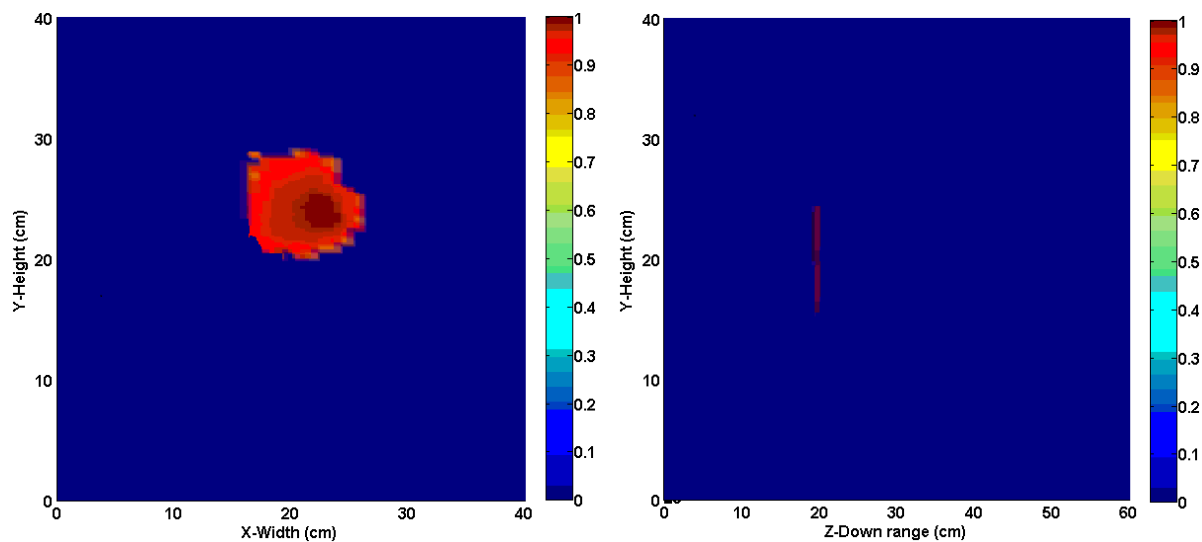
(a) Cross range image by DAS;   (b) Range image by DAS
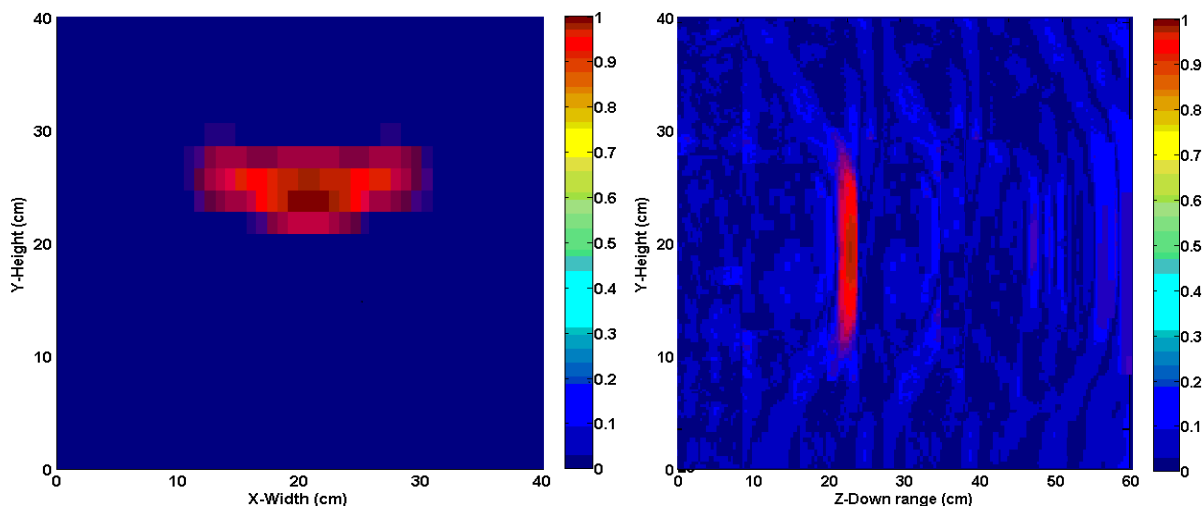
(c) Cross range image by TR;   (d) Range image by TR

Figure 5-5 Images of a single metallic target with the size of 10 x 10 cm^2 placed 20cm away from the receiving array in free space, by DAS and TR
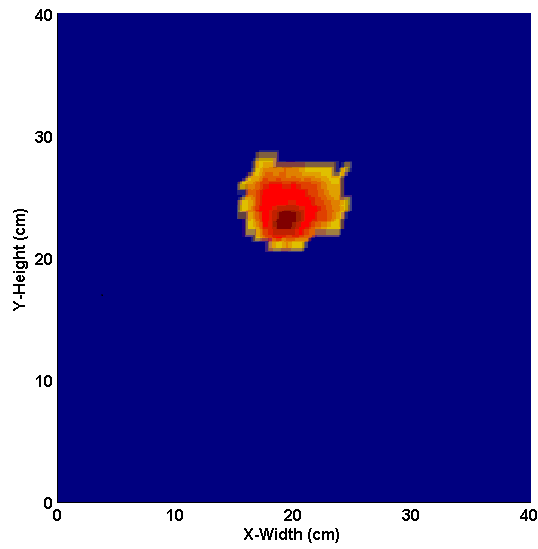
(a) Cross range image by DAS;   (b) Range image by DAS
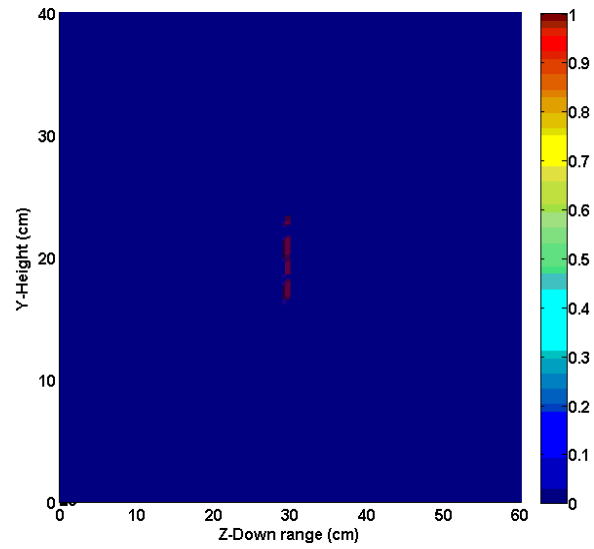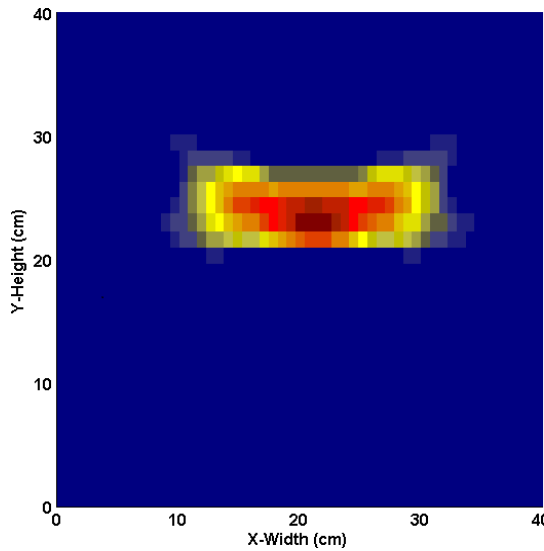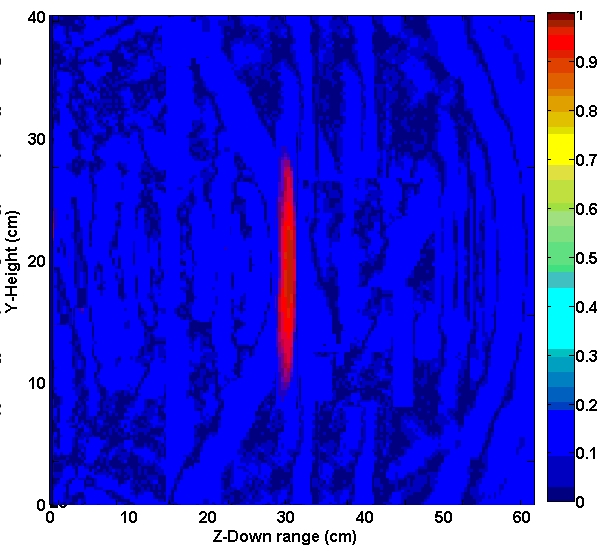
(c) Cross range image by TR;   (d) Range image by TR

Figure 5-6 Images of a single metallic target with the size of 10 x 10 cm^2 placed 30cm away from the receiving array in free space, by DAS and TR
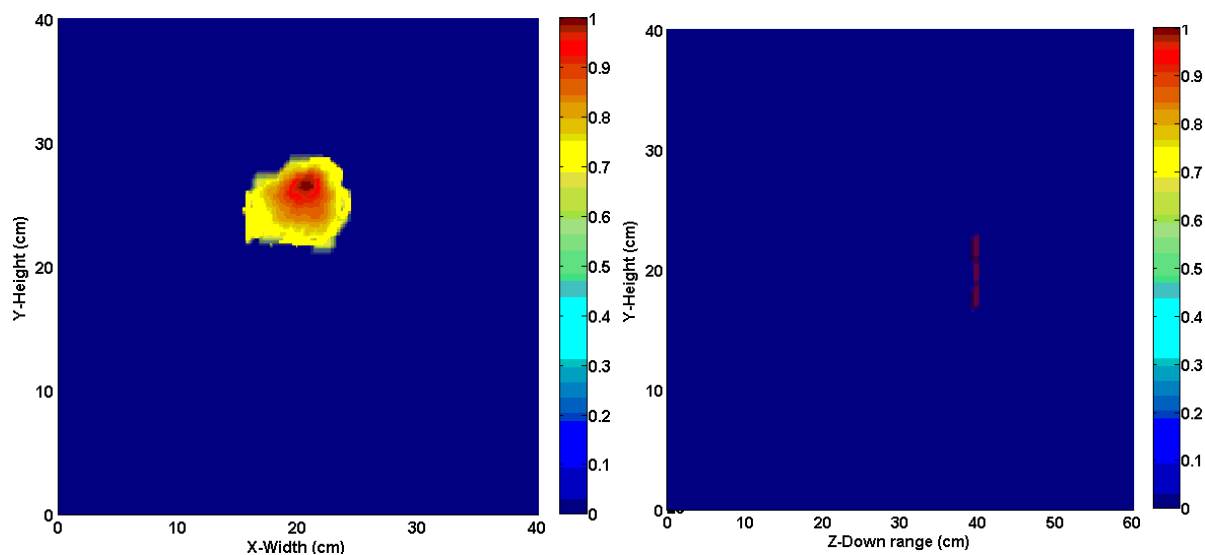
(a) Cross range image by DAS;   (b) Range image by DAS
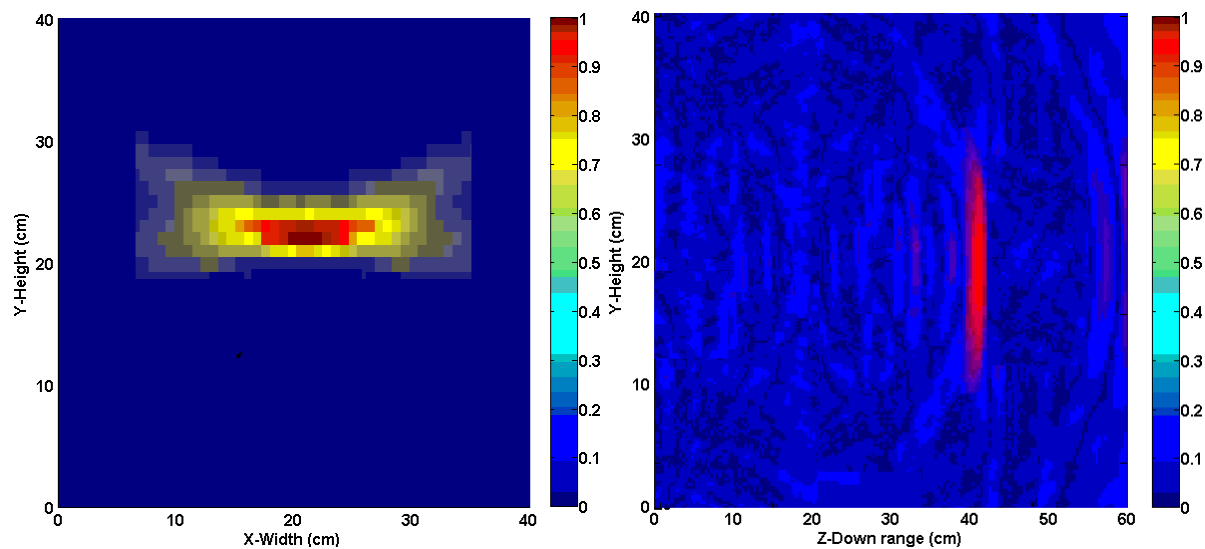
(c) Cross range image by TR;   (d) Range image by TR

Figure 5-7 Images of a single metallic target with the size of 10 x 10 cm^2 placed 40cm away from the receiving array in free space, by DAS and TR
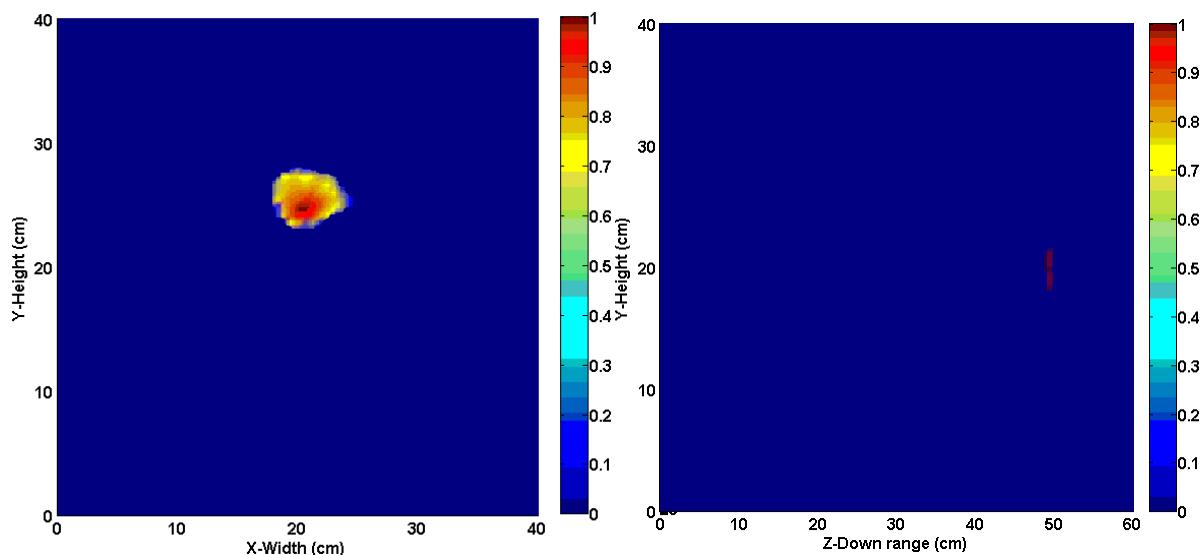
(a) Cross range image by DAS;   (b) Range image by DAS
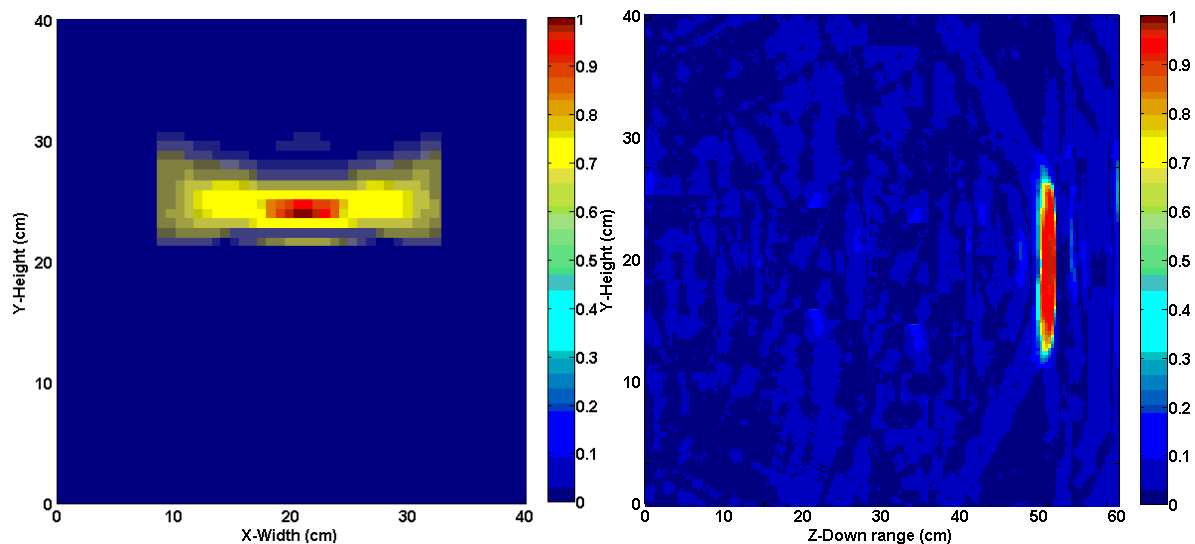
(c) Cross range image by TR;   (d) Range image by TR

Figure 5-8 Images of a single metallic target with the size of 10 x 10 cm^2 placed 50cm away from the receiving array, by DAS and TR

The same procedure is then applied to two smaller metallic square targets with the sizes of 8 x 8 cm^2 and 5 x 5 cm^2, respectively. In experiment, due to weak effective target signals, the target with the size of 8 x 8 cm^2 cannot be imaged at the range of 50cm and the target with the size of 5 x 5 cm^2 at the range of 40cm. So, for illustration purpose, only the images with the furthest testing down range are given below. The range and cross-range images of a target with the size of 8 x 8 cm^2 placed 40cm away from the array are shown in Figure 5-9. The range and

cross-range images of a target with the size of 5 x 5 cm^2 placed 30cm away from the array are shown in Figure 5-10.
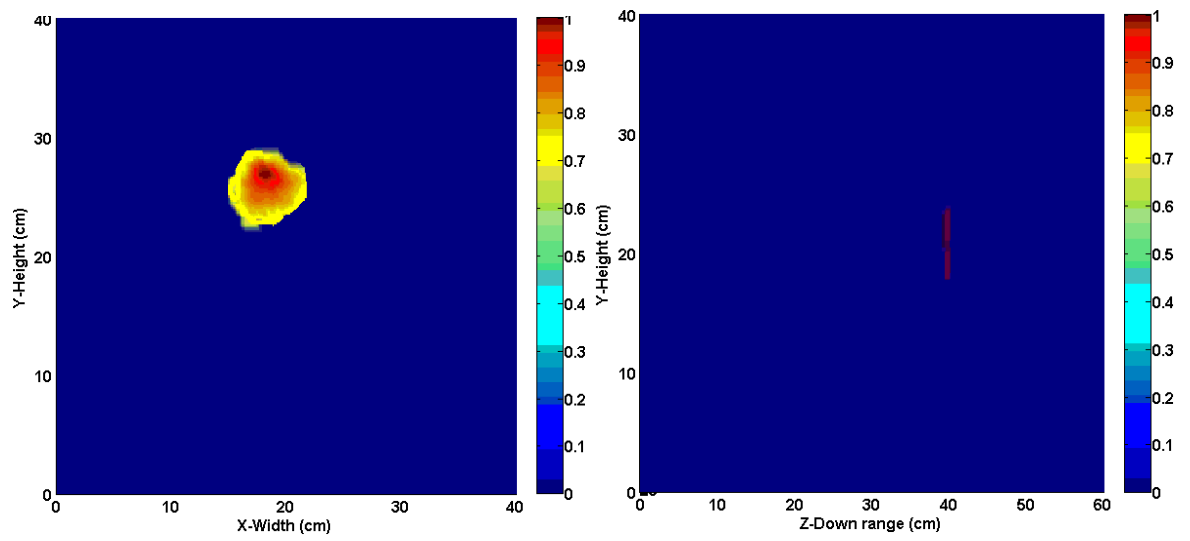
(a) Cross range image by DAS;   (b) Range image by DAS
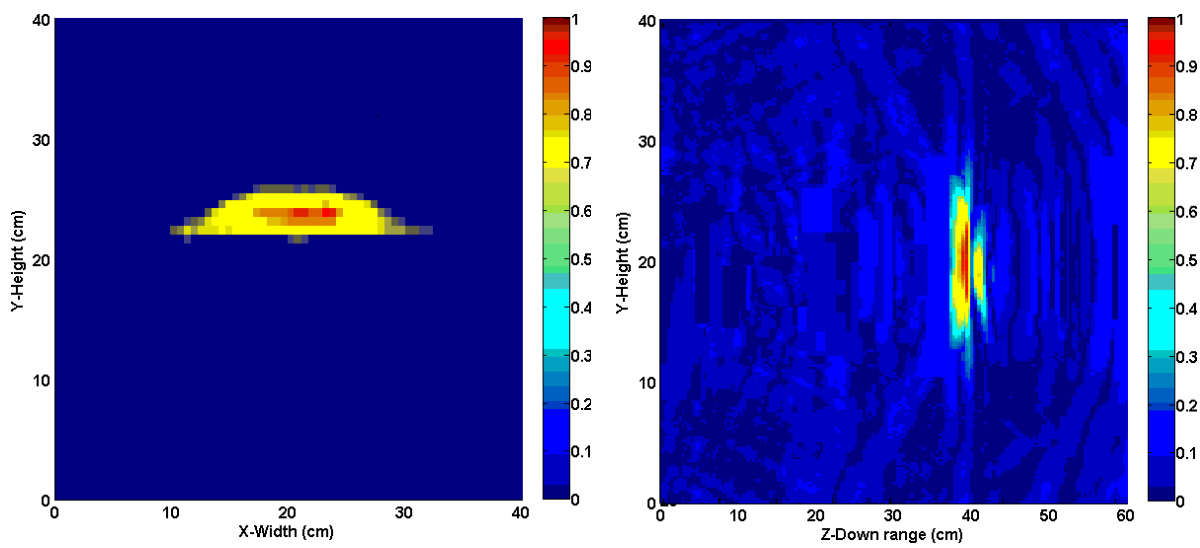
(c) Cross range image by TR;   (d) Range image by TR

Figure 5-9 Images of a single metallic target with the size of 8 x 8 cm^2 placed 40cm away from the receiving array in free space, by DAS and TR
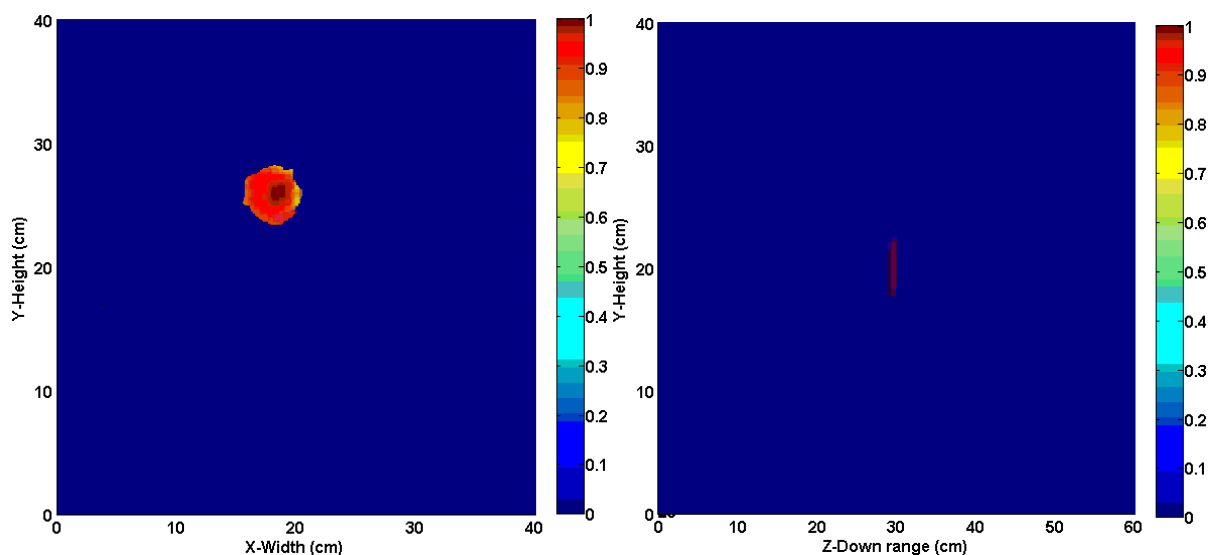
(a) Cross range image by DAS;   (b) Range image by DAS
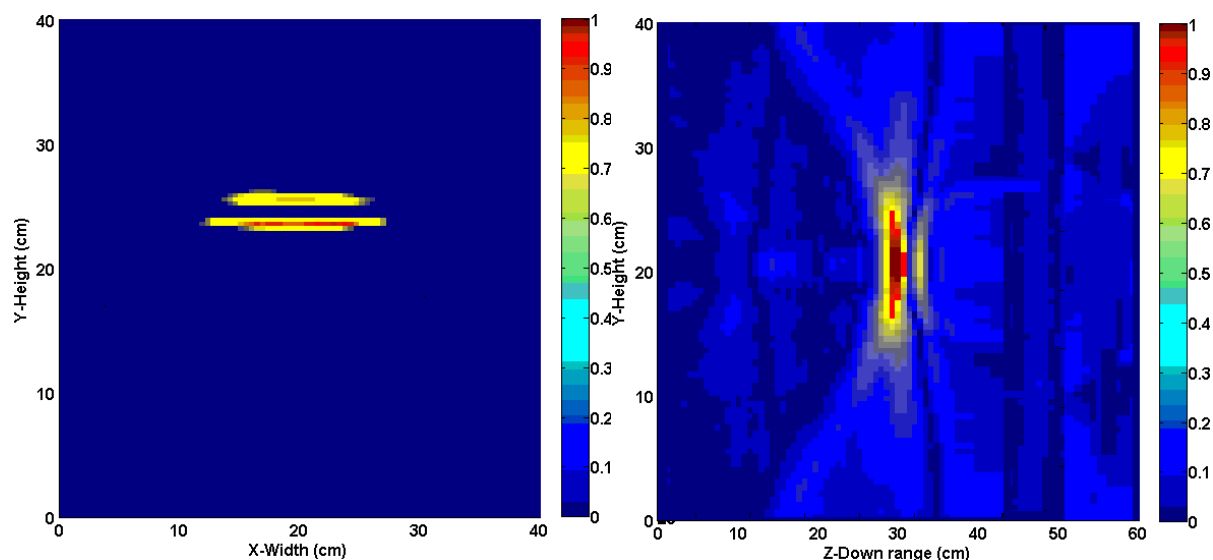
(c) Cross range image by TR;   (d) Range image by TR

Figure 5.10 Images of a single metallic target with the size of 5 x 5 cm^2 placed 30cm away from the receiving array in free space, by DAS and TR

As shown in the above results, both the images by the DAS and TR methods have demonstrated their abilities to image a single metallic rectangular target in different sizes at various distances. The images by the DAS method show better focusing ability than the TR method and can also recover more of the true cross-range area of the target. With the simulated data acquired from CST Microwave studio and the experimental data from related measurements, the error analyses of images by DAS and TR methods can be listed in Table 5.1 and 5.2. The simulation

work is carried out in free space and the detectable range for the target size of 5 x 5 cm^2 can reach 50cm. However, this cannot be realized in experiments due to the noise and signal interferences. It can be concluded that the error rate of range and cross range images by DAS is generally better than those by TR.

Table 5.1 Error analysis of single target imaging in free space by DAS and TR in simulation

Range / Cross Range	20 (cm)				30 (cm)				40 (cm)				50 (cm)			
	DAS	Error	TR	Error	DAS	Error	TR	Error	DAS	Error	TR	Error	DAS	Error	TR	Error
10x10 (cm^2)	10x10	**0%**	12x6	**28%**	10x9	**10%**	13x7	**9%**	9x9.5	**14.5%**	13x8	**4%**	9x9	**19%**	14x10	**40%**
	20	**0%**	20	**0%**	30	**0%**	30	**0%**	40	**0%**	40	**0%**	50	**0%**	50	**0%**
8x8 (cm^2)	8x7	**12.5%**	12x5	**6.25%**	8x8	**0%**	13x6	**21.9%**	8x8	**0%**	14x5	**9.4%**	10x9	40.6%	14x7	53.1%
	20	**0%**	20	**0%**	30	**0%**	30	**0%**	40	**0%**	40	**0%**	50	**0%**	50	**0%**
5x5 (cm^2)	5x4	**20%**	10x3	**20%**	5x5	**0%**	10x3	**20%**	6	20%	12x4	92%	8x8	156%	13x7	264%
	20	**0%**	20	**0%**	30	**0%**	30	**0%**	40	**0%**	40	**0%**	50	**0%**	50	**0%**

Table 5.2 Error analysis of single target imaging in free space by DAS and TR in experiment

Range Cross Range	20 (cm)				30 (cm)				40 (cm)				50 (cm)			
	DAS	Error	TR	Error	DAS	Error	TR	Error	DAS	Error	TR	Error	DAS	Error	TR	Error
10x10 (cm²)	10x9	**10%**	18x6	**8%**	10x7	**30%**	20x7	**40%**	9x7	**39%**	25x8	**100%**	5x5	**75%**	24x6	**44%**
	20	**0%**	21	**5%**	30	**0%**	30	**0%**	40	**0%**	40	**0%**	50	**0%**	51	**2%**
8x8 (cm²)	8x8	**0%**	19x6	**78%**	8x9	**12.5%**	25x4	**56%**	7x8	**12.5%**	21x4	**31%**	Not applicable			
	20	**0%**	19	**5%**	30	**0%**	29	**3%**	40	**0%**	38	**5%**				
5x5 (cm²)	5x5	**0%**	20x3	**140%**	5x5	**0%**	18x3	**112%**	Not applicable				Not applicable			
	20	**0%**	20	**0%**	30	**0%**	28	**7%**								

5.2.2 Two-target imaging in free space

After single target detection, one extra metallic square piece is introduced as the second target in the testing environment. The first metallic piece has a size of 10 x 10 cm^2 and the second target has a size of 8 x 8 cm^2, placed a certain distance away behind the first target., The distance between targets is 15cm and the first target is placed 20cm away from the array, i.e. the same as in the scenario used in Chapter 3. The reflections at four receiving antennas are given in Figure 5.11. Threshold straight lines are drawn in sub-figures to show the two sharp reflections.
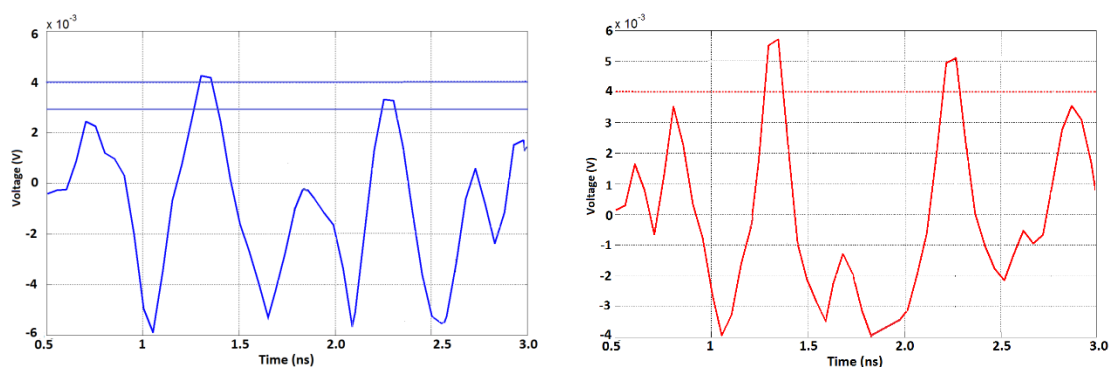
(a) Extracted received signal from antenna one;   (b) Extracted received signal from antenna two
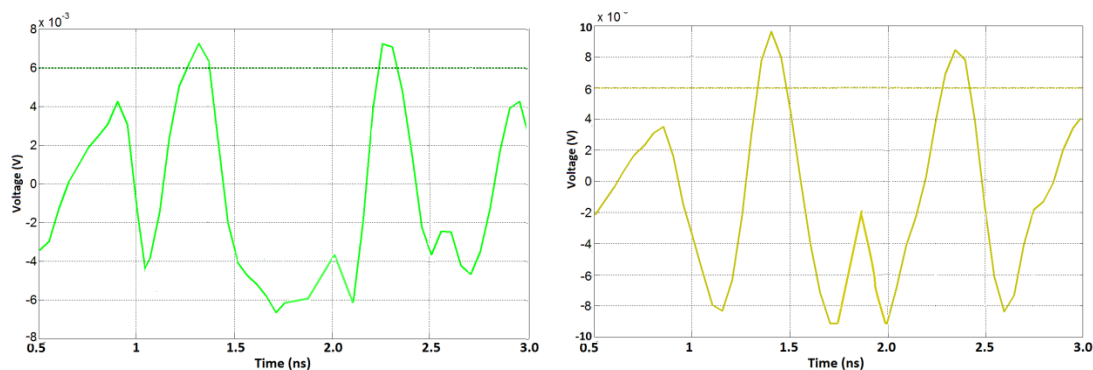
(c) Extracted received signal from antenna three;   (d) Extracted received signal from antenna four

Figure 5-11 Extracted received signals at four receiving antennas from two metallic targets with the size of 10 x 10 cm^2 and 8 x 8 cm^2 with a inner distance of 15cm

In Figure 5.11, the target reflections are shown after the signal calibration. The time difference is expected because there is a distinguishable distance between these two targets. However,

when the distance between targets is shortened and is too close, these two peaks inevitably overlap so as to make the separation of two targets impossible.

The inter distance between the targets can be denoted as "d_y". Different values from 5cm, 10cm to 15cm are used in experiment. DAS and TR imaging methods both are used to recover the images of targets. The first target is firmly fixed at the distance of 20cm away from the array, only the second target is moving forwards or backwards for testing purpose.

When the inter distance is 15cm, DAS and TR methods both can separate two targets successfully, as shown in Figure 5.12. However, when the inter distance is shortened to 10cm, the DAS image starts to produce unreliable estimation and the TR image starts to be weakened, as shown in Figure 5.13. The second smaller target can only be revealed by lowering the threshold value. The result is worse when the space is reduced further to 5cm, as shown in Figure 5.14. Two targets are merged together and become undistinguishable.
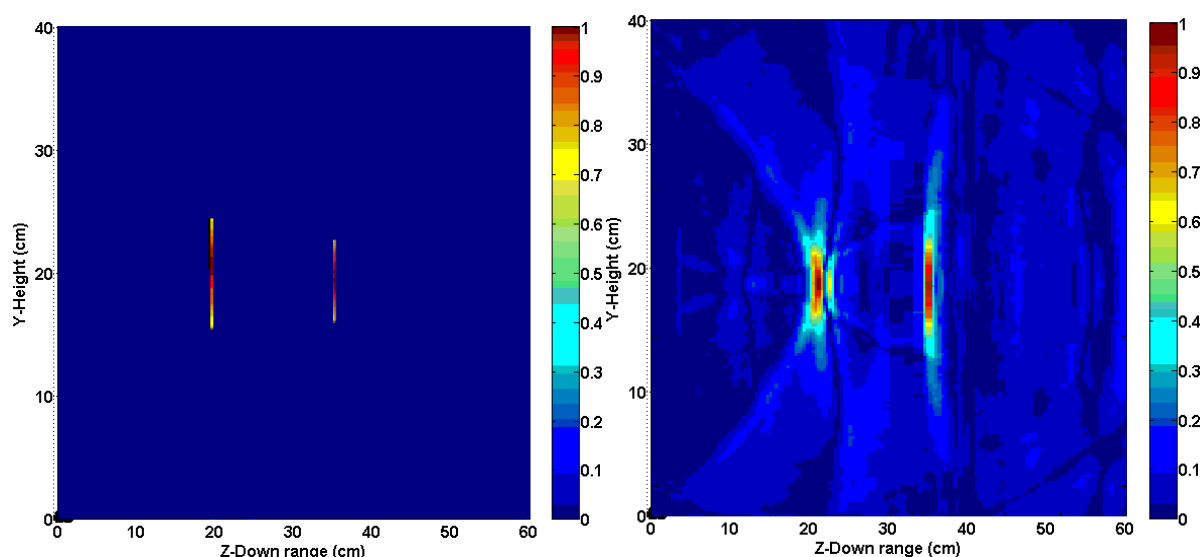
(a) Range image with d_y=15cm by DAS;   (b) Range image with d_y=15cm by TR

Figure 5-12 Images of two metallic targets with the size of 10 x 10 cm^2 and 8 x 8 cm^2 placed with an inter-distance of 15cm in free space, by DAS and TR
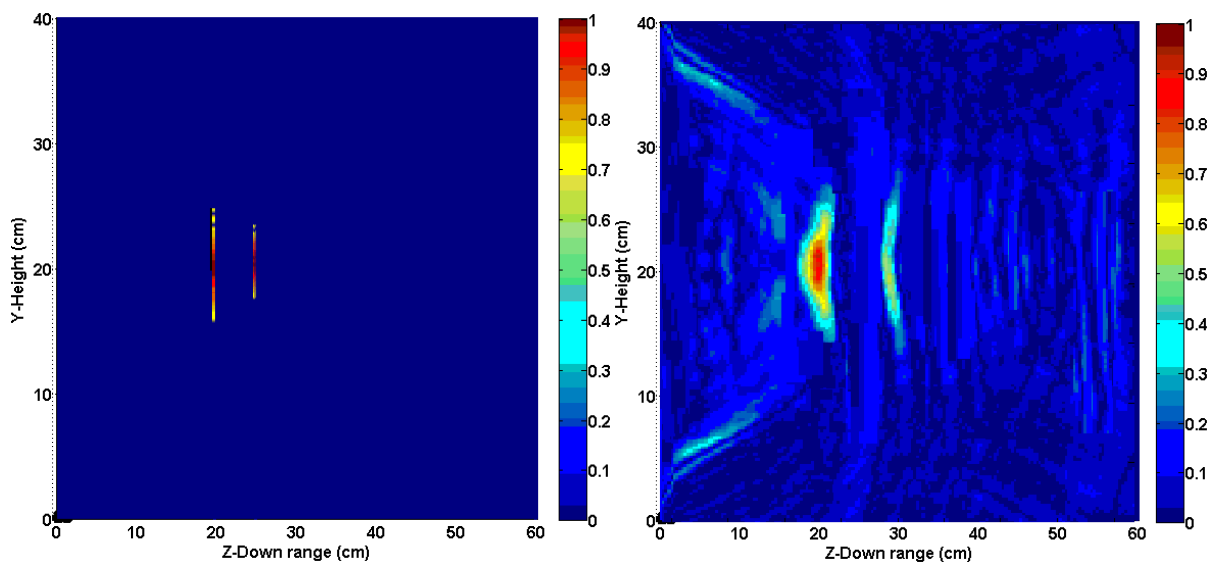
(a) Range image with d_y=10cm by DAS;   (b) Range image with d_y=10cm by TR

Figure 5-13 Images of two metallic targets with the size of 10 x 10 cm^2 and 8 x 8 cm^2 placed with an inter-distance of 10cm in free space, by DAS and TR
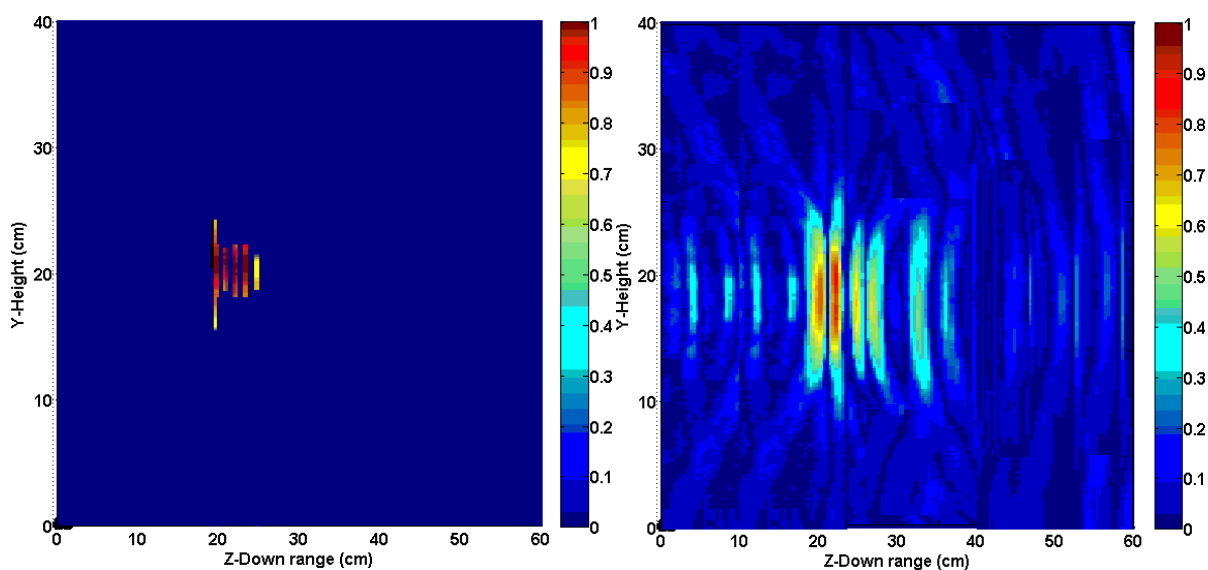
(a) Range image with d_y=5cm by DAS;   (b) Range image with d_y=5cm by TR

Figure 5-14 Images of two metallic targets with the size of 10 x 10 cm^2 and 8 x 8 cm^2 placed with an inter-distance of 5cm in free space, by DAS and TR

The other experimental placement is to arrange both targets side by side in front of the antenna array at the same distance from the array of 20cm. The inter distance between them is varied

from 4cm to, 6cm and 8cm and is denoted as "d_x". DAS and TR images are shown in Figure 5.15, 5.16 and 5.17.

In Figure 5.15, when the inter distance is only 4cm, both images show the lack of clear separation of the two targets. In Figure 5.16, the distance of 6cm has enabled the two images to be distinguishable with imprecise recovery of the shape of the targets. In Figure 5.17, when the distance is 8cm, DAS and TR methods have generated better images of the two targets.

Compared to the theoretical down-range and cross-range resolutions, the estimated images show very close recovery. The error analysis of DAS and TR images for two targets detection in simulation is given in Table 5.3, while the one in experiment in Table 5.4. The error study shows that TR and DAS cannot accurately distinguish two targets placed with dy<15cm/dx<6cm. However, both can achieve satisfactory resolutions when the inter distances are larger than these two values.
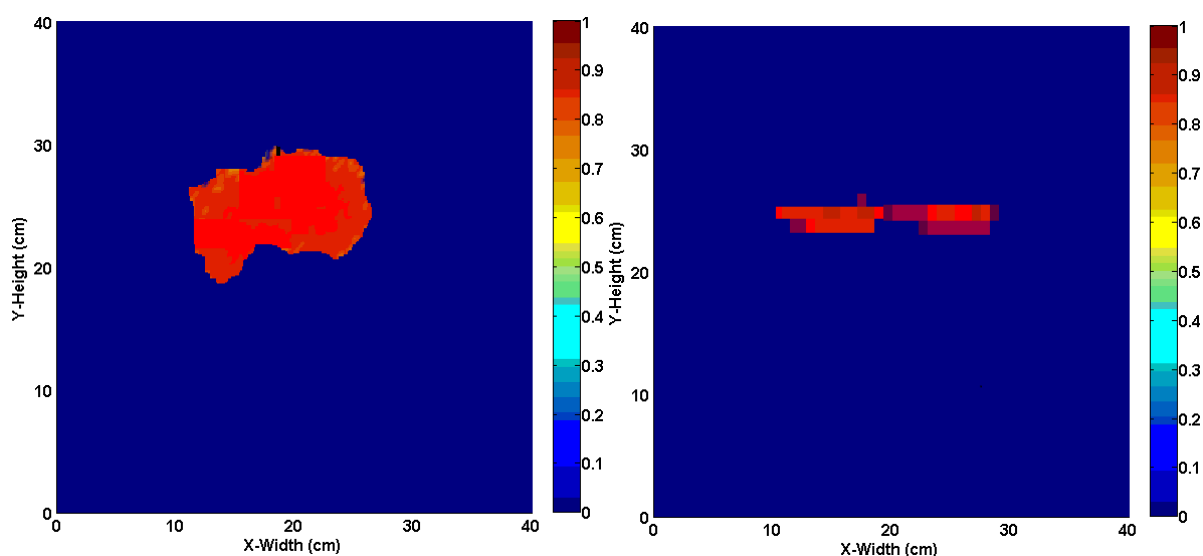
(a) Cross range image with d_x=4cm by DAS;   (b) Cross range image with d_x=4cm by TR

Figure 5-15 Images of two metallic targets with the size of 10 x 10 cm^2 and 8 x 8 cm^2 placed side by side with an inter-distance of 4cm in free space, by DAS and TR
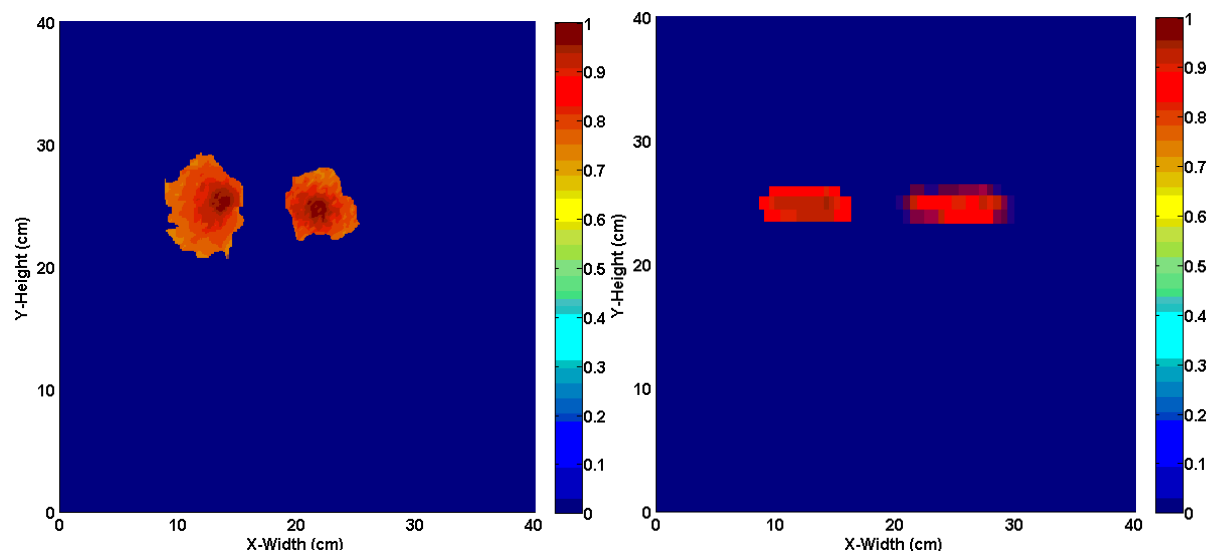
(a) Cross range image with d_x=6cm by DAS; (b) Cross range image with d_x=6cm by TR

Figure 5-16 Images of two metallic targets with the size of 10 x 10 cm^2 and 8 x 8 cm^2 placed side by side with an inter-distance of 6cm in free space, by DAS and TR
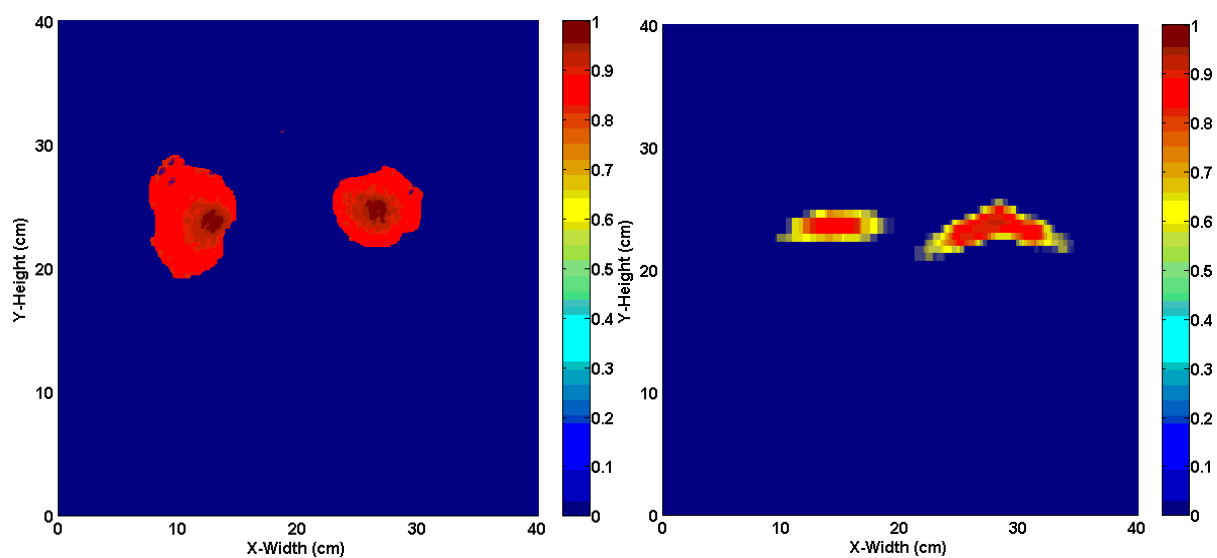
(a) Cross range image with d_x=8cm by DAS; (b) Cross range image with d_x=8cm by TR

Figure 5-17 Images of two metallic targets with the size of 10 x 10 cm^2 and 8 x 8 cm^2 placed side by side with an inter-distance of 8cm in free space, by DAS and TR

Table 5.3 Error analysis of two targets imaging in free space by DAS and TR in experiment

Inner distance d_y=5 (cm)				Inner distance d_y=10 (cm)				Inner distance d_y=15 (cm)			
DAS	Error	TR	Error	DAS	Error	TR	Error	DAS	Error	TR	Error
Non	Non	1cm	80%	6cm	40%	Non	Non	15cm	0%	16cm	6.7%
Inner distance d_x=4 (cm)				Inner distance d_x=6 (cm)				Inner distance d_x=8 (cm)			
DAS	Error	TR	Error	DAS	Error	TR	Error	DAS	Error	TR	Error
Non	Non	Non	Non	5cm	16.7%	5cm	17%	8cm	0%	6cm	25%

Table 5.4 Error analysis of two targets imaging in free space by DAS and TR in simulation

Inner distance d_y=5 (cm)				Inner distance d_y=10 (cm)				Inner distance d_y=15 (cm)			
DAS	Error	TR	Error	DAS	Error	TR	Error	DAS	Error	TR	Error
Non	Non	Non	Non	Non	Non	Non	Non	15cm	0%	14-19cm	0-27%
Inner distance d_x=4 (cm)				Inner distance d_x=6 (cm)				Inner distance d_x=8 (cm)			
DAS	Error	TR	Error	DAS	Error	TR	Error	DAS	Error	TR	Error
Non	Non	Non	Non	6cm	0%	5cm	17%	8cm	0%	7cm	12.5%

5.3 Imaging the targets behind one wooden board

The second scenario is to image the metallic target behind a wooden board, which completely obstructs the line-of-sight signal propagation. The metallic target is the same as the one used above, with a size of 10 x 10 cm^2 and thickness of 1cm. The distance between the target and the antenna array is 20cm and the distance between the wooden board and the antenna array is 10cm. Four compact corrugated BANAs are used as receiving antennas. The wooden board has a size of 58cm (length) by 21.5cm (width) by 1.8cm (thickness). The experimental set-up is shown in Figure 5.18 and reflected signals after the differentiation are given in Figure 5.19. Compared to the reflected signals from the single target in free space, the recorded time of arrival consistently increases by an amount from 0.035ns to 0.045ns. This change is to be expected due to the time delay caused by the wooden board.
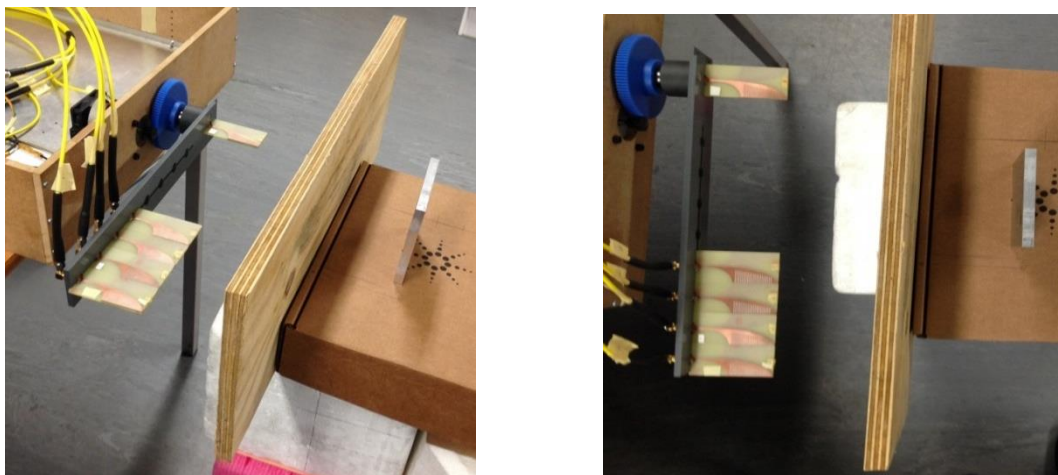
(a) Experimental set-up with a wooden board and a metallic target;   (b) Bird view of the set-up

Figure 5-18 Experimental set-up of one metallic target place behind one wooden board
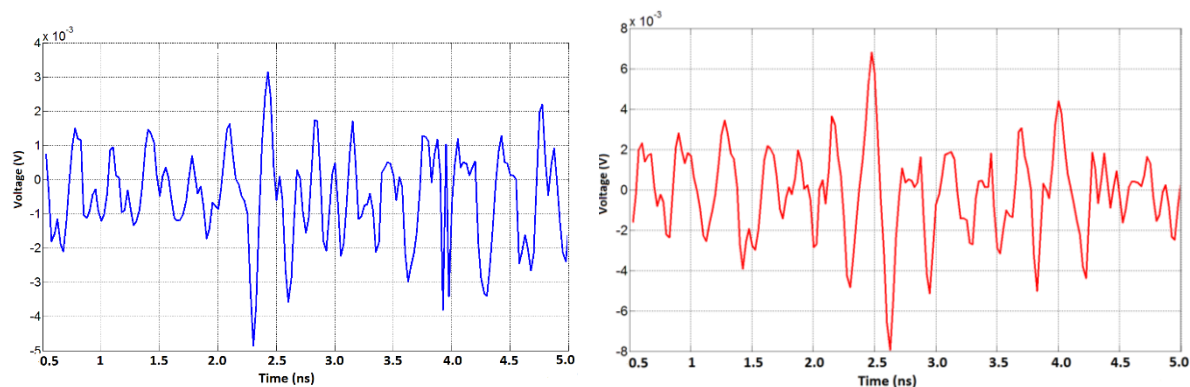
(a) Extracted received signal from antenna one; (b) Extracted received signal from antenna two
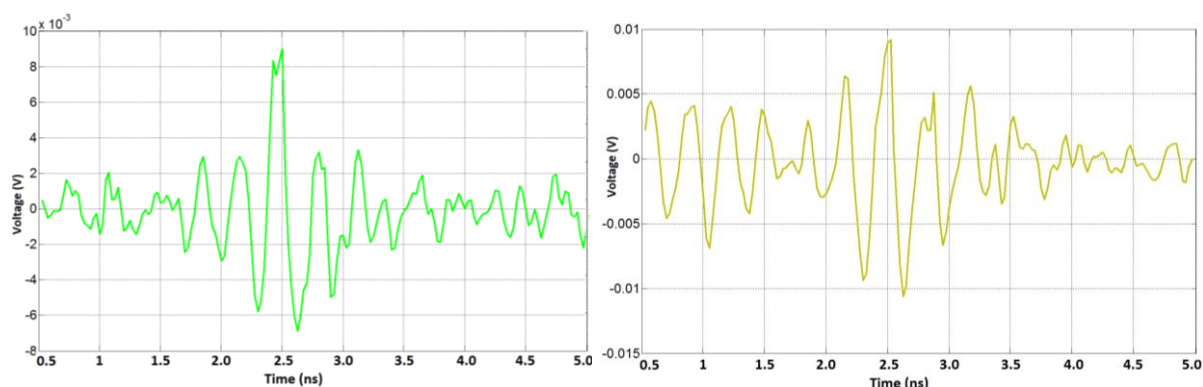
(c) Extracted received signal from antenna three; (d) Extracted received signal from antenna four

Figure 5-19 Experimental extracted received signals from one metallic target placed behind a wooden board after differentiation

5.3.1 Single target imaging behind a wooden board

In comparison with the imaging in free space, the presence of the wooden board has reduced the effective target signal. Therefore, the target with the size of 5 x 5 cm^2 is no longer able to be recovered. So in practice, a target of 10 x 10 cm^2 is put under test behind the wooden board. The inter distance between the wooden board and the metallic target is altered from 10cm; 20cm to 30cm. DAS and TR methods are used to recover the images of the target, as shown in Figure 5.20, 5.21 and 5.22. Similarly, one metallic piece with the size of 8cm by 8cm is used as the target with a furthest detectable down range of 40cm away from the antenna array, as shown in Figure 5.23.

The images have shown that the range information can be clearly recovered. When the target is moved away from the antenna array, the received signal level starts to drop, thus leaving the length of the highlighted range image shrinking in both images by DAS and TR. In comparison, DAS method can achieve better range detection accuracy because the recovered images can focus more sharply and be closer to the real length of the target. However, the location of the targets starts to shift slightly inward towards the boards. Images by TR tend to focus more when the target is placed further away, but in general, have much wider range estimation. The influence of the wooden board can be seen as the yellowish part and can be cancelled out by adjusting the colour threshold level.

Images by DAS also show better cross range estimation than the ones by TR. Images by TR are generally flatter but have improved in comparison with themselves in free space imaging. In both cases the recovered images tend to be elliptical.
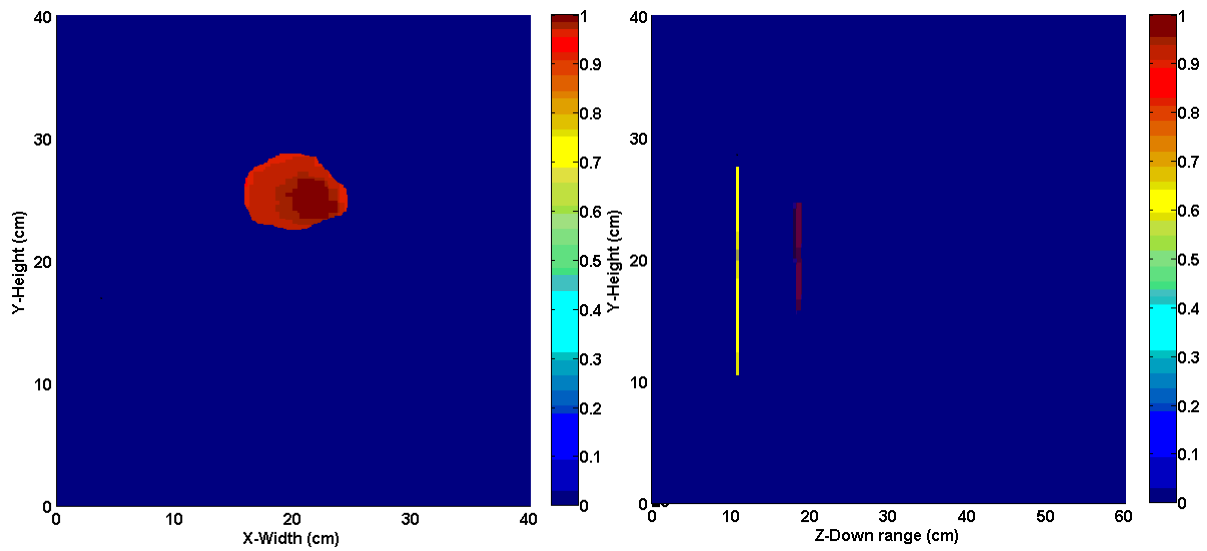
(a) Cross range image by DAS; (b) Range image by DAS
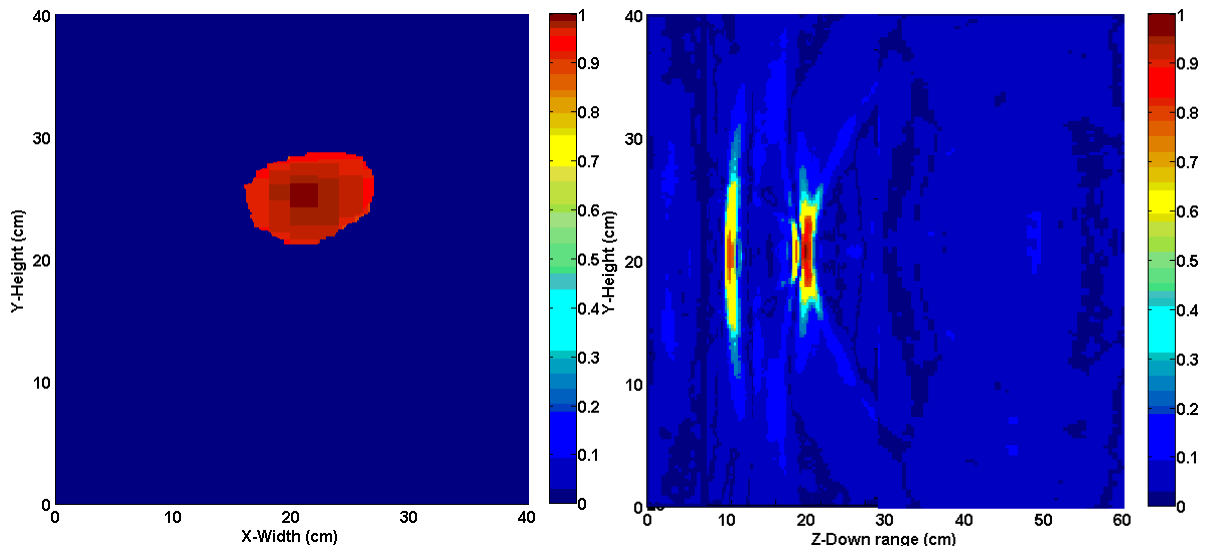
(c) Cross range image by TR; (d) Range image by TR

Figure 5-20 Images of a single metallic target with the size of 10 x 10 cm^2, placed 20cm away from the receiving array, and behind a wooden board, by DAS and TR

(a) Cross range image by DAS;

(b) Range image by DAS

(c) Cross range image by TR;
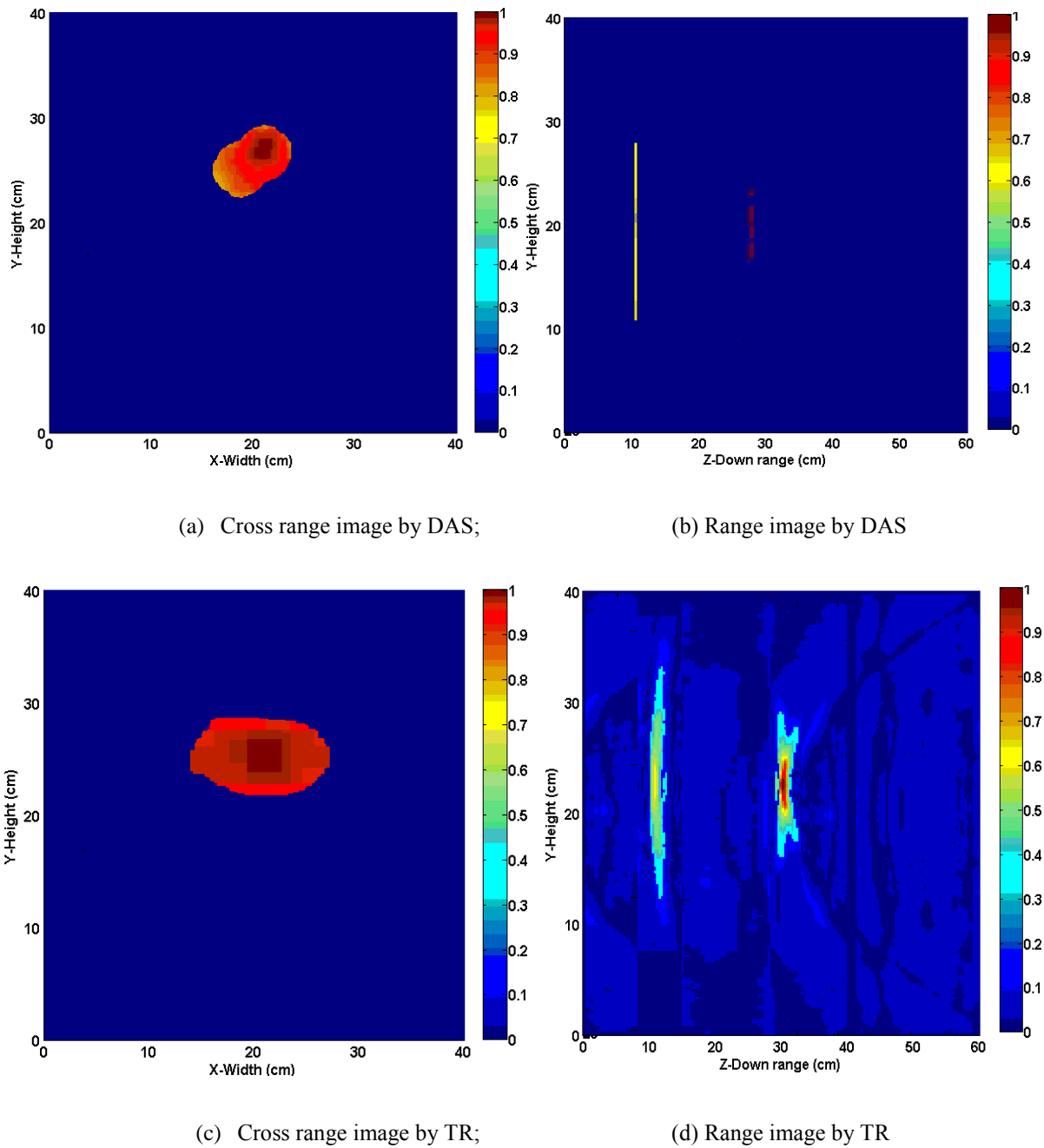
(d) Range image by TR

Figure 5-21 Images of a single metallic target with the size of 10 x 10 cm^2, placed 30cm away from the receiving array, and behind a wooden board, by DAS and TR
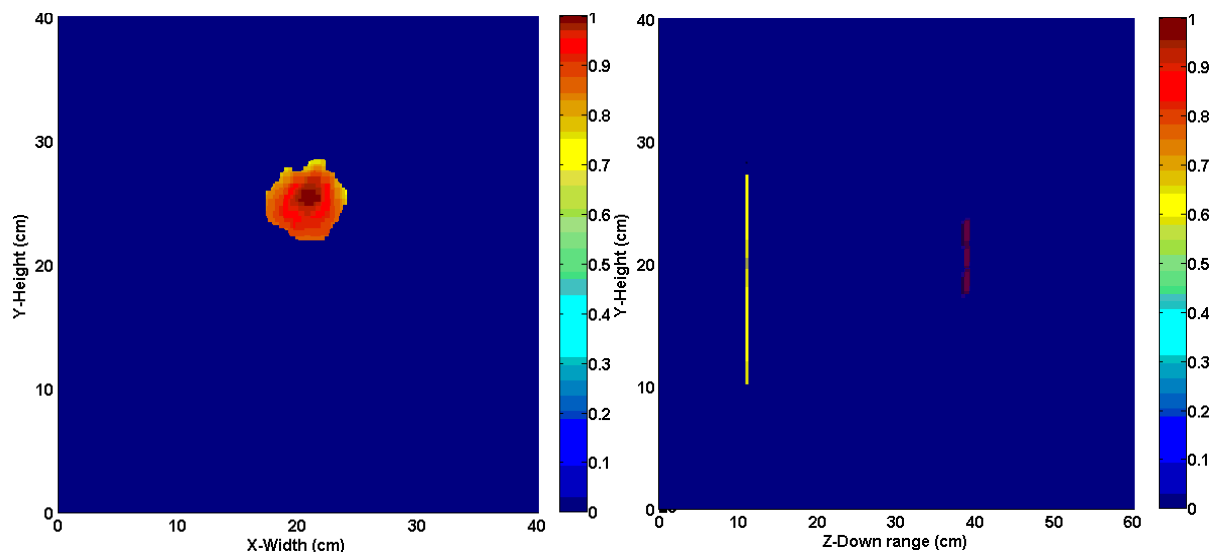
(a) Cross range image by DAS;   (b) Range image by DAS
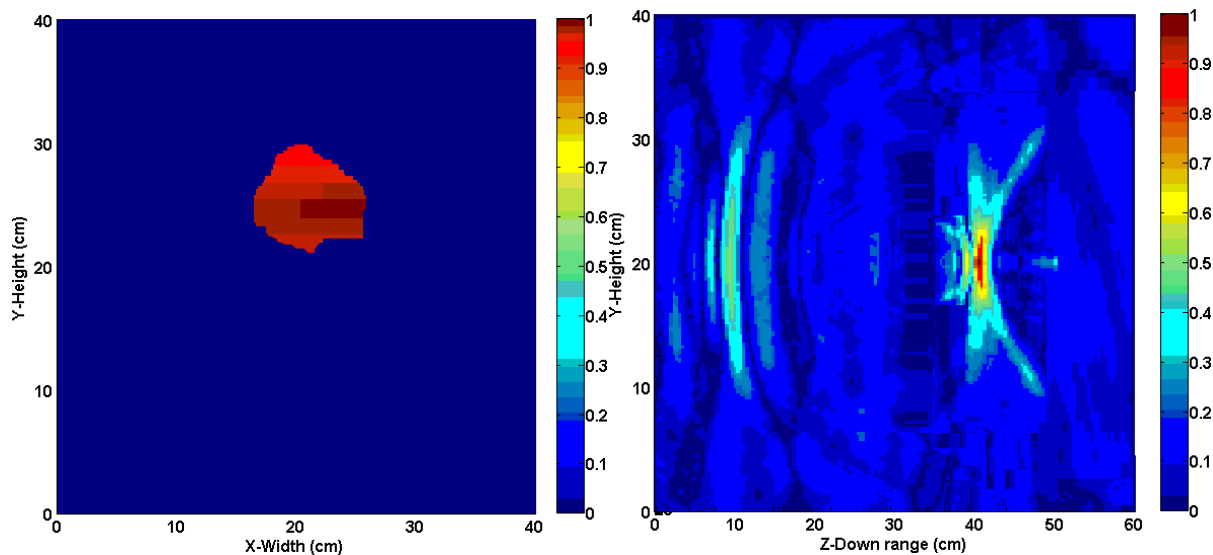
(c) Cross range image by TR;   (d) Range image by TR

Figure 5-22 Images of a single metallic target with the size of 10 x 10 cm^2, placed 40cm away from the receiving array, and behind a wooden board, by DAS and TR
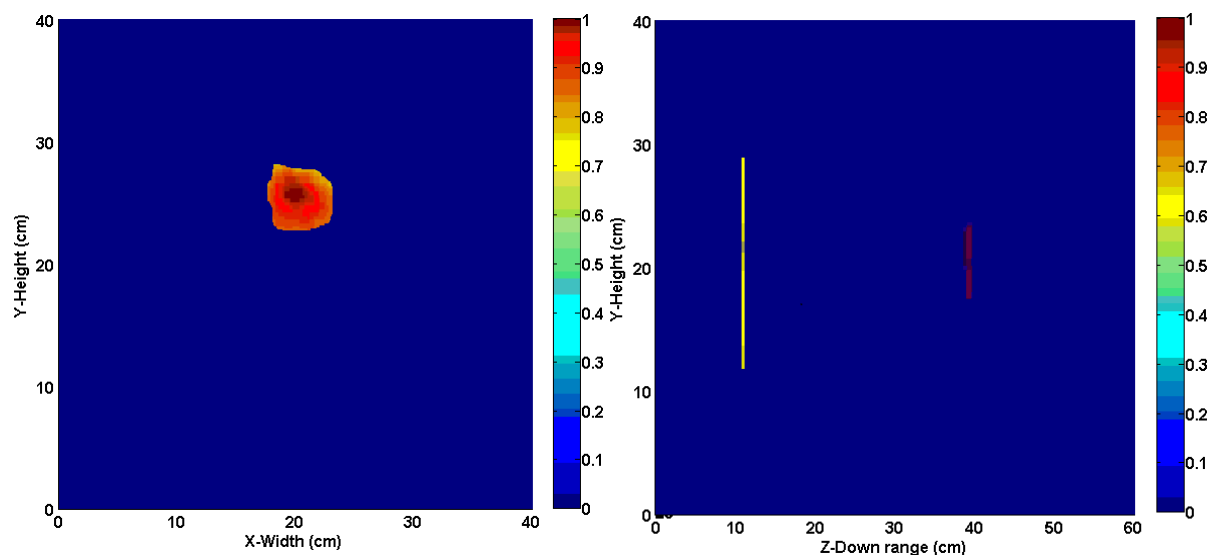
(a) Cross range image by DAS;   (b) Range image by DAS
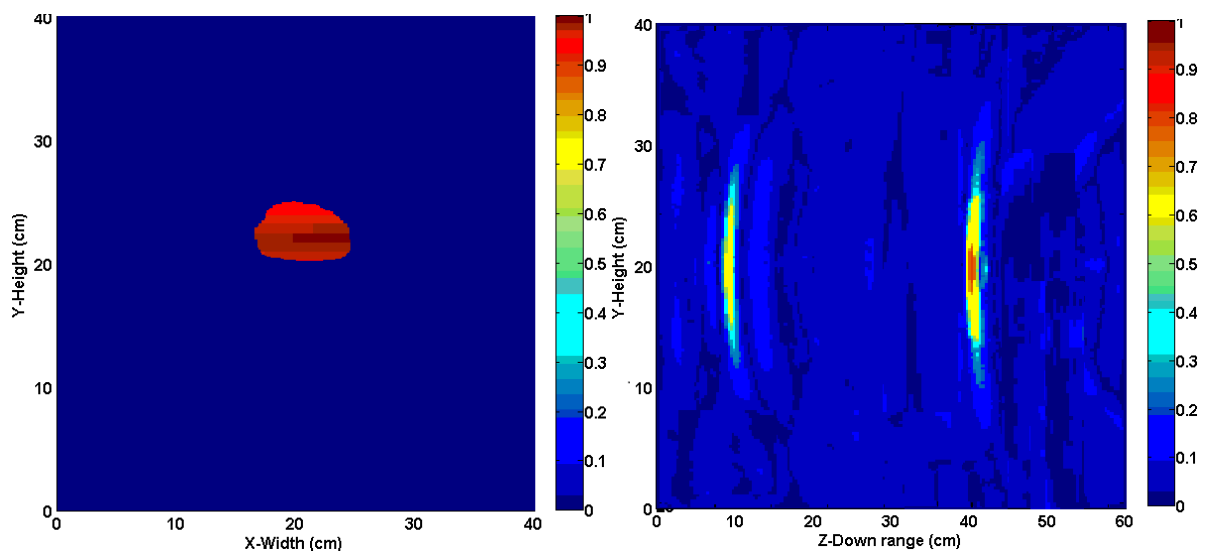
(c) Cross range image by TR;   (d) Range image by TR

Figure 5-23 Images of a single metallic target with the size of 8 x 8 cm², placed 40cm away from the receiving array, and behind a wooden board, by DAS and TR

The error analysis of the images by DAS and TR is given in Table 5.5. Some new observations can be concluded here. When the target with the size of 10 x 10 cm² is chosen, the cross range and range errors in images by TR are much less than DAS. When the target size is smaller, error rates by TR are larger than the ones by DAS when the detecting range is 20cm and 30cm, but the opposite for 40cm. This fluctuation shows that the introduction of the wooden board has enabled the TR method, in some cases, to produce better results than DAS, which is an

improvement in comparison with the situation in free space. The error analysis in simulation is shown in Table 5.6 for validation of the experimental results.

Table 5.5 Error analysis of one target imaging behind a wooden board by DAS and TR in experiments

Range / Cross Range	20 (cm)				30 (cm)				40 (cm)			
	DAS	Error	TR	Error	DAS	Error	TR	Error	DAS	Error	TR	Error
10x10 (cm²)	8x7	**44%**	15x9	**35%**	9.2x7	**35.6%**	14.2x8.5	**20.7%**	8.5x8	**32%**	11.5x9	**3.5%**
	20	**0%**	20	**0%**	28	**6.7%**	30	**0%**	39	**2.5%**	40	**0%**
8x8 (cm²)	7.4x8	**7.5%**	9.2x4	**42.5%**	6.2x8	**22.5%**	9.2x4	**42.5%**	5x5	**61%**	10x5	**21.9%**
	19	**5%**	20	**0%**	29	**3.3%**	30	**0%**	39	**2.5%**	40	**0%**

Table 5.6 Error analysis of one target imaging behind a wooden board by DAS and TR in simulation

Range / Cross Range	20 (cm)				30 (cm)				40 (cm)			
	DAS	Error	TR	Error	DAS	Error	TR	Error	DAS	Error	TR	Error
10x10 (cm^2)	10x9	**10%**	15x10	**50%**	11x10	**10%**	14x9	**26%**	12x15	**80%**	10x12	**20%**
	20	**0%**	20	**0%**	30	**0%**	30	**0%**	40	**0%**	40	**0%**
8x8 (cm^2)	10x8	**25%**	12x8	**50%**	10x8	**25%**	10x7	**9%**	8x6	**25%**	10x12	**87.5%**
	20	**0%**	20	**0%**	30	**0%**	30	**0%**	40	**0%**	40	**0%**

5.3.2 Two-target imaging behind a wooden board

As in the experiment in free space, two metallic targets are used in this measurement behind a wooden board. The sizes of the targets are 10 x 10 cm^2 and 8 x 8 cm^2. The inter distance "d_x" between the two targets is set to change from 4cm, 6cm to 8cm, and the inter distance "d_y" between the two targets varies from 5cm, 10cm to 15cm. In the presence of two targets, the wooden board is fixed at a range distance of 10cm from the array and obstructs line-of-sight signal propagations between the target and the antenna array. The first set of images shows two targets placed one behind the other at a distance of 5cm, 10cm and 15cm each in Figures 5.24, 5.25 and 5.26. The second set shows two targets placed in a row with a gap of 4cm, 6cm and 8cm, as given in Figures 5.27, 5.28 and 5.29.

While the inter distance is increasing, the range information of both targets becomes clearer and more accurate. When "d_y" is as short as 5cm, images of two targets start to add up and overlap. When "d_y" is 10cm, two targets begin to separate with uncertain blurring in the middle

gap. When "d_y" reaches 15cm, two targets are visibly clear and the images become reliable. TR images have the similar tendency but with less accuracy in the estimation of the target's true dimension.

When the two targets are separated with a "d_x" of 4cm, the DAS method cannot distinguish them. However, TR images show slightly better results. When "d_x" is increased to 6cm and then 8cm, both images by DAS and TR can show good separation of two targets.
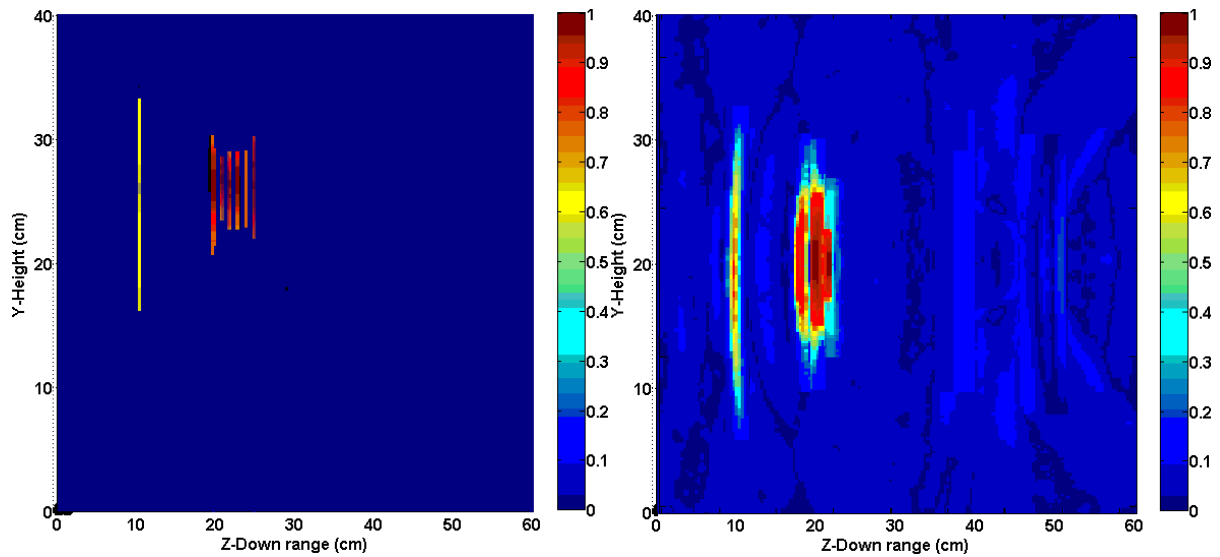
(a) Range of two targets with d_y =5cm by DAS;   (b) Range of two targets with d_y =5cm by TR

Figure 5-24 Images of two metallic targets with the size of 10 x 10 cm^2 and 8 x 8 cm^2 placed one behind the other with d_y =5cm behind a wooden board, by DAS and TR
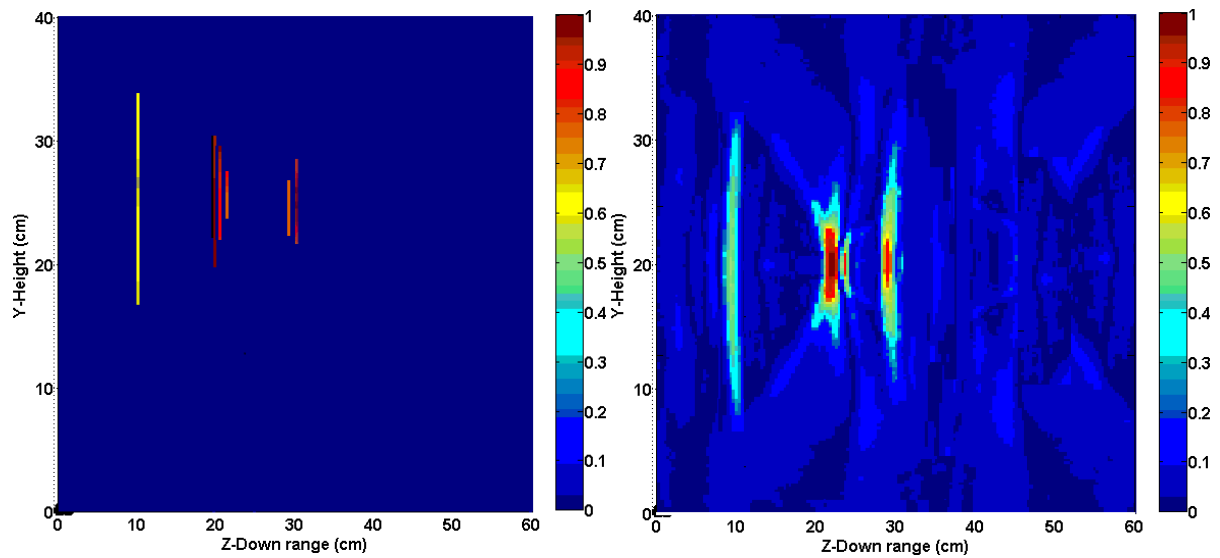
(a) Range of two targets with d_y=10cm by DAS;   (b) Range of two targets with d_y =10cm by TR

Figure 5-25 Images of two metallic targets with the size of 10 x 10 cm^2 and 8 x 8 cm^2 placed one behind the other with d_y =10cm behind a wooden board, by DAS and TR
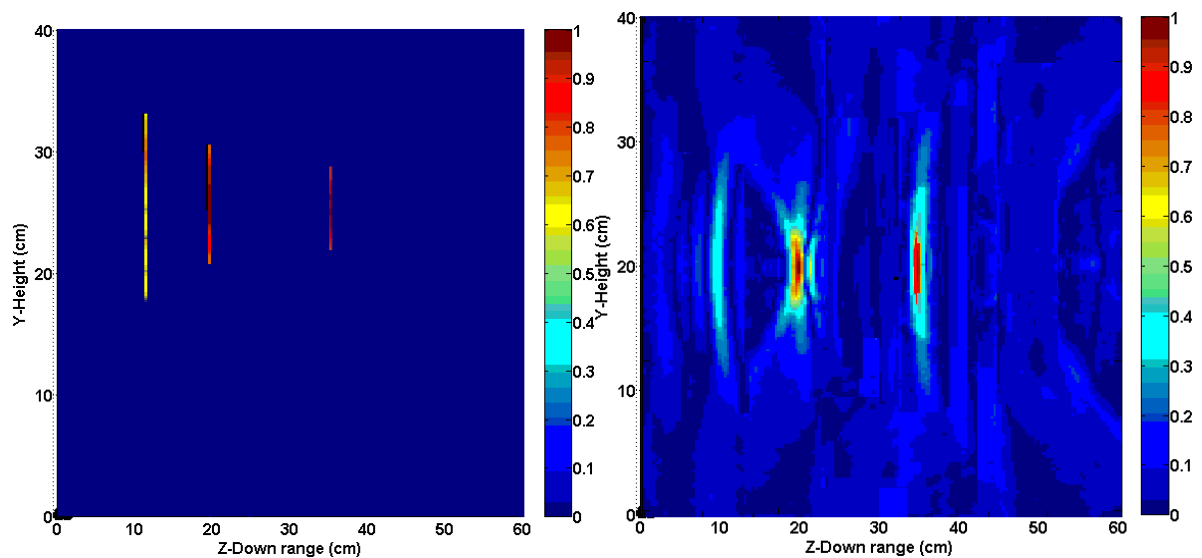
(a) Range of two targets with d_y =15cm by DAS;   (b) Range of two targets with d_y =15cm by TR

Figure 5-26 Images of two metallic targets with the size of 10 x 10 cm^2 and 8 x 8 cm^2 placed one behind the other with d_y =15cm behind a wooden board, by DAS and TR
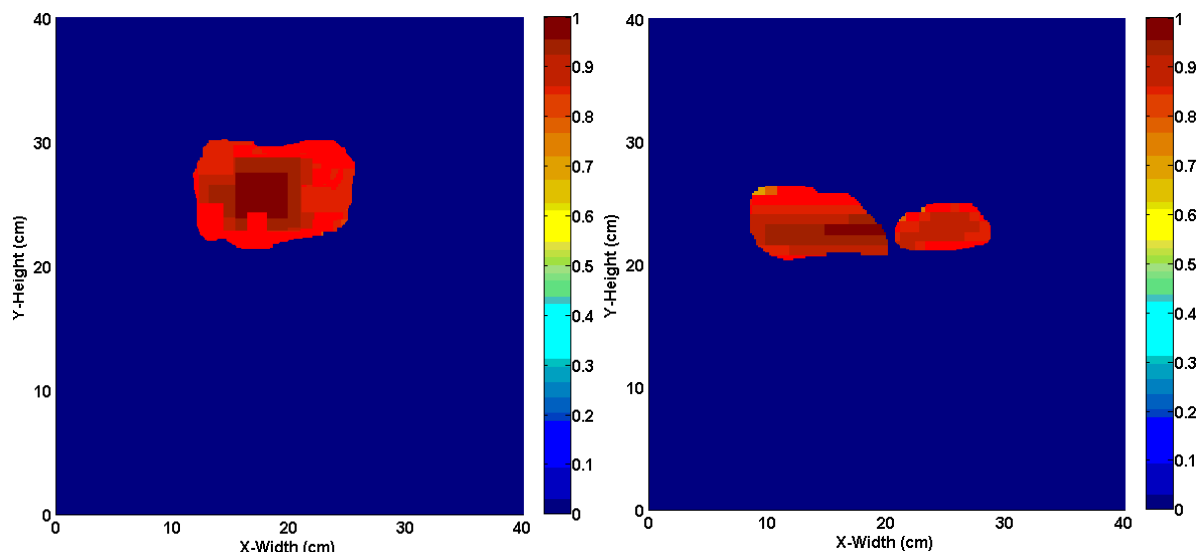
(a) Cross range of two targets with d_x=4cm by DAS;   (b) Cross range of two targets with d_x=4cm by TR

Figure 5-27 Images of two metallic targets with the size of 10 x 10 cm^2 and 8 x 8 cm^2 placed in a row with d_x=4cm behind a wooden board, by DAS and TR
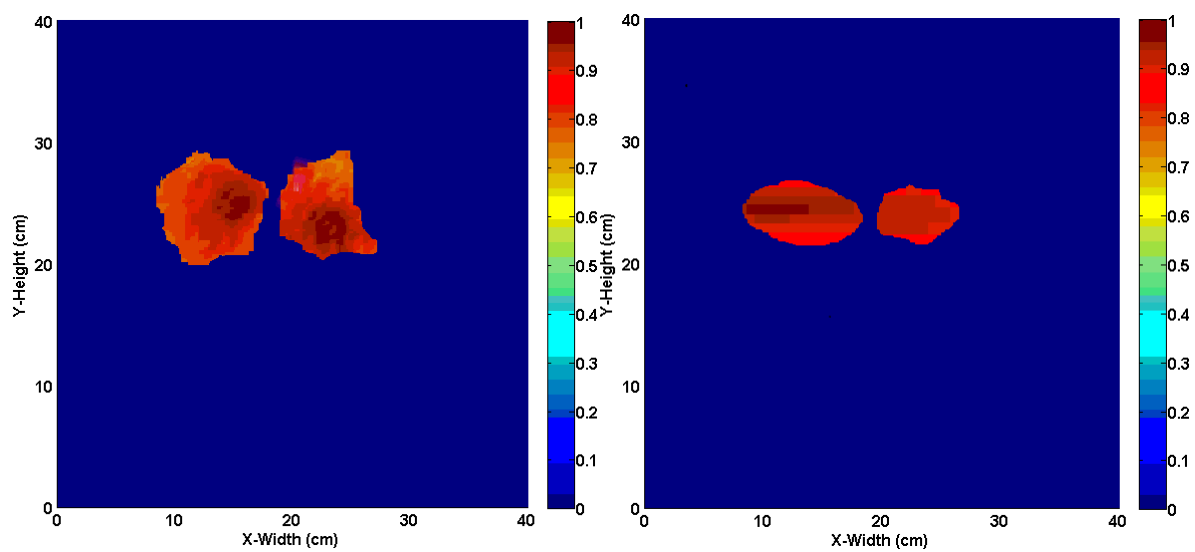
(a) Cross range of two targets with d_x=6cm by DAS;   (b) Cross range of two targets with d_x=6cm by TR

Figure 5-28 Images of two metallic targets with the size of 10 x 10 cm^2 and 8 x 8 cm^2 placed in a row with d_x=6cm behind a wooden board, by DAS and TR
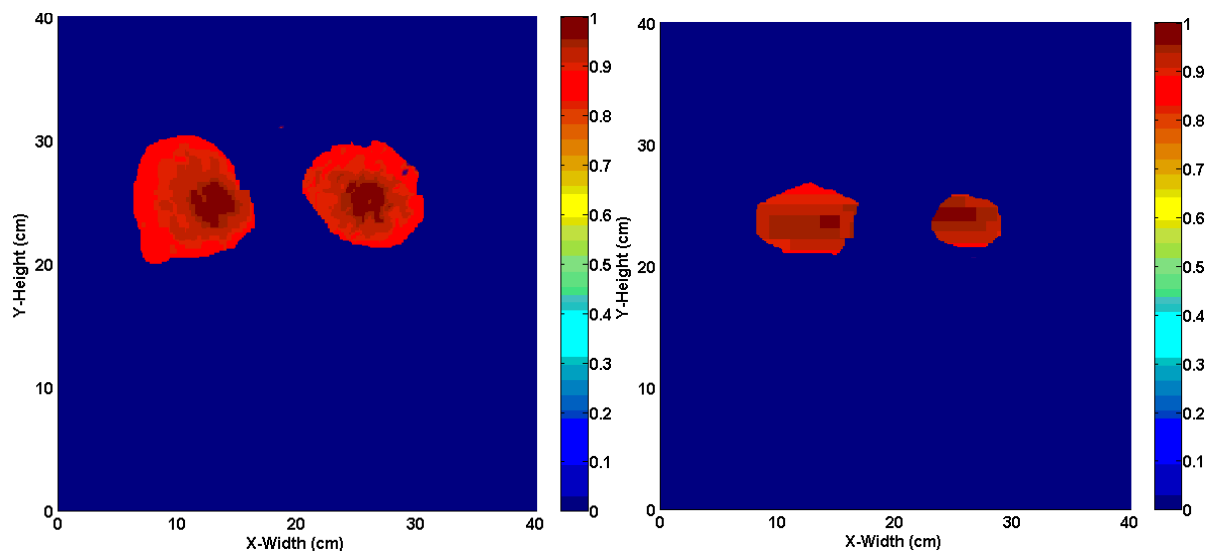
(a) Cross range of two targets with d_x=8cm by DAS; (b) Cross range of two targets with d_x=8cm by TR

Figure 5-29 Images of two metallic targets with the size of 10 x 10 cm^2 and 8 x 8 cm^2 placed in a row with d_x=8cm behind a wooden board, by DAS and TR

Table 5.7 Error analysis of two targets imaging behind a wooden board by DAS and TR in experiments

Inner distance d_y=5 (cm)				Inner distance d_y =10 (cm)				Inner distance d_y =15 (cm)			
DAS	Error	TR	Error	DAS	Error	TR	Error	DAS	Error	TR	Error
Non	Non	Non	Non	Non	Non	Non	Non	16cm	6.7%	16cm	6.7%
Inner distance d_x=4 (cm)				Inner distance d_x=6 (cm)				Inner distance d_x=8 (cm)			
DAS	Error	TR	Error	DAS	Error	TR	Error	DAS	Error	TR	Error
Non	Non	1cm	75%	2cm	66.7%	3cm	50%	5.5cm	31.3%	7cm	12.5%

Table 5.8 Error analysis of two targets imaging behind a wooden board by DAS and TR in simulation

Inner distance d_y=5 (cm)				Inner distance d_y =10 (cm)				Inner distance d_y =15 (cm)			
DAS	Error	TR	Error	DAS	Error	TR	Error	DAS	Error	TR	Error
Non	Non	Non	Non	Non	Non	Non	Non	15cm	0%	12cm	20%
Inner distance d_x=4 (cm)				Inner distance d_x=6 (cm)				Inner distance d_x=8 (cm)			
DAS	Error	TR	Error	DAS	Error	TR	Error	DAS	Error	TR	Error
Non	Non	3cm	25%	1cm	83.3%	5cm	16.7%	7cm	12.5%	7cm	12.5%

The error analyses of the images by DAS and TR for two targets placed behind the wooden board in experiment and simulation are given in Table 5.7 and 5.8 as shown above. Neither method can produce separated reliable images when two targets are placed one behind the other until the inter distance "d_y" reaches 15cm. When two targets are placed in a row as close as 4cm, the DAS method fails to show the separation and the TR method produces an image with very high error rate. When "d_x" increases to 6cm and 8cm, the error rates by DAS and TR methods both decrease and the TR method can achieve a better error rate.

5.4 Testing with targets in clutters

The third scenario is an artificial multipath environment created by a large number of metal rods. The dimension of the each rod is 13cm (height) by 1cm (width) by 0.3cm (length) and its electrical length is twice the wavelength (6cm) of the centre operating frequency (5GHz). The array of metal rods with a matrix of 7 by 5 occupies a 2D dimension of 30cm by 24cm. The horizontal inter distance between the rods in the array is 5.5cm and their vertical size is 6cm. The aim of the set-up is to make use of the rods to create interference with the propagating

signals relevant to the target placed within the rods at various locations. The experimental set-up of the rods array is given in Figure 5.30 and the simulation model in CST Microwave Studio is given in Figure 5.31.
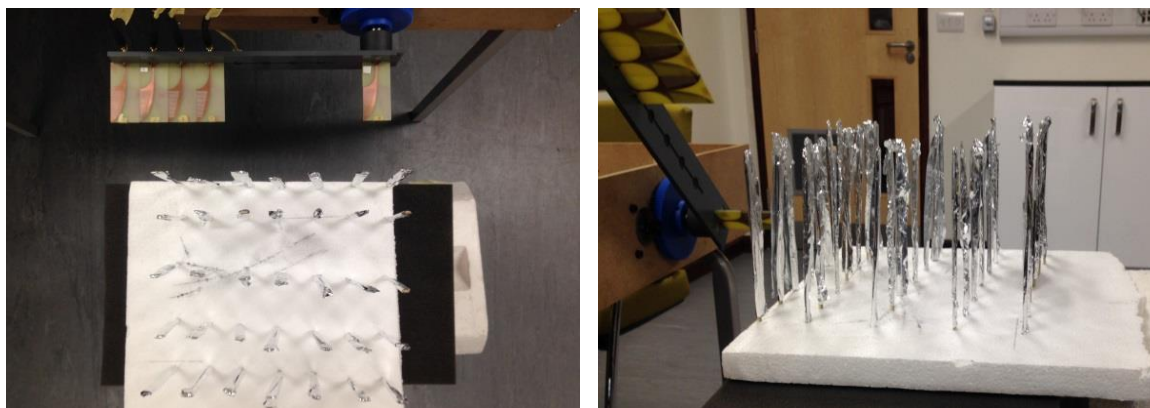
(a) Bird's eye view of experimental set-up with rods; (b) Side view of the rods with rotating antenna array

Figure 5-30 The experimtntal set-up of rods in testing environment
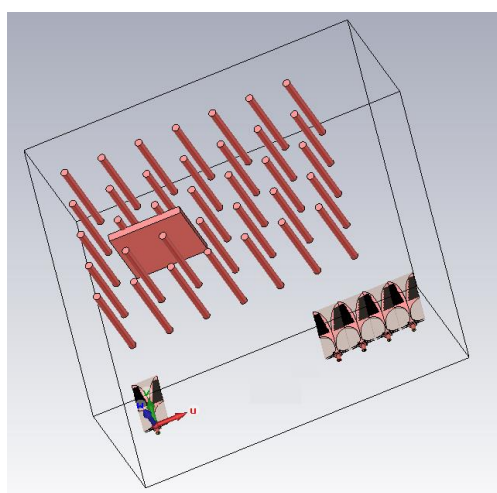
Figure 5-31 The model of the rods in simulation

In experiment, the rods have a great impact on the reflected signals. The extracted signals after the differentiation are shown in Figure 5.32. There are a few major changes in comparison with the counterparts in previous experiments. First, the target signature is further weakened. The peak time, which should point to the exact spatial location of the target, starts to shift, to be divided or to be buried. The received signal voltage levels continue to decrease by 20%. The blurring of the time peaks keeps deteriorating the target signal, making it difficult to use a

concise and simple window function in the DAS algorithm. However, this does not have an effect on the signal processing in the TR method.
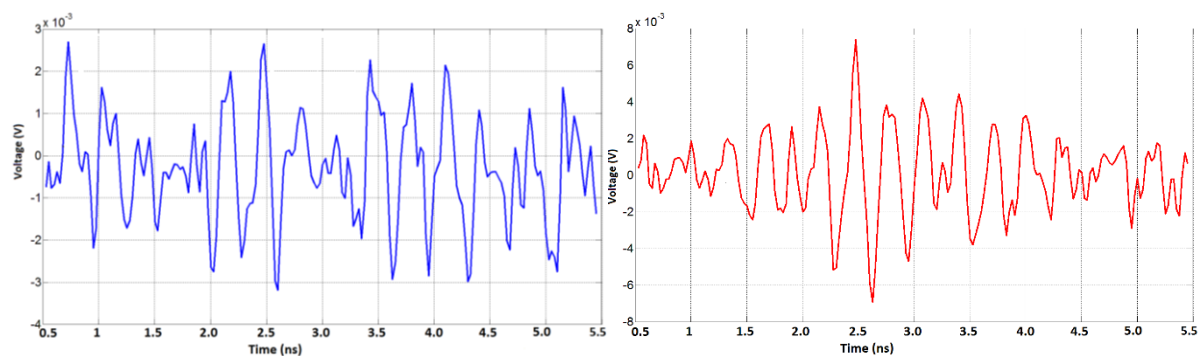
(a) Extracted received signal from antenna one; (b) Extracted received signal from antenna two
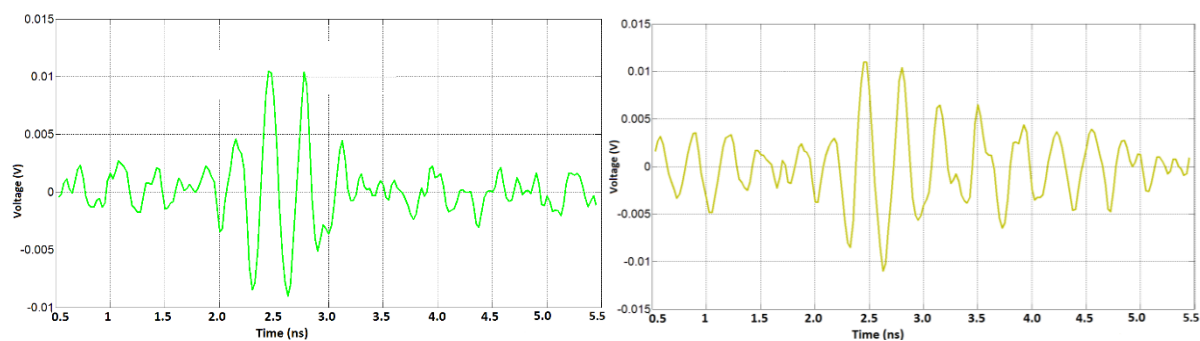
(c) Extracted received signal from antenna three; (d) Extracted received signal from antenna four

Figure 5-32 Experimental extracted received signals from one metallic target of 10 x 10 cm^2 placed 20cm away from the antenna array inside an array of metal rods

5.4.1 One target imaging in an array of metal rods

In the set-up, the target with the size 10 x 10 cm^2 is placed inside the rods. Three locations are chosen as the distance between the target and the array of metal rods: 20cm, 30cm and 40cm. DAS and TR methods are used to recover the images of the target, as shown in Figures 5.33, 5.34 and 5.35.
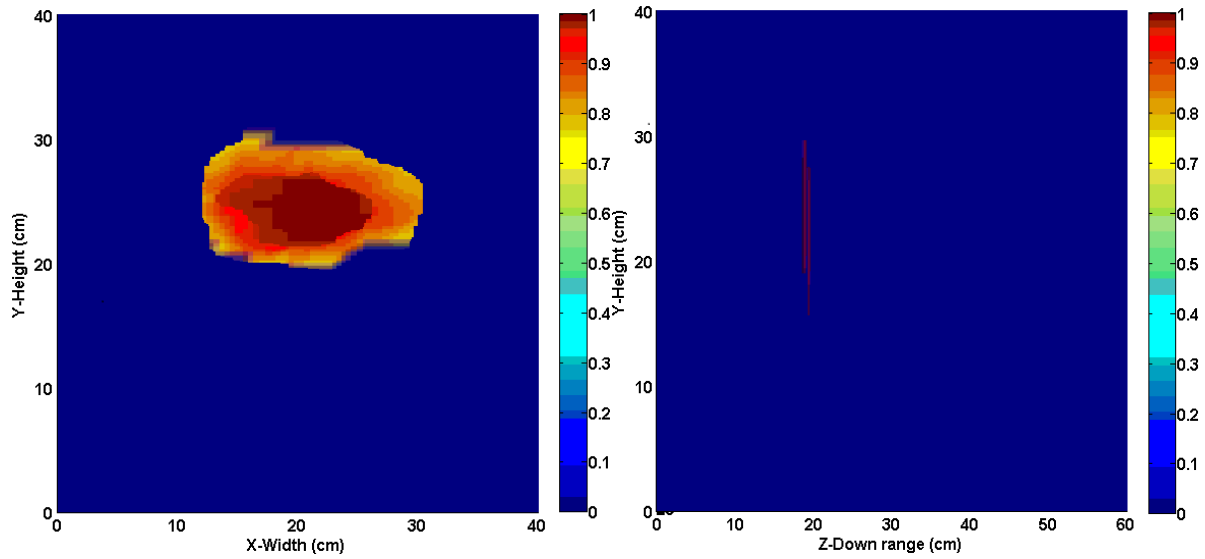
(a) Cross range image by DAS;   (b) Range image by DAS
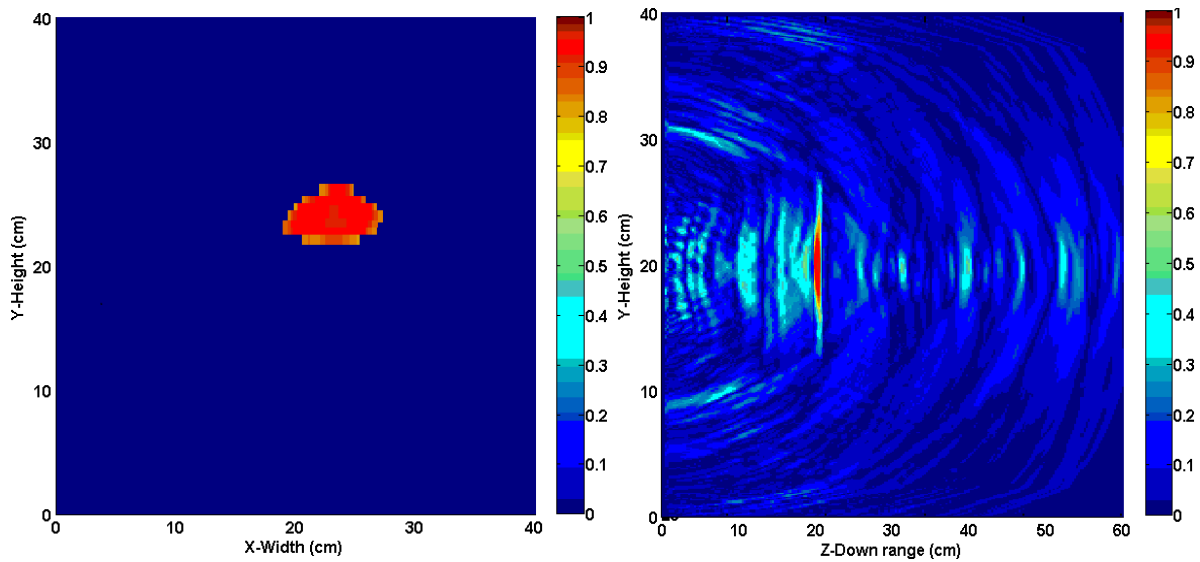
(c) Cross range image by TR;   (d) Range image by TR

Figure 5-33 Images of one metallic target with the size of 10 x 10 cm^2, placed 20cm away from the receiving array in an array of metal rods, by DAS and TR
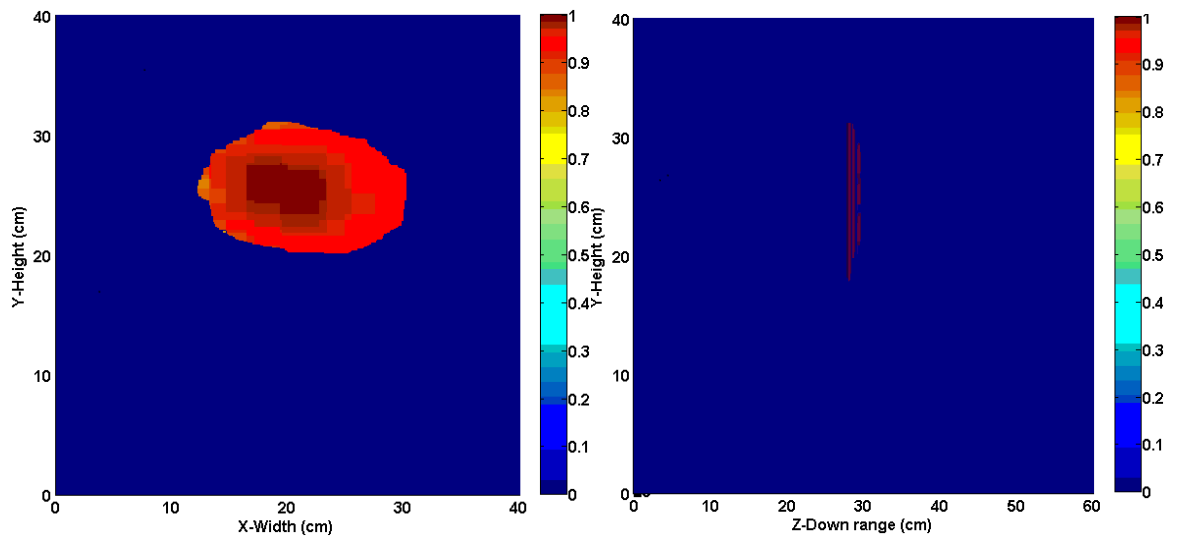
(a) Cross range image by DAS; (b) Range image by DAS
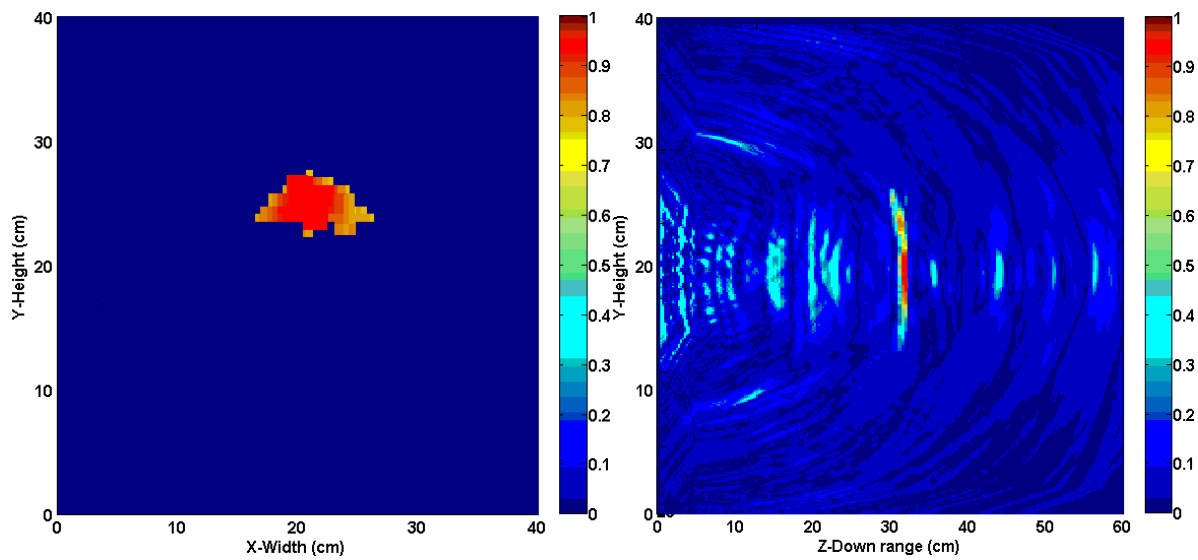
(c) Cross range image by TR; (d) Range image by TR

Figure 5-34 Images of one metallic target with the size of 10 x 10 cm², placed 30cm away from the receiving array in an array of metal rods, by DAS and TR
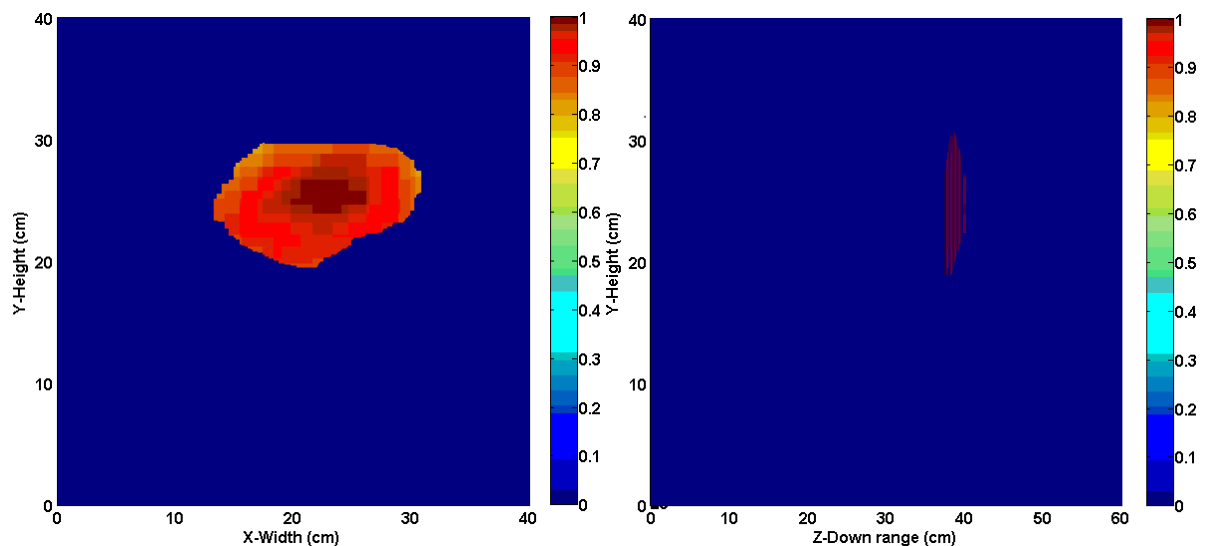
(a) Cross range image by DAS;   (b) Range image by DAS
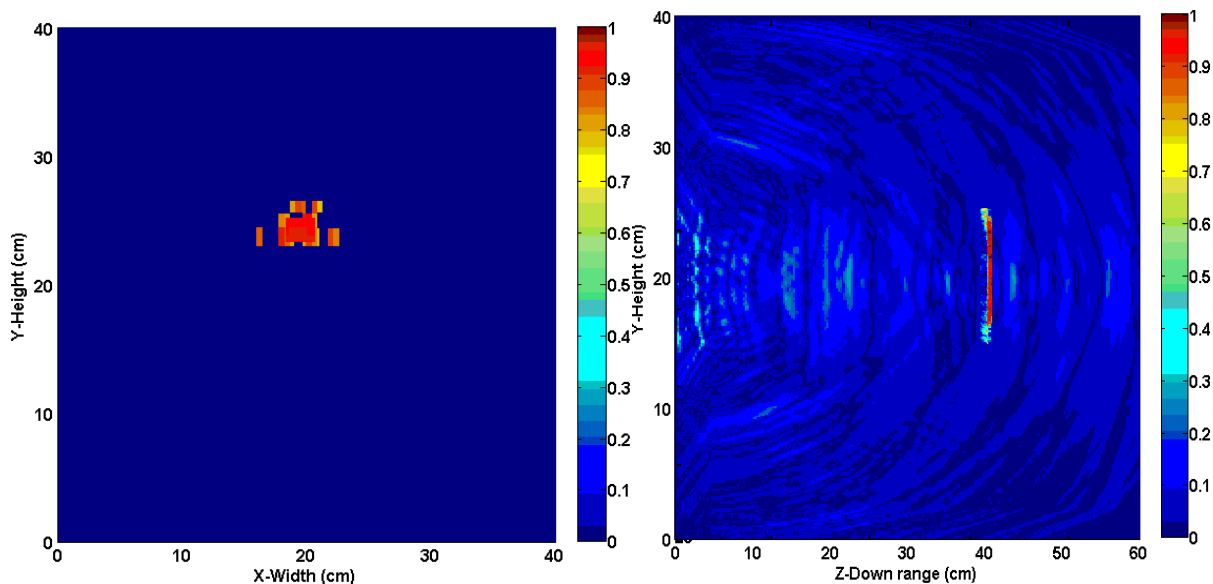
(c) Cross range image by TR;   (d) Range image by TR

Figure 5-35 Images of one metallic target with the size of 10 x 10 cm^2, placed 40cm away from the receiving array in an array of metal rods, by DAS and TR

A target with the smaller size of 8 x 8 cm^2 is used in experiment too. 40cm down-range is the furthest effectively detected distance and the images of range and cross range are shown in Figures 5.36.
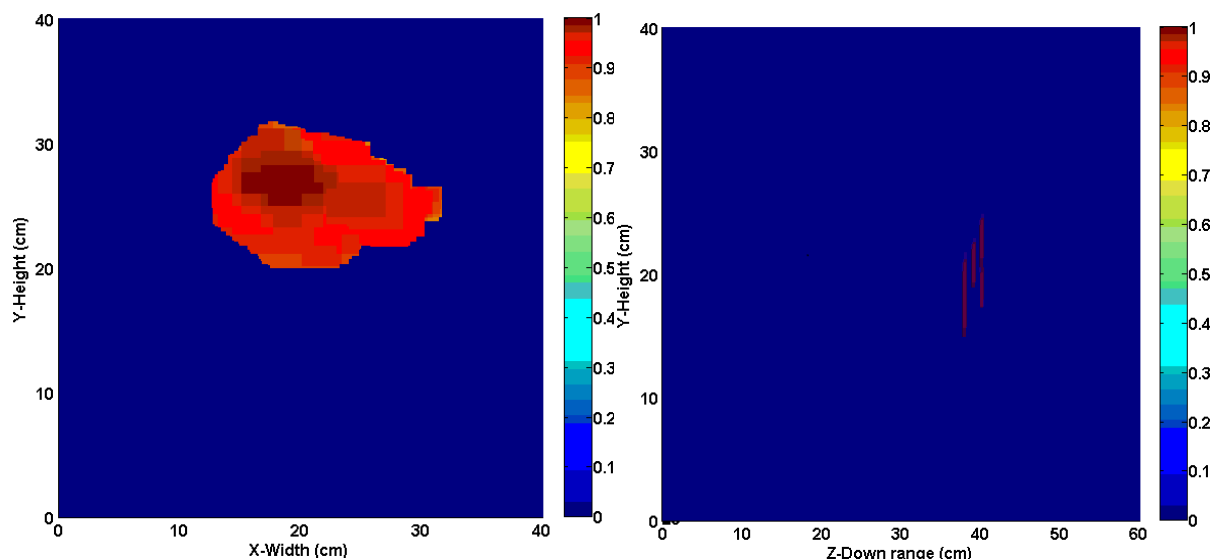
(a) Cross range image by DAS;   (b) Range image by DAS
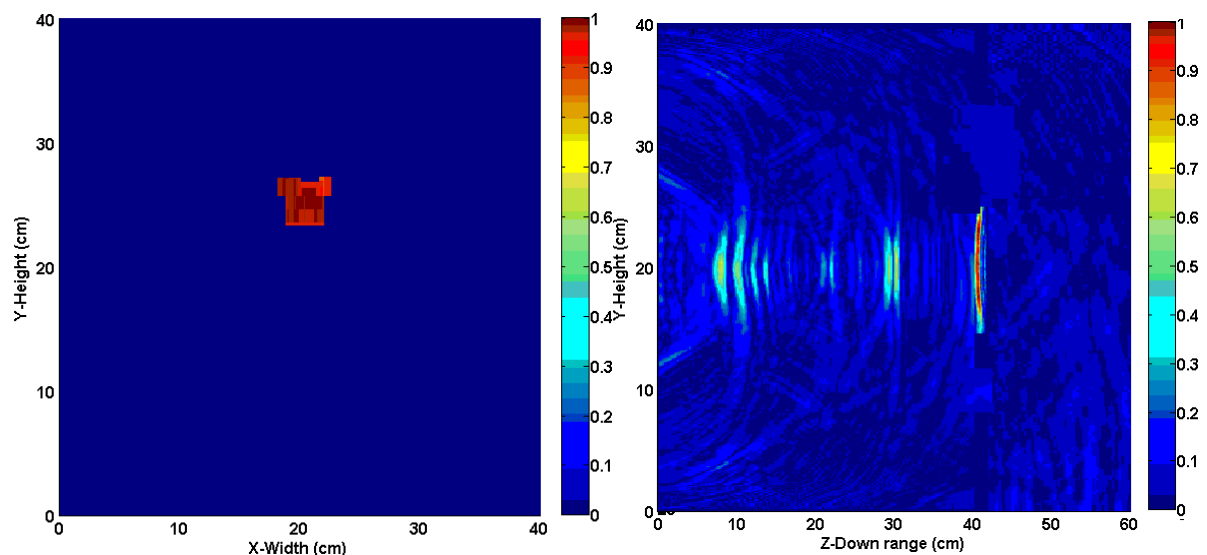
(c) Cross range image by TR;   (d) Range image by TR

Figure 5-36 Images of one metallic target with the size of 8 x 8 cm^2, placed 40cm away from the receiving array in an array of metal rods, by DAS and TR

The error analysis of the images by the DAS and TR methods for one target imaging in the metal rods in experiments is given in Table 5.9. Compared to previous experimental results, the major change in the error rates is the better sharpness of TR imaging algorithm. Particularly for cross range imaging, the error rates of recovered images by DAS are twice or triple of those by TR. TR Range imaging also shows the relatively better accuracy. This is expected because the window functions used in the DAS algorithm have to be adjusted for each individual signal

reflection. The length of the window varies and multiple window functions are needed to cover the possible reflection peaks. This is due to signal interferences caused by the metal rods array.

Table 5.9 Error analysis of one target imaging in an array of metal rods by DAS and TR in experiments

Range \ Cross Range	20 (cm)				30 (cm)				40 (cm)			
	DAS	Error	TR	Error	DAS	Error	TR	Error	DAS	Error	TR	Error
10x10 (cm²)	20x11	**120%**	8x6	**52%**	18x11	**98%**	9x6	**46%**	19x11	**109%**	8x5	**60%**
	20	**0%**	20	**0%**	30	**0%**	30	**0%**	38	**5%**	40	**0%**
8x8 (cm²)	20x10	**212.5%**	8x6	**25%**	18x12	**237.5%**	9x8	**12.5%**	20x13	**306%**	5x5	**61%**
	20	**0%**	20	**0%**	30	**0%**	30	**0%**	38	**5%**	40	**0%**

Table 5.10 Error analysis of one target imaging in an array of metal rods by DAS and TR in simulation

Range	20 (cm)				30 (cm)				40 (cm)			
Cross Range	DAS	Error	TR	Error	DAS	Error	TR	Error	DAS	Error	TR	Error
10x10 (cm²)	15x11	**65%**	8x8	**36%**	14x12	**68%**	8x8	**36%**	17x10	**70%**	8x7	**44%**
	20	**0%**	20	**0%**	30	**0%**	30	**0%**	40	**0%**	40	**0%**
8x8 (cm²)	12x10	**86.2%**	8x7	**12.5%**	12x12	**125%**	7x8	**12.5%**	14x12	**162.5%**	7x5	**45.3%**
	20	**0%**	20	**0%**	30	**0%**	30	**0%**	40	**0%**	40	**0%**

5.4.2 Two-target imaging in an array of metal rods

Two metallic pieces are placed inside the wooden rods on the foam in front of the antenna array in this measurement. Their sizes are 10 x 10 cm² and 8 x 8 cm². The measurement of the down-range resolution is considered first, so two metallic pieces are placed in front of the antenna array with one behind the other. The inter distance varies from 5cm, 10cm to 15cm. Images by DAS and TR are given in Figure 5.37, 5.38 and 5.39.

It is shown that range images by DAS have consistent blurring around the true location of the targets. When the inter distance "d_y" is 5cm, two targets are merged together under either DAS method or TR method. When the distance is changed to 10cm and 15cm, the two targets become visible with some blurring. In contrast, Images by TR tend to have sharper focus on the true location of the target without much erroneous blurring.
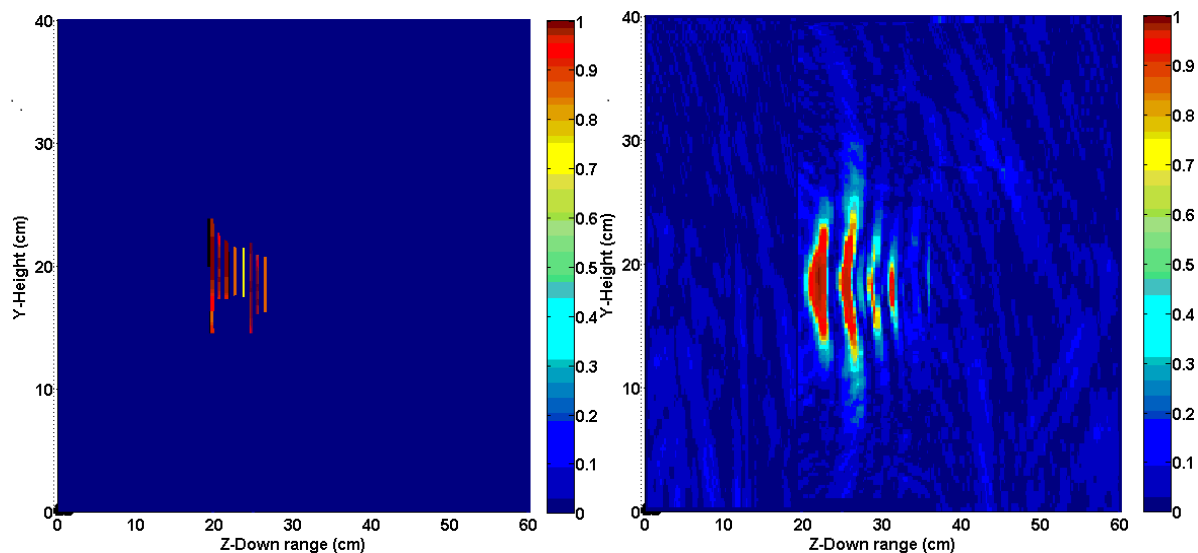
(a) Range image with d_y=5cm by DAS;   (b) Range image with d_y =5cm by TR

Figure 5-37 Images of two metallic targets with the size of 10 x 10 cm^2 and 8 x 8 cm^2 placed one behind the other, with an inter-distance of 5cm in an array of metal rods, by DAS and TR
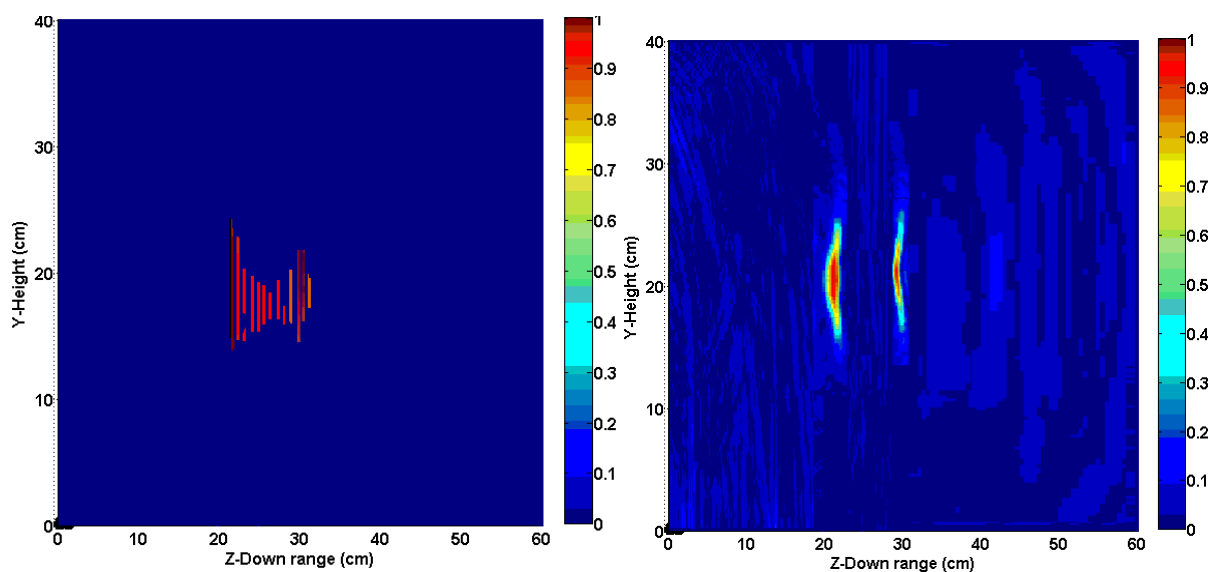
(a) Range image with d_y =10cm by DAS;   (b) Range image with d_y =10cm by TR

Figure 5-38 Images of two metallic targets with the size of 10 x 10 cm^2 and 8 x 8 cm^2 placed one behind the other, with an inter-distance of 10cm in an array of metal rods, by DAS and TR
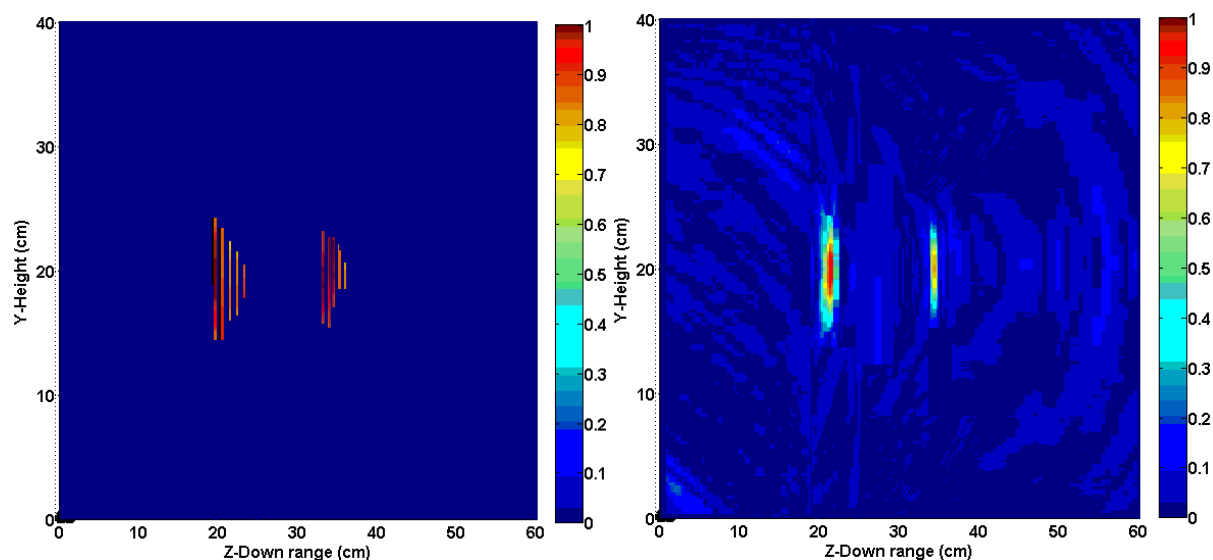
(a) Range image with d_y =15cm by DAS;   (b) Range image with d_y =15cm by TR

Figure 5-39 Images of two metallic targets with the size of 10 x 10 cm^2 and 8 x 8 cm^2 placed one behind the other, with an inter-distance of 15cm in an array of metal rods, by DAS and TR

Cross-range resolution is investigated next. Two metallic pieces are placed side by side inside the array of rods. The inter distance "d_x" between them is 4cm, 6cm and 8cm. Recovered images by DAS and TR methods are shown in Figure 5.40, 5.41 and 5.42.
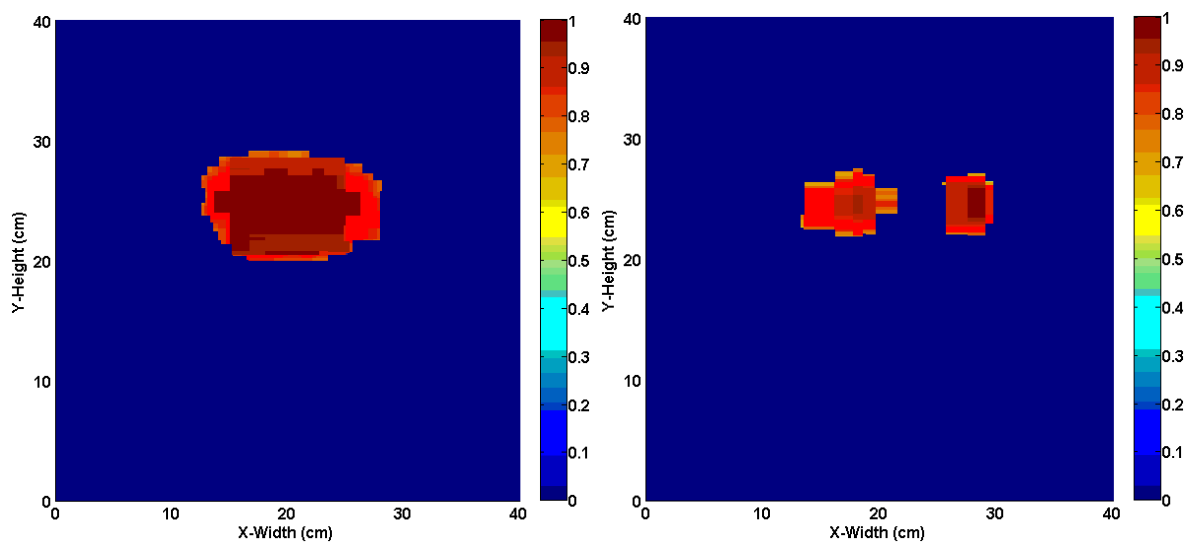
(a) Range image with d_x=4cm by DAS;   (b) Range image with d_x =4cm by TR

Figure 5-40 Images of two metallic targets with the size of 10 x 10 cm^2 and 8 x 8 cm^2 placed side by side, with an inter-distance of 4cm in an array of metal rods, by DAS and TR

(a) Range image with d_x =6cm by DAS;   (b) Range image with d_x =6cm by TR
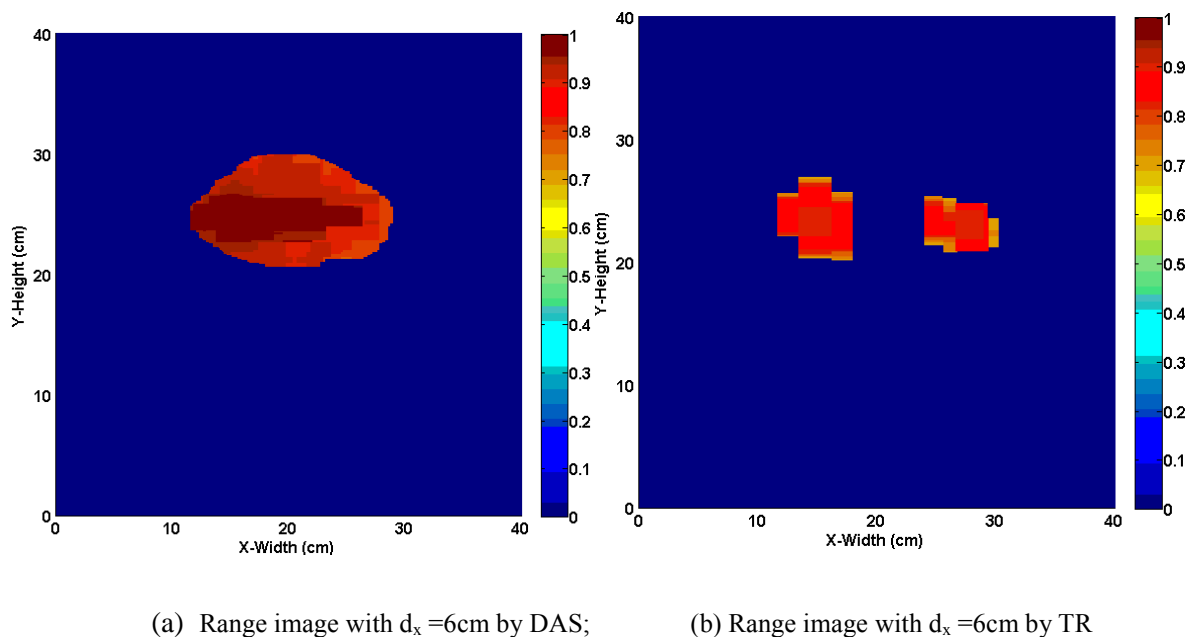
Figure 5-41 Images of two metallic targets with the size of 10 x 10 cm^2 and 8 x 8 cm^2 placed side by side, with an inter-distance of 6cm in an array of metal rods, by DAS and TR

(a) Range image with d_x =8cm by DAS;   (b) Range image with d_x =8cm by TR
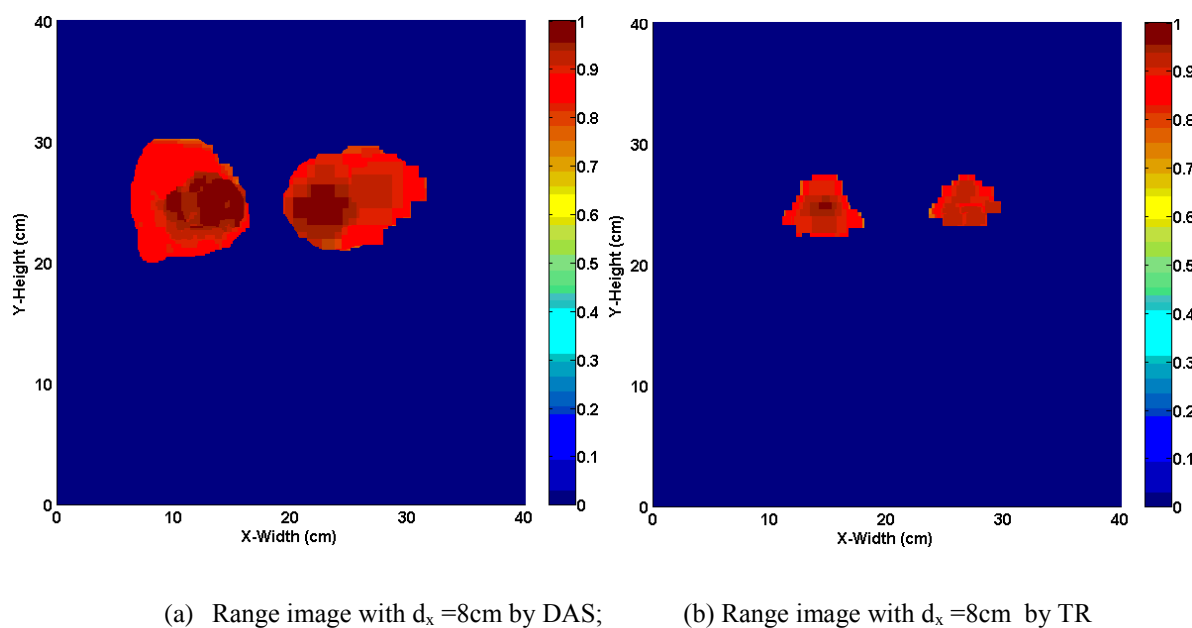
Figure 5-42 Images of two metallic targets with the size of 10 x 10 cm^2 and 8 x 8 cm^2 placed side by side, with an inter-distance of 8cm in an array of metal rods, by DAS and TR

Cross-range images by DAS show that two targets with a "d_x" of 4cm and 6cm cannot be effectively resolved. In contrast, cross-range images by TR show much better accuracy. By the TR method, when the inner distance "d_x" is 4cm, two targets are clearly separated. When the

distance is changed to 6cm and 8cm, two targets can be fully distinguished. This demonstrates that in a testing environment with severe multipath, the TR method is capable of achieving a better cross range resolution than DAS.

The error analysis of two targets imaging in the metal rods array by DAS and TR methods in experiment is given in Table 5.11. The simulation analysis is given in Table 5.12. The error analyses show that range resolution and cross-range resolution recovered by the TR method is universally better than the ones by DAS method under this circumstance.

Table 5.11 Error analysis of two targets imaging in the metal rods array by DAS and TR in experiments

Inner distance d_y=5 (cm)				Inner distance d_y =10 (cm)				Inner distance d_y =15 (cm)			
DAS	Error	TR	Error	DAS	Error	TR	Error	DAS	Error	TR	Error
Non	Non	Non	Non	Non	Non	8	20%	12cm	20%	15cm	0%
Inner distance d_x=4 (cm)				Inner distance d_x=6 (cm)				Inner distance d_x=8 (cm)			
DAS	Error	TR	Error	DAS	Error	TR	Error	DAS	Error	TR	Error
Non	Non	5cm	25%	Non	Non	6cm	0%	4cm	50%	8cm	0%

Table 5.12 Error analysis of two targets imaging in the metal rods array by DAS and TR in simulation

Inner distance d_y=5 (cm)				Inner distance d_y =10 (cm)				Inner distance d_y =15 (cm)			
DAS	Error	TR	Error	DAS	Error	TR	Error	DAS	Error	TR	Error
Non	Non	Non	Non	4cm	60%	10	0%	15cm	0%	15cm	0%
Inner distance d_x=4 (cm)				Inner distance d_x=6 (cm)				Inner distance d_x=8 (cm)			
DAS	Error	TR	Error	DAS	Error	TR	Error	DAS	Error	TR	Error
Non	Non	3cm	25%	Non	Non	6cm	0%	6cm	25%	8cm	0%

5.5 Imaging the targets in a stuffed sports bag

One useful "see-through" application is to detect suspicious metallic targets hidden in luggage or bags. Often the problem is that when the detection is performed, some items rather than the target are randomly placed around the targets inside the bag, such as clothes, toiletries, leather, books or shoes etc. They all contribute to creating a heterogeneous testing environment with undesired signal interferences and multipath.

In the following measurement, the metallic target is concealed in a cylindrical sports bag made of denim, which itself can cause some minor reflections due to its rather low permittivity. The size of the bag is 52 x 26 x 26 cm^3. In order to create a real testing environment, the bag is stuffed with one towel, two bed sheets, three tooth brushes and one book. The metallic target is placed inside among them. The experimental set-up is given in Figure 5.43.

All the materials used in the experiments can be modelled in simulation. The towel and two bed sheets are made of cotton and the permittivity of cotton is ranged between 1.8 and 2.2.

Tooth brushes are made of plastics and its permittivity is between 2.1 and 3.6. The 270 pages book is 2cm think and the permittivity of paper is usually 2.3.

Figure 5-43 Experimental set-up of one metallic target in a stuffed sports bag
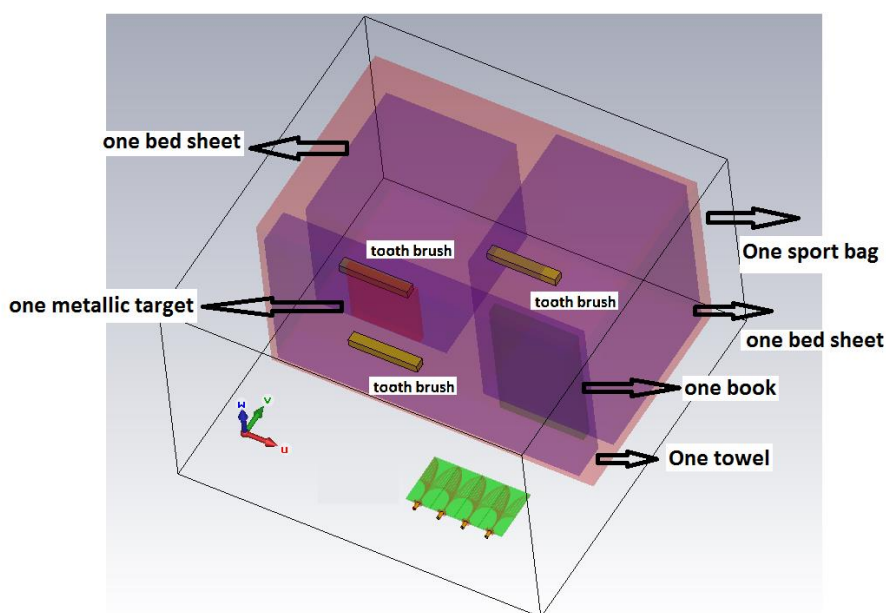
Figure 5-44 Model of one target in the simulated stuffed sports bag

5.5.1 Single target imaging in a stuffed sports bag

In experiment, the target is supported upright by the items inside the bag. The target is moved at a distance of 20cm, 30cm and 40cm away from antenna array respectively. Recovered images by DAS and TR methods are shown in Figures 5.45, 5.46 and 5.47.
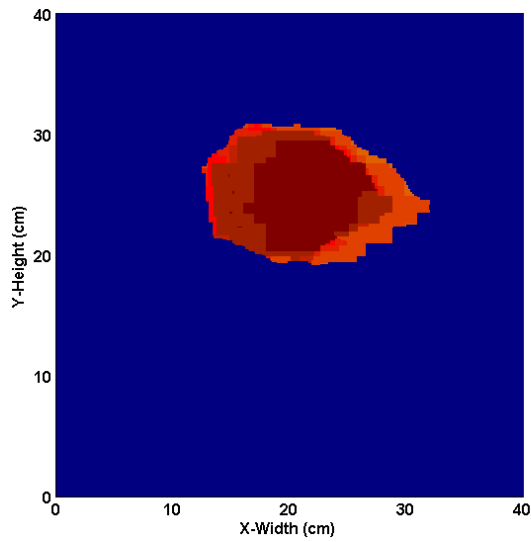
(a) Cross-range image by DAS;   (b) Range image by DAS
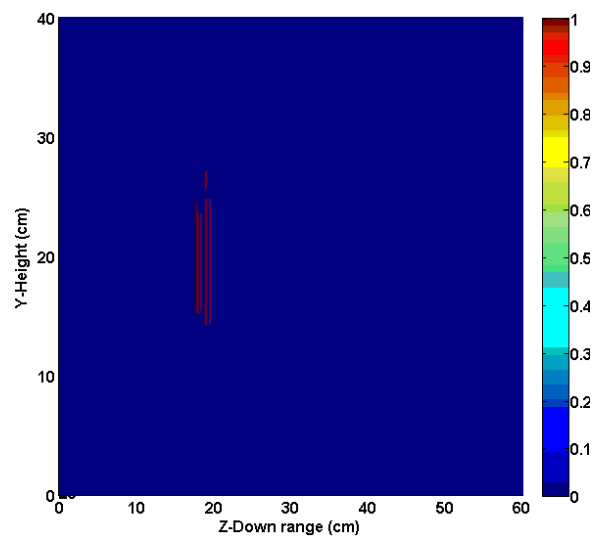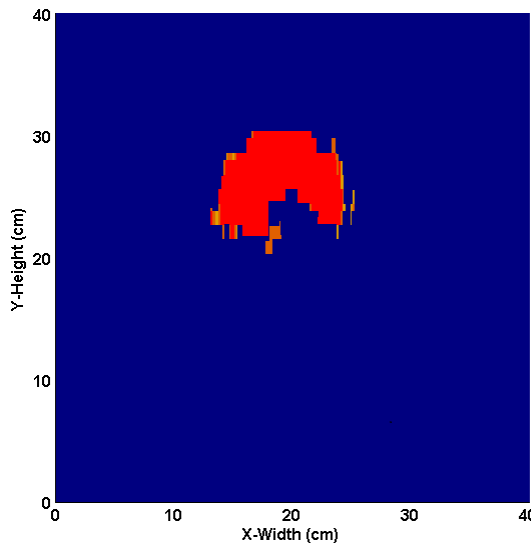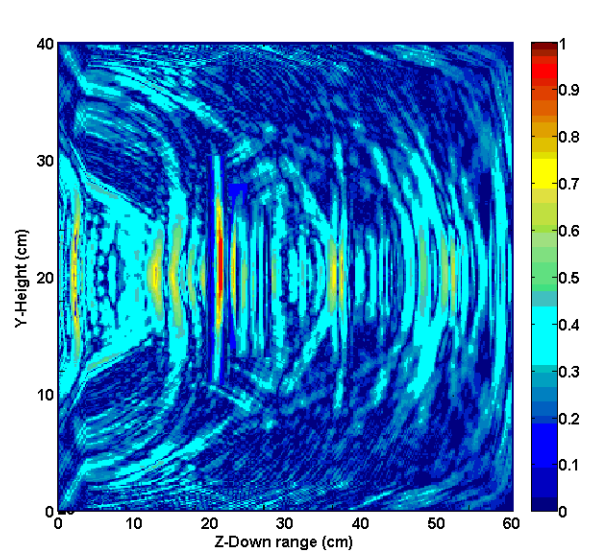
(c) Cross-range image by TR;   (d) Range image by TR

Figure 5-45 Images of a single metallic target with the size of 10 x 10 cm^2, placed 20cm away from the array in a stuffed sports bag, by DAS and TR
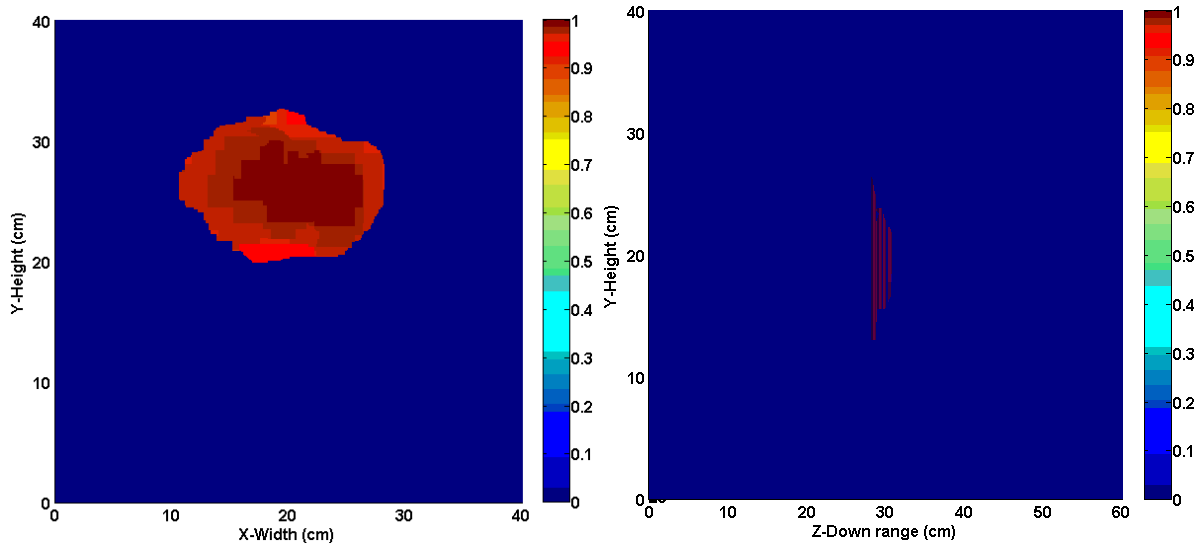
(a) Cross-range image by DAS;   (b) Range image by DAS
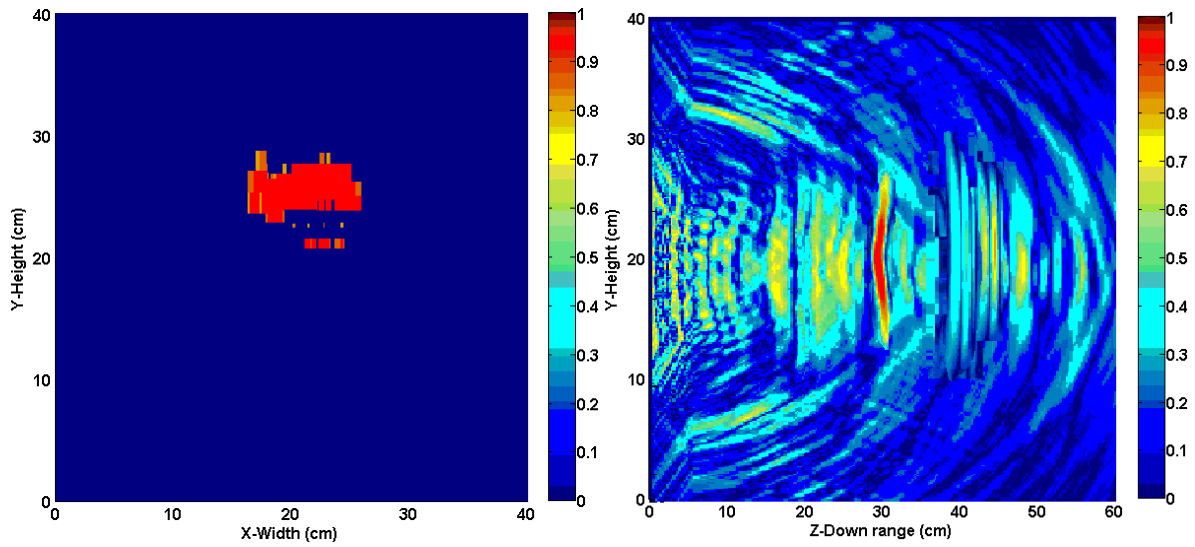
(c) Cross-range image by TR;   (d) Range image by TR

Figure 5-46 Images of a single metallic target with the size of 10 x 10 cm^2, placed 30cm away from the array in a stuffed sports bag, by DAS and TR
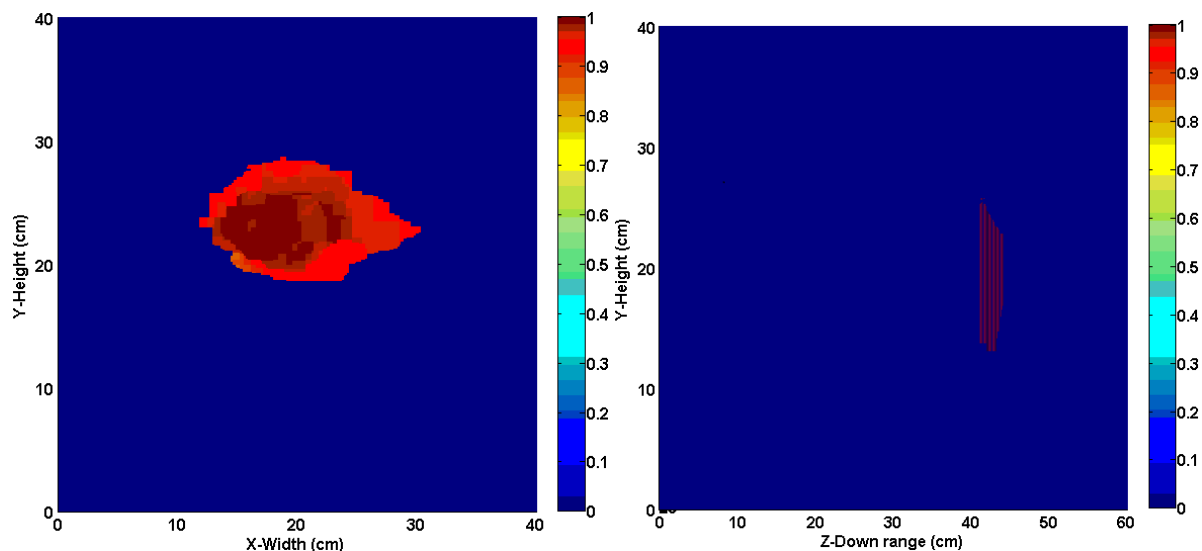
(a) Cross range image by DAS;   (b) Range image by DAS
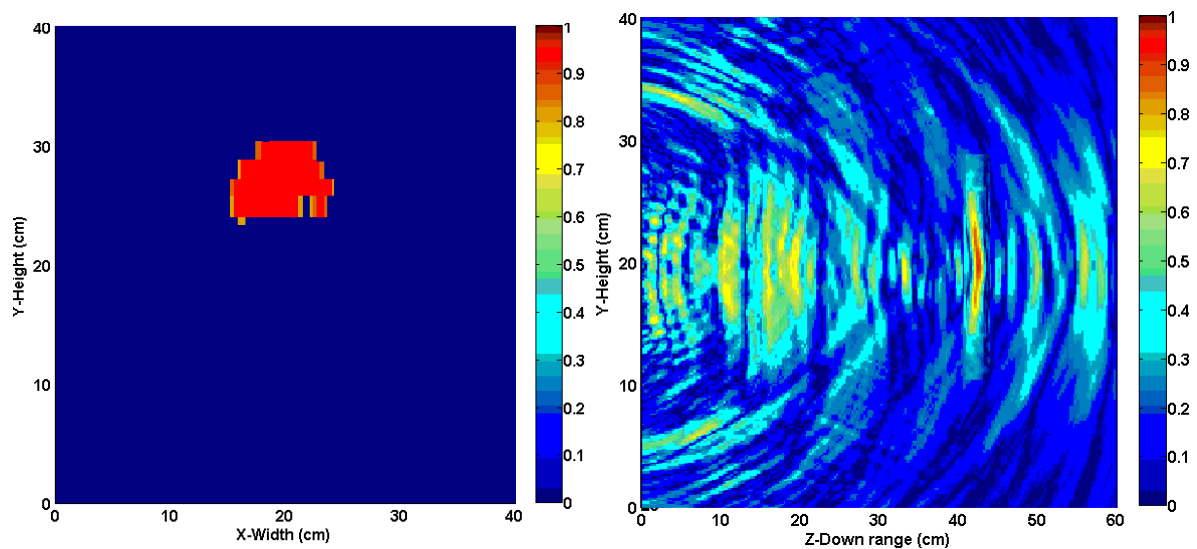
(c) Cross range image by TR;   (d) Range image by TR

Figure 5-47 Images of a single metallic target with the size of 10 x 10 cm^2, placed 40cm away from the array in a stuffed sports bag, by DAS and TR

The stuffed sports bag has provided a tougher testing environment. The range images by DAS and TR methods have shown more ripples and undulations. One principle of the TR method is to keep the testing environment time-invariant. This means that the stuffed sports bag in the experiment needs to be same as the simulated one. However, there is always some minor discrepancy in the modelling and permittivity set-up. In the second set-up of re-transmission

after many adjustments, the best images are given here. In terms of cross-range estimation, images by the TR method consistently show a much more focused concentration on the target than the DAS method. The error analysis for one target imaging in a stuffed sports bag in experiment is given in Table 5.13. The similar error rates from simulated results are given in Table 5.14. Cross-range images by TR methods show less error rates while both methods can maintain the range distance error rate within 10%.

Table 5.13 Error analysis of one target imaging in a stuffed sports bag by DAS and TR in experiments

Range Cross Range	20 (cm)				30 (cm)				40 (cm)			
	DAS	Error	TR	Error	DAS	Error	TR	Error	DAS	Error	TR	Error
10x10 (cm²)	20x12	**140%**	11x9	**1%**	18x13	**134%**	9x8	**28%**	18x10	**80%**	10x7	**30%**
	18	**10%**	20	**0%**	29	**3.3%**	32	**6.7%**	42	**5%**	42	**5%**

Table 5.14 Error analysis of one target imaging in a stuffed sports bag by DAS and TR in simulation

Range Cross Range	20 (cm)				30 (cm)				40 (cm)			
	DAS	Error	TR	Error	DAS	Error	TR	Error	DAS	Error	TR	Error
10x10 (cm²)	15x12	**80%**	12x5	**40%**	16x12	**92%**	11x5	**45%**	16x14	**124%**	10x5	**50%**
	20	**0%**	20	**0%**	30	**0%**	30	**0%**	40	**0%**	40	**5%**

5.5.2 Two-target imaging in a stuffed sports bag

This section investigates two targets imaging in a stuffed bag and a resolution study. Two metallic targets are placed inside the bag. Their sizes are 10 x 10 cm^2 and 8 x 8 cm^2.

Down-range resolution is discussed first and is shown in Figures 5.48, 5.49 and 5.50. The first target is fixed inside the bag and has a distance of 20cm from the antenna array. The second target is placed behind the first one with an inter distance of 5cm, 10cm and 15cm respectively. When the distance is 5cm, images by DAS and TR cannot effectively tell them apart. When the distance increases to 10cm, the images give a better visual separation, but still lack adequate accuracy. When the targets are placed apart with a inter distance of 15cm, Both the DAS and TR methods are able to separate them. It is found in the images created by the DAS method, shows some blurring effect still exists, while, the TR method can continue to separate two targets without losing focus.

In terms of the cross-range resolution, two metallic pieces are placed 20cm away from the antenna array side by side inside the stuffed bag. The inter distance is 4cm, 6cm and 8cm respectively. Images by DAS and TR methods are shown in Figures 5.51, 5.52 and 5.53. The images show that DAS method cannot effectively separate two targets when the distance is 4cm and 6cm. In comparison, TR images have shown much better separation and accuracy in all the inter distances of 4cm, 6cm and 8cm. This contrast proves that in this scenario with the strongest signal interferences and multipath, the TR imaging method can achieve a better, more accurate and stable cross-range resolution estimation.
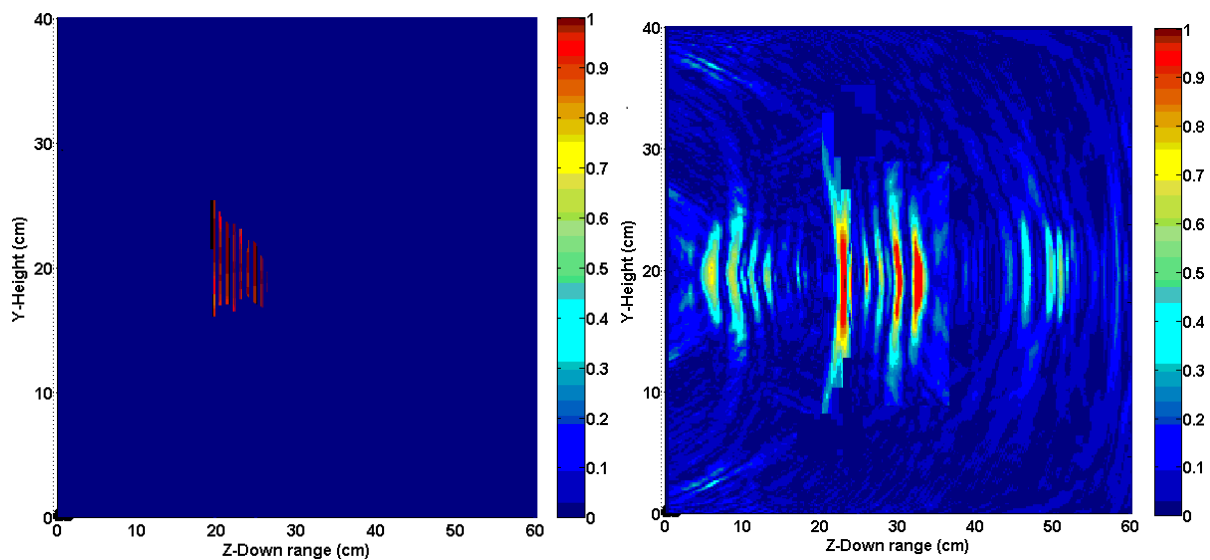
(a) Range image with d_y=5cm by DAS;   (b) Range image with d_y =5cm by TR

Figure 5-48 Images of two metallic targets with the size of 10 x 10 cm^2 and 8 x 8 cm^2 placed one behind the other, with an inter-distance of 5cm in a stuffed sports bag, by DAS and TR
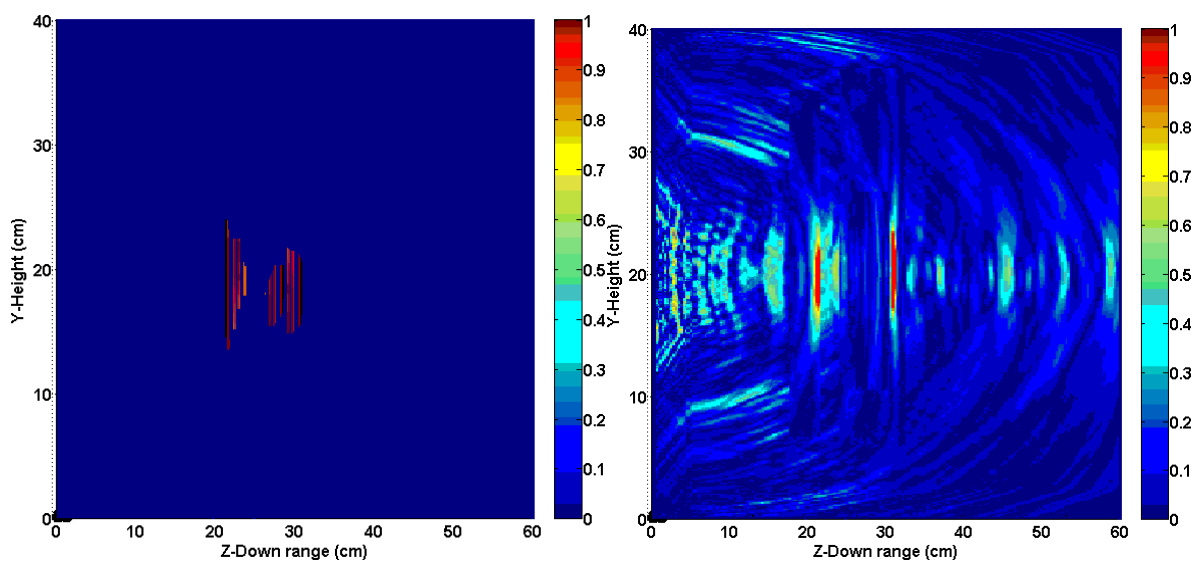
(a) Range image with d_y =10cm by DAS;   (b) Range image with d_y =10cm by TR

Figure 5-49 Images of two metallic targets with the size of 10 x 10 cm^2 and 8 x 8 cm^2 placed one behind the other, with an inter-distance of 10cm in a stuffed sports bag, by DAS and TR
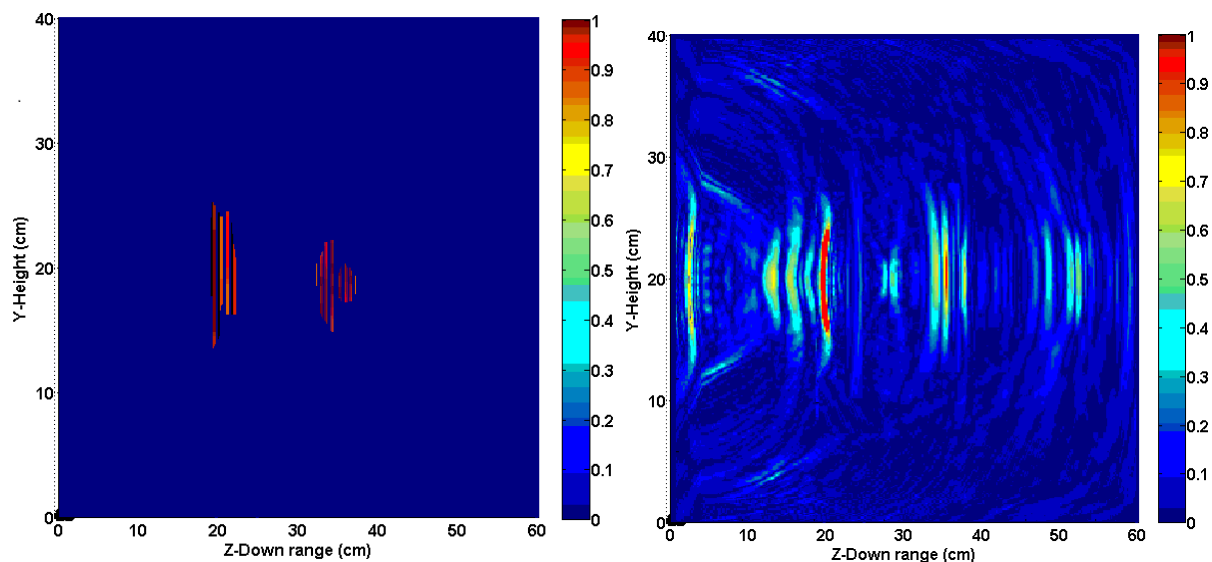
(a) Range image with d_y =15cm by DAS;   (b) Range image with d_y =15cm by TR

Figure 5-50 Images of two metallic targets with the size of 10 x 10 cm^2 and 8 x 8 cm^2 placed one behind the other, with an inter-distance of 15cm in a stuffed sports bag, by DAS and TR
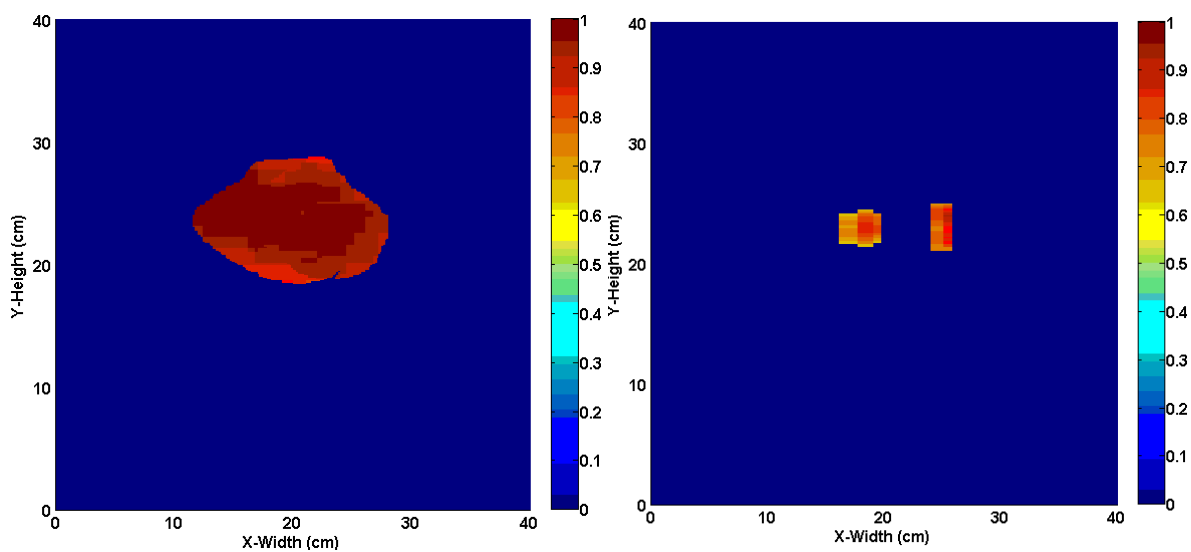
(a) Cross range image with d_x=4cm by DAS;   (b) Cross range image with d_x =4cm by TR

Figure 5-51 Images of two metallic targets with the size of 10 x 10 cm^2 and 8 x 8 cm^2 placed side by side, with an inter-distance of 4cm in a stuffed sports bag, by DAS and TR
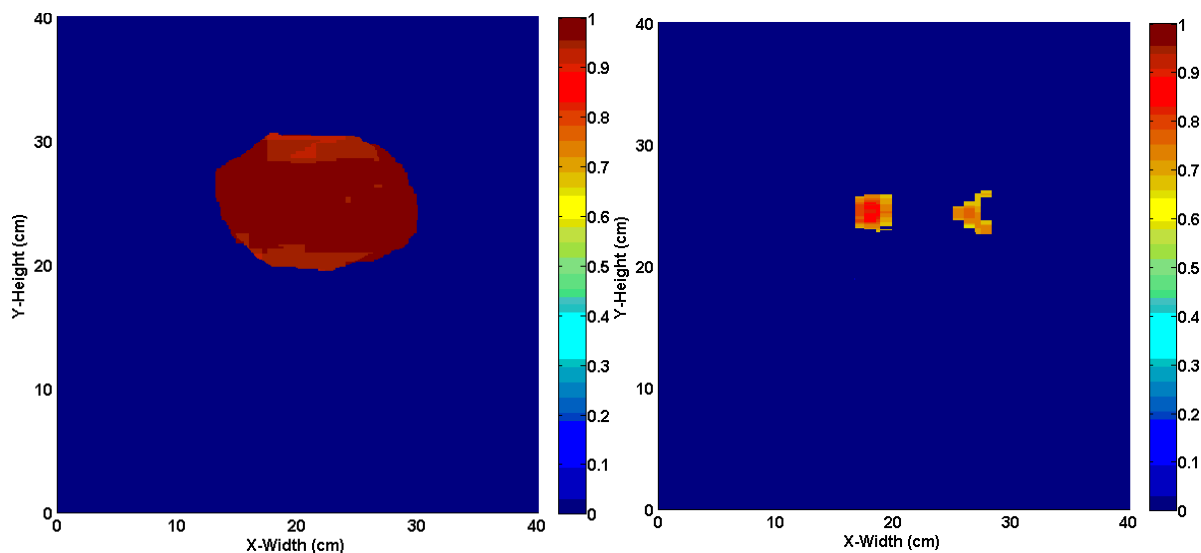
(a) Cross range image with d_x =6cm by DAS;   (b) Cross range image with d_x =6cm by TR

Figure 5-52 Images of two metallic targets with the size of 10 x 10 cm^2 and 8 x 8 cm^2 placed side by side, with an inter-distance of 6cm in a stuffed sports bag, by DAS and TR
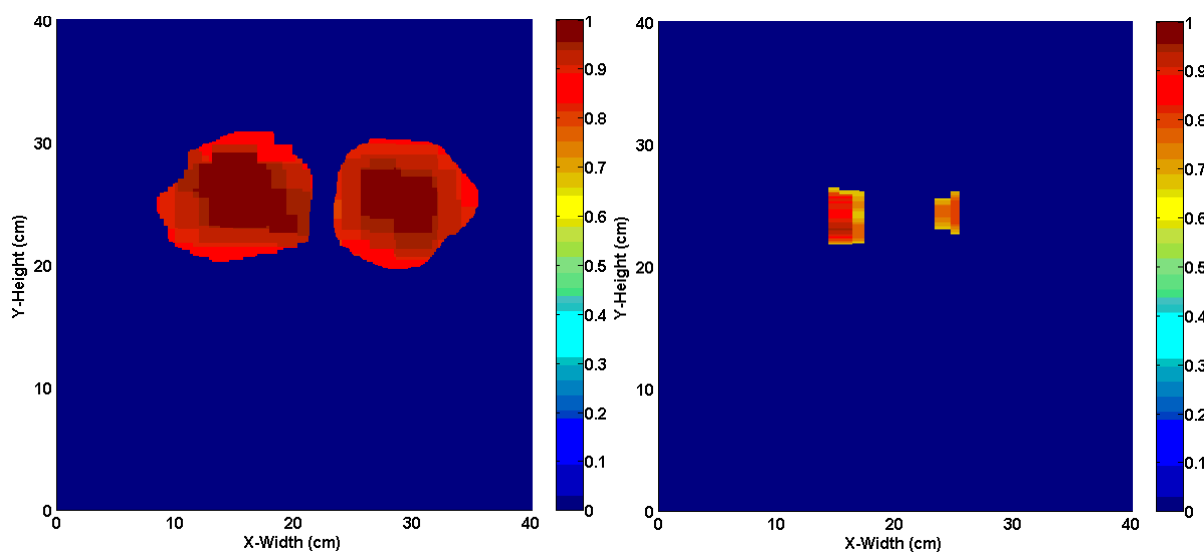
(a) Cross range image with d_x =8cm by DAS;   (b) Cross range image with d_x =8cm by TR

Figure 5-53 Images of two metallic targets with the size of 10 x 10 cm^2 and 8 x 8 cm^2 placed side by side, with an inter-distance of 8cm in a stuffed sports bag, by DAS and TR

The error analysis of two targets imaging in a stuffed sports bag by DAS and TR methods in experiments is given in Table 5.15. The simulated error analysis is given in Table 5.16. It shows that the recovered down-range and cross-range resolutions by TR method are consistently

better than DAS method. When the inter distance between the targets is diminishing, the TR method can continue to separate them with reasonable error rates, while DAS method fails to distinguish them.

Table 5.15 Error analysis of two targets imaging in a stuffed bag by DAS and TR in experiments

Inner distance d_y=5 (cm)				Inner distance d_y =10 (cm)				Inner distance d_y =15 (cm)			
DAS	Error	TR	Error	DAS	Error	TR	Error	DAS	Error	TR	Error
Non	Non	Non	Non	5cm	50%	9cm	10%	16cm	6.7%	16cm	6.7%
Inner distance d_x =4 (cm)				Inner distance d_x =6 (cm)				Inner distance d_x =8 (cm)			
DAS	Error	TR	Error	DAS	Error	TR	Error	DAS	Error	TR	Error
Non	Non	4cm	0%	Non	Non	7cm	16.7%	2cm	75%	7cm	12.5%

Table 5.16 Error analysis of two targets imaging in a stuffed bag by DAS and TR in simulation

Inner distance d_y=5 (cm)				Inner distance d_y =10 (cm)				Inner distance d_y =15 (cm)			
DAS	Error	TR	Error	DAS	Error	TR	Error	DAS	Error	TR	Error
Non	Non	Non	Non	6cm	40%	10cm	0%	12cm	20%	15cm	0%
Inner distance d_x =4 (cm)				Inner distance d_x =6 (cm)				Inner distance d_x =8 (cm)			
DAS	Error	TR	Error	DAS	Error	TR	Error	DAS	Error	TR	Error
Non	Non	4cm	0%	Non	Non	6cm	0%	1cm	87.5%	8cm	0%

5.6 Summary

In this chapter, four scenarios are explored, ranging from the easiest case in free space to the more complex case with multipath and strong signal interferences. Free space and single wooden board penetration are comparably easier testing environments. An array of metal rods creates a relatively more difficult scenario for target imaging. Finally, a practical testing scenario for security purposes is used with a stuffed bag as the package under radiation. The non-metallic items inside the bag contribute to strong signal interferences, thus making it the most difficult case to distinguish two targets with various inter spaces.

For a single metallic square target in free space, the smallest detectable size is 5 x 5 cm^2 at a maximum testing down range distance of 30cm away from the antenna array. Meanwhile, the maximum detectable down range distance for a target with the size of 10 x 10 cm^2 is 50cm. For two targets imaging, the down-range resolution of 15cm and cross-range resolution of 6cm are achievable by DAS and TR methods with a down range distance of 20cm in the developed

UWB imaging system. Generally, the TR method cannot produce better cross-range images when compared to DAS method. So the latter is a better option in this situation.

The second testing scenario introduces a wooden board. The presence of the wooden board changes the conclusion drawn in free space. First, the smallest detectable size of the target is 8 x 8 cm^2 at the maximum down range distance of 40cm. TR images show slightly better range estimation than DAS, but DAS still produces better cross-range estimation. For two targets, the same down-range resolution of 15cm and cross-range resolution of 6cm are produced by both DAS and TR methods.

The third testing scenario is a multipath environment with an array of metal rods. This set-up takes account of the interaction between the target and the rods after the differential procedure. The smallest detectable size is 8 x 8 cm^2 at the maximum range distance of 40cm. The biggest change is that recovered images by the TR method start to show better down range estimation than DAS. For two targets, cross-range images by the TR method have shown that a spacing of 4cm can be accurately separated, beating the minimal spacing of 6cm by DAS method.

The images from the last testing scenario, where the targets are places inside a packed sports bag, show more meaningful features. First, two different orientations of the single target are investigated. The maximum detectable range for one target is 40cm. For two targets, the images by the TR method have shown better error rates than DAS, particularly in the cross-range resolution with a 20cm down range distance from the antenna array. The DAS method can only distinguish cross-range resolution of 8cm with a considerable error rate. In comparison, the TR method can successfully image two targets apart with a cross-range spacing of 4cm with less error rates.

In conclusion, the TR imaging method has proved to be a better imaging tool to cope with more complicated testing environments with signal multipath and interferences. It can enhance the range resolution to a limited degree but can greatly improve cross-range resolution for two metallic targets. In contrast, the DAS imaging method is very efficient for tackling simpler scenarios, with much less computing time and modelling and coding difficulty. Both methods have taken advantage of a differential procedure to reduce the influence of the signal interference and clutter component; however, it is impossible to exclude completely the interactions between the target and the surroundings. The reason why the TR method can

achieve better cross-range resolution with lower error rate is that it can incorporate these interactions to the advantage of imaging, alternatively enlarging the effective receiving antenna aperture. This effect is reinforced by the superposition of the rotating receiving array, which transforms a linear array aperture into a 2D one.

Reference

[1] Kingsley, S. Quegan, "Understanding Radar Systems", McGraw-Hill, 1992

Chapter 6 Summary and Future Work

6.1 Summary

This thesis mainly focuses on the imaging of hidden metallic targets in different testing environments by a proposed UWB radar system. A number of aspects have been covered in the investigation, which consists of the modelling and simulation of the UWB sub-systems, the design and fabrication of a compact system, and the application and comparisons of two imaging reconstruction methods, "Delay and Sum (DAS)" and "Time Reversal (TR)".

In the simulation of the system, the analyses have provided useful insight into the capability of the UWB radar imaging system. Furthermore, considering various off-the-shelf commercial RF components in the experimental set-up and the initial testing results, the link budget and dynamic range of the developed UWB system can be estimated. At the front end of the system, a rotating antenna array is adopted to achieve a circular synthetic 2D array aperture, supported by a compact step motor positioning sub-system. This design successfully reduces the complexity of the antenna array and the cost. The step rotation of the array and the 5-port RF switch for each propagation link is controlled by the programs in the LabVIEW environment and the data acquisition tool from the National Instrument. The RF sub-system has been assembled in a 50 x 50 x 12 cm^3 wooden box with one metal sheet, leaving half of the space for more function circuitry modules in the next generation.

Two image reconstruction methods: "Delay and Sum (DAS)" and "Time Reversal (TR)", are extensively studied to image the hidden metallic targets of interest in simulation and in experiment. At each rotation angle, one linear image is generated. A complete circular rotation can create 60-72 linear images in total. After the procedure of image superposition, a better and clearer image can be achieved.

In simulation and experiment, four different testing scenarios are investigated: free space, penetration of a wooden board, radiation through a perpendicular metal rods array, and a stuffed sports bag with non-metallic items. Both DAS and TR imaging methods are applied to

the simulated and experimental data produced by the developed UWB radar system. The recovered images reveal four relevant imaging factors: range estimation, cross range estimation, down range resolution and cross range resolution.

The recovered images have shown that the TR method is better at distinguishing two metallic targets placed in a row in more complicated testing scenarios, such as the metal rods array and the stuffed sports bag. An inter distance of separation of 4cm can be realised by the TR method when the DAS method fails to achieve separation of two targets. In contrast, the DAS method is better at imaging one or two targets in a simpler environment, such as free space or penetration of one homogeneous wooden board.

6.2 Key contributions

In conclusion, the key contributions in the thesis are listed as below:

1. First and foremost, a time-domain UWB radar system for imaging is developed and implemented. The system is capable of operating from 4 to 5GHz and presents a reliable platform for target imaging. The RF transceiver has been carefully designed, achieving a good receiver dynamic range of 69dB and a receiver sensitivity of -78dBm.

2. A comprehensive simulation of the imaging system has been carried out to guide the development of the UWB radar system, assisted by the initial test of some commercial components in the lab.

3. Some procedures to achieve a compact system have been made. First, the implementation of the step motor, driver card and gears has created a convenient and compact positioning sub-system. Next, the integration of modules in the LabVIEW environment with NI DAQ has enabled the operator to control the rotation of the antenna array and the selection of propagation links from a laptop, greatly reducing the size of the system.

4. Two image reconstruction methods: "Delay-and-Sum (DAS)" and "Time-Reversal (TR)" are used to obtain the images of the targets. The comparison is made to show their own advantages when the testing scenarios become more and more complicated. Generally, when the multipath effect prevails, the DAS imaging method has difficulty in producing reliable results, while the TR imaging method is particularly effective in

imaging two targets placed in a row with better cross range estimation. The DAS imaging method can successfully image a pair of metal targets with a cross range distance of 6cm, in free space and by penetration of a single wooden board, but fails to achieve this in the other two more complicated scenarios. The TR imaging method can obtain a much tighter cross range resolution of 4cm in the latter two scenarios with the acceptable low error rate.

6.3 Future work

Future work will mainly focus on the build-up of the next generation of the UWB imaging system with more optimisations in hardware and software.

1. A new design of the rotating antenna deployment is needed. The cables used for connection with the antennas and the RF switch need to be removed to reduce any possible risk during the rotation.

2. Further measures are needed to reduce the size of the system. It includes the creation of a newly designed pulse generator in circuitry. A wider range of available pulses and adjustable pulse widths are the main focus in this design.

3. FPGA circuitry is needed to replace the signal synthesiser used in the lab, further reducing the size of the system while improving the stability and portability. A scheme to produce a synthetic high sampling rate is to fully recover the discretised time-domain data in experiment. Additionally, the ADCs are needed along with the FPGA board for signal transformation.

4. The passive and active commercial packaged components in use are to be replaced by surface-mounted chips. A cascade of integration procedures is to consider the consistency in wide band and the EM compatibility issues involved.

5. Imaging algorithms with more optimisations are to be developed to enable target imaging in real time. Moving target detection and imaging are also to be investigated. A possible design of full transceivers in the array would facilitate the more advanced TR methods, such as DORT and TR-MUSIC.

List of publications

Journal papers

[1] **Lei Li**, Xiaodong Chen, Min Zhou, Clive Parini, "Analysis of the UWB Imaging System with rotating antenna array and the images based on Delay-and-Sum and Time-Reversal Methods", to be submitted to IEEE Transactions on Antennas and Propagation.

Conference papers:

[1] Min Zhou, Xiaodong Chen, **Lei Li**, Clive Parini, "The UWB Imaging System with Rotating Antenna Array for Concealed Metallic Object", *The 8th European Conference on Antennas and Propagation*, EuCAP 2014,6-11 Apr. 2014, the Netherlands.

[2] **Lei Li**, Min Zhou, Xiaodong Chen, Clive Parini, "CST Microwave Studio Simulation of an UWB Image System", European User Conference (EUC), 28-29 Apr. 2015, Darmstadt, Germany

[3] **Lei Li**, Xiaodong Chen, Clive Parini, "Development of the UWB Imaging System with Rotary Antenna Array and Image reconstruction algorithms for Concealed Metal Target in Multipath Environments", ICEAA 2015, 7-11 Sep. 2015, Torino, Italy. *(Accepted)*

Appendix A:

Vector wave equation in TR analysis

The initial investigation of TR method is made on the basis of model of time-reversal cavity in acoustics. In acoustical research, the scalar wave equation is analysed. However, in EM field, electromagnetic wave propagation is an issue of vector problem. Both the electric vector and magnetic vector should satisfy the vector wave equations. One difference between scalar wave equation analysis and the vector one is the manifest of Green's function. The scalar wave equation makes use of standard Green's function, while dyadic Green's function is in use for vector EM TR problem.

The Kirchhoff equation is used to describe the motion of a rigid body in an ideal fluid. It can illustrate the theory: the solution of wave equation to any random point within a sealed volume can be deduced with the information of the source, the fields on the sealed volume and its normal derivatives. The source and field distributions are shown in Figure B-1.
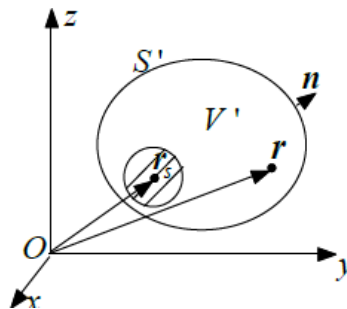

Figure B-1 Illustration of the source and field distributions

The volume 'V`' is enclosed by the curve surface 'S`'. 'r' refers to the random point within the volume. The surface unit normal vector 'n' points outwards. The current source lies in the shadow within the volume and can be expressed by electric current density vector $\bar{J}(\bar{r}, t)$ as below:

$$\bar{J}(\bar{r}, \omega) = \frac{1}{2\pi} \int_{-\infty}^{+\infty} \bar{J}(\bar{r}, t) e^{-j\omega t} dt \tag{B.1}$$

The electric vector 'E' satisfies the vector wave equation in frequency domain:

$$\nabla \times \nabla \times \bar{E}(\bar{r}, \omega) - k^2 \bar{E}(\bar{r}, \omega) = -j\omega\mu\bar{J}(\bar{r}, \omega) \tag{B.2}$$

The electric dyadic Green's function, which is related to electric vector 'E', should satisfy the wave equation. Note that $\bar{\bar{I}}$ here means the dyadic unit factor.

$$\nabla \times \nabla \times \bar{\bar{G}}(\bar{r}, \omega) - k^2 \bar{\bar{G}}(\bar{r}, \omega) = \delta(\bar{r} - \bar{r}')\bar{\bar{I}} \tag{B.3}$$

Based on the dyadic green's theorem, the transformation below can be achieved:

$$\iiint_V \left(P(r')\nabla' \times \nabla' \times Q(\bar{r}') - Q(\bar{r}')\cdot\nabla' \times \nabla' \times P(r') \right) dV'$$

$$= \oiint_S \left(Q(\bar{r}') \times \nabla' \times P(r') - P(r') \times \nabla' \times Q(\bar{r}') \right) \cdot n' dS' \tag{B.4}$$

Let $P(\bar{r}) = \bar{E}(\bar{r}, \omega)$ and $Q(\bar{r}) = \bar{\bar{G}}(\bar{r}, \bar{r}')\bar{a}$ ($\bar{a}$ is the random vector), the equation above can be rewritten as:

$$\iiint_V \left(\bar{E}(\bar{r}', \omega) \cdot \nabla' \times \nabla' \times \bar{\bar{G}}(\bar{r}', \bar{r})\bar{a} - \bar{\bar{G}}(\bar{r}', \bar{r})\bar{a}\cdot\nabla' \times \nabla' \times \bar{E}(\bar{r}', \omega) \right) dV'$$

$$= \oiint_S \left(\bar{\bar{G}}(\bar{r}', \bar{r})\bar{a} \times \nabla' \times \bar{E}(\bar{r}', \omega) - \bar{E}(\bar{r}', \omega) \times \nabla' \times \bar{\bar{G}}(\bar{r}', \bar{r})\bar{a} \right) \cdot n' dS' \tag{B.5}$$

Note the equation of $u' \cdot \bar{\bar{D}}v' = v' \cdot \bar{\bar{D}}^T u$. Here, $\bar{\bar{D}}$ is the dyadic function, u' and v' are vectors. Symbol 'T' means the matrix transposition. Meanwhile, dyadic green's function satisfied reciprocity theorem $\bar{\bar{G}}(\bar{r}', \bar{r}) = \bar{\bar{G}}(\bar{r}, \bar{r}')$. So the left part of equation (B.5) can be written as below:

$$\iiint_V \left(\bar{E}(\bar{r}', \omega) \cdot \nabla' \times \nabla' \times \bar{\bar{G}}(\bar{r}', \bar{r})\bar{a} - \bar{\bar{G}}(\bar{r}', \bar{r})\bar{a}\cdot\nabla' \times \nabla' \times \bar{E}(\bar{r}', \omega) \right) dV'$$

$$= \bar{E}(\bar{r}, \omega)\bar{a} + j\omega\mu \iiint_V \left(\bar{\bar{G}}(\bar{r}', \bar{r})\bar{J}(\bar{r}', \omega) \right) dV' \cdot \bar{a} \qquad (B.6)$$

Considering the equations above, electric field can be obtained as below:

$$\bar{E}(\bar{r}, \omega)\bar{a} = -j\omega\mu \iiint_V \left(\bar{\bar{G}}(\bar{r}', \bar{r})\bar{J}(\bar{r}', \omega) \right) dV' \cdot \bar{a} + \oiint_S \left(\bar{\bar{G}}(\bar{r}', \bar{r})\bar{a} \times \nabla' \times \bar{E}(\bar{r}', \omega) - \right.$$
$$\left. \bar{E}(\bar{r}', \omega) \times \nabla' \times \bar{\bar{G}}(\bar{r}', \bar{r})\bar{a} \right) \cdot n' dS' \qquad (B.7)$$

Similarly, the volume integral refers to the field generated within the volume 'V`' by the source of $\bar{J}(\bar{r}', \omega)$ and the surface integral represents the field generated outside of it.

Next, the TR field is under investigation.

Let's assume that the initial excitation point source is defined as "$\delta(\bar{r} - \bar{r}_s)\bar{\iota}(\omega)$". $\bar{\iota}(\omega)$ is the electric current intensity vector and is a constant vector. So the field collected by all the receivers around the surface can be expressed as below:

$$\bar{E}(\bar{r}, \bar{r}_s)|\bar{r} \in S = -j\omega\varphi\bar{G}(\bar{r}, \bar{r}_s)\bar{\iota}|\bar{r} \in S \qquad (B.8)$$

Then the time reversed field can be written as:

$$\bar{E}^*(\bar{r}, \bar{r}_s)|\bar{r} \in S = j\omega\varphi\bar{G}^*(\bar{r}, \bar{r}_s)\bar{\iota}|\bar{r} \in S \qquad (B.9)$$

Then, the initial excitation is taken out and let the time-reversed field emit backwards to the same domain as the secondary source on the surface. The field is recorded inside of the closed cavity, named as "TR field": $\bar{E}^{TR}(\bar{r}, \bar{r}_s)$.

$$\bar{E}^{TR}(\bar{r}, \bar{r}_s) \cdot \bar{a} = \oiint_S \left(\bar{\bar{G}}(\bar{r}', \bar{r})\bar{a} \times \nabla' \times \bar{E}^*(\bar{r}', \bar{r}_s) - \bar{E}^*(\bar{r}', \bar{r}_s) \times \nabla' \times \bar{\bar{G}}(\bar{r}', \bar{r})\bar{a} \right)$$
$$\cdot n' dS' \qquad (B.10)$$

The volume integral is omitted because of the change of excitation from the point source inside of the volume to the one surrounding the surface. $\bar{E}^{TR}(\bar{r}, \bar{r}_s)$ can be further deduced into:

$$\bar{E}^{TR}(\bar{r}, \bar{r}_s) \cdot \bar{a} = \bar{E}^*(\bar{r}, \bar{r}_s) \cdot \bar{a} - j\omega\mu\bar{\bar{G}}(\bar{r}_s, \bar{r}) \cdot \bar{a} \cdot \bar{\iota}^* = j\omega\mu\{\bar{G}^*(\bar{r}, \bar{r}_s) - \bar{\bar{G}}(\bar{r}, \bar{r}_s)\} \cdot \bar{a} \cdot \bar{\iota}^*$$

$$(B.11)$$

Its expression in frequency domain can be written as:

$$\bar{E}^{TR}(\bar{r},\bar{r}_s;\omega) \cdot \bar{a} = j\omega\mu\{\bar{\bar{G}}^*(\bar{r},\bar{r}_s) - \bar{\bar{G}}(\bar{r},\bar{r}_s)\} \cdot \bar{\iota}^*(\omega) \qquad (B.12)$$

The dyadic Green's function is given as:

$$\bar{\bar{G}}(\bar{r},\bar{r}_s;\omega) = \left(\bar{\bar{I}} + \frac{\nabla\nabla}{k^2}\right) G(\bar{r},\bar{r}_s) \qquad (B.13)$$

The point $\bar{r}$ is again regarded to be unlimitedly close to the initial exciting point $\bar{r}_s$ and all the scattering and reflections are neglected, the Green Function can be simplified as below:

$$G(\bar{r},\bar{r}_s) \approx \frac{e^{-jk|\bar{r}-\bar{r}_s|}}{4\pi|\bar{r}-\bar{r}_s|} \qquad (B.14)$$

So $\bar{E}^{TR}(\bar{r},\bar{r}_s;\omega)$ in frequency domain can be expanded as below:

$$\bar{E}^{TR}(\bar{r},\bar{r}_s;\omega) = j\omega\mu\left\{\left(\bar{\bar{I}} + \frac{\nabla\nabla}{k^2}\right)\left(G^*(\bar{r},\bar{r}_s) - G(\bar{r},\bar{r}_s)\right)\right\} \cdot \bar{\iota}^*(\omega)$$

$$\approx -\frac{\omega\mu}{\lambda}\left\{\left(\bar{\bar{I}} + \frac{\nabla\nabla}{k^2}\right)\left(\frac{\sin(k|\bar{r}-\bar{r}_s|)}{k|\bar{r}-\bar{r}_s|}\right)\right\} \cdot \bar{\iota}^*(\omega) \qquad (B.15)$$

It can be observed that "TR field" is getting focused at the initial exciting point $\bar{r}_s$. The first part of $\bar{E}^{TR}(\bar{r},\bar{r}_s;\omega)$ is $\left(\frac{\sin(k|\bar{r}-\bar{r}_s|)}{k|\bar{r}-\bar{r}_s|}\right)\bar{\bar{I}}$. The second part of $\bar{E}^{TR}(\bar{r},\bar{r}_s;\omega)$ is $\left(\nabla\nabla\frac{\sin(k|\bar{r}-\bar{r}_s|)}{k|\bar{r}-\bar{r}_s|}\right)$, indicating a faster attenuation of the field beyond the first null position. Relatively speaking, it has a sharper focusing compared to the other positions after TR procedure.

The temporal focus can be proved by Fourier Transformation (FT). The TR electric field in time domain can be expressed as:

$$\bar{E}^{TR}(\bar{r},\bar{r}_s;t) = \mu\frac{\partial}{\partial t}\int_{-\infty}^{+\infty}\{\bar{\bar{G}}^*(\bar{r},\bar{r}_s) - \bar{\bar{G}}(\bar{r},\bar{r}_s)\} \cdot \bar{\iota}^*(\omega)e^{j\omega t}d\omega \qquad (B.16)$$

It is found that it has nothing to do with the surface 'S'. This means that all the re-emitted TR signals is focusing on the same location $\bar{r}_s$ at the same time.

Appendix B:

The specifications of some components used in the developed UWB imaging radar system

Table B-1 Technical specifications of the step motor

Rated voltage	12v
Rated current	0.6A
Resistance	20
inductance	35
Detent torque	29.6
Holding torque	500
Step angle accuracy	5
Step angle	1.8
Frame size	23

The specifications of Voltage Controlled Oscillator

Coaxial
Voltage Controlled Oscillator   ZX95-5400+

Linear Tuning   4300 to 5400 MHz

Features
· linear tuning characteristics
· low harmonics, -30 dBc typ.
· low pulling
· low pushing
· protected by US patent 6,790,049

Applications
· r & d
· lab
· instrumentation
· wireless communications
· point-to-point

CASE STYLE: GB956

Connectors	Model	Price	Qty.
SMA	ZX95-5400-S+	$40.95 ea.	(1-9)

+RoHS Compliant
The +Suffix identifies RoHS Compliance. See our web site for RoHS Compliance methoddogies and qualifications

Electrical Specifications

MODEL NO.	FREQ. (MHz)		POWER OUTPUT (dBm)	PHASE NOISE dBc/Hz SSB at offset frequencies,kHz Typ.				TUNING					NON HARMONIC SPURIOUS (dBc)	HARMONICS (dBc)		PULLING pk-pk @12 dBr (MHz)	PUSHING (MHz/V)	DC OPERATING POWER	
								VOLTAGE RANGE (V)		SENSI-TIVITY (MHz/V)	PORT CAP (pF)	3 dB MODULATION BANDWIDTH (MHz)						Vcc (volts)	Current (mA)
	Min.	Max.	Typ.	1	10	100	1000	Min.	Max.	Typ.	Typ.	Typ.	Typ.	Typ.	Max.	Typ.	Typ.		Max.
ZX95-5400+	4300	5400	-1.3	-58	-83	-105	-126	0.5	19	95-135	20	95	-90	-30	-15	7	10	5	30

Maximum Ratings
Operating Temperature	-55°C to 85°C
Storage Temperature	-55°C to 100°C
Absolute Max. Supply Voltage (Vcc)	6.5V
Absolute Max. Tuning Voltage (Vtune)	21.0V
All specifications	50 ohm system

Permanent damage may occur if any of these limits are exceeded.

Outline Drawing
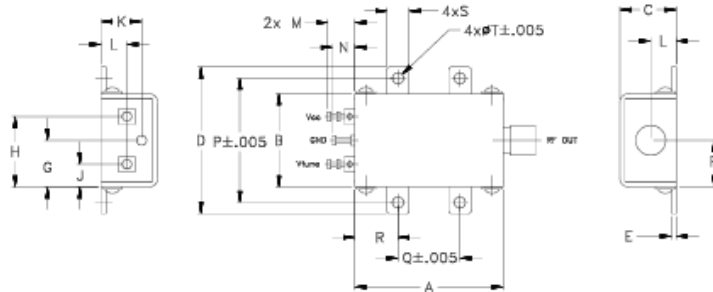
Outline Dimensions ($\frac{inch}{mm}$)

A	B	C	D	E	F	G	H	J	K	L	M	N	P	Q	R	S	T	wt.
1.20	.75	.46	1.18	.04	.38	.38	.57	.18	.33	.21	.22	.18	1.00	.50	.35	.18	.106	grams
30.48	19.05	11.68	29.97	1.02	9.65	9.65	14.48	4.57	8.38	5.33	5.59	4.57	25.40	12.70	8.89	4.57	2.69	35.0

Performance Data & Curves*

ZX95-5400+

V TUNE	TUNE SENS (MHz/V)	FREQUENCY (MHz)			POWER OUTPUT (dBm)			Icc (mA)	HARMONICS (dBc)			FREQ. PUSH (MHz/V)	FREQ. PULL (MHz)	PHASE NOISE (dBc/Hz) at offsets				FREQ OFFSET (KHz)	PHASE NOISE at 4850 MHz (dBc/Hz)
		-55°C	+25°C	+85°C	-55°C	+25°C	+85°C		F2	F3	F4			1kHz	10kHz	100kHz	1MHz		
0.00	72.56	4039.4	4031.0	4065.5	0.84	-0.55	-2.45	22.38	-23.2	-35.8	-38.0	2.33	8.07	-61.9	-87.1	-108.6	-128.8	1.0	-58.43
0.50	61.47	4074.8	4067.3	4099.8	0.94	-0.42	-2.38	22.36	-23.4	-34.7	-39.7	2.06	7.04	-62.4	-86.8	-107.9	-128.2	2.0	-65.90
1.00	55.88	4104.7	4098.0	4127.2	1.04	-0.40	-2.34	22.40	-23.8	-35.1	-38.1	1.19	8.13	-64.2	-88.8	-110.3	-130.3	3.5	-71.91
2.50	77.59	4202.9	4195.3	4225.0	0.95	-0.47	-2.47	22.32	-24.6	-40.7	-41.6	0.05	13.36	-62.7	-86.9	-108.1	-128.4	6.0	-77.84
3.00	102.33	4241.4	4234.1	4267.0	0.79	-0.71	-2.54	22.25	-24.9	-38.5	-42.9	0.74	7.21	-61.9	-87.6	-107.9	-128.2	8.5	-81.38
4.00	123.63	4341.7	4334.2	4357.8	0.20	-1.28	-2.79	22.08	-26.7	-35.8	-46.1	5.06	10.59	-61.0	-84.1	-105.9	-126.2	10.0	-83.16
5.00	130.46	4469.4	4456.5	4471.8	-0.27	-1.65	-2.89	21.91	-29.5	-43.9	-55.5	10.15	10.03	-57.5	-82.4	-104.1	-124.5	20.8	-90.66
6.00	122.67	4601.0	4589.4	4596.0	-0.36	-1.59	-2.80	21.85	-30.6	-40.2	-54.0	10.59	8.13	-57.1	-83.0	-105.3	-125.6	35.5	-95.83
7.00	121.99	4726.6	4715.3	4717.2	-0.37	-1.44	-2.62	21.90	-32.4	-36.7	-52.1	10.44	10.28	-57.0	-83.5	-106.0	-126.6	60.7	-100.87
7.50	115.65	4790.4	4776.3	4775.1	-0.17	-1.53	-2.70	21.88	-33.7	-33.8	-54.0	12.78	10.35	-57.2	-83.1	-104.4	-125.1	86.7	-104.15
8.00	121.63	4847.4	4834.1	4832.1	-0.36	-1.30	-2.40	21.96	-33.6	-34.1	-55.5	11.16	4.70	-58.0	-82.6	-105.9	-126.6	100.0	-105.32
9.00	114.31	4963.4	4947.7	4941.8	-0.27	-1.24	-2.29	22.01	-33.8	-47.1	-54.6	12.55	10.18	-56.3	-82.5	-105.5	-126.0	148.1	-109.07
10.00	110.92	5071.6	5055.5	5046.4	-0.05	-1.00	-1.96	22.07	-33.4	-40.0	-54.7	12.69	4.49	-57.2	-82.1	-105.0	-125.7	177.0	-110.67
12.00	107.29	5292.6	5268.9	5249.4	-0.61	-1.25	-1.90	22.23	-36.4	-29.1	-44.8	10.44	7.95	-60.3	-82.8	-106.2	-126.9	211.6	-112.31
13.00	102.20	5397.6	5371.0	5348.3	-0.62	-1.49	-2.12	22.35	-40.5	-34.8	-51.6	11.98	9.33	-58.2	-82.1	-104.8	-125.9	302.4	-115.44
13.50	96.82	5446.0	5422.1	5397.5	-0.12	-1.03	-2.18	22.46	-42.7	-37.0	-53.2	10.75	5.03	-57.3	-83.2	-106.0	-127.0	361.5	-117.13
15.00	91.83	5589.5	5562.3	5534.1	0.33	-0.38	-1.09	22.79	-43.7	-43.7	-54.0	10.84	4.86	-55.7	-83.8	-106.3	-127.4	507.5	-120.10
16.00	82.61	5678.5	5649.8	5619.0	0.53	0.13	-0.75	23.01	-39.5	-42.6	-53.7	12.46	3.64	-55.1	-82.5	-105.3	-126.7	606.7	-121.75
18.00	73.00	5837.2	5805.1	5769.2	1.28	0.22	-0.08	23.50	-34.2	-46.6	-53.6	14.89	5.07	-54.7	-81.0	-104.3	-125.3	851.6	-124.71
19.00	65.54	5905.5	5872.7	5837.4	0.80	0.64	0.07	23.82	-33.1	-50.1	-52.8	14.02	5.93	-54.8	-81.9	-104.8	-126.1	1000.0	-125.89

*at 25°C unless mentioned otherwise

ZX95-5400+
Frequency and Tuning Sensitivity

ZX95-5400+
Power Output

ZX95-5400+
Harmonics Level

ZX95-5400+
Frequency Pulling & Pushing (Vcc ± 5%)

ZX95-5400+
Phase Noise Vs. Tuning Voltage

ZX95-5400+
Phase Noise

The specifications of Low Noise Amplifier

SQUARE-WAVE   **A-0110**
LO BUFFER-AMPLIFIER

Features

- Frequency Range 1.0 to 10.0 GHz
- Very Broadband
- Surface Mount Package
- 0 to +5 dBm Typical Input Power
- +21 dBm Typical Saturated Output Power

Electrical Specifications - Specifications guaranteed from -30 to +70°C, measured in a 50-Ohm system.

Parameter	Frequency (GHz)	Min	Typ	Max
Input (dBm)	1.0-10.0		0 to +5	
Saturated Output Power (dBm)	1.0-10.0	+18	+21	
Small Signal Gain (dB)	1.0-10.0		26	
Noise Figure (dB)	1.0-10.0		3.5	
Bias Requirements (mA)[1]				
+5.0 Volts DC			200	250
-0.7 Volts DC (-5 volt DC Option)			10	20

[1]It is recommended that the negative bias be applied before or concurrent with the positive bias.

*Note: EZ-Carrier Buffer Amplifiers are not suitable for in-line reflow solder. Manual assembly only.
(Refer to EZ Installation Notes).

Part Number Options

Model Number	Description	Package Style(s)[1]
A-0110EZ (Add "5" for -5V Option) A-0110EZP (Add "5" for -5V Option)	1.0 to 10.0 GHz Amplifier	EZ, EZP

[1]Connectorized test fixtures available for most surface mount packages. Contact factory.

215 Vineyard Court, Morgan Hill, CA 95037 | Ph: 408.778.4200 | Fax 408.778.4300 | info@markimicrowave.com

Marki
microwave

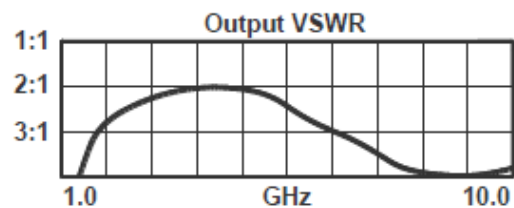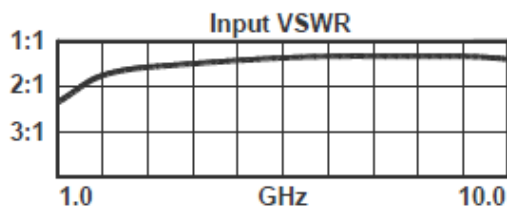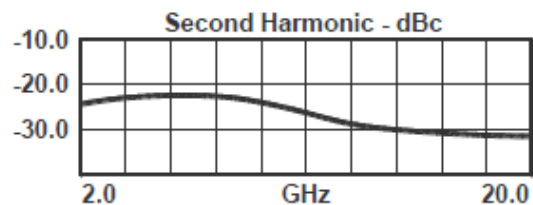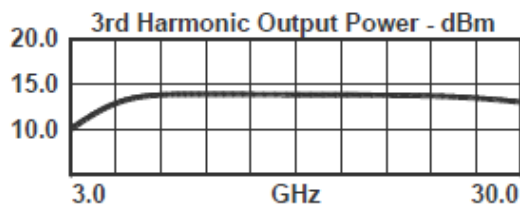## LO BUFFER-AMPLIFIER

A-0110

Page 2

Frequency 1.0 to 10.0 GHz

Typical Performance

Saturated Output Power - dBm
0 dBm In

3rd Harmonic Output Power - dBm

Second Harmonic - dBc

Input VSWR

Output VSWR
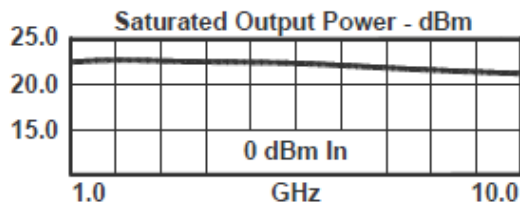
DATA SHEET NOTES:

1. Maximum input power without damage is +20 dBm at +70°C.
2. Specifications are subject to change without notice. Contact Marki Microwave for the most recent specifications and data sheets.

The specifications of Double-Balanced Mixers

DOUBLE-BALANCED MIXERS   M1-0212

Features

- LO/RF 2.0 to 12.0 GHz
- IF DC to 2.0 GHz
- 6.0 dB Typical Conversion Loss
- 35 dB Typical LO to RF Isolation
- Ultra-Broadband LO and RF

Electrical Specifications - Specifications guaranteed from -55 to +100°C, measured in a 50-Ohm system.

Parameter	LO (GHz)	RF (GHz)	IF (GHz)	Min	Typ	Max	Diode Option LO drive level (dBm)
Conversion Loss (dB)	2.0-12.0	2.0-12.0	DC-1.0		6.0	7.5	
	2.0-12.0	2.0-12.0	1.0-2.0		7.0	8.5	
Isolation (dB)							
LO-RF	2.0-12.0	2.0-12.0		25	35		
LO-IF	2.0-12.0	2.0-12.0			20		
RF-IF	2.0-12.0	2.0-12.0			25		
Input 1 dB Compression (dBm)	2.0-12.0	2.0-12.0			+2		L (+7 to +10)
					+5		M (+10 to +13)
					+8		N (+13 to +16)
					+11		H (+16 to +19)
					+14		S (+19 to +22)
Input Two-Tone Third Order Intercept Point (dBm)	2.0-12.0	2.0-12.0			+12		L (+7 to +10)
					+15		M (+10 to +13)
					+18		N (+13 to +16)
					+21		H (+16 to +19)
					+24		S (+19 to +22)

Part Number Options

Please specify diode level and package style by adding to model number.					
Package Styles		**Examples**			
Connectorized[1]	A	M1-0212LA, M1-0212LE-2			
Microstrip [2,3]	E	M1-0212	L	E	-2
Surface Mount [2,3]	EZ	(Model)	(Diode Option)	(Package)	(I-Port Configuration)

[1]B, C, P style connectorized packages available (not recommended for new designs).
[2]Connectorized test fixtures available for most microstrip and surface mount packages. Consult factory.
[3]For non-connectorized packages, specify I-port configuration by adding –1 or –2 suffix to model number. Default is –2 configuration when not specified.

215 Vineyard Court, Morgan Hill, CA 95037 | Ph: 408.778.4200 | Fax 408.778.4300 | info@markimicrowave.com
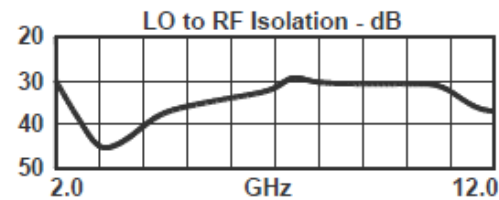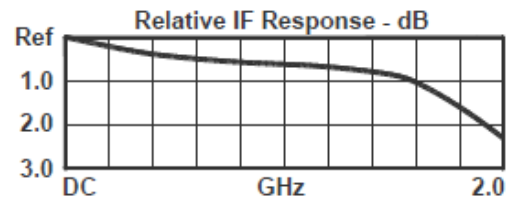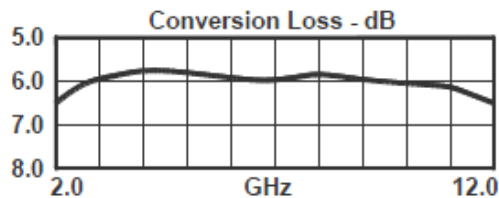
Appendix B

DOUBLE-BALANCED MIXERS

Page 2

M1-0212

LO/RF 2.0 to 12.0 GHz
IF DC to 2.0 GHz

Typical Performance
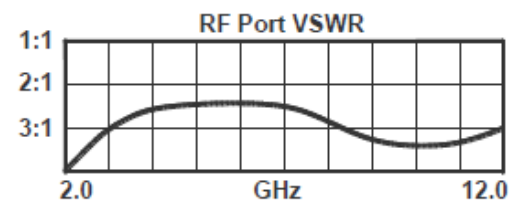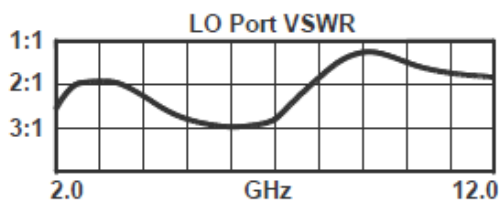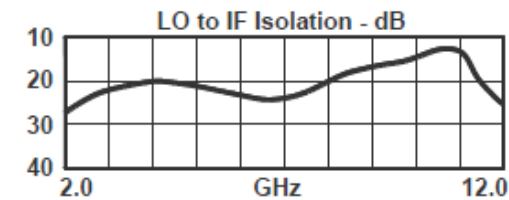
DATA SHEET NOTES:

1. Mixer Conversion Loss Plot IF frequency is 100 MHz.
2. Mixer Noise Figure typically measures within +0.5 dB of conversion loss for IF frequencies greater than 5 MHz.
3. Conversion Loss typically degrades less than 0.5 dB for LO drives 2 dB below the lowest and 3 dB above highest nominal LO drive levels.
4. Conversion Loss typically degrades less than 0.5 dB at +100°C and improves less than 0.5 dB at -55°C.
5. Maximum input power is +23 dBm at +25°C, derated linearly to +20 dBm at +100°C.
6. Specifications are subject to change without notice. Contact Marki Microwave for the most recent specifications and data sheets.
7. Standard configuration for A, B, and C outlines are with connectors and bottom spacer.
8. Catalog mixer circuits are continually improved. Configuration control requires custom mixer model numbers and specifications.